



Available online at www.sciencedirect.com



Progress in Aerospace Sciences 41 (2005) 192–300

PROGRESS IN
AEROSPACE
SCIENCES

www.elsevier.com/locate/paerosci

High-order accurate, low numerical diffusion methods for aerodynamics

John A. Ekaterinaris

Foundation for Research and Technology FORTH, Institute of Applied and Computational Mathematics IACM, FORTH/IACM,
71110 Heraklion, Crete, Greece

Abstract

In recent years numerical methods have been widely used to effectively resolve complex flow features of aerodynamics flows with meshes that are reasonable for today's computers. High-order numerical methods were used mainly in direct numerical simulations and aeroacoustics. For many aeronautical applications, accurate computation of vortex-dominated flows is important because the vorticity in the flow field and the wake of swept wings at an incidence and rotor blades largely determines the distribution of loading. The main deficiency of widely available, second-order accurate methods for the accurate computation of these flows is the numerical diffusion of vorticity to unacceptable levels. Application of high-order accurate, low-diffusion numerical methods can significantly alleviate this deficiency of traditional second order methods. Furthermore, higher-order space discretizations have the potential to improve detached eddy simulation predictions of separated flows with significant unsteadiness. Recently developed high-order accurate finite-difference, finite-volume, and finite-element methods are reviewed. These methods can be used as an attractive alternative of traditional low-order central and upwind computational fluid dynamics methods for improved predictions of vortical and other complex, separated, unsteady flows. The main features of these methods are summarized, from a practical user's point of view, their applicability and relative strength is indicated, and examples from recent applications are presented to illustrate their performance on selected problems.

© 2005 Elsevier Ltd. All rights reserved.

Contents

1. Introduction	194
1.1. Prior work on high-order numerical methods	196
2. Governing equations	198
2.1. Conservative form of the NS equations	198
2.2. Entropy splitting	199
2.3. Time integration of the Euler and NS equations	200
2.3.1. Explicit temporal schemes	201
2.3.2. Implicit schemes	202
2.3.3. Time accurate solutions with multigrid	202

E-mail address: ekaterin@iacm.forth.gr.

3.	High-order finite-difference schemes	203
3.1.	Centered compact schemes	203
3.2.	Boundary closures for high-order schemes	204
3.3.	Simultaneous evaluation of the first and second derivative with compact schemes	205
3.4.	Modified high-order finite-difference schemes	206
3.4.1.	Upwind high-order schemes	206
3.4.2.	Dispersion-relation-preserving (DPR) scheme	207
3.5.	Spectral-type filters	207
3.6.	Characteristic-based (ACM) filters	208
3.6.1.	ENO and WENO ACM filters	210
3.7.	Finite-volume compact difference-based schemes	211
3.8.	Results with ACM filters	212
3.9.	Results with compact schemes and filters	218
4.	ENO and WENO schemes	227
4.1.	High-order reconstruction	228
4.2.	Approximation in one dimension	228
4.3.	One-dimensional conservative approximation of the derivative	229
4.4.	ENO reconstruction	230
4.5.	1D finite-volume ENO scheme	231
4.6.	1D finite-difference ENO scheme	232
4.7.	WENO approximation	232
4.8.	Multidimensional ENO and WENO reconstruction	234
4.8.1.	Finite-volume reconstruction for Cartesian mesh	234
4.8.2.	Two-dimensional reconstruction for triangles	235
4.8.3.	Multidimensional finite-difference ENO	236
4.9.	Optimization of WENO schemes	236
4.10.	Compact WENO approximation	237
4.11.	Hybrid compact-WENO scheme for the Euler equations	239
4.12.	Applications of ENO and WENO	240
5.	The discontinuous Galerkin (DG) method	256
5.1.	DG space discretization	257
5.2.	Element bases	258
5.3.	Arbitrary high-order DG schemes	260
5.4.	Analysis of the DG method for wave propagation	260
5.5.	Dissipative and dispersive behavior of high-order DG method	261
5.6.	Limiting of DG expansions	261
5.6.1.	Rectangular elements	262
5.6.2.	Triangular elements	262
5.6.3.	Component-wise limiters	263
5.7.	DG stabilization operator	264
5.8.	DG space discretization of the NS equations	264
5.9.	The DG variational multiscale (VMS) method	265
5.10.	Implicit time marching of DG discretizations	269
5.11.	p-type multigrid for DG	270
5.12.	Results with the DG method	270
6.	The spectral volume (SV) method	276
6.1.	Fundamentals of the SV method	277
6.2.	SV method in one dimension	279
6.2.1.	Reconstruction for SV in one dimension	279
6.3.	Polynomial reconstruction in triangular SVs	281
6.4.	Linear, quadratic, and cubic SV reconstructions	283
6.5.	Spectral volume partitions	284
6.6.	Multidimensional limiters	284
6.7.	The SV method for two-dimensional systems	285
6.8.	Multidimensional TVD and TVB limiters	286
6.9.	The SV method for the Navier–Stokes equations	287

6.9.1. SV formulation for 2D convection-diffusion equation	287
6.9.2. Extension of the SV method to the NS equations	287
6.10. The SV method in three dimensions	288
6.11. Results with the SV method	288
7. Conclusions	292
. Appendix	293
References	293

1. Introduction

In this paper, we explore applications of high-order methods in aerodynamics. High-order methods typically have at least third-order spatial accuracy. Traditionally, second-order accurate numerical methods are often preferred in practical aerodynamic calculations because of their simplicity and robustness. High-order accurate methods are often perceived as less robust, costly to run, and complicated to understand and code. As a result, there are very few working computational fluid dynamics (CFD) codes that use higher-order accurate schemes for production numerical simulations of compressible flow. This is especially true for codes designed to compute steady flows. We will attempt to dispel this negative impression about high-order methods.

Before presenting the essential details of high-order methods, we point out that in many practical aerodynamic problems, the solution structures are so complicated and their time evolution is so long, that it is impossible to obtain an acceptable solution with today's computing speeds using high-grid density and low-order methods. These problems often involve regions of complicated but smooth flow structures, such as vortices interacting with each other or with shear layers, and regions that contain both shocks and complex smooth structures. Some examples of these flows are briefly discussed in the following paragraphs.

Vortical flow fields are especially challenging for the low-order numerical methods that are typically found in current Euler and Navier–Stokes flow solvers. The main cause for this deficiency is that these vortical flow features deform and dissipate prematurely due to excessive numerical diffusion in the solution algorithms. It is well recognized that low-order CFD algorithms require extremely fine grid resolution to accurately convect and preserve the strength of vortical flow fields. This fine grid resolution requirement leads to extremely large computational problems that cannot be solved on even the largest parallel computer architectures.

It is straightforward to demonstrate the power of high-order numerical methods by examining the numerical approximation of a smooth function on a regular grid. For a second-order accurate numerical scheme, the error in the functional approximation is proportional to h^2 , where h the mesh size Δx . For an n th-order accurate numerical scheme, the error in the functional approx-

imation is proportional to h^n . If we cut the grid spacing in half, the error in the second-order scheme reduces by a factor of 4 and the error in the fourth-order scheme reduces by a factor of 16. Provided that the computational requirements for the second- and fourth-order schemes are similar, the fourth-order scheme is clearly more efficient. Efficiency improvements are even greater for higher-order approximations. A demonstration of the superior performance of high-order, low-dissipative, centered schemes compared to lower-order more dissipative TVD schemes in preserving vorticity [1] is shown in Fig. 1. The conversion of a two-dimensional isentropic vortex is carried out for long time with the numerical solution of the inviscid compressible flow equations on a Cartesian mesh. At the absence of physical viscosity, the loss in vortex strength due to the numerical diffusion of the scheme is evident. For three-dimensional computations, grid refinement in all three directions, which is necessary for better resolution of vortical structures that are isotropic, becomes very expensive computationally. Therefore, application of high-order schemes is expected to significantly decrease computing cost.

To better demonstrate the potential of higher-order methods make the following assumptions: (1) The error in the solution is $\mathcal{O}(h^p)$ where h is the mesh length and p is the order of accuracy. (2) The number of intervals N_i in the grid, or elements for a finite-element method, is related to the cell size by $N_i = \mathcal{O}(h^{-d})$, where d is the spatial dimension of the problem. (3) Higher-order of accuracy is achieved by increasing the stencil, or the number of unknowns per element, $N_s = \mathcal{O}(p^d)$. Thus the total number of operations or unknowns, N , scales as $N = N_i N_s = \mathcal{O}((p/h)^d)$. (4) The operation count, W , required to solve the discrete problem scales as $W = \mathcal{O}(N^w)$, where w is the complexity of the discretization method. (5) The total time required for the numerical solution is $T = W/F$, where $1/F$ is the time for a single operation, which depends on the processor speed. These assumptions lead to the conclusion that the computing time, T , required to achieve a specific error tolerance E scales as

$$T = \mathcal{O}((p/E^{1/p})^{wd}/F)$$

or taking the logarithm

$$\log T \approx wd \left(-\frac{1}{p} \log E + \log p \right) - \log F.$$

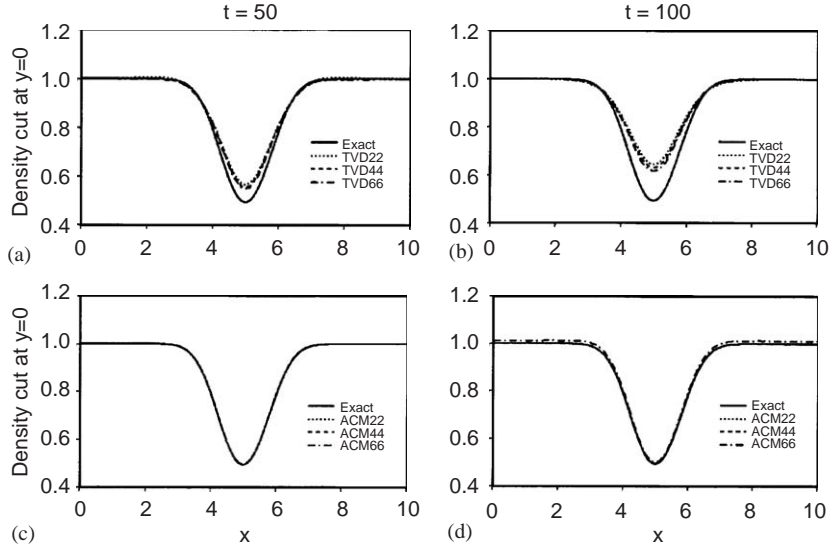


Fig. 1. Stationary vortex: comparison of the various orders of TVD and ACM methods with the exact solution, illustrated by density profiles at the centerline $y = 0$, at $t = 50$ and 100 for a 401×81 grid ($\kappa = 0.05$).

For stringent accuracy requirements ($E \ll 1$), it is expected that the term $\log E$ dominates the $\log p$ terms. Therefore, the computing time will depend exponentially on the order of accuracy, p , the complexity of the method, w , and the grid resolution d . The above reasoning demonstrates that, from a practical point of view, it pays off to improve the order of accuracy provided that the operation count does increase dramatically. Furthermore, from the first equation it is evident that small changes of the ratio w/p can reduce computing time, which scales only inversely by the processor speed F .

The most widely used flow solvers for aerospace applications are based on the solution of the Reynolds-averaged Navier-Stokes (RANS) equations. These RANS methods have recently benefited from improved performance of workstations, supercomputers, and parallel processors. Hardware improvements combined with advances in areas such as grid generation and more computationally efficient solution algorithms made RANS a tool that often complements wind tunnel. RANS flow solvers have proven useful for airloads prediction, examination of detailed and gross flow features, as well as engineering design. The primary limitation of RANS is the inability to predict turbulent, separated flow. Turbulence models used in RANS, model the entire spectrum of turbulence and they are unable to accurately predict phenomena dominated by turbulent eddies of massively separated flows. The deficiency of RANS to predict turbulent separated flow combined with the unphysical diffusion of vorticity by the numerical scheme in flow regions away from the

wall, where the grid density is small, is responsible for inaccuracies of the computed flow field.

Attempts to overcome these deficiencies of RANS methods to accurately compute turbulent separated flow have led to the development of large eddy simulation (LES) [2–7], and more recently the detached eddy simulation (DES) approaches [8–10]. Both of these techniques, fully resolve the three-dimensional vortical structures and turbulent motions in detached flow regions. In addition, LES methods also resolve certain range of the small-scale turbulent flow structures in the attached or separated flow boundary layers. DES methods, on the other hand, model the attached flow regions with RANS techniques. As a result, the resolution requirements of DES are significantly lower than LES for the attached boundary layers, where the RANS turbulence model is used. In the separated flow field, however, the resolution requirements for DES are comparable to those for LES calculations. Like the RANS, LES and DES can also benefit from the application of high-order numerical algorithms to better resolve separated flow regions. Most of the high-order numerical methods that we will discuss in this paper are therefore expected to have applications to RANS, LES and DES flow solvers.

In particular, high-resolution requirements that are encountered in typical LES of complex flows can be met with the application of high-order numerical methods. For LES of flows in simple domains, the resolution problem is solved with the use of the highly accurate spectral methods [11,12]. Spectral methods are not, however, easy to apply for complex domains and

compressible flows with discontinuities. For flows with complex geometries that preclude the use of spectral methods, the use of high-order numerical methods is a necessity in order to minimize the overall computational cost. The continued increase of computing power and developments of parallel computing are expected to make possible DES or even LES of flows with increased complexity. For these applications, use of high-order accurate CFD methods is necessary.

While the use of high-order accurate numerical methods is relatively common for direct numerical simulations (DNS) and LES methods, high-order numerical methods have not been commonly used for DES. As a result, DES of complex flows often exhibit significant grid dependence. It is expected that use of high-order spatially accurate numerical schemes combined with improvements of DES models [13] will eliminate the grid dependencies in DES calculations. We hope that the resulting high-order RANS/DES hybrid models will yield reliable predictions of realistic, separated, unsteady flows in a computationally efficient manner.

1.1. Prior work on high-order numerical methods

The favorable effects of high-order accurate methods was early recognized even in several RANS simulations. For example, simulations of delta wing vortical flows [14], wind tip vortices [15], and helicopter rotor [16]. The sensitivity of the numerical solution on grid resolution [14,16], and the order of accuracy of the numerical scheme [14,15] on the resolution of vortices was demonstrated. Delta wing flows are dominated by the leading edge vortices and accurate capturing of the correct strength of the leading edge vortex strength is essential for the prediction of loads and the vortex breakdown location. Fig. 2 shows the effects of increased grid resolution and high-order of accuracy for the computation of the leading edge vortices over a double delta wing [14]. It appears that the increase in order of accuracy can yield better resolution of the vortices even with lower grid resolution. Similar conclusions are reported for the numerical prediction of the wing-tip vortex [15]. In this study, increased grid density and higher-order numerical schemes significantly improved the accuracy of the final results. The comparisons of the predicted peak velocity in the vortex core [15] shown in Fig. 3 demonstrate that in addition to turbulence model the order of the scheme plays a very significant role.

Furthermore, computations of rotorcraft flows [16,17] demonstrated that the tip vortex is severely diffused by the first passage even in computations performed with 10 million grid points. These computations used curvilinear structured meshes and suffered from an inappropriate placement of the grid points and insufficient

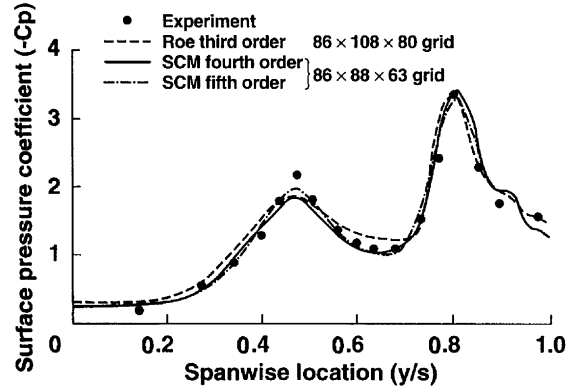


Fig. 2. Computed surface pressure distribution with different grid densities and order of accuracy over a double delta wing at $M = 0.22$, $\alpha = 19^\circ$, $Re = 4 \times 10^6$.

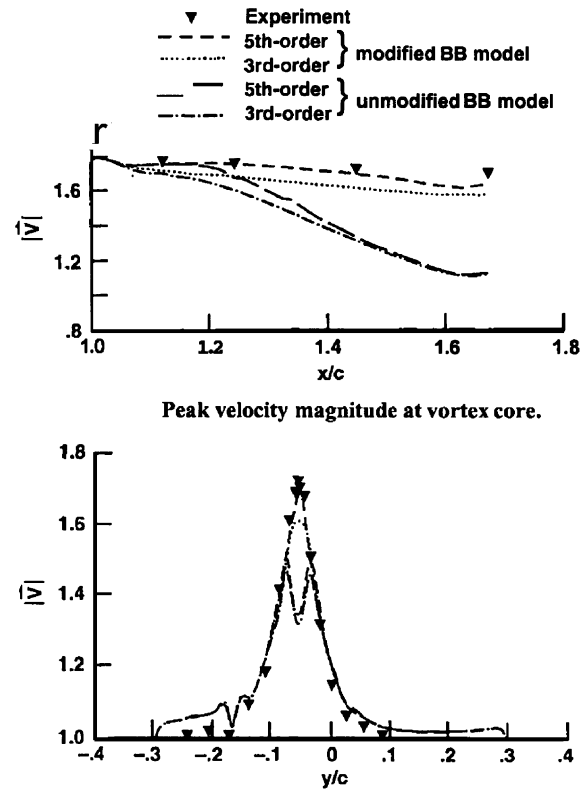


Fig. 3. Comparison of third- and fifth-order accurate differencing on the solution for a wake-case grid having 371,000 points ($35 \times 103 \times 103$).

grid resolution for the tip vortex. This problem was addressed by the tetrahedral unstructured flow solver approach [17]. It was concluded, however, that adaptive tetrahedral mesh approaches could have only limited

success for even the simplest hovering rotor cases because the adapted grid is anisotropic with computational cells of very large aspect ratio. The overset grid approach [18] appears to resolve some of the problems associated with grid topology but it still requires very high grid resolution (greater than 60 million grid points) for accurate capturing of the tip vortex. On the other hand, calculations performed with high-order accurate schemes in [19–21] and more recently in [22] demonstrated that significant improvements in the accuracy of rotor performance predictions can be obtained with just a small increase in computing cost.

For the computation of flows with shocks, methods designed to regularize the numerical solution have been studied since the early attempts of von Neumann and Richtmayer [23] who used finite-difference techniques combined with the so-called artificial viscosity or numerical dissipation. Use of numerical dissipation in the finite-difference and finite-volume context has found widespread application in solution methods for compressible aerodynamic flows. The main difficulty in the application of these methods in DNS, DES, and LES of compressible flows is the control of numerical dissipation necessary to capture discontinuities that occur in such flows. Too much numerical dissipation smears out important flow field features. Too little numerical dissipation yields unstable solutions. It was recently demonstrated (see [24] and references therein) that the inherent dissipation of nonlinear high-resolution methods can be exploited to successfully compute certain types of turbulent flows [25] without need to resort to an explicit turbulence model.

In previous numerical investigations [26,27], it was shown that even the reduced numerical dissipation of high-order, shock-capturing schemes can lead to significant damping of turbulence fluctuations and mask the effects of the subgrid-scale (SGS) models. For these cases, a local application of the shock-capturing scheme was found absolutely necessary in order to minimize numerical dissipation. In the study of [26], for example, this requirement was achieved by means of the application of an essentially non-oscillatory (ENO) scheme only in the shock-normal direction and over a few mesh points around the mean shock position. Unfortunately, in most cases, the shock position is unknown and one needs to introduce a sensor to detect possible discontinuities.

In recent years, efforts were made to alleviate the effects of numerical diffusion introduced by shock capturing schemes and upwind methods. It was shown [28–31] that for compressible flows without discontinuities, high-order centered finite-difference schemes are sufficiently stable and accurate for the computation of convecting vortical structures and aeroacoustic disturbances when they are combined with explicit, spectral-type filtering for numerical stability [28]. In addition,

centered schemes were found particularly useful for prediction of noise sources. These high-order centered schemes, which can be extended into finite-volume context, and the spectral-type or characteristic-based filters, which are necessary to stabilize centered schemes and suppress spurious modes, are summarized in Section 3.

For high-speed flows with shocks, numerical solutions that are uniformly high-order accurate up to the discontinuity can be obtained with ENO [32] and weighted ENO (WENO) [33,34] schemes. These methods are presented in detail in Section 4. On the other hand, it was shown that explicit filters [30] could also be used with high-order centered schemes to obtain shock capturing. Application of explicit filters [30] yielded improved computational efficiency of flows with discontinuities compared to ENO [32] or WENO methods [33,34]. Explicit filters can be easily implemented into existing codes because the filter step is essentially independent of the basic differencing scheme and is applied as post processing. In the same spirit, Yee et al. [1] showed that the dissipative part of a shock-capturing scheme could be applied after each time step to regularize the numerical solution and acts like a filter. Moreover, to meet the requirement of a local application of the numerical dissipation, the amplitude of the dissipation is evaluated with a sensor derived from the artificial compression method (ACM) of Harten [35]. The filters of Yee et al. [1] are referred to as characteristic-based filters and they are summarized in Section 3. The numerical test in Yee et al. [1] used total variation diminishing (TVD) schemes to construct the characteristic-based, non-linear filter. The possibility of using high-order non-linear filters based on essentially non-oscillatory (ENO) reconstruction has been demonstrated in [36].

In parallel with the finite-difference [37], finite-volume methods [38], and high-resolution methods [39], which found widespread application in CFD and turbulence simulation, finite-element methods [40–44] were also used for convection-dominated problems. Application of the finite-element method is far from trivial for non-linear convective problems, such as compressible flow with discontinuities. For such cases, the finite-element numerical solution must capture the physically relevant discontinuities without introducing spurious oscillations. This issue is addressed successfully by the discontinuous Galerkin (DG) method [45]. The DG method assumes discontinuous approximate solutions. Subsequently, it treats discontinuities in a manner analogous to high-resolution finite-difference and finite-volume methods for nonlinear hyperbolic systems by incorporating suitably defined numerical fluxes and slope limiters into the finite-element framework. Due to its local character, the DG finite-element method is very suitable for local grid refinement and becomes highly

parallelizable. This method is also presented and analyzed in Section 5.

Recently, another type of high-order accurate, conservative and computationally efficient scheme was introduced for the solution of conservation laws in unstructured grids. This scheme is known as the spectral volume (SV) method [46]. The concept of a “spectral volume” was introduced to achieve high-order accuracy in an efficient manner similar to spectral methods and at the same time retain the benefits of the finite-volume formulations for problems with discontinuities. In the SV method, each spectral volume, which is the same as the traditional triangular or tetrahedral finite volume, is further subdivided into volumes called control volumes. Cell-averaged data from these control volumes are used to reconstruct a high-order approximation in the spectral volume, while Riemann solvers are used to compute the fluxes at the spectral volume boundaries. The main difference of the SV method and DG method is that for the SV method, the cell-averaged variables in the control volumes are updated independently. Similar to the DG method, the SV method uses TVD or total variation bounded (TVB) limiters to eliminate/reduce spurious oscillations near discontinuities. A very desirable feature of the SV method is that the reconstruction is carried out analytically, and does not involve large stencils in contrast to the computationally intensive reconstruction in high-order finite-volume methods.

The DG and SC methods are both suitable for high-order discretization of complex domains using unstructured meshes. In addition, they are fully conservative due to the use of Riemann fluxes across element boundaries. Another high-order conservative scheme for unstructured quadrilateral grids is the multidomain spectral method on a staggered grid recently developed by Kopriva and Kolias [12,47–49]. The multidomain spectral method is similar to the spectral element method by Patera [50]. The spectral element method is high-order accurate and more flexible compared to spectral methods for discretizations of complex domains. It is however not conservative. Although very high order of accuracy can be achieved with both the multidomain spectral and the spectral element method, these methods are difficult to extend to other cell types such as triangles or tetrahedral cells [51]. These spectral methods and other recent, less widely used, high-order methods [52,53] will not be presented here. Further information about these methods can be found in the original references. A detailed presentation of the theory and implementation of the spectral element method can also be found in the recent book by Karniadakis and Sherwin [43].

This paper is organized as follows: The governing equations in differential and integral form are presented in Section 2. Time integration methods for high-order

accurate schemes are also summarized in Section 2. The presentation of high-order accurate spatial discretization methods is given in Sections 3–6. In Section 3, high-order accurate discretization with finite-difference and finite-volume centered methods is presented. In Section 4, ENO and WENO reconstruction is explained and WENO and ENO high-order schemes are presented. The discontinuous Galerkin method is presented and analyzed in Section 5. In Section 6, the recently developed spectral volume method is presented. At the end of each section selected examples from the application of the high-order methods are shown. Finally, in Section 7, some comparisons and general remarks are given.

2. Governing equations

The full Navier–Stokes (NS) equations govern nonlinear fluid dynamics and aeroacoustics over complex configurations. For the majority of compressible flow simulations, these equations are cast in the strong conservation form [37]. For numerical solutions based on the Galerkin/least-squares method, different sets of variables may be used [54]. For all sets of variables tested with the Galerkin/least-squares method [54], global conservation and correct shock structure was achieved for any set of variables. This is not, however, true for finite-difference and finite-volume numerical methods traditionally used in aerodynamics. These methods use the conservative flow variables to ensure conservation and discontinuity capturing. The primitive variable formulation was used rarely in aerodynamics either with shock fitting schemes [55], or for the computation of subsonic compressible flows without discontinuities [56]. The transformation from conservative to primitive variables or other sets of variables is obtained by multiplying the conservative variables vector with the appropriate flux Jacobian. For example, primitive variables are obtained by multiplying with $M = \partial U / \partial V$, $U = [\rho, \rho u, \rho v, E_T]$, $V = [\rho, u, v, p]$ see [57] for more details.

2.1. Conservative form of the NS equations

The conservative variable formulation of the N–S equations in divergence form is

$$\frac{\partial \mathbf{U}}{\partial t} + \nabla \cdot \mathbf{F}_i = \frac{1}{Re} \nabla \cdot \mathbf{F}_v, \quad (2.1)$$

where \mathbf{U} is the conservative variable vector, \mathbf{F}_i is the inviscid flux vector, and \mathbf{F}_v is the viscous flux vector.

Numerical solutions with finite-volume (FV) methods are obtained with the integral form of the NS equations

for a control volume Ω with boundary $\partial\Omega$

$$\frac{\partial}{\partial t} \int_{\Omega} \mathbf{U} d\mathbf{x} + \oint_{\partial\Omega} [F(\mathbf{U}, \mathbf{n}) - F_v(U, \nabla U, \mathbf{n})] dS = 0, \quad (2.2)$$

where $\mathbf{U} = [\rho, \rho\mathbf{V}, \rho E]^T$, $F(\mathbf{U}, \mathbf{n}) = \mathbf{V} \cdot \mathbf{n} \mathbf{U}$, $F_v(\mathbf{U}, \nabla \mathbf{U}, \mathbf{n}) = [0, \mathbf{t}, \mathbf{t} \cdot \mathbf{V} - \mathbf{q} \cdot \mathbf{n}]^T$, with \mathbf{t} and \mathbf{q} representing the stress and heat flux vectors, $\mathbf{V} = (u, v, w)^T$ is the velocity vector, and \mathbf{n} is the outward unit normal vector to the boundary $\partial\Omega$. For flows with discontinuities the integral form holds and any discrete scheme must obey both local and global conservation in order to capture correctly weak solutions [58]. Finite-volume (FV) methods gained popularity in aerodynamics because they make possible numerical solutions in complex domains with unstructured or mixed type grids [59]. During the 1980s upwind mechanisms were introduced into FV algorithms leading to increased robustness of FV for applications with strong shocks and provided better resolution of viscous layers due to the decrease of numerical dissipation compared to FV methods that employed artificial dissipation [60,61].

Finite-element (FE) methods, which use the weak form of Eq. (2.1), gained popularity in aerodynamics with the development of the discontinuous Galerkin method [45] and the stabilized finite-element methods [62–64]. The weak form is obtained by multiplying the strong form of Eq. (2.1) by a test function W^t and integrating over the domain. The weak form of Eq. (2.1) is

$$\begin{aligned} \frac{\partial}{\partial t} \int_{\Omega} W^t \mathbf{U} d\mathbf{x} + \oint_{\partial\Omega} W^t [F(\mathbf{U}, \mathbf{n}) - F_v(U, \nabla U, \mathbf{n})] \cdot \mathbf{n} dS \\ - \int_{\Omega} \nabla W^t [F(\mathbf{U}, \mathbf{n}) - F_v(U, \nabla U, \mathbf{n})] d\mathbf{x} = 0. \end{aligned} \quad (2.3)$$

The integral form, Eq. (2.2), is the weak form of Eq. (2.3) for unity weight function. The stabilized finite-element methods augment the weak form of the governing equations with stabilization terms [63–65].

The real power of unstructured grid methods with FV or FE discretization is their ability to adapt not only to complex geometries but also to solution features without being constrained by considerations such as grid structure, orthogonality or topology. However, anisotropic grid adaptation of three-dimensional, high Reynolds number flows, which contain both discontinuities and smooth but complex flow features, still remains a challenge. Consider for example high-lift systems where shock waves, confluent boundary layers, and wake roll-ups may be present in the flowfield. Grid adaption for these flows, which are common in aerodynamic applications, combined with high-order methods offers the additional possibility of *hp*-type refinement [43,66]. *hp* refinement uses low-order accurate solution and high grid density (*h*-refinement) at the

neighborhood of discontinuities. For the resolution of smooth but complex flow features and for wave propagation, the order of accuracy of the numerical solution increases (*p*-refinement) and a relatively coarse, canonical mesh is used.

Finite-difference methods on structured type grids are often used for the numerical solution of the governing equations because of their efficiency. The major difficulty with finite-difference methods is structured-type grid generation. The task of generating structured grids over complex configurations is still a serious challenge even with the multiblock structured grid approach. The powerful approach of overlapping grids, or Chimera-type grids [67], where structured grids generated about different simple components are allowed to overlap, further facilitates volume grid generation. Numerical solutions in complex domains with finite-difference methods on body-fitted deformed meshes [68] are obtained by expressing, Eq. (2.1) (see [37]) in terms of a generalized non-orthogonal curvilinear coordinate system (ξ, η, ζ) using general transformations $\xi = \xi(x, y, z)$, $\eta = \eta(x, y, z)$, $\zeta = \zeta(x, y, z)$ as follows:

$$\frac{\partial}{\partial t} \left(\frac{U}{J} \right) + \frac{\partial \hat{F}}{\partial \xi} + \frac{\partial \hat{G}}{\partial \eta} + \frac{\partial \hat{H}}{\partial \zeta} = \frac{1}{Re} \left[\frac{\partial \hat{F}_V}{\partial \xi} + \frac{\partial \hat{G}_V}{\partial \eta} + \frac{\partial \hat{H}_V}{\partial \zeta} \right]. \quad (2.4)$$

For turbulent flow calculations, the molecular viscosity μ is replaced by the turbulent eddy viscosity $\mu + \mu_t$. The turbulent eddy viscosity μ_t is obtained from turbulence models developed during the last decades. These turbulence models range from simple algebraic models to one- and two-equation turbulence models, or more sophisticated Reynolds stress models [69].

2.2. Entropy splitting

The unique properties of the compressible Euler equations for a perfect gas allows splitting of the flux vectors [70]. A special splitting of the flux derivative can be obtained using a convex entropy function and certain homogeneous properties. This splitting yields a sum of a conservative portion and a non-conservative portion of the flux derivative referred to by Yee et al. [71] as the “entropy splitting”. Yee et al. [71] investigated the choice of the arbitrary parameter that determines the amount of splitting and its dependence on the type of physics of interest to CFD. In addition, the manner the splitting affects the nonlinear stability of central schemes for long time integration of unsteady flows, such as in nonlinear aeroacoustics and turbulence dynamics, was assessed.

The first step for the derivation of the entropy splitting for the compressible Euler equations for a perfect gas ($p = \rho RT$) is to introduce a symmetry

transformation from the vector of the conservative variables U to a new vector of symmetry variables W , referred to as the “entropy variables”. The transformation is chosen so that the flux Jacobian matrix with respect to W , $F_W = \partial F / \partial W$ is symmetric and positive definite. A family of symmetry transformations based on a scalar convex function η , referred to as “entropy function” have been derived for the Euler equations for a perfect gas by Harten [72] and Gerritsen and Olsson [73,74]. The entropy function η has the form

$$\eta = \rho \xi(\bar{s}), \quad (2.5)$$

where the function $\xi(\bar{s})$ is an arbitrary but differentiable function of a dimensionless physical entropy $\bar{s} = \log(p\rho^{-\gamma})$.

The entropy variables W are then given by $W = \partial \eta / \partial U$ and are chosen such that $F(U(W))$, $G(U(W))$, $H(U(W))$ and $U(W)$ are homogeneous functions of W of degree β , i.e. there is a constant β such that for all ϕ the conservative variable vector and the flux satisfy:

$$\begin{aligned} U(\phi W) &= \phi^\beta U(W), \\ F(\phi W) &= \phi^\beta F(W). \end{aligned} \quad (2.6)$$

The homogeneity property implies that

$$\begin{aligned} F_W W &= \beta F(U(W)), \\ U_W W &= \beta U, \end{aligned} \quad (2.7)$$

where $U_W = \partial U / \partial W$ is the transformation matrix from conservative variables to entropy variables and $U_W = \partial F / \partial W$ is the flux Jacobian with respect to entropy variables. The splitting of the flux derivative F_x is

$$\begin{aligned} F_x &= \frac{\partial F}{\partial x} = \frac{1}{\beta+1} (F_W W)_x + \frac{1}{\beta+1} F_W W_x \\ &= \frac{\beta}{\beta+1} F_x + \frac{1}{\beta+1} F_W W_x. \end{aligned} \quad (2.8)$$

The entropy variables vector is

$$W = \begin{bmatrix} W_1 \\ W_2 \\ W_3 \\ W_4 \\ W_5 \end{bmatrix} = \frac{p^*}{\rho} \begin{bmatrix} e + \frac{\alpha-1}{\gamma-1} p \\ -\rho u \\ -\rho v \\ -\rho w \\ \rho \end{bmatrix}. \quad (2.9)$$

Expressions for $F(U(W))$ and F_W appearing in splitting of the flux derivative of Eq. (2.8) can be found in [71].

Introduction of entropy splitting increases significantly the computing cost of the inviscid part. It was shown however in [71] that the increase in computing cost is justified because for turbulent flow simulations, for example, that involve long time integrations and contain weak shock waves, entropy splitting can minimize the use of numerical dissipation due to its nonlinear stability property. For example the compar-

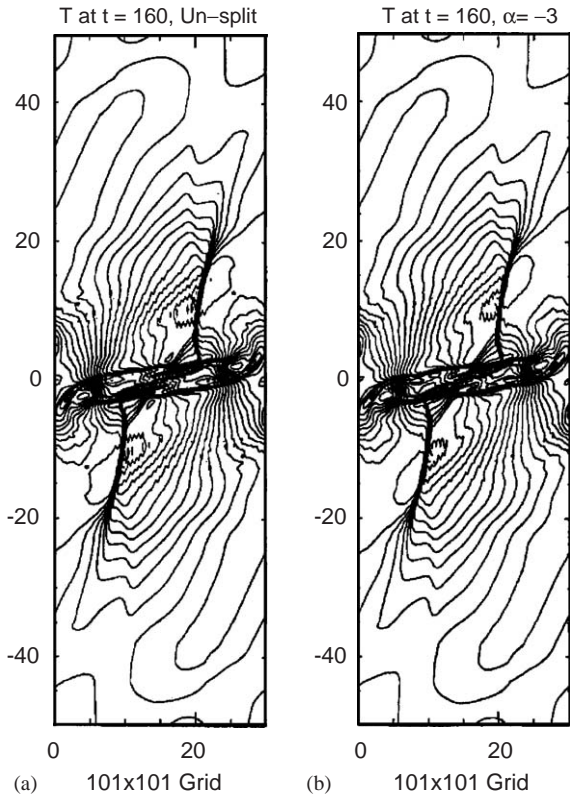


Fig. 4. Vortex pairing: comparison of normalized temperature contours for $\alpha = -3$ with the un-split approach at time $t = 160$ on a 101×101 grid with $\kappa = 0.7$ for the nonlinear fields and $\kappa = 0$ for the linear fields using ACM66.

ison of Fig. 4 demonstrated improvements of the numerical solutions for vortex pairing computed with entropy splitting and the unsplit scheme. For the value $\alpha = -3$ ($\beta = 4$), used in [71] the improvements of the entropy split scheme are evident. A comparison of computations obtained with entropy split and unsplit schemes for shock wave impingement on a spatially evolving mixing layer is shown in Fig. 5. Deterioration is obtained for $\alpha = 10$ ($\beta = -28.5$) corresponding to 103.6% conservative portion, but for $\alpha = -10$ ($\beta = 21.5$) corresponding to less than 100% conservative portion the solution shows reduction of spurious noise.

Increase of the conservative portion beyond 80% often defeats the purpose of using splitting since any gains in stability are diminished by the expense of added CPU computation required by splitting. For additional comments and details on the choice of the splitting parameters β , see Yee et al. [71].

2.3. Time integration of the Euler and NS equations

The time scales of turbulence are very small and the evolution of turbulent structures is very rapid.

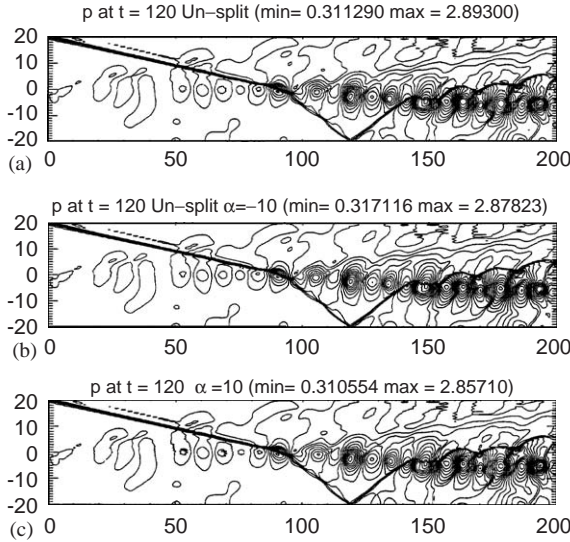


Fig. 5. Shock–shear-layer interaction: comparison of the pressure contours for $\alpha = \pm 10$ with the un-split approach using ACM66 at $t = 120$ on a 321×81 grid with $\kappa = 0.35$ for the nonlinear fields and $\kappa = 0.175$ for the linear fields.

As a result, in DNS and LES of transitional and turbulent flows the time step is not determined by stability considerations but from time resolution requirements. For this class of problems, explicit schemes, which are computationally efficient, easy to parallelize, and provide high accuracy in time, are the methods of choice. In many cases, use of explicit methods is also necessary for wave propagation applications, such as aeroacoustics, where dissipation and dispersion must be kept at very low level. For this class of problems, optimized explicit schemes have been developed.

In many CFD applications, steady-state solutions are needed. Convergence to a steady state is often obtained using explicit and/or implicit methods with multigrid acceleration or with implicit methods. For time-dependent aerodynamic problems, where time accuracy is of interest, such as rotor aerodynamics, time integration of the Euler and Navier–Stokes equations is often obtained with implicit methods that are second order accurate in time. Implicit methods [75] are more intensive computationally compared to explicit methods and they do not offer high accuracy in time. However they do not have limitations in time step due to numerical stability for highly stretched meshes required for viscous flow simulations. Another class of methods for time integration of time-dependent viscous flow problems is explicit methods with multigrid acceleration and dual time stepping. Multigrid methods [76,77] for convergence acceleration is a wide topic and will not be presented here. A brief overview of explicit and implicit method used in CFD is given in the following sections.

2.3.1. Explicit temporal schemes

Time integration can be obtained with the method of lines by considering the governing equations as a system of ordinary differential equations ODEs in time where the right-hand side contains the space discretization. Possible choices for explicit time stepping of these ODEs are the third- or higher-order explicit linear multistep methods (LMMs) Gear [78], Lambert [79] and Bucher [80]. For non-stiff or moderately stiff multidimensional problems, high-order accuracy (higher than second) temporal accuracy may be obtained with the Runge–Kutta (RK) methods. RK methods advance in time the following semi-discrete form of the governing equations $U_t = R(U)$, where R is the spatial discretization operator that is discussed in detail in the following sections.

A general RK can be written in the form

$$U^{(i)} = \sum_{k=0}^{i-1} a_{ik} U^{(k)} + \Delta t b_{ik} R(U^{(k)}), \quad i = 1, \dots, m, \quad (2.10)$$

where

$$U^{(0)} = U^n, \quad U^{(m)} = U^{n+1}$$

for $a_{ik} \geq 0$, $b_{ik} \geq 0$ Eq. (2.10) is just a convex combination of Euler forward operator with Δt replaced by $(b_{ik}/a_{ik})\Delta t$ since $\sum_{k=0}^{i-1} a_{ik} = 1$. The general RK method of Eq. (2.10) is TVD under the CFL condition $\Delta t \leq c\Delta t$ if $c = \min_{i,k}(a_{ik}/b_{ik})$, and $a_{ik} \geq 0$, $b_{ik} \geq 0$. In many CFD applications the third-order (TVD) Runge–Kutta method, RK3-TVD [81] that is compatible with TVD, ENO or WENO schemes was used. This RK method is TVD in the sense that the temporal operator itself does not increase the total variation of the solution. The TVD property of the time integration scheme plays an important role for time marching of nonlinear hyperbolic problems. It was shown in Ref. [81] that the TVD property is achieved with a four-stage, fourth-order TVD RK-4 method which is, however, quite intensive computationally because during the second and third stage two additional \tilde{R} 's, the adjoint operator of R , must be computed. In addition, a fifth-order accurate RK method was presented by Shu and Osher in [32]. For order of accuracy higher than four, however, the number of stages is larger than the order of accuracy and RK methods with order of accuracy higher than four become very intensive computationally. For multidimensional calculations storage is usually of importance. Therefore, in [82,83] low storage RK method, which only require two storage units, have been developed.

Numerical schemes for computations of wave propagation have special requirements. In computational aeroacoustics, for example, numerical schemes that have minimal dissipation and dispersion errors in both time

and space discretization are desired because the acoustic waves are non-dispersive and non-dissipative in their propagation. High-order spatial discretization is applied in aeroacoustics while time integration is often performed with RK methods. In the multistage RK methods of Eq. (2.10), the coefficients are chosen such that the maximum possible order of accuracy is obtained for a given number of stages. It is possible, however, Hu et al. [84], to choose the coefficients of the RK method so as to minimize the dissipation and dispersion errors for the propagation of waves, rather than to obtain the maximum possible formal order of accuracy. The optimized schemes are referred to in [84] as low-dissipation, low-dispersion RK (LDDRK) schemes. Optimization strategies of numerical schemes for wave propagation has been conducted in several other studies [85,86]. The LDDRK schemes have certain advantages because they are applicable to different spatial discretization methods. The optimization is carried out only for the resolved wavenumbers in the spatial discretization, they preserve the frequency in the time integration and thus are dispersion relation preserving in the sense of [86], and they are low storage. Other optimized schemes are the multistage Runge–Kutta-type time marching methods for Mac Cormack-type schemes developed by Hixon and Turkel [87].

2.3.2. Implicit schemes

An implicit time marching method that was used successfully in computations where high order of spatial accuracy was implemented with finite differences is the approximately factored Beam-Warming algorithm [88] augmented with Newton-like subiterations in order to achieve second-order time accuracy. The factored implicit Beam-Warming algorithm, as well as other implicit time marching schemes, assumes second-order accurate in time linearization of the fluxes $F(U)$ as follows:

$$\begin{aligned} F^{n+1} &= F^n + \left(\frac{\partial F}{\partial U} \right)^n \Delta U^n + \mathcal{O}(\Delta t)^2, \\ &= F^n + A^n \Delta U^n + \mathcal{O}(\Delta t)^2, \end{aligned} \quad (2.11)$$

where $\Delta U^n = U^{n+1} - U^n$. As a result, these schemes can achieve second order of accuracy in time at most, provided that linearization errors are eliminated during the time integrations process. Therefore, for time accurate solutions with the Beam-Warming algorithm and other implicit algorithms, which use the linearization of Eq. (2.11), require one or more Newton-type subiterations in order to eliminate linearization and/or factorization errors and obtain second-order accuracy in time.

The approximately factorized Beam-Warming (BW) algorithm is compatible with centered finite difference discretizations of right-hand side and is often used in CFD application. Central differences on the right-hand side of the BW-factored algorithm were replaced by first-

order upwinding using Steger–Warming flux vector splitting [89] for numerical solution with upwind discretizations of the right-hand side. The BW algorithm is formally second accurate in space and compatible with centered discretizations of right-hand side. For higher-order discretizations of the right-hand side, high-order accuracy of the implicit operators was obtained [90] where the derivatives in the LHS operator were evaluated with a fourth-order accurate, three-point, compact stencil. Using a fourth-order accurate compact scheme for the evaluation of the right-hand side the algorithm has fourth-order formal accuracy in space. The resulting high-order accurate in space implicit, compact algorithm was tested and analyzed in [90,91]. It was found that it is unconditionally stable in two dimension as the original Beam–Warming second-order accurate algorithm. Furthermore, it was shown that it yields accurate solutions of time dependent problems with fewer subiterations and converges faster to the steady state [90].

Starting from the control volume formulation Yoon and Jameson [92] obtained an unfactored implicit scheme from the nonlinear implicit scheme by linearizing the flux vectors about the preceding time step and dropping terms of second order or higher. Recently, the LU-SGS scheme was further extended by Zhang and Wang [93] for time accurate solutions by introducing dual time-stepping.

2.3.3. Time accurate solutions with multigrid

Implicit methods in the finite-volume context algorithm can be found in Refs. [95,94]. After applying finite-volume discretization and using the method of lines [94], the following coupled system of ordinary differential equations is obtained

$$\frac{dU}{dt} + R(U) = 0 \quad (2.12)$$

applying three-point backward difference approximation for the time derivative in Eq. (2.12) obtain

$$\frac{3}{2\Delta t} U^{n+1} - \frac{2}{\Delta t} U^n + \frac{1}{2\Delta t} U^{n-1} + R(U^{n+1}) = 0. \quad (2.13)$$

For time accurate computations with multigrid [94], this equation is treated as a steady-state equation by introducing a pseudo-time variable t^* and using a multigrid strategy to solve the following nonlinear system to steady state using local time steps Δt^* .

$$\frac{\partial W}{\partial t^*} + R^*(W) = 0, \quad (2.14)$$

where W is the approximation to U^{n+1} and the residual $R^*(W)$ defined by

$$\begin{aligned} R^*(W) &= \frac{3}{2\Delta t} W + R(W) - S(U^n, U^{n-1}), \\ S(U^n, U^{n-1}) &= \frac{2}{\Delta t} U^n - \frac{1}{2\Delta t} U^{n-1}. \end{aligned} \quad (2.15)$$

Time integration of Eq. (2.14) is obtained with a multistage Runge–Kutta method that performs the role of the smoother in the multigrid process.

3. High-order finite-difference schemes

In the past, efforts were made towards developing high-order finite-difference (FD) methods in the areas direct and large eddy simulations. For nonlinear problems, straightforward application of high-order accurate central difference schemes is not possible, because the spurious modes that develop from the unresolvable by the numerical discretization high-frequency modes lead to instabilities. Rai and Moin [96] found that high-order upwind schemes are more promising to simulate turbulent flows. However, early attempts to apply high-order finite differences were often frustrated because of lack of robustness of the proposed high-order (FD) schemes compared to spectral methods. In spite of the difficulties, some success was achieved for the computation of incompressible [96] and compressible [56] flows with high order, upwind FD schemes. The fifth-order accurate derivatives in [96] were computed with upwind-biased formulas based on the sign of the velocity as

$$\begin{aligned} u_i = & -\frac{1}{120}[6u_{i+2} + 60u_{i+1} + 40u_i - 120u_{i-1} \\ & + 30u_{i-2} - 4u_{i-3}] \quad \text{for } u_i > 0, \\ u_i = & \frac{1}{120}[4u_{i+3} - 30u_{i+2} + 12u_{i+1} - 40u_i \\ & - 60u_{i-1} + 6u_{i-2}] \quad \text{for } u_i < 0. \end{aligned} \quad (3.1)$$

Upwinding alleviated some of the problems encountered with centered schemes and yielded some promising results for both incompressible [96] and compressible flow [56] direct numerical simulations.

Upwind biased, high-order accurate stencils (up to fifth-order) for the evaluation of the derivatives were also used successfully for the computation of complex incompressible flows [97,98] and wave propagation [99]. Upwind-biased schemes, however, based only on formal accuracy (truncation error) inherently introduce some form of artificial smoothing that makes them inappropriate for long time integration and direct simulation or large eddy simulation or turbulence.

Application of Taylor series expansion yields centered, explicit and compact finite difference formulas for space differentiation on equally spaced meshes. Central-difference schemes gained popularity in the simulation of wave propagation phenomena because in contrast to upwind methods, which in addition to dispersion naturally introduce artificial dissipation, the dominant error in centered discretizations is depressive. The stencils for the fourth-, sixth-, and eighth-order accurate symmetric, explicit, centered schemes are five-, seven- and nine-point wide, respectively. As a result, only the

fourth-order explicit scheme was used in CFD. Explicit fourth-order, finite-difference formulas are often used to discretize the second derivatives in the viscous terms by taking the first derivative twice. In order to reduce the stencil width the inner derivative is evaluated at half-points.

The first systematic attempt to develop high-order accurate, narrow stencil, finite-difference schemes appropriate for problems with a wide range of scales was presented by Lele [100]. Compared to the traditional FD approximations the compact schemes presented by Lele [100] provided a better representation of the short-length scales. As a result, compact high-order schemes are closer to spectral methods and at the same time maintain the freedom to retain accuracy in complex stretched meshes. Emphasis in the development of compact schemes was given on the resolution characteristics of the difference approximations rather than formal accuracy (i.e. truncation error). The notion of resolution was quantified by Lele [100] using a Fourier analysis of the differencing scheme [101,102]. This analysis compares the resolving power of different schemes based on a more general notion of intervals per wavelength of Swartz and Wendroff and Kreiss and Oliger. Using these ideas, Lele [100] analyzes the resolution characteristics of the schemes based on the accuracy with which the difference approximation represents the exact result over the full range of length scales that can be realized for a given mesh.

3.1. Centered compact schemes

Of particular interest in recent applications has been the class of centered schemes that require small stencil support. These “compact” schemes presented by Lele [100] can be derived from Taylor series expansions and compute simultaneously the derivatives along an entire line in a coupled fashion. The main advantage of compact schemes is simplicity in boundary condition treatment and smaller truncation error compared to their noncompact counterparts of equivalent order. Compact schemes are, however, more intensive computationally compared to explicit schemes because they require matrix inversion.

A seven-point wide stencil, finite-difference discretization of any first-order derivative f' of a scalar pointwise discrete quantity, f , in the governing equations, such as metric terms or flow variables, is obtained in the computational domain on an equally spaced mesh by

$$\begin{aligned} Bf'_{j+2} + Af'_{j-1} + f'_j + Af'_{j+1} + Bf'_{j+2} \\ = a \frac{f_{j+1} - f_{j-1}}{2h} + b \frac{f_{j+2} - f_{j-2}}{4h} + c \frac{f_{j+3} - f_{j-3}}{6h}, \end{aligned} \quad (3.2)$$

where A, B, a, b and c determine the spatial accuracy of the discretization. Different values of the coefficients in

the formula of Eq. (3.2) yield schemes of different accuracy ranging from the fourth-order explicit method (E4) to the compact tenth-order accurate scheme (C10). The values of the coefficients in Eq. (3.2) for schemes of different order of accuracy are shown in Table 1.

In Table 1, C8/3 refers to the eight-order compact scheme that requires tridiagonal matrix inversion and C8/5 refers to the eight-order compact scheme that requires pentadiagonal matrix inversion.

Compact approximations for the second-order derivative f'' are obtained from the following general form:

$$\begin{aligned} Bf''_{j-2} + Af''_{j-1} + f''_j + Af''_{j+1} + Bf''_{j+2} \\ = \frac{a}{h^2} (f_{j+1} - 2f_j + f_{j-1}) + \frac{b}{4h^2} (f_{j+2} - 2f_j + f_{j-2}) \\ + \frac{c}{9h^2} (f_{j+3} - 2f_j + f_{j+3}). \end{aligned} \quad (3.3)$$

Explicit schemes can also be used for the evaluation of the viscous terms because application of the compact schemes is more expensive computationally. Furthermore, there are no very significant improvements in wavespace resolution with the use of compact schemes [100].

The wavespace resolution of various explicit and compact schemes is obtained using Fourier analysis [100–102] for Eqs. (3.2) or (3.3). Considering that the exact result is a sinusoidal function $f_j = e^{ikh}$, where $h = \Delta x_j$ is a uniform grid spacing and k is the wavenumber, the exact value of the derivative is $f'_j = ikf_j$. The derivative computed with finite difference formulas, on the other hand, is given by $\tilde{f}'_j = i\hat{k}f_j$, where \hat{k} the modified wavenumber, which depends on the form of the FD formulas used for the evaluation of the first-order derivative. The difference between the true wavenumber k and the modified wavenumber \hat{k} is a measure of the scheme's resolving ability. The modified wavenumber of various finite difference schemes can be obtained using standard shift operators $f'_{j\pm n} = f'_j e^{\pm ik}$. For example, the modified number of the fourth-order accurate explicit scheme of Eq. (3.2) is given by $\hat{k} = i(8 \sin k - \sin 2k)/6$, with analogous expression for the other methods. A comparison of the modified wavenumbers of the first derivative for several central

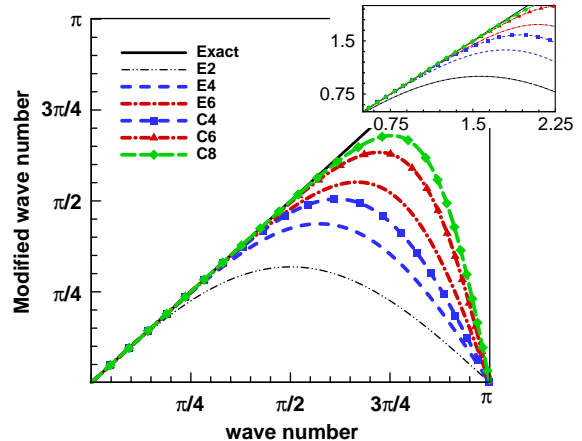


Fig. 6. Wave space resolution of explicit and compact centered schemes for the first-order derivative.

compact and non-compact schemes is shown in Fig. 6. Using the scaled wavenumber $\omega = 2\pi kh/\lambda$ where λ is the wavelength and the number of intervals or grid points per wavelength is $2\pi k/\omega$. Therefore, the lower the scheme's resolving ability the higher is the number of points per wavelength required to resolve accurately certain predetermined portion of the range $[0, 2\pi]$.

Stable, accurate formulas for the boundary points can be found in [103]. Numerical solutions of nonlinear hyperbolic equations with central-difference methods develop spurious modes arising from unresolvable scales and inaccuracies in the application of boundary conditions. Spectral-type [28] or characteristic-based [1] filters that can be used to stabilize numerical solutions performed with central-difference methods are presented in the following sections.

3.2. Boundary closures for high-order schemes

The primary difficulty in using higher-order schemes is identification of stable boundary schemes that preserve their formal accuracy. Boundary closures for various explicit and compact high-order centered schemes were presented by Carpenter et al. [103]. The stability characteristics of compact fourth- and sixth-order spatial operators with boundary closures were assessed [103] with the theory of Kreiss [104] and Gustafsson, Kreiss and Sundstrom (GKS) [105] for the semidiscrete initial value problem.

Numerical solutions of hyperbolic systems preserve their formal spatial accuracy when an N th-order inner scheme is closed with at least an $(N-1)$ th-order boundary scheme. Furthermore, determination of the numerical stability of a fully discrete approximation (including boundary schemes) for a linear hyperbolic partial differential equation is a difficult task. Fourier techniques are not straightforward to apply and do not

Table 1
Schemes with five-point stencil of Eq. (3.2)

Scheme	A	B	a	b	c
E4	0	0	$\frac{4}{3}$	$-\frac{1}{3}$	0
C4	$\frac{1}{4}$	0	$\frac{3}{5}$	0	0
C6	$-\frac{1}{3}$	0	$\frac{14}{9}$	$\frac{1}{9}$	0
C8/5	$\frac{4}{9}$	$\frac{1}{36}$	$\frac{40}{27}$	$\frac{25}{54}$	0
C8/3	$-\frac{3}{8}$	0	$\frac{75}{48}$	$\frac{1}{5}$	$-\frac{1}{80}$
C10	$-\frac{1}{2}$	$\frac{1}{20}$	$\frac{17}{12}$	$\frac{101}{150}$	$\frac{1}{100}$

provide sufficient conditions for numerical stability. Gustafsson et al. [105] developed stability analysis techniques based on normal modal analysis. The theory of [105], generally referred to as GKS stability theory, established conditions that the inner and boundary schemes must satisfy to ensure stability. The GKS theory was used by Carpenter et al. [103] to assess the stability of boundary schemes proposed for the fourth- and sixth-order compact schemes.

Consider the finite-difference representation of the continuous derivative $U_x = U'_j$ on an equally spaced mesh. The discrete form of the first derivative U'_j involves functional values U_j , $j = 1, \dots, N$ at discrete points. For an explicit uniformly fourth-order accurate in space scheme, the spatial discretization with boundary closures is obtained by Carpenter et al. [103] as

$$\begin{aligned} U'_1 &= \frac{1}{12\Delta x} (-25U_1 + 48U_2 - 36U_3 + 16U_4 - 3U_5), \\ U'_2 &= \frac{1}{12\Delta x} (-3U_1 - 10U_2 + 18U_3 - 6U_4 + U_5), \\ U'_j &= \frac{1}{12\Delta x} (U_{j-2} - 8U_{j-1} + 8U_{j+1} - U_{j+2}), \\ j &= 3, \dots, N-2, \\ U'_{N-1} &= \frac{1}{12\Delta x} (-U_{N-4} + 6U_{N-3} - 18U_{N-2} \\ &\quad + 10U_{N-1} + 3U_N), \\ U'_N &= \frac{1}{12\Delta x} (3U_{N-4} - 16U_{N-3} + 36U_{N-2} \\ &\quad - 48U_{N-1} + 25U_N). \end{aligned} \quad (3.4)$$

The fourth-order, compact FD scheme for the approximation of U'_j that has narrower stencil requires closures only at $j = 1$ and $j = N$. The fourth-order compact scheme with boundary closures is

$$\begin{aligned} U'_1 + 3U'_2 &= \frac{1}{6\Delta x} (-17U_1 + 9U_2 + 9U_3 - U_4), \\ U'_{j-1} + 4U'_j + U'_{j+1} &= \frac{1}{\Delta x} (-3U_{j-1} + 3U_{j+1}), \\ 3U'_{N-1} + U'_N &= \frac{1}{6\Delta x} (U_{N-3} - 9U_{N-2} \\ &\quad - 9U_{N-1} + 17U_N). \end{aligned} \quad (3.5)$$

The sixth-order compact scheme has a five point-wide stencil and utilizes information from all five points explicitly and three points implicitly (tridiagonal system). Boundary closures must be provided at two points at each end of the domain $j = 1, 2$ and $j = N-1, N$. To ensure formal sixth-order formulas, e.g. the optimal scheme, in shorthand nomenclature, would be (5, 5-6-5, 5), e.g. fifth order at the boundaries $j = 1, 2$ and $j = N-1, N$ and sixth order in the interior. Formally sixth-order accurate GKS stable schemes are difficult to find. Therefore, the (3, 5-6-5, 3) and the

(4, 5-6-5, 4) schemes are used for full discretization with the sixth-order compact scheme.

The third order closure at $j = 1$ is:

$$2U'_1 + 4U'_2 = \frac{1}{\Delta x} (-5U_1 + 4U_2 + U_3).$$

The fourth-order closure at $j = 1$ is

$$6U'_1 + 18U'_2 = \frac{1}{\Delta x} (-17U_1 + 9U_2 + 9U_3 - U_4)$$

and the fifth-order closure at $j = 2$ is accomplished by

$$3U'_1 + 18U'_2 + 9U'_3 = \frac{1}{\Delta x} (-10U_1 - 9U_2 + 18U_3 + U_4).$$

The two key issues encountered with higher-order finite-difference schemes used in CFD are boundary treatments and grid uniformity. The boundary treatment was carefully addressed by Carpenter et al. [103]. It was found that the effect of boundary closures to the overall resolution is indeed small [106] even for highly accurate DNS. The grid non-uniformity issue is, however, more important and its effect on the overall accuracy of higher-order finite-difference schemes on non-uniform grids was recently assessed in [107].

The use of non-uniform grids in turbulent flow simulations is inevitable. The typical ratio of the maximum to the minimum grid spacing is about 100. The behavior of the second- and fourth-order explicit centered schemes and the fourth- and sixth-order compact schemes was assessed in [107] for smooth stretched grids. It was found that grid quality has stronger effects on the higher-order compact schemes than on the explicit schemes. Furthermore, an accuracy deterioration of higher-order compact schemes with low grid density was observed for non-uniform meshes.

3.3. Simultaneous evaluation of the first and second derivative with compact schemes

A more general version of the standard compact schemes presented by Lele [100] was developed by Mahesh [108]. These schemes are symmetric and differ from the standard compact schemes in that the first and second derivatives are evaluated simultaneously. In addition, for the same stencil width the schemes proposed by Mahesh are two orders higher in accuracy, they have significantly better spectral representation, and the computational cost for the evaluation of both derivatives is shown to be essentially the same as standard compact schemes. As a result, the proposed schemes appear to be attractive alternative to standard compact schemes for the Navier–Stokes equations that include second-order derivative evaluation in the viscous terms. The schemes that compute simultaneously the first f' and the second derivative f'' of a function f given

at uniform mesh, $\Delta x = h$, are defined by

$$\begin{aligned} & a_1 f'_{j-1} + a_0 f'_j + a_2 f'_{j+1} + h (b_1 f''_{j-1} + b_0 f''_j + b_2 f''_{j+1}) \\ & = \frac{1}{h} (c_1 f_{j-2} + c_2 f_{j-1} + c_0 f_j + c_3 f_{j+1} + c_4 f_{j+2}). \end{aligned} \quad (3.6)$$

Enforcing symmetry for the coefficients and considering $a_0 = 1$ and $b_0 = 1$ Mahesh [108] obtain from Eq. (3.6) a sixth- and an eight-order compact scheme for the simultaneous evaluations of the first- and second-order derivative

For example, the sixth-order scheme is

$$\begin{aligned} & 7f'_{j-1} + 16f'_j + 7f'_{j+1} + h(f''_{j-1} - f''_{j+1}) \\ & = \frac{15}{h} (f_{j+1} - f_{j-1}) \\ & - 9f_{j-1} - 9f'_{j+1} - h(f''_{j-1} - 8f''_j + f_{j+1}) \\ & = \frac{24}{h} (f_{j-1} - 2f_j + f_{j+1}). \end{aligned} \quad (3.7)$$

Comparing the new scheme of Eq. (3.7) with the standard compact sixth-order compact schemes for the first- and second-order derivative of the previous section

$$f'_{j-1} + 3f'_j + f'_{j+1} = \frac{7}{3h} (f_{j+1} - f_{j-1}) + \frac{1}{12h} (f_{j+2} - f_{j-2}),$$

$$\begin{aligned} 2f''_{j-1} + 11f''_j + 2f''_{j+1} &= \frac{12}{h^2} (f_{j-1} - 2f_j + f_{j+1}) \\ &+ \frac{3}{4h^2} (f_{j-2} - 2f_j + f_{j+2}). \end{aligned} \quad (3.8)$$

It is evident that the Mahesh scheme [108], which computes the first and second derivative in a coupled fashion, uses a more narrow stencil compared to the standard compact scheme. In addition, to the sixth-order compact scheme an eight-order compact scheme was developed in [108]. Boundary closures were also applied for both the sixth- and eight-order compact schemes for simultaneous computation of the first and second derivative.

3.4. Modified high-order finite-difference schemes

The idea of modifying or optimizing a finite difference schemes by calculating values of the coefficients that introduce upwinding or minimize a particular type of error instead of the truncation error has been used successfully in the design of new schemes with desired properties. Some form of upwinding is often needed for the computation of flows with discontinuities and nonlinearities. Modifications of standard centered, explicit and compact schemes were carried out by Zhong [109]. For the modified schemes, the formal order of the scheme for certain stencil size was sacrificed and high-order upwinding with low dissipation was introduced.

Other optimized schemes have also been developed [110] in the field of computational aeroacoustics

[86,111,112]. The rationale for optimizing numerical schemes for short waves is that for long waves, even lower-order schemes can do well. The short waves, however, require high-resolution in order to obtain accurate representation of the broadband acoustic waves. The optimized FD scheme of Tam and Webb [86], for example, referred to as the dispersion relation preserving (DPR) scheme, uses central differences to approximate the first derivative. The approximation is therefore, non-dissipative in nature. The maximum formal order of accuracy of the centered scheme [86] for certain stencil size is again sacrificed in order to optimize resolution of the high wavenumbers. Although non-dissipative schemes are ideal for aeroacoustics, numerical dissipation is often required to damp non-physical waves generated by boundary and/or initial conditions. In many practical applications, therefore, high-order dissipative terms were added to the centered scheme of Ref. [86]. To remedy this problem optimized DPR schemes were developed by Zhuang and Chen [111] and Lockard et al. [110]. In the following sections, the upwind high-order schemes of Zhong [109] and the DPR scheme of Tam and Webb [86] are presented.

3.4.1. Upwind high-order schemes

A family of finite-difference high-order upwind compact and explicit schemes for the discretization of convective terms was derived in [109]. The general compact and explicit finite-difference approximation of $\partial u / \partial x = u'$ is

$$\sum_{k=-M+M_0+1}^{M_0} b_{i+k} u'_{i+k} = \frac{1}{h} \sum_{k=-N+N_0+1}^{N_0} a_{i+k} u_{i+k}, \quad (3.9)$$

where h is the uniform grid spacing, u'_{i+k} is the numerical approximation of the first derivative at the $(i+k)$ th grid point, and N_0 , M_0 are biases with respect to the base point i . The family of upwind compact and explicit schemes with central grid stencils $N = 2N_0 + 1$, $M = 2M_0 + 1$, was considered in [109]. The coefficients a_{i+k} and b_{i+k} of these upwind schemes were determined such that the order of the schemes is one order lower than the maximum achievable order for the standard central stencil. As a result, the orders of the upwind schemes are always odd integers $p = 2(N_0 + M_0) - 1$, and there is a free parameter θ in the coefficients a_{i+k} and b_{i+k} . The value of θ is set to be the coefficient of the leading truncation term, which is an even order derivative.

$$\begin{aligned} \sum_{k=-M_0}^{M_0} b_{i+k} u'_{i+k} &= \frac{1}{h} \sum_{k=-N_0}^{N_0} a_{i+k} u_{i+k} \\ &- \frac{\theta}{(p+1)!} h^p \left(\frac{\partial U^{p+1}}{\partial x^{p+1}} \right)_i + \dots \end{aligned} \quad (3.10)$$

Schemes of Eq. (3.10) are $(p+1)$ th order accurate for $\theta = 0$ and p th order accurate for $\theta \neq 0$. The choice of θ affects the magnitude of numerical dissipation and the stability of the scheme. The third-, fifth- and seventh-order explicit and compact schemes based on this idea were derived by Zhong [109].

3.4.2. Dispersion-relation-preserving (DPR) scheme

Numerical solutions of the linearized Euler equations with high-order finite-difference schemes are used to assure that the computed results have the same number of wave modes (acoustic, vorticity and entropy), the same propagation characteristics (isotropic, non-dissipative and non-dispersive), and the same wave speeds as those of the solution of these equations, which govern acoustic disturbance propagation. These conditions are satisfied by the numerical solution if the discrete equations have the same dispersion relation with the continuous equation. Finite difference schemes which yield the same dispersion relations as the original partial differential equations are referred to as dispersion-relation-preserving (DPR) schemes. A way to construct time marching DPR schemes was proposed in [86] by optimizing the finite difference approximations of the derivatives in the wavenumber and frequency space. The new optimized, high order, finite difference scheme [86] designed with these criteria meets the usual conditions of consistency, stability, and hence convergence. In addition, it supports, in the case of small amplitude waves, wave solutions which have the same characteristics as those of the linearized Euler equations as nearly as possible.

Consider the approximation of the first derivative $\partial f / \partial x$ at the j th node on a uniform grid using N values of f to the left. The finite difference approximation is

$$\left(\frac{\partial f}{\partial x} \right)_i \simeq \frac{1}{\Delta x} \sum_{j=-N}^M a_j f_{i+j}. \quad (3.11)$$

The usual way to determine the coefficients a_j in Eq. (3.11) is to expand in Taylor series and equate coefficients of the same powers in Δx . In Ref. [86], it was proposed to determine the coefficients by requiring the Fourier transform of the finite difference scheme on the right of Eq. (3.11) to be a close approximation of the partial derivative.

The finite difference representation of Eq. (3.11) can be written as

$$\frac{\partial f}{\partial x} \simeq \frac{1}{\Delta x} \sum_{j=-N}^M a_j f(x + j\Delta x). \quad (3.12)$$

Considering the Fourier transform of the left and right of Eq. (3.12) obtain

$$ik\tilde{f} \simeq \left(\frac{1}{\Delta x} \sum_{j=-N}^M a_j e^{ijk\Delta x} \right) \tilde{f} = \tilde{k}\tilde{f}. \quad (3.13)$$

Clearly the quantity $\tilde{k} = -ik$ is effectively the wavenumber of the Fourier transform for the finite-difference schemes of Eqs. (3.11) and (3.12).

The Fourier transform of the finite difference scheme is a good approximation of that of the partial derivative over the range of wavenumbers $|k\Delta x| \leq \pi/2$ when the coefficients a_j are chosen to minimize the integral of the error defined by

$$E = \int_{-\pi/2}^{\pi/2} |k\Delta x - \tilde{k}\Delta x|^2 d(k\Delta x) \\ = \int_{-\pi/2}^{\pi/2} \left| iK - \sum_{j=-N}^M a_j e^{ijkK} \right|^2 dK. \quad (3.14)$$

The condition of the minimum is

$$\frac{\partial E}{\partial a_j} = 0, \quad j = -N, \dots, M. \quad (3.15)$$

The solution of the algebraic system given by Eqs. (3.15) determines the values of the coefficients a_j that give a good approximation of the derivative for $|k\Delta x| \leq \pi/2$.

In Ref. [86], the condition of Eq. (3.12) was imposed for $n = M = 3$ (fourth-order accuracy) and a_1 was left as free parameter. Minimization of Eq. (3.14) yielded the following values for the coefficients $a_0 = 0$, $a_1 = -a_{-1} = 0.79926643$, $a_2 = -a_{-2} = -0.18941314$, $a_3 = -a_{-3} = 0.02651995$. Therefore, the formal accuracy of the scheme with the coefficients from Eq. (3.14) was sacrificed, since a fourth-order accurate scheme was obtained for a seven-point-wide stencil, but the resolution in wavespace was improved.

3.5. Spectral-type filters

High-order accurate centered schemes are non-dissipative and they are particularly suitable for convection of small-scale disturbances governed by the linearized Euler equations. Non-dissipative, central-difference discretizations for nonlinear problems, however, produce high-frequency spurious modes that originate from mesh non-uniformities, inaccuracies of the boundary conditions, and nonlinear interactions. In order to prevent numerical instabilities due to growth of high-frequency modes while retaining the high-order accuracy of the compact or non-compact central discretizations, filtering of the computed solution is required. Filtering of the solution with explicit-type filters was proposed by Lele [100]. More recently, high-order compact filters were introduced by Gaitonde and Visbal [28]. These compact filters are applied on the components of the computed solution vector. Denoting by ϕ , the computed value, the filtered value $\hat{\phi}$ is obtained by solving the system

$$a_l \hat{\phi}_{j-1} + \hat{\phi}_j + a_r \hat{\phi}_{j+1} = \sum_{n=0}^N \frac{a_n}{2} (\phi_{j+n} + \phi_{j-n}). \quad (3.16)$$

The compact filter of Eq. (3.16), which was proposed in Ref. [28], provides a $2N$ th-order accurate formula on a $2N + 1$ point stencil. Application of the compact filter makes possible high-resolution, low-diffusion numerical solutions of flows without discontinuities. The coefficients a_n of the filter are functions of the filtering parameter a_f . These coefficients for different order filters are given in Table 2.

The filtering ability of the filters given by Eq. (3.16) is determined by the transfer function in wavespace. Therefore, the compact filters of Eq. (3.16) are referred to from now on as spectral-type filters. The transfer function for the spectral-type filter of Eq. (3.16) is given by

$$S(\omega) = \frac{\sum_{n=0}^N a_n \cos(n\omega)}{1 + 2a_f \cos(\omega)}. \quad (3.17)$$

The parameter, a_f , which is in the range $0.5 < a_f < 0.5$ determines the filtering properties. High values of the parameter a_f yield less dissipative filters.

At the boundary points, the order of the filter must be dropped in order to reduce the stencil size. It was demonstrated [28] that the filtering ability of the low-order filters could approximate the filtering performance of high-order filters by varying the value of the filtering parameter a_f . The variation of the spectral function of Eq. (3.17) for constant value of the filtering parameter $a_f = 0.45$ for the second up to eighth-order filters is shown in Fig. 7. The spectral function of Eq. (3.17) for the second-, and eighth-order filter is plotted in Fig. 8 for different values of the filtering parameter $a_f = 0.45 - 0.49$. It is evident that as the value of the filtering parameter a_f becomes larger low-pass filtering is obtained even with the second-order filter.

Centered schemes with spectral-type filters are not appropriate for computations of flows with shock waves and other discontinuities. High-order accurate computation of transonic or supersonic flows with compact centered schemes can be obtained with the application of characteristic-based filters [1] described in the following section.

Table 2
Coefficients for the spectral-type filter of Eq. (3.16)

	F2	F4	F6	F8	F10
a_0	$\frac{1}{2} + a_f$	$\frac{5}{8} + \frac{3a_f}{4}$	$\frac{11}{16} + \frac{5a_f}{8}$	$\frac{93}{128} + \frac{70a_f}{128}$	$\frac{193-126a_f}{256}$
a_1	$\frac{1}{2} + a_f$	$\frac{1}{2} + a_f$	$\frac{15}{32} + \frac{17a_f}{16}$	$\frac{7}{16} + \frac{18a_f}{16}$	$\frac{105-302a_f}{256}$
a_2	0	$-\frac{1}{8} + \frac{a_f}{4}$	$\frac{-3}{32} + \frac{3a_f}{8}$	$\frac{-7}{32} + \frac{14a_f}{32}$	$\frac{-15+30a_f}{64}$
a_3	0	0	$\frac{1}{32} - \frac{a_f}{16}$	$\frac{1}{16} - \frac{a_f}{8}$	$\frac{45-90a_f}{512}$
a_4	0	0	0	$\frac{-1}{128} + \frac{a_f}{64}$	$\frac{-5+10a_f}{256}$
a_5	0	0	0	0	$\frac{1-2a_f}{512}$
Order of accuracy	2nd	4th	6th	8th	10th

3.6. Characteristic-based (ACM) filters

Characteristic filters of Yee et al. [1] can be applied instead of spectral-type filters with implicit and explicit methods for time discretization of Section 2. Characteristic-based filters remove spurious oscillations and in addition can be used for shock capturing. They can be applied at every stage of an RK method or after each Newton-type subiteration of an implicit-type time integration scheme for flows with strong shock interactions. For computational efficiency, however, the filter is often applied at the end of the full RK step or at the final update of an implicit time scheme.

Let L_f be the filter operator defined as

$$L_f(F^*, G^*)_{i,j} = \frac{1}{\Delta x} [\tilde{F}_{i+1/2,j}^* - \tilde{F}_{i-1/2,j}^*] + \frac{1}{\Delta y} [\tilde{G}_{i,j+1/2}^* - \tilde{G}_{i,j-1/2}^*], \quad (3.18)$$

where $\tilde{F}_{i+1/2,j}^*$ and $\tilde{G}_{i,j+1/2}^*$ are the dissipative numerical fluxes of the filter operator to be discussed below. Then the new time level $n + 1$ (or next stage $p + 1$ for implicit schemes with subiterations) is defined as

$$U^{n+1} = \hat{U}^{n+1} + \Delta t \mathcal{L}_f(F^*, G^*)_{i,j}, \quad (3.19)$$

where the filter numerical fluxes $\tilde{F}_{i+1/2,j}^*$ and $\tilde{G}_{i,j+1/2}^*$ are evaluated at \hat{U}^{n+1} . The simplest form for L_f is the linear filter proposed by Gustafsson and Olsson [113] where a switch similar to that of Harten [35] was used.

The filter numerical flux may be written in the form similar to TVD schemes, as in [72,114–116] as follows

$$\tilde{F}_{i+1/2,j} = \frac{1}{2}[F_{i+1,j} + F_{i,j} + \mathcal{D}_{i,j}], \quad (3.20)$$

where $\frac{1}{2}[F_{i+1,j} + F_{i,j}]$ is the central difference portion of the numerical flux, which is substituted by a high-order centered approximation in the schemes proposed by Yee et al. [1], and the term $\mathcal{D}_{i,j}$ is the nonlinear dissipation. For characteristic-based methods, e.g. methods where the dissipative term is evaluated in characteristic variable space $\mathcal{D}_{i,j} = R_{i+1/2,j} \Phi_{i+1/2,j}$ where $R_{i+1/2,j}$ is the right eigenvector of the flux Jacobian matrix $\partial F / \partial U$.

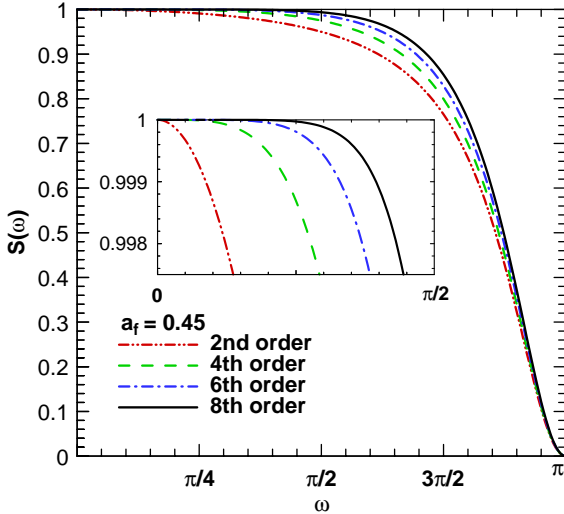


Fig. 7. Transfer function for filters of different order for constant value of the filtering parameter $A_f = 0.45$.

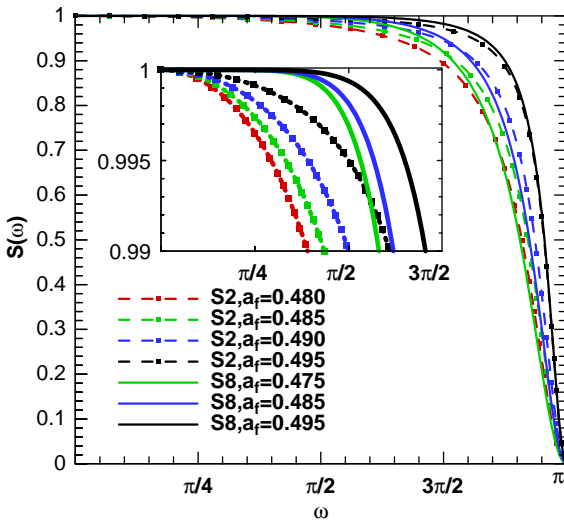


Fig. 8. Transfer function of the second and eighth-order filter for different values of the filtering parameter A_f .

In order to introduce some upwinding the elements of $R_{i+1/2}$ are computed at Roe's approximate average state.

The artificial compression method (ACM) of Harten's idea [35] was generalized in [1] to achieve a low-dissipative high-order shock-capturing scheme by nearly maintaining the accuracy to high order. The ACM filter numerical flux $\tilde{F}_{i+1/2,j}^*$ in Ref. [1] has the form

$$\tilde{F}_{i+1/2,j}^* = \frac{1}{2} R_{i+1/2} \Phi_{i+1/2}^*, \quad (3.21)$$

where $R_{i+1/2}$ is the right eigenvector matrix of the flux Jacobian $A = \partial F / \partial U$ at Roe's approximate average state and the elements of the matrix $\Phi_{i+1/2}^*$ denoted by $\phi_{i+1/2}^*$ are

$$\phi_{i+1/2}^* = \kappa \theta_{i+1/2}^l \phi_{i+1/2}^l. \quad (3.22)$$

The function $\kappa \theta_{i+1/2}^l$ in Eq. (3.22) is the key mechanism for achieving high accuracy of the fine scale flow structures as well as capturing of shock waves in a stable manner. The elements of $\Phi_{i+1/2}^*$ can be identified as the nonlinear dissipation portion of a TVD, ENO, or WENO scheme with the exception that they are premultiplied by $\kappa \theta_{i+1/2}^l$. Yee et al. [1] defined $\Phi_{i+1/2}^*$ using a TVD scheme. Garnier et al. [36], on the other hand, defined $\Phi_{i+1/2}^*$ using the dissipative part of ENO or WENO schemes.

The main disadvantage with characteristic-based filters is that the parameter κ is problem depended. Numerous simulations and tests were carried out by Yee et al. [1] for different flows. It was found, however, that different examples require a different value of κ . The suggested range of κ in [1] was $0.03 \leq \kappa \leq 2$ where larger values of κ are used for flows with discontinuities and smaller values are required for smooth flows including complex features, such as vortex convection or vortex pairing. In order to remedy this problem, Sjogreen and Yee [117] used a regularity estimate obtained from the wavelet coefficients of the solution to obtain a better value for the filter sensor.

The function $\theta_{i+1/2}^l$ in Eq. (3.22) is the Harten switch. This switch for a general $2m + 1$ points scheme is given by

$$\hat{\theta}_{i+1/2}^l = \max(\hat{\theta}_{i-m+1}, \dots, \hat{\theta}_{i+m}), \quad (3.23)$$

$$\hat{\theta}_i^l = \left| \frac{|e_{i+1/2}^l| - |e_{i-1/2}^l|}{|e_{i+1/2}^l| + |e_{i-1/2}^l|} \right|^p. \quad (3.24)$$

In Eq. (3.24), p is a second parameter that determines the performance of the filter and can be varied to better capture the particular physics instead of varying κ . The higher the parameter p the less is the amount of numerical dissipation added to the numerical solution. For $p \geq 1$ the order of accuracy of the dissipation term is essentially increased. For all numerical examples in [1,117], a constant value $p = 1$ was used. Furthermore, in order to keep the stencil of the scheme compact the Harten's switch was computed as

$$\theta_{i+1/2}^l = \max(\theta_i^l, \theta_{i+1}^l). \quad (3.25)$$

In Eq. (3.24), $e_{i+1/2}^l$ are elements of $R_{i+1/2}^{-1}(U_{i+1} - U_i)$ where $R_{i+1/2}^{-1}$ is the left eigenvector of the flux Jacobian $\partial F / \partial U$ that transforms back to the conservative variable space the filter operator.

The elements $\phi_{i+1/2}^l$ in Eq. (3.20) are evaluated based on TVD schemes [115,116,118]. Choosing Harten–Yee upwind TVD for example obtain

$$\phi_{i+1/2}^l = \frac{1}{2} \psi(c_{i+1/2}^l)(g_{i+1}^l) - \psi(c_{i+1/2}^l + \gamma_{i+1/2}^l)e_{i+1/2}^l, \quad (3.26)$$

where

$$\gamma_{i+1/2}^l = \frac{1}{2} \psi(c_{i+1/2}^l) = \begin{cases} (g_{i+1}^l - g_i^l)/e_{i+1/2}^l & e_{i+1/2}^l \neq 0, \\ 0 & e_{i+1/2}^l = 0. \end{cases} \quad (3.27)$$

$$\psi(c_{i+1/2}^l) = \begin{cases} |c_{i+1/2}^l| & |c_{i+1/2}^l| \geq \delta_1, \\ \frac{c_{i+1/2}^l + \delta_1^2}{2\delta_1} & |c_{i+1/2}^l| < \delta_1. \end{cases} \quad (3.28)$$

In Eq. (3.26), $e_{i+1/2}^l$ are the characteristic speeds of the flux Jacobian matrix $\partial F/\partial U$ evaluated at the Roe's average state [119], ψ is an entropy correction [120] where $0 < \delta \ll 1$, and g_i^l is a limiter function.

Examples of commonly used limiter functions are:

- (a) $g_j^l = \text{minmod}(e_{j-1/2}^l, e_{j+1/2}^l)$,
- (b) $g_j^l = (e_{j+1/2}^l e_{j-1/2}^l + |e_{j+1/2}^l e_{j-1/2}^l|)/(e_{j+1/2}^l + e_{j-1/2}^l)$,
- (c) $g_j^l = \{e_{j-1/2}^l [(e_{j+1/2}^l)^2 + \delta_2] + e_{j+1/2}^l [(e_{j-1/2}^l)^2 + \delta_2]\}/[(e_{j+1/2}^l)^2 + (e_{j-1/2}^l)^2 + 2\delta_2]$,
- (d) $g_j^l = \text{minmod}(e_{j-1/2}^l, 2e_{j+1/2}^l \cdot \frac{1}{2}(e_{j+1/2}^l + e_{j-1/2}^l))$,
- (e) $g_j^l = S \max[0, \min(2|e_{j+1/2}^l|, S \cdot e_{j-1/2}^l)]$,
 $\min(|e_{j+1/2}^l|, 2S \cdot e_{j-1/2}^l)];$
 $S = \text{sgn}(e_{j+1/2}^l).$

Here δ_2 is a small dimensionless parameter to prevent division by zero and $\text{sgn}(e_{j+1/2}^l) = \text{sgn}(e_{j-1/2}^l)$. In practical calculations $10^{-7} \leq \delta_2 \leq 10^{-5}$ is a commonly used range. For $e_{j+1/2}^l + e_{j-1/2}^l = 0$, g_j^l is set to zero in (b). The minmod function of a list of arguments is equal to the smallest number in absolute value if the list of arguments is of the same sign, or is equal to zero if any arguments are of opposite sign.

To facilitate computer implementation the entropy correction $\psi(c)$ in Eq. (3.28) is evaluated as

$$\psi(c) = \sqrt{(c^2 + \delta^2)}, \quad \delta = \frac{1}{16} \quad (3.29)$$

and $\gamma_{i+1/2}^l$ in Eq. (3.27) is computed by

$$\gamma_{i+1/2}^l = \frac{\psi(c_{i+1/2}^l)(g_{i+1/2}^l - g_i^l)e_{i+1/2}^l}{2(c_{i+1/2}^l)^2 + \varepsilon}, \quad \varepsilon = 10^{-7}. \quad (3.30)$$

In addition, the switch in Eq. (3.24) is modified to avoid division by zero

$$\theta_i^l = \frac{|\epsilon_{i+1/2}^l| - |\epsilon_{i-1/2}^l|}{|\epsilon_{i+1/2}^l| + |\epsilon_{i-1/2}^l| + \varepsilon}. \quad (3.31)$$

Recently, Sjogreen and Yee [121] proposed further improvements to the estimation of the filter numerical flux introducing regularity estimates from the wavelet coefficients of the solution. This recent development is as follows. Considering the l th element of the filter numerical flux function $\tilde{f}_{i+1/2}^l$ (see Eq. (3.22)) as the product of the sensor $\omega_{i+1/2}^l$ and a nonlinear dissipation function $\phi_{i+1/2}^l$

$$\tilde{f}_{i+1/2}^l = \omega_{i+1/2}^l \phi_{i+1/2}^l \quad (3.32)$$

the sensor $\omega_{i+1/2}^l$ that in Eq. (3.24) is modified while the numerical dissipation portion $\phi_{i+1/2}^l$ of Eq. (3.26) of Harten and Yee TVD scheme remains the same.

3.6.1. ENO and WENO ACM filters

A recent improvement of ACM filters is application of ENO and WENO procedure in the evaluation of the dissipative fluxes [36]. The dissipative numerical fluxes for TVD-MUSCL schemes (see Eq. (3.21)) are

$$\tilde{F}_{i+1/2}^{*M} = \frac{1}{2} R_{i+1/2} \Phi_{i+1/2}^{*M}, \quad (3.33)$$

where the elements $\phi_{i+1/2}^l$ of $\Phi_{i+1/2}^{*M}$ are given by

$$\phi_{i+1/2}^l = \kappa g_{i+1/2}^l |c_{i+1/2}^l| e_{i+1/2}^l, \quad (3.34)$$

where

$$e_{i+1/2}^l = R_{i+1/2}^{-1} (U_{i+1/2}^R - U_{i+1/2}^L)$$

and $c_{i+1/2}^l$ are the eigenvalues of the flux Jacobian $U_{i+1/2}^R, U_{i+1/2}^L$ are the upwind-biased interpolation of the neighboring U_i values with the slope limiters imposed. The MUSCL approach can be extended to r th order accurate ENO schemes of Ref. [1] as follows. The dissipative numerical flux is written as

$$\tilde{F}_{i+1/2}^{*ENO} = R_{i+1/2} \Phi_{i+1/2}^{*ENO}, \quad (3.35)$$

where the element $\phi_{i+1/2}^l$ of $\Phi_{i+1/2}^{*ENO}$ is obtained from the dissipative part of the ENO scheme, which results (see Section 4) by subtracting an m th-order accurate, centered scheme from an r th-order accurate ENO approximation as

$$\phi_{i+1/2}^l = \theta_{i+1/2}^l \left(\sum_{p=0}^{r-1} c_{k,p}^r R_{i+1/2}^{-1} F_{i-r+1+k+p} - \sum_{p=0}^{m-1} c_{\frac{m}{2},p}^m R^{-1} F_{i-m+1+\frac{m}{2}+p} \right), \quad (3.36)$$

where $c_{k,p}^r$ are the reconstruction coefficients of the ENO reconstruction, and k is the stencil index selected among

the r candidate stencils S_k that are defined as

$$\begin{aligned} S(k) &= \{I_{i-r+k+1}, \dots, I_i, \dots, I_{i+k}\} \\ &= (x_{i-r+k+1}, \dots, x_i, \dots, x_{i+k}), \quad k = 0, \dots, r-1. \end{aligned} \quad (3.37)$$

The m th-order accurate centered scheme is a subclass of ENO coordinate stencils with $k = m/2$ and m even. All choices $m \geq 2l$, $l = 1, 2, \dots$ are valid for the construction of error-dissipative terms. However, in order to keep the accuracy of the base scheme the same with order of the dissipative terms $m = q$ since larger values of m do not improve the formal accuracy and increase the computing cost.

An increased order of accuracy can be achieved by exploiting the WENO idea in the construction of the $\phi_{i+1/2}^l$ dissipative terms as follows:

$$\begin{aligned} \phi_{i+1/2}^l &= \sum_{k=0}^{r-1} \omega_k \left[\theta_{i+1/2}^l \left(\sum_{p=0}^{r-1} c_{k,p}^r R_{i+1/2}^{-1} F_{i-r+1+k+p} \right. \right. \\ &\quad \left. \left. - \sum_{p=0}^{m-1} c_{m/2,p}^m R_{i+1/2}^{-1} F_{i-m+1+m/2+p} \right) \right]. \end{aligned} \quad (3.38)$$

The WENO approach (see Section 4) achieves $(2r-1)$ th-order of accuracy by performing linear, convex combination with weights ω_k of the r possible r th order ENO stencils.

3.7. Finite-volume compact difference-based schemes

Finite-volume (FV) methods offer several advantages compared to finite-difference (FD) formulation especially for the numerical simulation of nonlinear phenomena. The advantage of the FV formulation with respect to the FD formulation is that the former is based on the integral form of the conservation laws. As a result, flux conservation is enforced even on arbitrary meshes since the fluxes collapse telescopically by construction. Furthermore, analysis of the finite-volume methods shows that they have superior performance in the high wavenumber range and that they exhibit lower truncation error. The main disadvantage of the FV formulation, especially when high-order accuracy is required, is the significantly higher computing cost of the FV methods compared to FD formulation.

For complex aerodynamic simulations, there is little place left for tuning parameters that regulate accuracy and stability of the computed solutions. The upwind-differencing schemes used in CFD, although computationally more intensive than finite differences were proven unsurpassed in their computational accuracy and robustness. The properties of these schemes are well justified and explained only for one-dimensional flows. Application of upwind-differencing schemes in the FV

context for two- and three-dimensional flows, similar to the FD formulation, is however based on one-dimensional physics. Namely, the multidimensional FV formulation is based on the solution of the one-dimensional Riemann problem that describe the interaction between two fluid cells by finite-amplitude waves normal to their interface. The inadequacy of this approach however clearly shows up, irrespective of the order of accuracy, when the numerical solution contains shocks or shear waves not aligned with the grid. Roe [122] recognized this deficiency as early as 1985. The remedy to one-dimensional upwinding is incorporation of genuinely multidimensional physics in upwind algorithms [123,124]. Numerous efforts were made in the past to apply Riemann solvers in several physically appealing directions. Closer to the genuinely multidimensional approach is the work of Rumsey et al. [125] where multidimensional wave models were developed that minimize wave strengths and require only two inputs states, just as a classic high-order solver.

In support to quasi-, and genuinely multidimensional approaches, aimed at putting better physics in to interface fluxes some investigators have dedicated efforts in achieving more accurate process of flux calculation by improving Godunov scheme [126] in the reconstruction step that is the most important task in the solution process. Piecewise linear approximations based on adjacent values of the solution that do not produce spurious oscillations near discontinuities and regions of high solution gradients are obtained with the MUSCL schemes developed by van Leer [127,128] and/or quadratic approximations by Colella and Woodward [129]. Furthermore, for applications on structured-type grids high-order accuracy may be introduced into the finite-volume formulation performing reconstruction by means of primitive function as is described in the next section.

The solution procedure of the multidimensional problem with the finite-volume method consists of the following steps:

1. *Reconstruction:* Given the average values of the solution, reconstruct a polynomial approximation to the solution in each control volume. This polynomial may vary discontinuously from control volume to control volume.
2. *Flux quadrature:* Using the piecewise polynomial reconstruction of the solution approximate the flux integral or in the discrete form the summation of fluxes by numerical quadrature.
3. *Evolution and projection:* simply referred to as evolution where a Riemann solver and an appropriate temporal discretization scheme are used to evolve the numerical approximation of the flux integral.

Barth [130] describes in detail several reconstruction methods. Among them the k -exact reconstruction approach of Barth and Frederickson [131] is most commonly used for high-order accurate numerical solutions with the finite-volume method.

High-order (fourth- and sixth-order) compact difference-based schemes were developed by Gaitonde and Shang [132] in the finite volume context. The formulation of these schemes utilizes the primitive function approach. Optimization of the schemes for better linear wave propagation characteristics is performed by minimizing dispersion and isotropy errors. The one-dimensional advection equation is used as the prototype for scheme development.

$$\frac{\partial u}{\partial t} + \frac{\partial f}{\partial x} = 0, \quad f = cu, \quad c > 0. \quad (3.39)$$

For equally spaced mesh $\Delta x = h$ the finite-volume formulation is

$$h \frac{\partial \bar{u}}{\partial t} + \left[f\left(u\left(x + \frac{h}{2}, t\right)\right) - f\left(u\left(x - \frac{h}{2}, t\right)\right) \right] = 0, \quad (3.40)$$

where \bar{u} is the cell average

$$\bar{u} = \frac{1}{h} \int_{x-h/2}^{x+h/2} u \, dx. \quad (3.41)$$

A mesh is introduced (see Fig. 9) with cells $1, 2, \dots, i, \dots, N$ and cell interfaces $1/2, 3/2, \dots, i-1/2, i+1/2, \dots, N+1/2$. The discrete approximation of Eq. (3.40) on this mesh is

$$\frac{\partial \bar{u}_i}{\partial t} + \frac{1}{h} [\hat{f}_{i+1/2} - \hat{f}_{i-1/2}] = 0, \quad (3.42)$$

here \hat{f} is the numerical flux function approximating f with reconstructed values $\hat{u}_{i+1/2}$ at the cell interfaces

$$\hat{f}_{i+1/2} = \hat{f}(\bar{u}_{i-1}, \bar{u}_i, \bar{u}_{i+1}) = \hat{f}(\hat{u}_{i+1/2}). \quad (3.43)$$

The order of accuracy, k , is introduced in Eq. (3.43) as

$$\hat{f}(\hat{u}_{i+1/2}) = f(u_{i+1/2}) + \mathcal{O}(h^k). \quad (3.44)$$

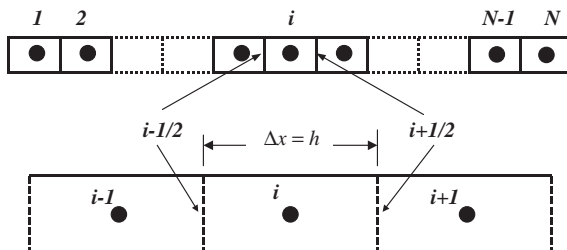


Fig. 9. One-dimensional finite volume mesh.

The crucial step in this finite-volume formulation is the reconstruction, e.g. approximation of the pointwise quantity $\hat{u}_{i+1/2}$ at the cell interfaces to the desired accuracy using known average values at the \bar{u}_i cell centers so that the accuracy requirement of Eq. (3.44) is satisfied, e.g. determine $\hat{u}_{i+1/2}$ such that

$$\hat{u}_{i+1/2} = u_{i+1/2} + \mathcal{O}(h^k). \quad (3.45)$$

The first step for the solution of this reconstruction problem is to form a primitive function U of $u(x)$ defined as

$$U = \int_0^x u(\xi) \, d\xi. \quad (3.46)$$

Then (see Section 5 for more details)

$$u_{i+1/2} = u_{i-1/2} + \bar{u}_i h, \quad i = 1, \dots, N \quad (3.47)$$

and the desired point values $\hat{u}_{i+1/2}$ are obtained by

$$\hat{u}_{i+1/2} = \frac{dU}{dx} + \mathcal{O}(h^k). \quad (3.48)$$

Using a three- or five-point compact scheme for the evaluation of $U' = dU/dx$ (see Section 3.1) one obtains fourth or sixth order accuracy for the evaluation of $\hat{u}_{i+1/2}$.

3.8. Results with ACM filters

Application of the ACM filters with discretizations obtained from fourth- and sixth-order accurate in space compact schemes showed good performance [1] for long time convection of isentropic vortices. Numerous examples presented in [1] demonstrate the superior performance of high-order discretizations with ACM filters. The effect of parameters, which are involved in the filter (see Eqs. (3.22) and (3.24)), on the performance of the ACM filter was tested extensively.

The first complex flow problem considered in [1] is vortex pairing in time-developing mixing layer. The base parallel flow, $u = \tanh(2y)/2$, is disturbed with a normal velocity perturbation v' given by

$$v' = \sum_{k=1}^2 \alpha_k \cos(2\pi kx/L_x + \phi_k) e^{-y^2/b},$$

where $L_x = 30$, $b = 10$, $\alpha_1 = 0.01$, $\phi_1 = \pi/2$, and $\alpha_2 = 0.05$, $\phi_2 = -\pi/2$. Fig. 10 shows the temperature field obtained from fourth order in space and time computation with the ACM filter at $t = 40, 80, 120$ and 160 . This computation was performed on a fine 201×201 stretched mesh with $\kappa = 0.7$ and the recommended value of the parameter $\delta = \frac{1}{16}$ was used.

The effect of the ACM filter on the resolution of the computed solution is shown in Fig. 11. It appears that higher resolution is obtained with the ACM filter and the advantage of using high-order methods for the computation of complex flow features is evident. This

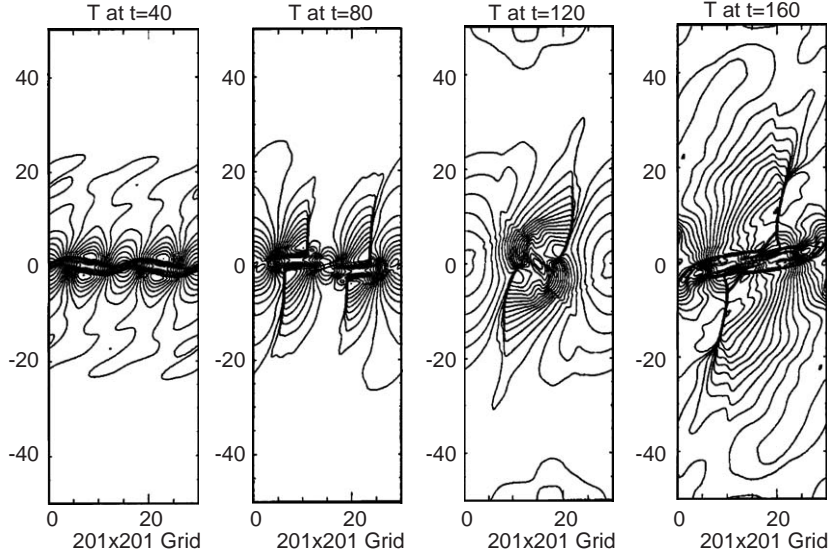


Fig. 10. Four stages in the vortex pairing, at times $t = 40, 80, 120, 160$, showing the temperature contours for a 201×201 grid with $\kappa = 0.7$ for the nonlinear fields and $\kappa = 0.35$ for the linear fields using ACM44.

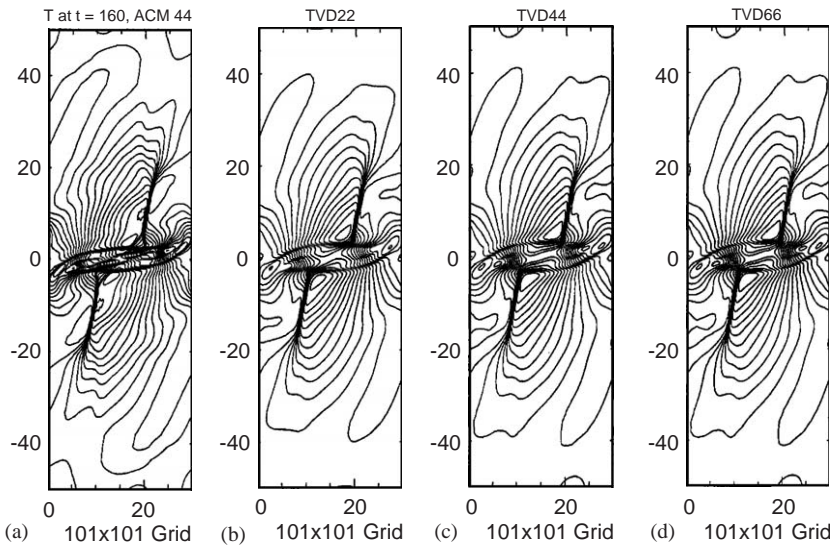


Fig. 11. Effect of order of accuracy on TVD methods (TVD22, TVD44, and TVD66), compared with the ACM44 solution at $t = 160$, illustrated by temperature contours at $t = 160$ for a 101×101 grid.

latter effect is further demonstrated in Fig. 12 where increase of the order of accuracy with increasingly higher order base schemes results into crisper resolution of fine flow features in the vortex region while the resolution of smooth flow remains the same. The effect of the limiter is shown in Fig. 13 where four different limiters were tested with the same ACM44 scheme. The effect of the smoothing parameter δ in Eq. (3.27) was also investigated. The computations of Fig. 14, for

example, demonstrate that the value of δ cannot be reduced very much without introducing spurious oscillations.

Another example used in [1] was the shock wave impingement on a spatially evolving mixing layer. The mixing layer was again generated with a hyperbolic tangent profile with $u_1 = 3$ and $u_2 = 2$ and perturbed in the normal to the main flow direction. A strong oblique shock at $\beta = 12^\circ$ impinged on the shear layer and the

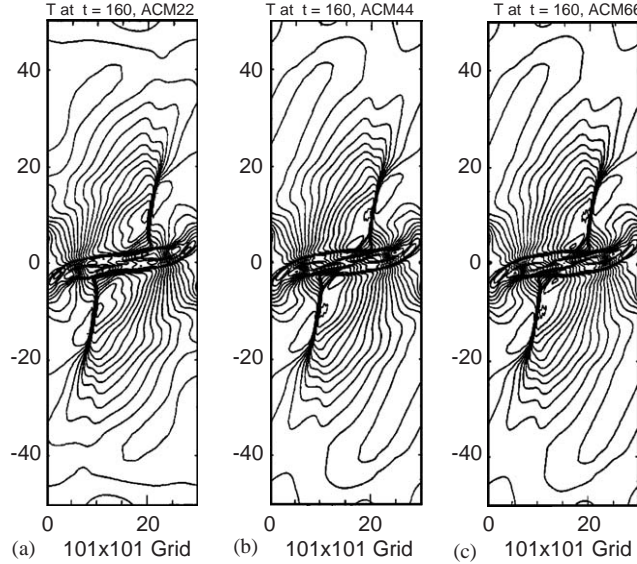


Fig. 12. Effect of order of accuracy on ACM methods (ACM22, ACM44, and ACM66) at $t = 160$ for a 101×101 grid compared with the reference solution (ACM44, 201×201 grid) using $\kappa = 0.7$ for the nonlinear fields and $\kappa = 0.35$ for the linear fields.

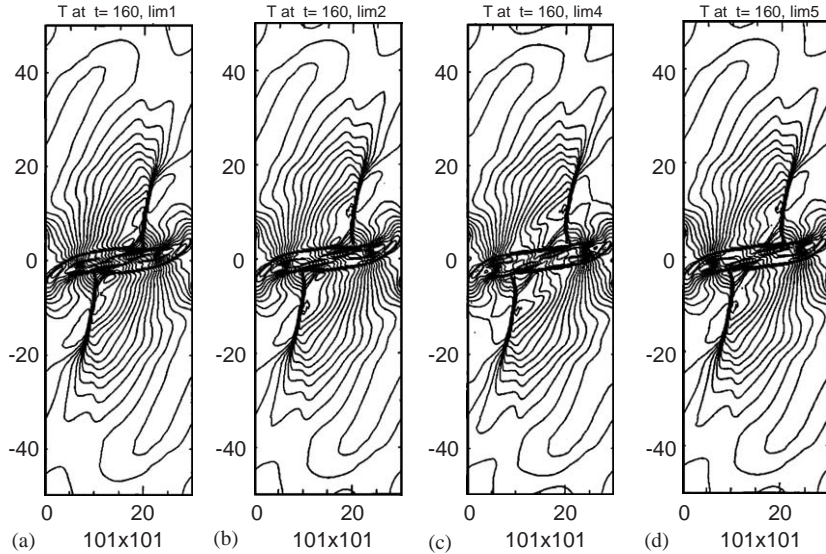


Fig. 13. Effect of flux limiters in the ACM44 scheme on the solution resolution, illustrated by temperature contours at $t = 160$.

flow after the interaction remained supersonic throughout up to the outflow boundary. The main features of the computed flow field with the ACM44 method (fourth-order accurate for the inviscid terms plus fourth-order accurate in space viscous terms) is shown in Fig. 15. The effect of the order of accuracy is shown in Fig. 16 for computations obtained with second-, fourth- and sixth-order accurate schemes. Similarly to the

simple shear layer case, the effect of the parameter δ in Eq. (3.27) on the stability is shown in Fig. 17.

A viscous shock tube problem was considered in [36]. Computed flow fields with different base schemes and grid densities are shown in Fig. 18. It is demonstrated that the centered schemes with ACM filter reach the same resolution and solution quality as the well-established WENO schemes. Comparisons of solutions

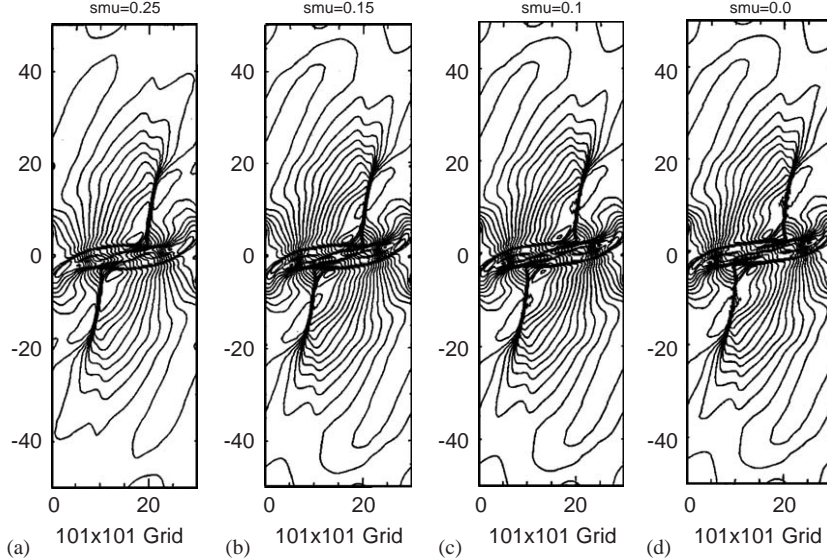


Fig. 14. Effect of δ , $((\text{smu})^2)$ in the ACM44 scheme on the solution resolution, illustrated by temperature contours at $t = 160$.

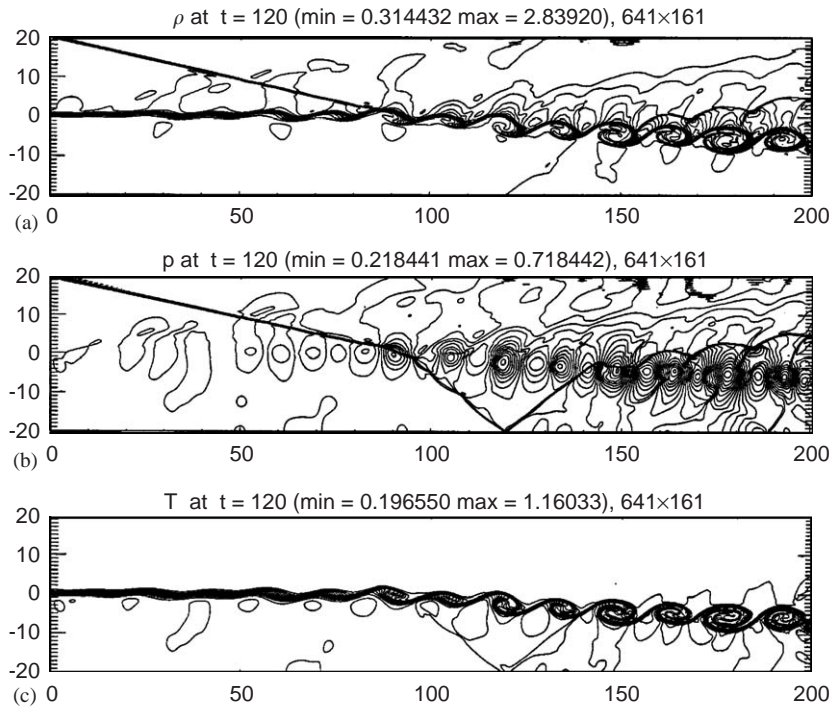


Fig. 15. The reference solution for the shock–shear-layer interaction problem at $t = 120$.

computed with finer and finer meshes and evaluation of the ACM sensor using wavelets shown in Fig. 19 demonstrate that at all grid densities the performance is very good. For comparison, computations with the

original ACM sensor of Eq. (3.27) are shown in Fig. 20. Comparisons of the computed density distribution on the wall obtained from numerical solutions with different methods is shown in Fig. 21.

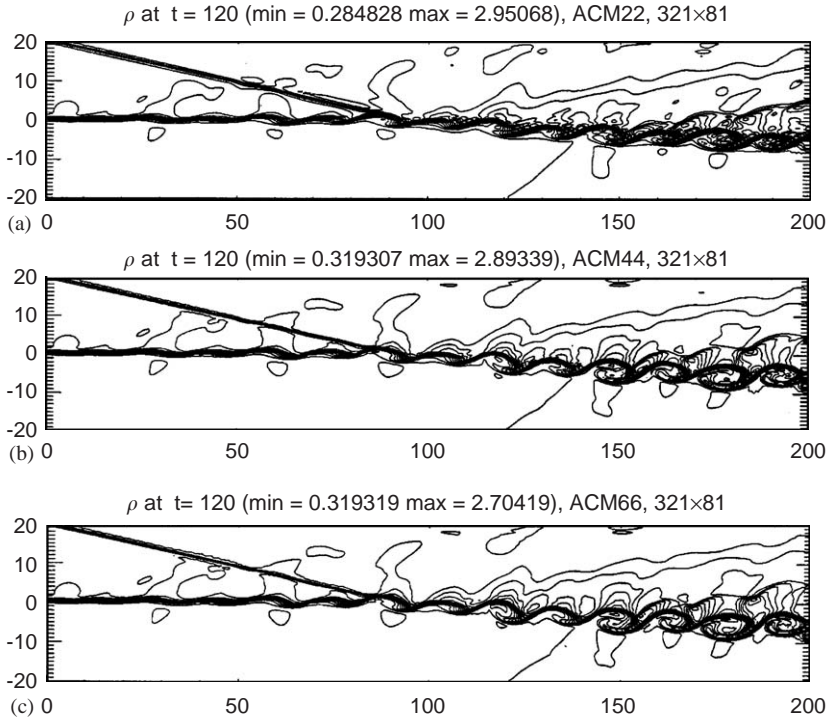


Fig. 16. Comparison of density contours at $t = 120$ for the shock–shear-layer test case.

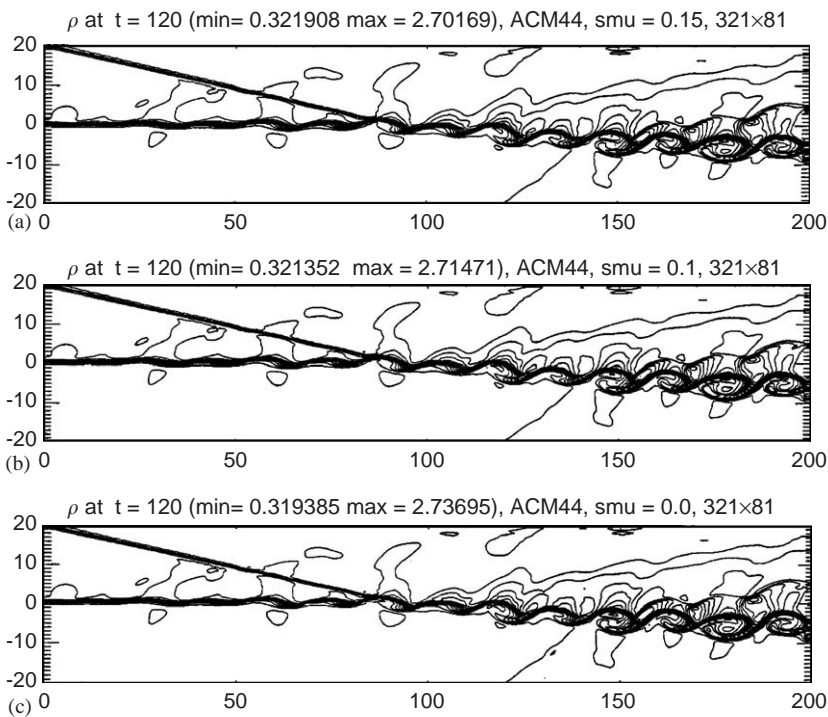


Fig. 17. Effect of δ , $((\text{smu})^2)$ in the ACM44 scheme on the solution resolution, illustrated by density contours at $t = 120$.

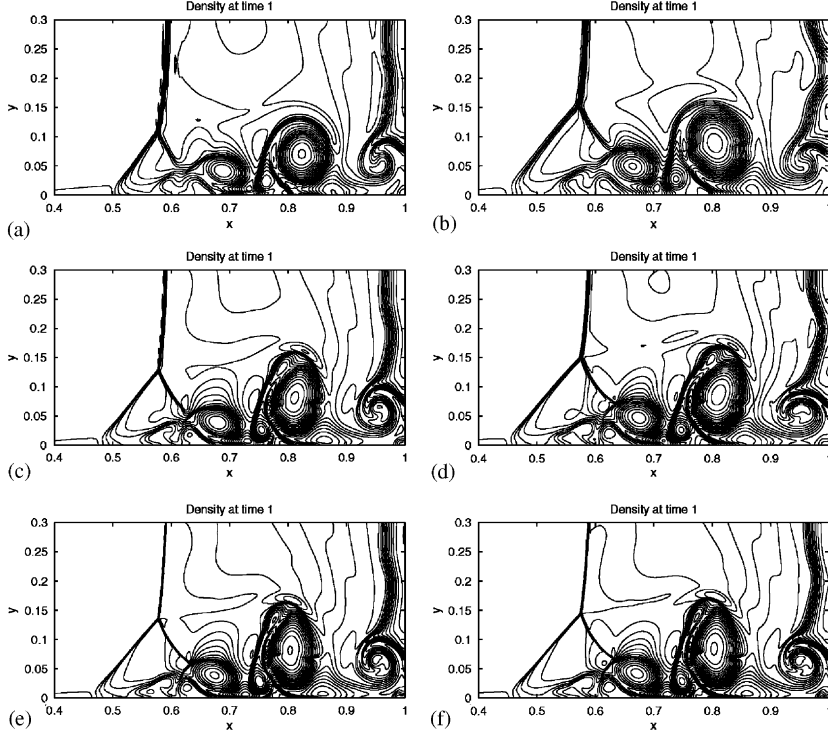


Fig. 18. Grid refinement comparison of ACM66-RK4 and WENO5-RK4 for $Re = 200$. Density contours. (a) ACM66-RK4, 250×125 grid; (b) WENO5-RK4, 250×125 grid; (c) ACM66-RK4, 500×250 grid; (d) WENO5-RK4, 500×250 grid; (e) ACM66-RK4, 1000×500 grid; (f) WENO5-RK4, 1000×500 grid.

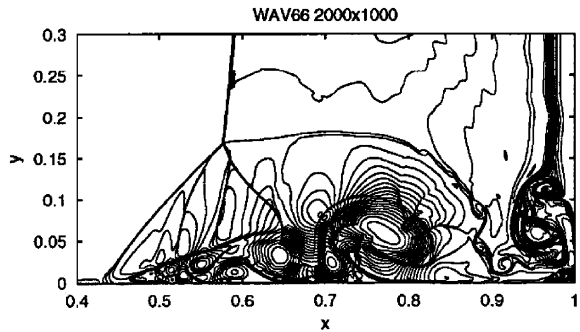


Fig. 19. Grid refinement of WAV66-RK4 for $Re = 1000$. Density contours, 2000×1000 grid.

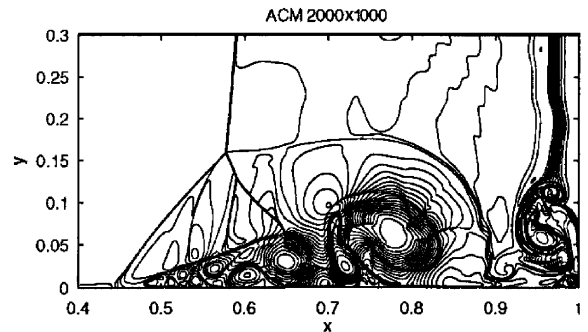


Fig. 20. Grid refinement of ACM66-RK4 for $Re = 1000$. Density contours, 2000×1500 grid.

High-order accurate solutions with ACM filters were also obtained in [117] for more complex problems containing finite-rate chemistry. The flow field resulting from the interaction of a planar Mach 2 shock in air with a circular zone of hydrogen was considered. The computed flow field at different times is shown in Fig. 22. The improvements with grid refinement

obtained for the computation of the flow with very complex flow features is shown in Fig. 23. For comparison, in Fig. 24 the computed flow fields with the WENO fifth-order accurate scheme on the same meshes is shown. It appears that the high order in space-centered scheme with the ACM filter yields the same solution quality as the WENO scheme.

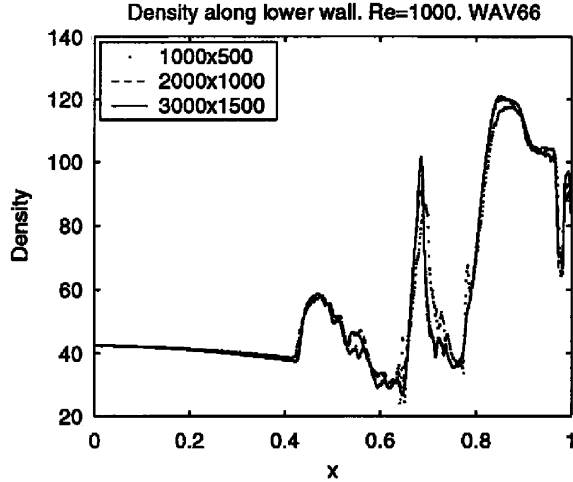


Fig. 21. Density along lower wall on different grids for $R_e = 1000$. WAV66-RK4.

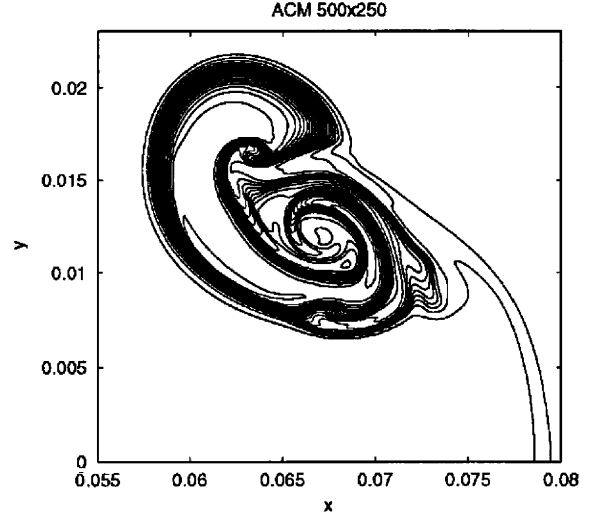


Fig. 23. Grid refinement of the ACM66-RK4 scheme. Hydrogen mass fraction contours at time $60 \mu\text{s}$.

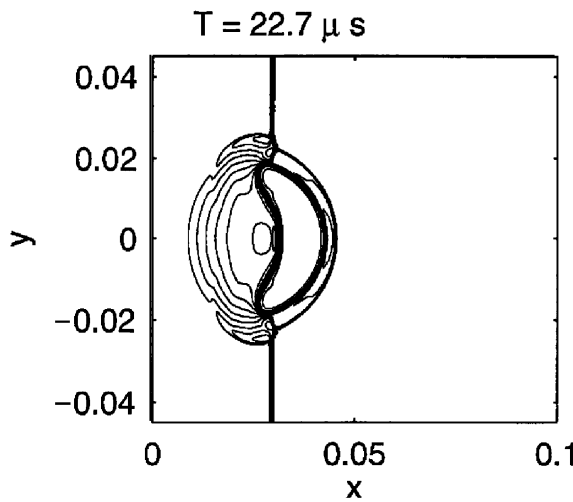


Fig. 22. Density contours of ACM66-RK4 on a 500×250 grid.

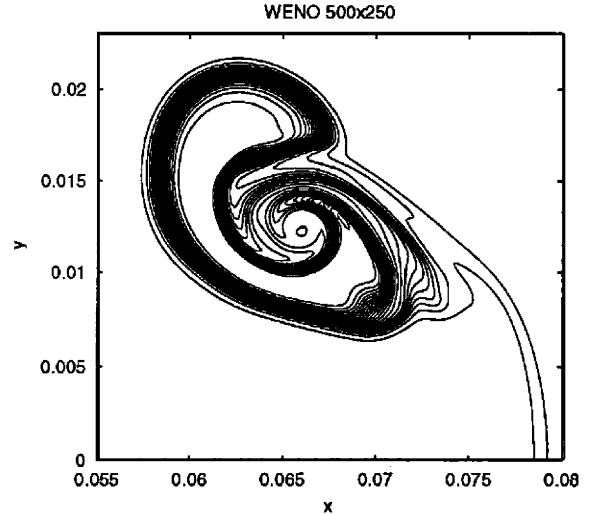


Fig. 24. Grid refinement of the WENO5-RK4 scheme. Hydrogen mass fraction contours at time $60 \mu\text{s}$.

3.9. Results with compact schemes and filters

Application of compact centered schemes found widespread application in the numerical simulation of noise sources from compressible flow such as vortices and jets. Several examples of computations obtained with compact schemes are presented in the following paragraphs. The far-field sound generated by compressible co-rotating vortices was computed by the numerical solution of the two-dimensional, compressible Navier–Stokes using the sixth-order compact scheme to evaluate the spatial derivatives [133]. Time marching

was performed with the fourth-order Runge–Kutta scheme. The computational domain extended to two acoustic wavelengths in all directions. A major numerical consideration in the aeroacoustic computations of [133] was the choice of boundary conditions. The appropriate boundary conditions for the analysis of flows in free space are non-reflecting boundary conditions which allow waves to freely leave the domain. The zeroth-order boundary conditions of [134] were used for the computations. It was found in [133] that the combination of spatial and temporal schemes with these boundary conditions has negligible

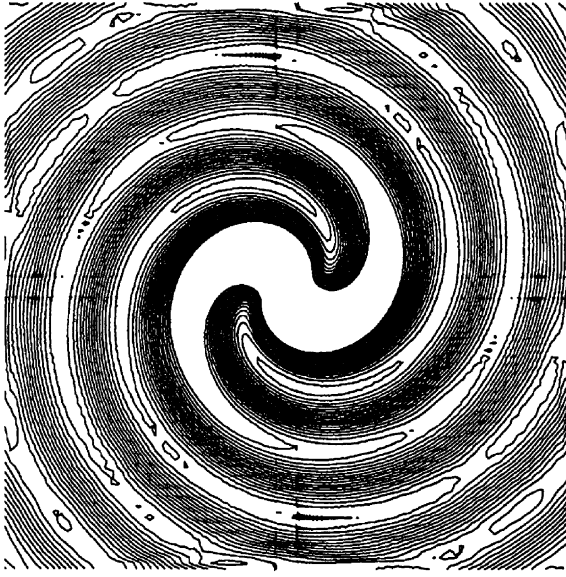


Fig. 25. The far-field pressure (ambient removed) at $t c_0 / R = 185$. The contour levels are from $P / (\rho_0 c_0^2) = \pm 4 \times 10^{-5}$ with $\Delta P / (\rho_0 c_0^2) = 0.05 \times 10^{-5}$. The ‘cross’ pattern is a plotting illusion caused by the high grid densities near the x - and y -axis.

numerical damping and preserves the physical property that, in the absence of viscosity waves propagate unattenuated. For the vortices separated by distance $2R$, the initial vorticity distribution was Gaussian as

$$\omega = 3.57 \frac{U_0}{r_0} e^{-1.25(r/r_0)^2}$$

with circulation $\Gamma_0 = 2\pi(0.7)^{-1} U_0 r_0$ and r_0 the distance from the vortex core where the maximum Mach number is attained for each vortex. The numerical results of [133] were compared with exact results from the acoustic analogue by Mohring [135]. The computed far-field pressure is shown in Fig. 25. Comparisons of the computed solutions [133] with the theoretical predictions of Mohring [135] are shown in Fig. 26. The agreement of the computations with the theory for the far-field sound from compact low-Mach-number flows is very good.

A second example of sound generation computation is the sound in a mixing layer [136]. The sound generated by vortex pairing in a two-dimensional compressible mixing layer was computed with DNS of the Navier–Stokes equations for the near-field and the acoustic field. Fourth- and sixth-order compact schemes were used for the computation of the derivatives. Time marching was performed with the fourth-order Runge–Kutta method. The computed acoustic field [136] is shown in

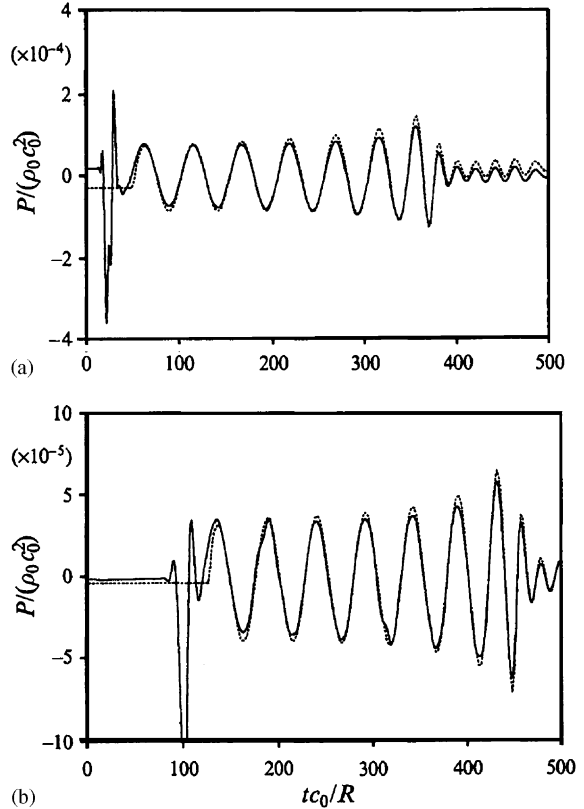


Fig. 26. Far-field pressure traces at (a) $r/\lambda = \frac{1}{2}$ and (b) $r/\lambda = 2$ showing the results of the simulation (—), and the prediction of Mohring’s equation (---). Both measurement points are located on the positive y -axis.

Fig. 27 for different frequencies. A comparison of the computed results with an acoustic analogy is shown in Fig. 28.

A third example of noise source calculation from free shear flow is the investigation of sound generation mechanisms in a Mach $M = 0.9$, $R_e = 3600$ turbulent jet [137]. The numerical solution of the governing equations was obtained for a cylindrical coordinates system. The azimuthal derivatives were computed with Fourier spectral methods and the radial and axial derivatives were computed with sixth-order compact finite differences. Again the fourth-order Runge–Kutta method was used to advance the solution in time. Some examples from the computation of [137] are presented. The instantaneous contours of vorticity are shown in Fig. 29. A visualization of the sound field is shown in Fig. 30. Comparisons of the computations with measurements are shown in Figs. 31–33. A comparison of the computed data with Lighthill’s equation is shown in Fig. 34. Further examples of jet noise prediction with explicit and compact finite-difference schemes can be

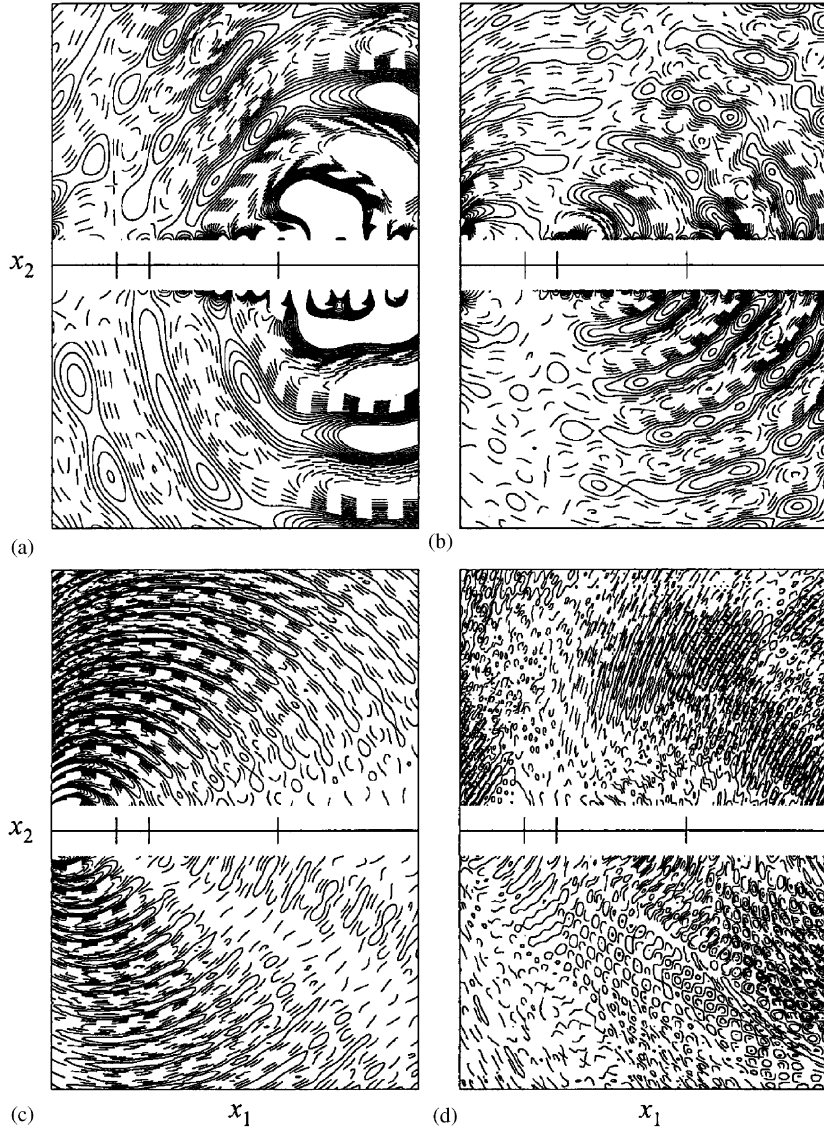


Fig. 27. Contours of the real part of the DFT of the dilatation away from the sheared region for several frequencies: (a) $f/4$, (b) $f/2$, (c) f , (d) $3f/2$.

found in recent publications [138–142] and references therein.

Sound generation flow low Mach number flow over a cylinder was computed by DNS of the two-dimensional Navier–Stokes equations [143]. The governing equations were again solved with a sixth-order accurate compact scheme and time integration was performed with the fourth-order accurate Runge–Kutta method. Examples from the computations of [143] are shown in Figs. 35–38. Fig. 35 shows the time-dependent vorticity field. Fig. 36 shows the development of the fluctuating pressure. Different views of pressure field are shown in

Fig. 37. The fluctuating pressure of Fig. 37b clearly shows the dipole radiation pattern of the sound generated by the cylinder unsteady wake. Comparisons of the DNS with the theory are shown in Fig. 38. The agreement with the theory of Curle is very good. Further applications of high-order finite-difference method to aeroacoustics can be found in recent publications [144–146] and references therein.

Comparisons of the numerical solution obtained with fourth-order accurate centered schemes with other solutions obtained by second-order centered schemes and upwind methods were carried out in [147]. It was

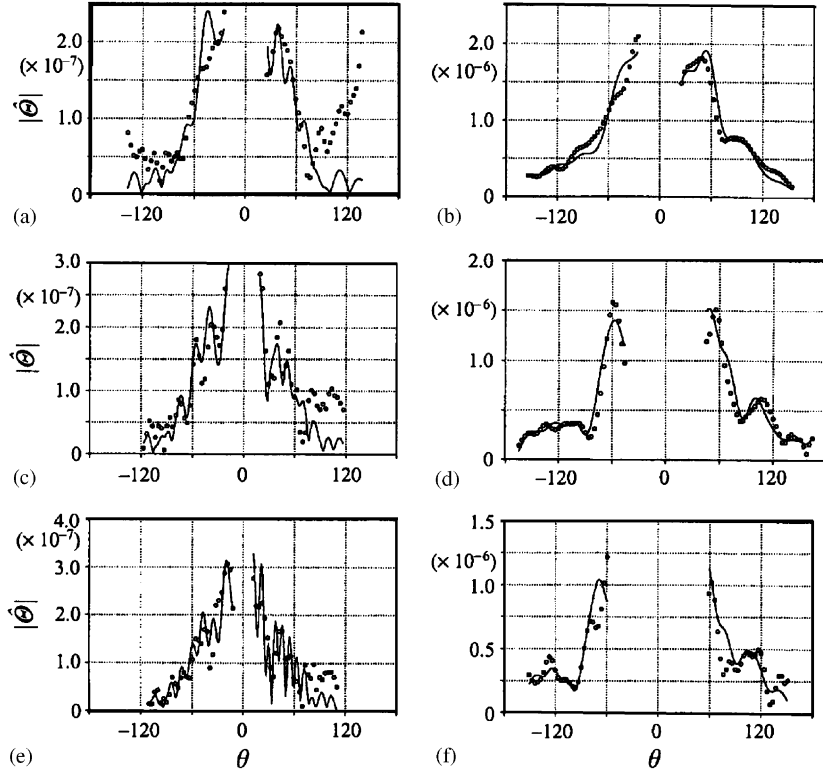


Fig. 28. Comparison of the magnitude of the acoustic waves (dilatation) predicted by solving the acoustic analogy (solid lines) and from the DNS (open circles).

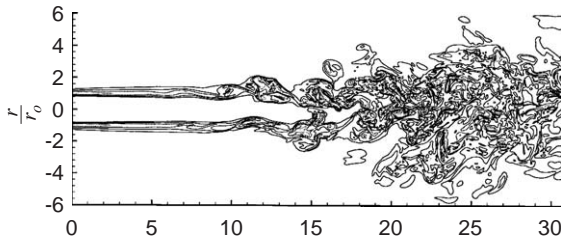


Fig. 29. Instantaneous contours of vorticity magnitude: levels are $\omega r_0/Uj = 0.35, 1, 2, 3, 4$ with lighter contours representing larger values. Peak vorticity magnitude (not shown) was $\omega r_0/Uj = 11$.

found that the discretization using higher-order approximation for all terms was substantially more accurate than the others. It produced less than two percent numerical error in lift and drag components on grids with less than 13,000 nodes for subsonic cases and less than 18,000 nodes for transonic cases. It was also concluded [147] that the higher-order discretization

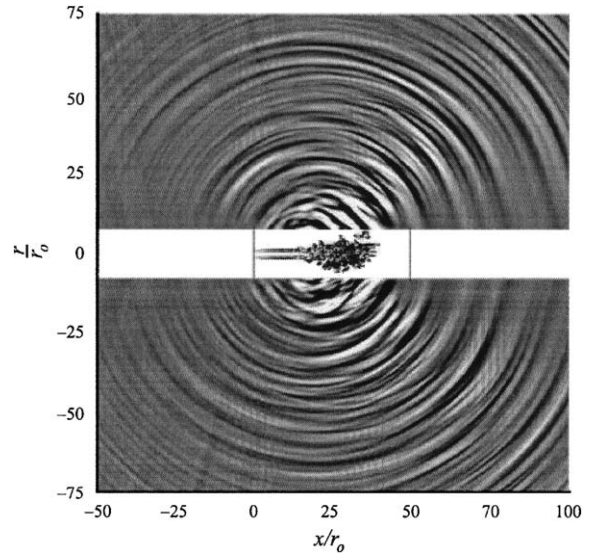


Fig. 30. Visualization of the far-field sound: black is $\Theta = \nabla \cdot \mathbf{u} < -0.0005a_0/r_0$ and white is $\Theta > 0.0005a_0/r_0$. The gray scale varies continuously between these extrema. The jet is visualized with contours of vorticity magnitude.

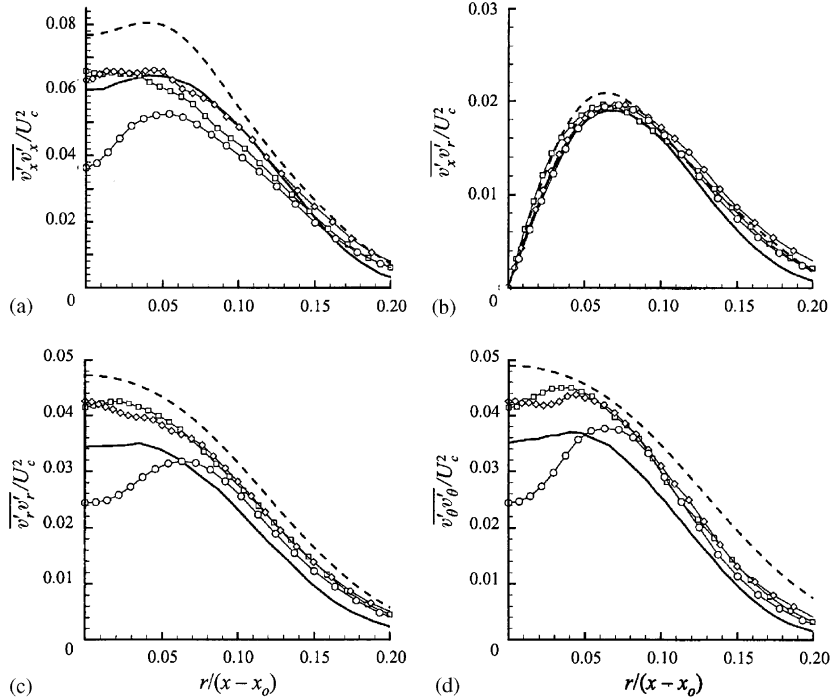


Fig. 31. Second moments of velocity: \circ , $x = 20r_0$; \diamond , $x = 25r_0$; \square , $x = 30r_0$; —, low-Mach-number experimental data from Panchapakesan and Lumley [268]; and - - -, low-Mach-number experimental data from Hussein et al. [269]. The Panchapakesan and Lumley [268] profiles were digitized and re-plotted from the least-squares fits in their publication; the Hussein et al. [269] profiles are the curve fits they provided. The simulation data were averaged in time for the entire simulation history and in space over a streamwise band of width $\Delta x_{\text{ave}} = 2r_0$.

produces solutions of a given accuracy much more efficiently than the others.

Shedding past a cylinder at $Re_D = 1000$ was computed in [148] with the second- and sixth-order compact schemes with tenth order spectral type filters (CD6F10 schemes). It was found that the higher-order scheme is well behaved for this general configuration, which was discretized with a high-aspect-ratio, stretched mesh. Fig. 39 shows that even at this low Reynolds number, results with the higher-order compact algorithm are superior in preserving the vortex street behind the cylinder. A quantitative comparison made at $R_D = 100$ with other highly resolved computations displayed good agreement the Strouhal number and maximum lift and drag coefficients for the high-order schemes. Preliminary direct numerical simulations of the three-dimensional wall-jet transition process are performed in [148] with the implicit time-integration scheme on a mesh of size $230 \times 125 \times 101$ with both the second and CD6F10 schemes. In the computations the jet is forced at the inflow plane with a two-dimensional forcing function. Fig. 40 shows the computed instantaneous flow structure in terms of contours of vorticity magnitude on a plane parallel to the plate at a distance of $1.3h$.

Spiral vortex breakdown above a slender delta wing with a sweep angle of 75° at 32° angle of attack was also computed in [148]. The free stream Mach number was $M = 0.2$, and the Reynolds number based on centerline chord is $Re_C = 9200$. Fig. 41a and b show the instantaneous y component of vorticity on a vertical plane cutting through the vortex core for the second-order method. At this angle of attack, the breakdown location is highly sensitive to details of the numerical simulation. Thus, on the coarse mesh the second-order scheme results in a premature break down of the vortex. By contrast, the CD6F10 solution shown in Fig. 41c displays a breakdown location similar to the second-order results on the fine mesh. The second-order method on the coarser mesh (Fig. 41a) shows relatively little detail with only two smeared concentrations of azimuthal vorticity in the vortex wake. On the other hand, CD6F10 results (Fig. 41c) exhibit a much richer structure corresponding to a stronger, tightly wound spiral in far better agreement with the grid-converged results of Fig. 41b obtained with the second order method with a fine grid.

Several test of vortex convection were performed in [149]. It was shown that for long-time propagation it is

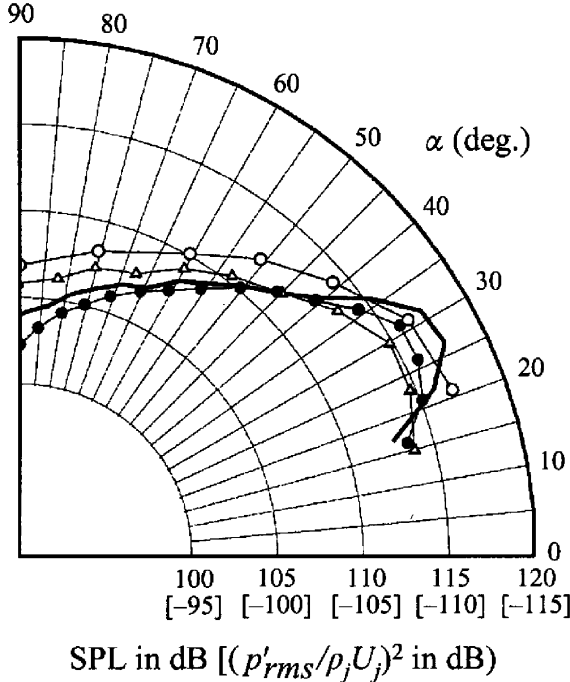


Fig. 32. Overall sound pressure level (and acoustic intensity in brackets) directivity on an arc at $60r_0$ from the nozzle and with α measured from the jet axis: —, $\Delta\tilde{p}_{\text{curle}}R_e = 3600$ present study; •, $R_e = 3600$, Stromberg et al. [270] experimental data; ○, $R_e = 2 \times 10^5$, Mollo-Christensen et al. [271] experimental data; △, $R_e = 6 \times 10^5$, Lush [272] experimental data (adjusted by 12 dB from 240 jet radii to 60).

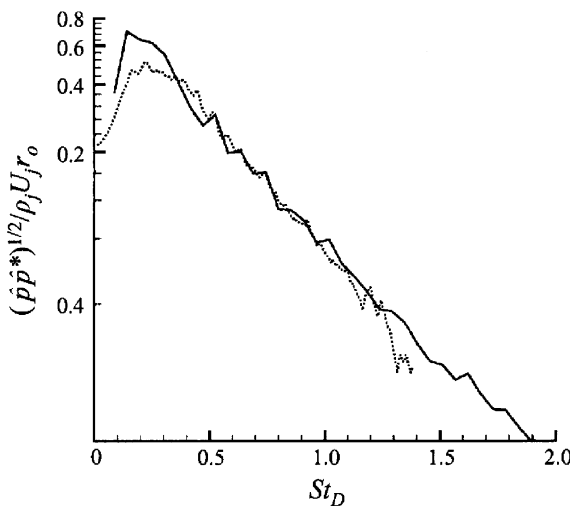


Fig. 33. Far-field pressure spectrum at $\alpha = 30$: —, present simulation; ·····, measurements of Stromberg et al.

important to compute the metric quantities with the same high order of accuracy as the base scheme for the convective terms. The performance of the high-order

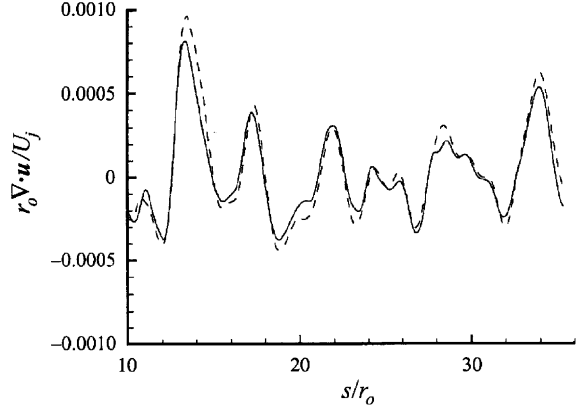


Fig. 34. Comparison of dilatation on a ray from $x = 18r_0$ and inclined at 45° from the jet axis: —, direct numerical simulation; - - -, Lighthill's equation.

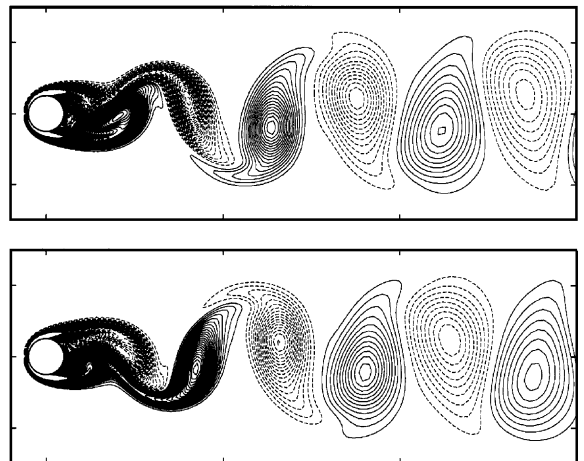


Fig. 35. Time development of a vorticity field. $M = 0.2$, $Re = 150$. The contour levels are from $\omega_{\min} = -1.0$ to $\omega_{\max} = 1.0$ with an increment of 0.02: —, $\omega > 0$; - - -, $\omega < 0$. (a) $t = 1930$, (b) $t = 1945$.

approach for a non-trivial column vortex convection on a 3-D dynamic mesh was considered in [149]. The axis of the vortex placed along $z = 0$. Inviscid calculations were performed with the E2 and C6 schemes using the RK4 method and a time step $\Delta t = 0.002$. A cross-section of the vortex on a $\zeta = \text{constant}$ plane at $T = 3.25$ is shown in Fig. 42a. At this instant, the grid has already experienced more than three cycles of the imposed oscillation with frequency $\omega = 1$. As the contours of velocity magnitude indicate, despite the significant unsteady mesh deformations, the high-order method is capable of preserving the axisymmetric character of the vortex even on this relatively coarse discretization

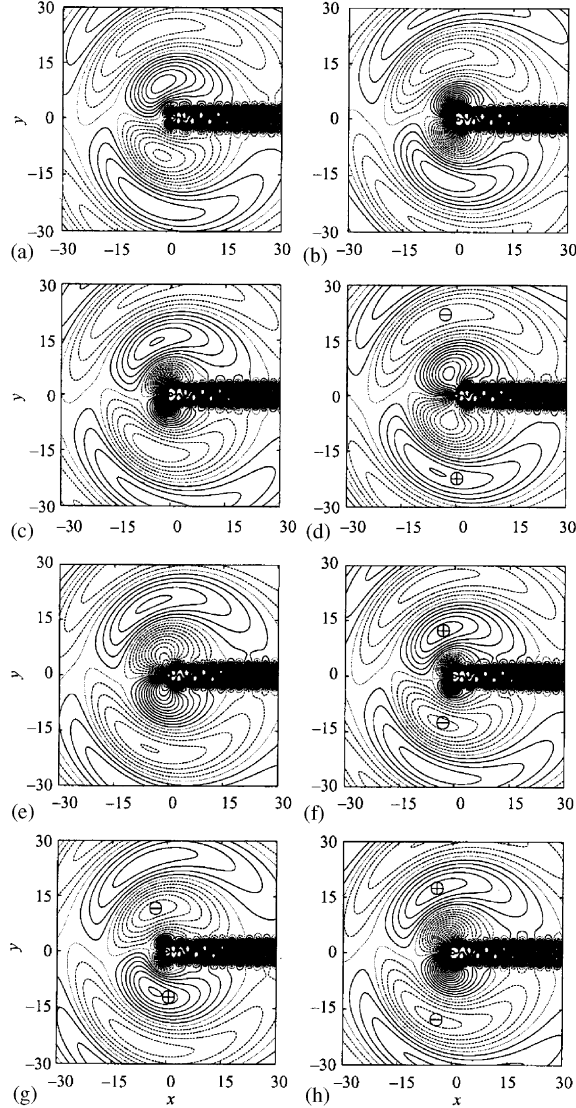


Fig. 36. Time development of a fluctuation pressure field, $\Delta\tilde{p}$. $M = 0.2$, $R_e = 150$. The contour levels are from $\Delta\tilde{p}_{\min} = -0.1M^{2.5}$ to $\Delta\tilde{p}_{\max} = 0.1M^{2.5}$ with an increment of $0.0025M^{2.5}$. —, $\Delta\tilde{p} > 0$; - - -, $\Delta\tilde{p} < 0$. (a) $t = 1925$, (b) $t = 1930$, (c) $t = 1935$, (d) $t = 1940$, (e) $t = 1945$, (f) $t = 1950$, (g) $t = 1955$, (h) $t = 1960$.

(approximately 10 points across the vortex). A comparison of the computed and exact solutions is shown in Fig. 42b in terms of the v component of velocity. The C6F10 results are observed to be in excellent agreement with the theoretical answer. This case demonstrates the advantage of the high-order methodology over standard low-order approaches even for 3-D applications in which the mesh is subjected to severe dynamic deformation.

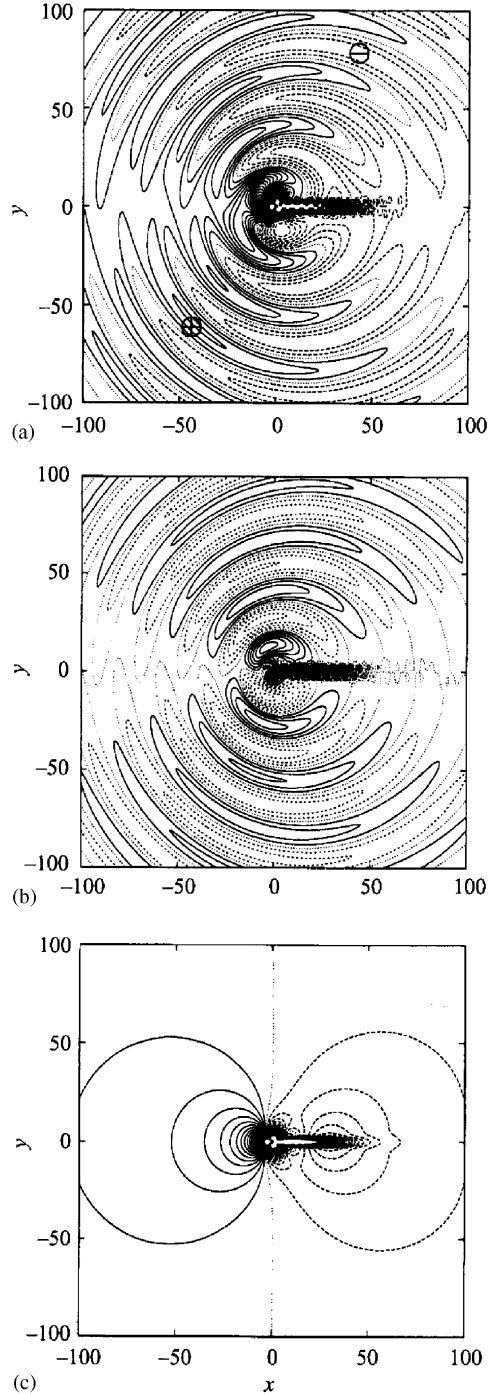


Fig. 37. Three different views of a pressure field at $M = 0.2$, $Re = 150$; —, positive pressure; - - -, negative pressure. (a) Total pressure, Δp , at $t = 2010$, (b) fluctuation pressure, $\Delta p'$, $t = 2010$, (c) mean pressure, Δp_{mean} .

Further demonstration of the high-order, dynamic-mesh technique was carried out in [149] with the simulation of the aeroelastic interaction arising from

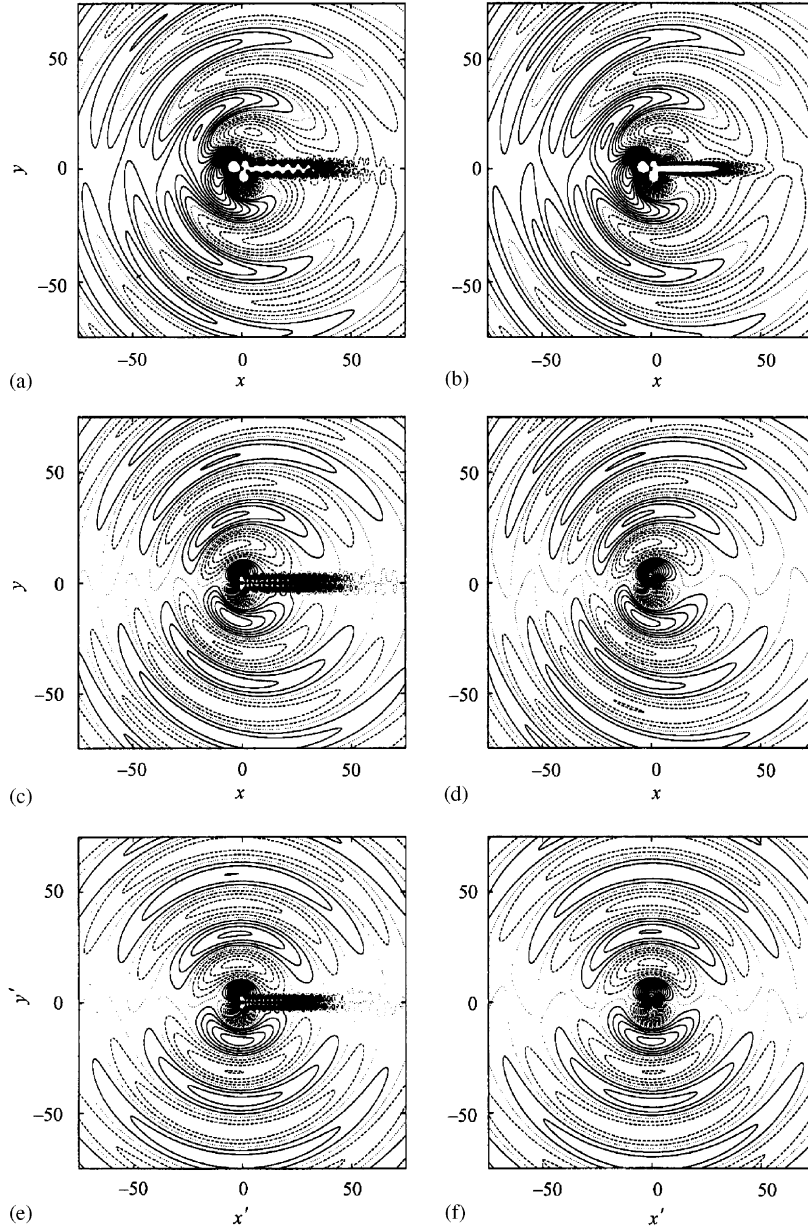


Fig. 38. Comparison of pressure distribution between DNS and Curle's solutions. $M = 0.2$, $R_e = 150$, $t = 2000$. The contour levels are from $-0.1M^{2.5}$ to $0.1M^{2.5}$ with an increment of $0.0025M^{2.5}$. —, Positive pressure, ---, negative pressure. (a) Δp (DNS), (b) $\Delta \tilde{p}$ (DNS), (c) $\Delta \tilde{p}^M$ (DNS), (d) $\Delta \tilde{p}_{\text{curle}}^D + \Delta p_{\text{mean}}$, (e) $\Delta \tilde{p}_{\text{curle}}^D$, (f) $\Delta \tilde{p}_{\text{curle}}$.

viscous laminar flow over a flexible surface. A schematic of the configuration considered is shown in Fig. 43a. The free-stream Mach number and Reynolds number (based on panel length, L) were $M = 0.9$ and $R_e = 1.0 \times 10^5$, respectively. The computed boundary-layer thickness at the leading-edge of the flexible panel was approximately $\delta = 0.04L$. The pressure in the cavity underneath the

flexible panel was assumed to be fixed at the free stream value p_∞ . The flow field was computed using the sixth-order scheme (C6) and the second-order, implicit Beam-Warming method (with $\Delta = 0.01$ and four subiterations). At each subiteration of the implicit time-marching method, the shape of the deforming panel is updated by the structural solver. Based on

the new boundary coordinates, the fluid dynamic mesh is evolved by propagating the panel deformations into the entire field. Following initial transients, a limit-cycle-oscillation with an approximate non-dimensional frequency $St = fL/u_\infty = 1.62$ was achieved by the combined fluid/structural system. A representative plot of the instantaneous panel deflection is shown in Fig. 43b. From this and many other instantaneous realizations of the panel shape (not shown), it became apparent that the panel dynamics comprises a first-mode mean downward deflection upon which a high-mode, high-frequency vertical fluctuation is superimposed. These high-frequency fluc-

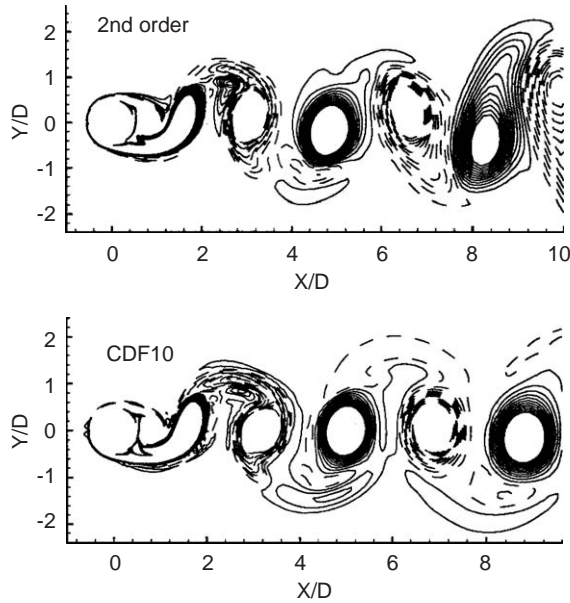


Fig. 39. Computed Karman vortex street behind cylinder at $Re_D = 1000$.

tuations result in a significant acoustic radiation pattern above the vibrating panel, shown in Fig. 43c in terms of a snapshot of the instantaneous pressure. Corresponding contours of vorticity are shown in Fig. 43d, with an enlarged scale (by a factor of 8) in the y direction for the purpose of clarity. Vorticity waves are clearly visible in the boundary layer and appear to roll up and interact with the wall resulting in the formation of secondary incipient separation regions. High-order accurate computations of compressible flows with centered schemes were carried out in numerous recent publications. See for example, [150–154], for more details.

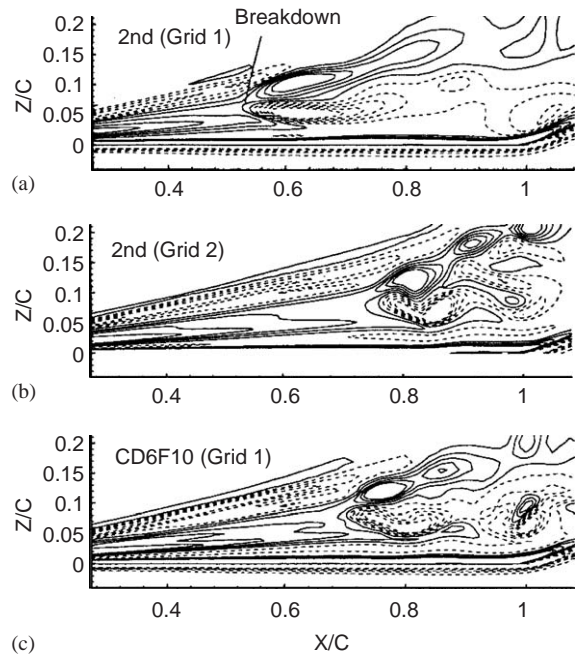


Fig. 41. Azimuthal component of vorticity on vertical plane passing through the core of the broken-down vortex.

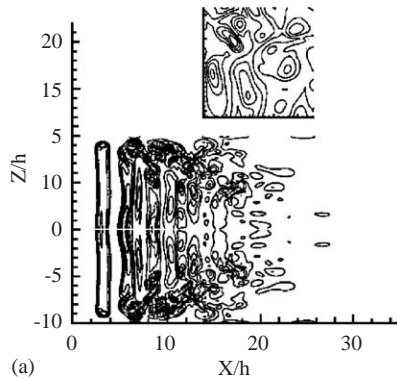
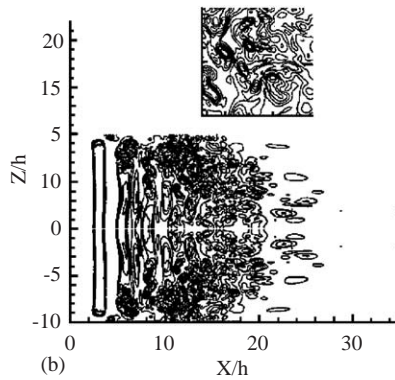


Fig. 40. Vorticity magnitude contours on y -dimensional wall-jet instability with (a) second order and (b) CD6F10 schemes.



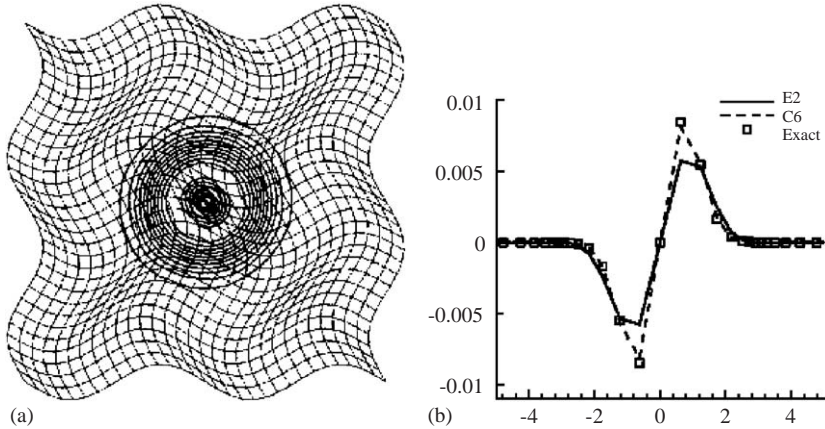


Fig. 42. Computed vorticity and comparison with the exact solution for the convection of a vortex in a three-dimensional deforming grid.

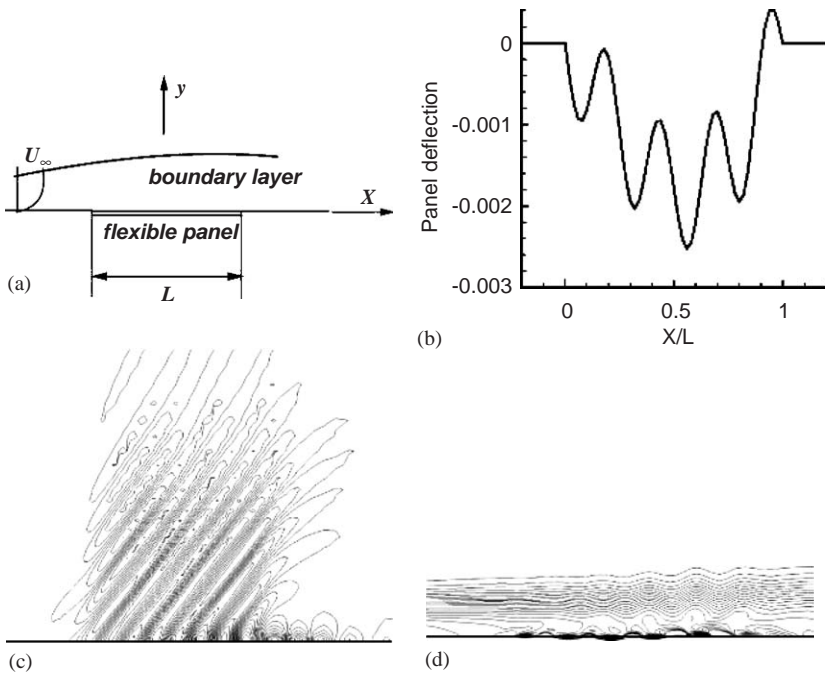


Fig. 43. Computed solution of the flow over a flexible panel.

4. ENO and WENO schemes

ENO and WENO schemes are high-order accurate finite-difference or finite-volume numerical methods designed for the solution of hyperbolic problems with piecewise smooth solutions containing discontinuities. The key idea of these methods is the design of the locally smoothest stencil that avoids crossing discontinuities as much as possible.

The ENO idea, proposed by Harten and Osher [155] and Harten et al. [156], is the first successful attempt to obtain no-mesh size-dependent (self-similar), uniformly high-order accurate, yet essentially non-oscillatory interpolation for piecewise smooth functions using an adaptive local stencil that satisfies certain measures of local smoothness. ENO offered significant improvements over earlier approaches, which attempt to eliminate or reduce spurious oscillations generated at

discontinuities by the fixed stencil, second- or higher-order accurate methods, which used artificial viscosity or limiters.

ENO and WENO schemes were proven suitable for CFD of compressible turbulence, aeroacoustics, and other applications where the solution contains both smooth but complex features and discontinuities. Several of ENO and WENO applications shown at the end of this section demonstrate the enhanced resolution of these schemes and their potential to replace traditional methods in large-scale computations. The presentation of ENO and WENO schemes starts with a review of interpolation and approximation theory used with these schemes.

4.1. High-order reconstruction

A basic approximation problem encountered in the numerical solution of hyperbolic conservation laws is to obtain high-order (second-order accurate or higher) reconstruction (finite-volume approximation) or *conservative* approximation of the derivatives (finite-difference approximation) from cell averaged or point values of the state variables, respectively. Numerical algorithms for conservation laws that have been extensively investigated in the past three decades laid the foundation for the development of modern schemes, [127,128,157] including TVD schemes [72] and the piecewise parabolic method [129] that reduce or eliminate spurious numerical oscillations at discontinuities. In the following sections, the basic ideas of ENO approximation and reconstruction, and the conservative approximation of the derivatives with an adaptive, smooth stencil, which uses the smoothest possible data for the reconstruction, are explained. Based on this idea, ENO and WENO schemes have a distinct advantage over TVD schemes that near every extrema, even smooth ones, degrade to first-order accuracy to suppress any spurious numerical oscillations. ENO schemes, on the other hand, which are based on high-order accurate conservative approximations of derivatives (FD) or polynomial reconstructions from the average state (FV), are high-order accurate and essentially non-oscillatory up to the discontinuity; i.e. the numerical oscillations, if any, decay with the order of the truncation error.

The one-dimensional high-order approximation problem of a function from given cell average values is described in Section 4.2. ENO obtains approximation with polynomials. This polynomial approximation procedure is the basis of finite volume ENO schemes for arbitrary grid spacing in one dimension. The conservative approximation of the derivative, which is also based on the one-dimensional polynomial approximation, is the basis of the finite-difference ENO schemes and presented in Section 4.3. In the following sections, the ENO and WENO reconstruction proce-

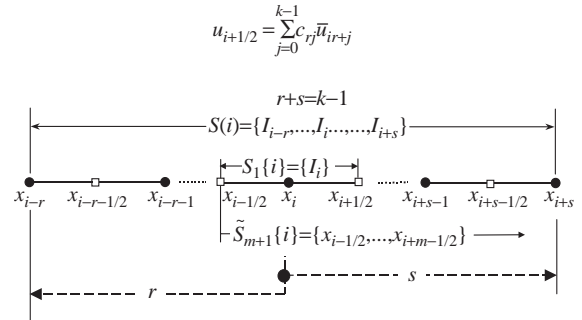


Fig. 44. ENO $r+s=k-1$ wide stencil for the k th order accurate approximation of $u_{i+1/2}$ from cell average values \bar{u}_i .

dures are presented. The implementation of ENO and WENO schemes is given and recent improvements of these schemes are discussed.

4.2. Approximation in one dimension

The basic information about polynomial interpolation and approximation is reviewed. This background is fundamental for the understanding of ENO interpolation and other numerical methods. The presentation is given in one space dimension. The formulation of the basic approximation problem is as follows:

Given a mesh in the interval between a and b

$$a = x_{1/2} < x_{3/2} < \dots < x_{i+1/2} \dots < x_{N-1/2} < x_{N+1/2} = b$$

with subintervals or cells $I_i \equiv [x_{i-1/2}, x_{i+1/2}]$, cell centers $x_i \equiv \frac{1}{2}(x_{i-1/2} + x_{i+1/2})$ and cell size $\Delta x_i \equiv x_{i+1/2} - x_{i-1/2}$, $i = 1, 2, \dots, N$, (see Fig. 44), consider the following reconstruction problem. Given the cell averages of a function $u(x)$ at the cell centers x_i

$$\bar{u}_i \equiv \frac{1}{\Delta x_i} \int_{x_{i-1/2}}^{x_{i+1/2}} u(\xi) d\xi, \quad i = 1, 2, \dots, N \quad (4.1)$$

find a polynomial $p_i(x)$, of degree $k-1$ at most, such that $p_i(x)$ is the k th order accurate approximation to the function $u(x)$ inside each cell I_i , e.g. a polynomial satisfying

$$p_i(x) = u(x) + \mathcal{O}(\Delta x^k), \quad x \in I_i, \quad i = 1, 2, \dots, N. \quad (4.2)$$

The approximations of the function $u(x)$ with the polynomial $p_i(x)$ at the I_i cell boundaries, $i-1/2$ and $i+1/2$, are also k th order accurate, e.g.

$$\begin{aligned} u_{i-1/2} &= p_i(x_{i-1/2}) = u(x_{i-1/2}) + \mathcal{O}(\Delta x^k), \\ u_{i+1/2} &= p_i(x_{i+1/2}) = u(x_{i+1/2}) + \mathcal{O}(\Delta x^k) \\ i &= 1, 2, \dots, N. \end{aligned} \quad (4.3)$$

The procedure to solve this problem is: Given the location I_i and the order of accuracy k , choose a stencil $S(i) = \{I_{i-r}, \dots, I_{i+s}\}$ including I_i itself, r cells to the

left of I_i , and s cells to the right, with $r + s + 1 = k$, (see Fig. 44), and use the average values \bar{u}_i in $S(i)$ to obtain the polynomial $p_j(x)$ that yields the k th order accurate approximation of $u(x)$ given in Eq. (4.2).

For a smooth function $u(x)$ in the region covered by the stencil $S(i)$, there is a unique polynomial of degree $k - 1 = r + s$ at most whose cell average in each cell of $S(i)$ agrees with the average of $u(x)$, e.g.

$$\frac{1}{\Delta x_i} \int_{x_{j-1/2}}^{x_{j+1/2}} p(\xi) d\xi = \bar{u}_i, \quad j = i - r, \dots, i + s. \quad (4.4)$$

The polynomial $p(x)$ is the k th order approximation we are looking for. Furthermore, since the mappings from the given cell average values \bar{u}_j in the stencil $S(i)$ to the values $u_{i-1/2}$ and $u_{i+1/2}$ at the cell boundary are linear, there exist constants c_{rj} , which depend on the left shift r , on the order of accuracy k and on the cell size Δx_i such that

$$u_{i+1/2} = \sum_{j=0}^{k-1} c_{rj} \bar{u}_{i-r+j} = u(x_{i+1/2}) + \mathcal{O}(\Delta x^k). \quad (4.5)$$

The constants c_{rj} are obtained using the primitive function $U(x)$ of $u(x)$ defined as

$$U(x) \equiv \int_{-\infty}^x u(\xi) d\xi. \quad (4.6)$$

The primitive function can be expressed by cell average values \bar{u}_i of $u(x)$ using the definition of Eq. (4.1) to obtain

$$U(x_{i+1/2}) = \sum_{j=-\infty}^i \int_{x_{j-1/2}}^{x_{j+1/2}} u(\xi) d\xi = \sum_{j=-\infty}^i \bar{u}_j \Delta x_j. \quad (4.7)$$

equation shows that the cell averages \bar{u}_i yield the exact values of the primitive function $U(x)$ at the cell boundaries.

Considering the unique polynomial $P(x)$ of degree k which interpolates the primitive function at the $k + 1$ cell boundaries $x_{i-r-1/2}, \dots, x_{i+s+1/2}$ and denoting its derivative $P'(x)$ by $p(x)$ it is easy to verify that $p(x)$ is the polynomial we are looking for and satisfies Eq. (4.4) as follows:

$$\begin{aligned} & \frac{1}{\Delta x_j} \int_{x_{j-1/2}}^{x_{j+1/2}} p(\xi) d\xi \\ &= \frac{1}{\Delta x_j} \int_{x_{j-1/2}}^{x_{j+1/2}} P'(\xi) d\xi \\ &= \frac{1}{\Delta x_j} \int_{x_{j-1/2}}^{x_{j+1/2}} u(\xi) d\xi = \bar{u}_j, \quad j = i - r, \dots, i + s \end{aligned} \quad (4.8)$$

in addition, have

$$P'(x) = U'(x) + \mathcal{O}(\Delta x^k) \quad \forall x \in I_i.$$

Since the exact value of the primitive function $U(x)$ of $u(x)$ at the cell boundaries are obtained from the cell

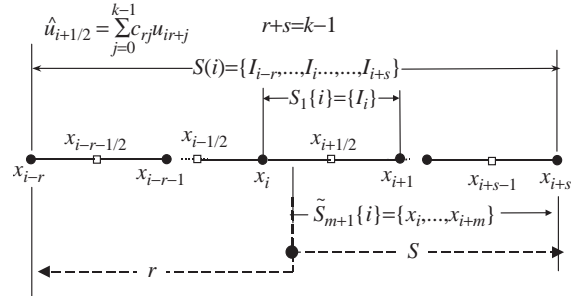


Fig. 45. ENO $r + s = k - 1$ wide stencil for the k th order accurate approximation of the numerical flux $\hat{u}_{i+1/2}$ from point values.

averages (see Eq. (4.7)) one can use Lagrange interpolation polynomials to obtain the constants c_{rj} in Eq. (4.5). The interpolation polynomials and the values of the constants c_{rj} for $k = 1$, up to $k = 4$ can be found in Appendix A.

4.3. One-dimensional conservative approximation of the derivative

For finite-difference schemes, the basic problem of high-order accurate discretization is the conservative approximation of the derivative of a function $u(x)$

$$u_i \equiv u(x_i), \quad i = 1, 2, \dots, N \quad (4.9)$$

from given point values at the nodes x_i of the mesh.

In the ENO and WENO framework, this is accomplished through the use of a numerical flux function $\hat{u}_{i+1/2}$ at the cell centers or half-nodes $x_{i+1/2}$

$$\hat{u}_{i+1/2} \equiv \hat{u}(u_{i-r}, \dots, u_{i+s}), \quad i = 0, 1, \dots, N. \quad (4.10)$$

This numerical flux depends on r point values on the left and s point values on the right (see Fig. 45) such that the flux difference approximates the derivative $u'(x) = du(x)/dx$ to k th order accuracy

$$\frac{1}{\Delta x_i} (\hat{u}_{i+1/2} - \hat{u}_{i-1/2}) = u'(x_i) + \mathcal{O}(\Delta x^k), \quad i = 0, 1, \dots, N. \quad (4.11)$$

For a uniform grid $\Delta x_i = \Delta x$, this problem can be solved with the same technique used to obtain k th order accurate reconstruction, which was presented in Section 4.2. The assumption of uniform grid spacing for the conservative evaluation of the derivative in the finite-difference formulation is essential. However, the reconstruction for the finite-volume formulation of Section 4.2 is valid for non-uniform grid spacing.

Assuming that a numerical flux function $h(x)$ exists, and that this function depends on the uniform grid

spacing Δx , such that

$$u_i \equiv \bar{u}_i = \frac{1}{\Delta x} \int_{x-\Delta x/2}^{x+\Delta x/2} h(\xi) d\xi \quad (4.12)$$

then

$$u'(x) = \frac{1}{\Delta x} \left[h\left(x + \frac{\Delta x}{2}\right) - h\left(x - \frac{\Delta x}{2}\right) \right] \quad (4.13)$$

therefore, the numerical flux function we are looking for must satisfy

$$\hat{u}_{i+1/2} = h(x_{i+1/2}) + \mathcal{O}(\Delta x^k). \quad (4.14)$$

It is not straightforward to find $h(x)$ because Eq. (4.12) defines the unknown function $h(x)$ implicitly. However, observing that the known function $u(x)$ is the cell average of $h(x)$, (see Eq. (4.12)), one can use the same reconstruction procedure of Section 4.2 to approximate $h(x)$.

Considering the primitive $H(x)$ of $h(x)$, where $H(x)$ satisfies

$$H(x) = \int_{-\infty}^x h(\xi) d\xi \quad (4.15)$$

then Eq. (4.12) implies

$$H(x_{i+1/2}) = \sum_{j=-\infty}^i \int_{x_{j-1/2}}^{x_{j+1/2}} h(\xi) d\xi = \Delta x \sum_{j=-\infty}^i u_j. \quad (4.16)$$

Summarizing: The conservative approximation of the derivative in the finite-difference context becomes equivalent to the reconstruction problem in the finite-volume formulation when the given point values u_i are identified as cell averages of an unknown function $h(x)$ that satisfies Eq. (4.12). The primitive function of $h(x)$, $H(x)$, is then exactly known at the cell interfaces (see Eq. (4.16)), or half-points $x_{i+1/2}$ from the point values u_i at the nodes. Using the same approximation procedure described in Section 4.2 obtain the k th order approximation to $h(x_{i+1/2})$, which according to Eq. (4.14) is the numerical flux $\hat{u}_{i+1/2}$ we are looking for.

For a stencil $S(i)$ around the point i (see Fig. 45), r points to the left and s points to the right, $(x_{i-r}, \dots, x_i, \dots, x_{i+s})$, where $r + s = k + 1$ the numerical flux is expressed as

$$\hat{u}_{i+1/2} = \sum_{j=0}^{k-1} c_{rj} u_{i-r+j}, \quad (4.17)$$

where the values of the constants c_{rj} are given in Table A.1 of Appendix A.

For a globally smooth function $u(x)$, the best approximation is obtained for even k by centered approximation $r = s - 1$. For example, the fourth-order accurate centered flux approximation from Eq. (4.17) and $k = 4$ is obtained by

$$\hat{u}_{i+1/2} = \frac{1}{12} [-u_{i-1} + 7u_i + 7u_{i+1} - u_{i+2}] + \mathcal{O}(\Delta x^4).$$

For k odd, the best approximation is obtained by one point upwind-biased stencils $r = s$ or $r = s - 2$. For example, third-order upwind fluxes for $k = 3$ are

$$\hat{u}_{i+1/2} = \frac{1}{6} [-u_{i-1} + 5u_i + 2u_{i+1}] + \mathcal{O}(\Delta x^3),$$

$$\hat{u}_{i-1/2} = \frac{1}{6} [-u_{i-2} + 5u_{i-1} + 2u_i] + \mathcal{O}(\Delta x^3)$$

which yield a third order accurate conservative approximation of the derivative

$$\begin{aligned} \frac{1}{\Delta x} [\hat{u}_{i+1/2} - \hat{u}_{i-1/2}] &= \frac{1}{6} [u_{i-2} - 6u_{i-1} + 3u_i + 2u_{i+1}] \\ &= u'(x_i) + \mathcal{O}(\Delta x^3). \end{aligned}$$

The selection of the most suitable stencils among different possible stencils of Sections 4.2 and 4.3 for fixed k is accomplished through the ENO or WENO reconstruction procedures that are described next.

4.4. ENO reconstruction

Approximation of discontinuous solutions that occur in hyperbolic conservation laws is accomplished with piecewise smooth functions. These functions $u(x)$ have derivatives at all points except at discontinuities where the function and its derivatives are assumed to have finite left and right limits. For such piecewise smooth functions, the order of accuracy is determined by the local truncation error in smooth regions of the definition of the function. A fixed stencil high-order approximation of a piecewise smooth function is not adequate near discontinuities, because stencils that contain discontinuous cells cause oscillations (Gibbs phenomenon) in the numerical solution.

The basic idea of the ENO approximation is to avoid including discontinuous cells in the stencil as much as possible. This is accomplished by the “adaptive stencil” where the left shift changes with the location x_i . In the ENO approximation, this is achieved by using the Newton divided differences of the interpolation polynomial as a smoothness indicator of the stencil.

The j th degree divided differences $F[x_{i-1/2}, \dots, x_{i+j-1/2}]$ of the primitive function $F(x)$, of $f(x)$ (see Eq. (4.15)), that is defined at the cell faces or half-points $x_{i-1/2}, \dots, x_{i+j-1/2}$ are given by the recursive formula

$$F[x_{i-1/2}] = F(x_{i-1/2})$$

$$F[x_{i-1/2}, \dots, x_{i+j-1/2}]$$

$$\equiv \frac{F[x_{i+1/2}, \dots, x_{i+j-1/2}] - F[x_{i-1/2}, \dots, x_{i+j-3/2}]}{x_{i+j-1/2} - x_{i-1/2}}.$$

(4.18)

A similar formula defines the divided differences of the cell averages $\bar{f}_i \equiv \bar{f}[x_i]$ of the function $f(x)$ defined at the cell centers $x_{i+1/2}, \dots, x_{i+1/2+j}$ (FV), or nodes x_i, \dots, x_{i+j}

(FD) approach. The divided differences for \bar{f}_i are

$$\bar{f}[x_i, \dots, x_{i+j}] = \frac{\bar{f}[x_{i+1}, \dots, x_{i+j}] - \bar{f}[x_i, \dots, x_{i+j-1}]}{x_{i+j} - x_i}.$$

The function $f(x)$ and its primitive $F(x) = \int_{-\infty}^x f(\xi) d\xi$ are related by

$$F(x_{i+1/2}) = \sum_{j=-\infty}^i \int_{x_{j-1/2}}^{x_{j+1/2}} f(\xi) d\xi = \sum_{j=-\infty}^i \bar{f}_j \Delta x_j \quad (4.19)$$

therefore

$$F[x_{i-1/2}, x_{i+1/2}] = \frac{F(x_{i+1/2}) - F(x_{i-1/2})}{x_{i+1/2} - x_{i-1/2}} = \bar{f}_i. \quad (4.20)$$

As a result Eq. (4.18) can be expressed in terms of \bar{f} , since the first degree divided differences of $F(x)$ are the zeroth degree divided differences of \bar{f} , and the computation of the primitive function F can be completely avoided.

Using the above definitions, the k th degree interpolation polynomial $P(x)$ that interpolates the primitive function $F(x)$ at $k + 1$ points is expressed with divided differences by

$$P(x) = \sum_{j=0}^k F[x_{i-r-1/2}, \dots, x_{i-r+j-1/2}] \times \prod_{m=0}^{j-1} (x - x_{i-r+m-1/2}) \quad (4.21)$$

and the polynomial $p(x) = P'(x)$ is expressed as

$$p(x) = \sum_{j=0}^k F[x_{i-r-1/2}, \dots, x_{i-r+j-1/2}] \times \sum_{m=0}^{j-1} \prod_{\substack{l=0 \\ l \neq m}}^{j-1} (x - x_{i+r+l-1/2}), \quad (4.22)$$

where again $p(x)$ can be expressed by divided differences of \bar{f} .

The ENO selection process of the smoothest stencil of $k + 1$ consecutive points that include $x_{i-1/2}$ and $x_{i+1/2}$ is based on Eq. (4.21) and is performed with the following steps:

- (1) Start with the two-point stencil $\tilde{S}_2(i) = \{x_{i-1/2}, x_{i+1/2}\}$ (see Figs. 44 and 45) of the primitive function U of u , which has a corresponding single-cell stencil $S(i) = \{I_i\}$ in terms of \bar{u} (see Eq. (4.20) and Figs. 4.1 and 4.2).
- (2) Obtain the linear (first degree) interpolation polynomial P^1 on the stencil $\tilde{S}_2(i)$ using Newton forms as

$$P^1(x) = U[x_{i-1/2}] + U[x_{i-1/2}, x_{i+1/2}] \times (x - x_{i-1/2}). \quad (4.23)$$

- (3) Obtain higher-order interpolation polynomials P_R^2 and P_S^2 by expanding the stencil to the left including $x_{i-3/2}$ or to the right including $x_{i+3/2}$, respectively.

$$P_R^2 = P^1(x) + U[x_{i-3/2}, x_{i-1/2}, x_{i+1/2}] \times (x - x_{i-1/2})(x - x_{i+1/2}),$$

$$P_S^2 = P^1(x) + U[x_{i-1/2}, x_{i+1/2}, x_{i+3/2}] \times (x - x_{i-1/2})(x - x_{i+1/2}). \quad (4.24)$$

The deviations from the linear approximation of P_R^2 and P_S^2 depend on the divided differences $U[x_{i-3/2}, x_{i-1/2}, x_{i+1/2}]$ and $U[x_{i-1/2}, x_{i+1/2}, x_{i+3/2}]$, respectively.

However, a divided difference is a measure of smoothness of the function in the stencil because for a smooth function $U(x)$ have $U[x_{i-1/2}, \dots, x_{i+j-1/2}] = V(j)(\xi)/j$ for some $x_{i-1/2} < \xi < x_{i+j-1/2}$, while if $U(x)$ is discontinuous inside the stencil $U[x_{i-1/2}, \dots, x_{i+j-1/2}] = \mathcal{O}(1/\Delta x^j)$.

Therefore, if

$$|U[x_{i-3/2}, x_{i-1/2}, x_{i+1/2}]| < |U[x_{i-1/2}, x_{i+1/2}, x_{i+3/2}]| \quad (4.25)$$

select the stencil

$$\tilde{S}_3(i) = \{x_{i-3/2}, x_{i-1/2}, x_{i+1/2}\} \text{ or } S_2(i) = \{I_{i-1}, I_i\} \quad (4.26)$$

otherwise, select the stencil

$$\tilde{S}_3(i) = \{x_{i-1/2}, x_{i+1/2}, x_{i+3/2}\} \text{ or } S_2(i) = \{I_i, I_{i+1}\}. \quad (4.27)$$

- (4) Continue this process until the stencil $\tilde{S}_k(i)$ with the desired number of points is reached.

Note again that all divided differences of the primitive are computed in terms of averages. For uniform mesh, the divided differences are replaced by undivided differences. The finite-volume and finite-difference ENO algorithms based on the approximation and reconstruction procedures of Sections 4.2–4.4 are summarized next.

4.5. 1D finite-volume ENO scheme

From the cell average values $\{\bar{u}_i\}$ of the function $u(x)$, (see Fig. 44) obtain a piecewise polynomial reconstruction of $u(x)$ of degree $k - 1$ at most as follows:

- (1) Using $\{\bar{u}_i\}$ compute the divided (or undivided differences for uniform mesh) of the primitive function $U(x)$ for degrees 1 to k with Eqs. (4.18) and (4.20).

- (2) Start with the two-point stencil for the primitive $\tilde{S}_2(i) = \{x_{i-1/2}, x_{i+1/2}\}$ which is equivalent to the one-point stencil $S_1(i) = \{I_i\}$ for the cell average.
- (3) Add one of the two neighboring points to the stencil $\tilde{S}_l(i)$, $l = 2, \dots, k$ following the ENO procedure of Eqs. (4.25)–(4.27).
- (4) Use the Lagrange form, Eq. (A.1) of Section 4.2, or Newton form Eq. (4.22) to obtain the polynomial $p_i(x)$ of degree $k - 1$ the most that satisfies the accuracy requirement.

In practice, however, once the stencil is known, it is more convenient to find the approximation at the cell boundaries using Eq. (4.5)

$$u_{i+1/2} = \sum_{j=0}^{k-1} c_{rj} \bar{u}_{i-r+j},$$

where the values of the constant c_{rj} are given by Eqs. (A.2) and (A.3), in Section 4.2–4.4 for non-uniform and uniform mesh, respectively.

4.6. 1D finite-difference ENO scheme

The finite-difference ENO reconstruction is valid only for fixed mesh size and includes the following steps:

- (1) Compute the numerical flux $\hat{u}_{i+1/2}$ using the given point values $\{u_j\}$ (see Fig. 45) and all k points fixed stencils, where $r + s = k - 1$, by

$$\hat{u}_{i+1/2} = \sum_{j=0}^{k-1} c_{rj} u_{i-r+j}.$$

Note that in the finite-difference ENO approximation the given point values $\{u_j\}$ are identified as cell averages of another function $h(x)$, which has a primitive $H(x)$ exactly known at the cell interfaces $x_{i+1/2}$, and the k th order approximation $h(x_{i+1/2})$ is the numerical flux $\hat{u}_{i+1/2}$.

- (2) Perform steps 1–4 of the finite-volume ENO reconstruction treating $\{u_j\}$ as cell averages to select the smoothest stencil.
- (3) Obtain a conservative k th order accurate approximation of the derivative as

$$\frac{1}{\Delta x} (\hat{u}_{i+1/2} - \hat{u}_{i-1/2}) = u'(x_i) + \mathcal{O}(\Delta x^k).$$

4.7. WENO approximation

In the previous sections, it was shown that the ENO reconstruction is uniformly high-order accurate right up to the discontinuity, and achieves this by adaptively choosing the smoothest stencil using the absolute values

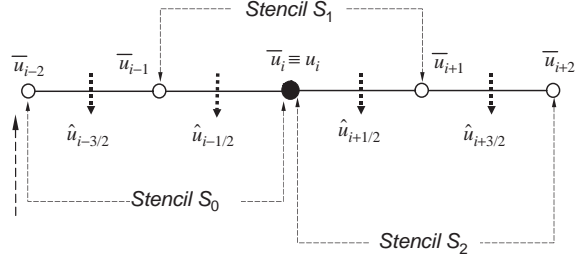


Fig. 46. Candidate stencils for $(2k - 1)$ th order accurate WENO; WENO5 for $k = 3$. The nodal values u_i , $i - r < i < i - r + k - 1$ are identified as cell averages for the computation of the WENO reconstruction of the numerical fluxes $u_{i-1/2}$ at half-point nodes.

of divided differences. However, ENO reconstruction in practice may face the following problems:

- (1) For finite-volume reconstructions, round-off error perturbations may change the stencil because they can result in sign change of divided differences even in the smooth regions of the solution [159,160]. This stencil-free adaption due to round-off error results into a non-smooth numerical flux in finite-difference ENO.
- (2) The reconstruction in FV or the numerical flux evaluation in FD ENO of k th order accuracy uses only one of the k candidate stencils that cover $2k - 1$ cells. However, if all candidate stencils were used, then $(2k - 1)$ th order accuracy could be achieved.

It was proposed in [160,161] to remedy the free adaption problem using a biasing strategy for the stencil selection process. However, the most recent improvement of ENO is the WENO (weighted ENO) approximation [33,162]. The basic idea of WENO is to use a convex combination of all candidate stencils to form the reconstruction. The WENO approximation is explained more precisely in this section.

Suppose that the k candidate stencils $S_r(i) = \{x_{i-r}, \dots, x_{i-r+k-1}\}$ (see Fig. 46 for $k = 3$) that produce k different reconstructions for the value $u_{i+1/2}$ at the cell interface or the numerical flux $\hat{u}_{i+1/2}$ are available. In both cases the reconstruction is obtained by

$$u_{i+1/2}^{(r)} = \sum_{j=0}^{k-1} c_{rj} \bar{u}_{i-r+j}, \quad r = 0, \dots, k - 1, \quad (4.28)$$

where the superscript r denotes the shift to the left.

Reconstruction with WENO considers a convex combination of all $u_{i+1/2}^{(r)}$ as a new approximation at

the cell boundary as follows:

$$u_{i+1/2} = \sum_{r=0}^{k-1} \omega_r u_{i+1/2}^{(r)}, \quad (4.29)$$

$$\sum_{r=0}^{k-1} \omega_r = 1, \quad \omega_r \geq 0 \quad (4.30)$$

when the function $u(x)$ includes a discontinuity in one or more of the stencils $S_r(i)$ then the corresponding weight ω_r must be essentially zero in order to follow as closely as possible the successful ENO idea. Furthermore, the weights should be smooth functions of the cell averages (FV) or the point values (FD) approximation. All these considerations [33] lead to the following forms of the weights:

$$\omega_r = \frac{\alpha_r}{\sum_{S=0}^{k-1} \alpha_S}, \quad r = 0, \dots, k-1, \quad (4.31)$$

$$\alpha_r = \frac{d_r}{(\varepsilon + \beta_r)^2} \quad (4.32)$$

where $\varepsilon > 0$ taken as $\varepsilon = 10^{-6}$ in [33] to avoid division by zero and β_r are the smoothness indicators of the stencil $S_r(i)$. The smoothness indicators in [33] are obtained by minimizing the total variation of the $(k-1)$ th degree reconstruction polynomial $p(x)$ constructed on each $S_r(i)$, which if evaluated at $x_{i+1/2}$ yields the k th order approximation of $u(x_{i+1/2})$.

Then the smoothness indicators β_r are defined by

$$\beta_r = \sum_{m=1}^{k-1} \int_{x_{i-1/2}}^{x_{i+1/2}} \Delta x^{2m-1} \left(\frac{\partial^m p_r(x)}{\partial^m x} \right)^2 dx. \quad (4.33)$$

The smoothness indicators for $k = 2$ and 3 obtained from Eq. (4.33) are

Smoothness indicators for $k = 2$, third-order WENO reconstruction

$$\begin{aligned} \beta_0 &= (\bar{u}_{i+1} - \bar{u}_i)^2, \\ \beta_1 &= (\bar{u}_i - \bar{u}_{i-1})^2. \end{aligned} \quad (4.34)$$

Smoothness indicators for $k = 3$, fifth order WENO reconstruction

$$\begin{aligned} \beta_0 &= \frac{13}{12}(\bar{u}_i - 2\bar{u}_{i+1} + \bar{u}_{i+2})^2 + \frac{1}{4}(3\bar{u}_i - 4\bar{u}_{i+1} + \bar{u}_{i+2})^2, \\ \beta_1 &= \frac{13}{12}(\bar{u}_{i-1} - 2\bar{u}_i + \bar{u}_{i+1})^2 + \frac{1}{4}(\bar{u}_{i-1} - 4\bar{u}_{i+1})^2, \\ \beta_3 &= \frac{13}{12}(\bar{u}_{i-2} - 2\bar{u}_i + \bar{u}_i)^2 + \frac{1}{4}(\bar{u}_{i-2} - 4\bar{u}_{i-1} + 3\bar{u}_i)^2, \end{aligned} \quad (4.35)$$

where for $k = 2$ obtain $(2k-1) =$ third-order accuracy and for $k = 3$ obtain $(2k-1) =$ fifth-order accuracy. The WENO idea presented for FV reconstruction carries over to the finite-difference context once the cell averages \bar{u}_i are replaced by nodal values u_i and the approximation at the cell boundaries of Eq. (4.29) are

replaced by the numerical flux function $\hat{u}_{i+1/2}$ at half-point nodes.

Implementation of WENO schemes is more convenient in practice with the formulation of Jiang and Wu [163]. For example, for $k = 3$, fifth-order scheme, the numerical flux $\hat{u}_{i+1/2}$ is taken as the weighted average of the numerical fluxes in the three stencils S_0 , S_1 , and S_2 of Fig. 46. The third-order accurate approximations $\hat{u}_{i+1/2}^s$, $s = 0, 1, 2$ are

$$\begin{aligned} \hat{u}_{i+1/2}^0 &= \frac{1}{3}\bar{u}_{i-2} - \frac{7}{6}\bar{u}_{i-1} + \frac{11}{6}\bar{u}_i, \\ \hat{u}_{i+1/2}^1 &= -\frac{1}{6}\bar{u}_{i-1} + \frac{5}{6}\bar{u}_i + \frac{1}{3}\bar{u}_{i+1}, \\ \hat{u}_{i+1/2}^2 &= \frac{1}{3}\bar{u}_i + \frac{5}{6}\bar{u}_{i+1} - \frac{1}{6}\bar{u}_{i+2}, \end{aligned} \quad (4.36)$$

where $\bar{u}_i \equiv u_i$ denotes the point value at the nodes i for the FD WENO formulation.

The fifth-order accurate WENO approximation of the numerical flux is

$$\hat{u}_{i+1/2} = \omega_0 \hat{u}_{i+1/2}^0 + \omega_1 \hat{u}_{i+1/2}^1 + \omega_2 \hat{u}_{i+1/2}^2, \quad (4.37)$$

where the $(2k-1) =$ fifth-order approximation to $\hat{u}_{i+1/2}$ is based on the five-point stencil $i-2 \leq k \leq i+2$.

For $\omega_0 = \frac{1}{10}$, $\omega_1 = \frac{6}{10}$, $\omega_2 = \frac{3}{10}$, which are referred to as optimal weights in Balsara and Shu [34], the approximation of Eq. (4.37) becomes

$$\hat{u}_{i+1/2} = \frac{1}{30}\bar{u}_{i-2} - \frac{13}{60}\bar{u}_{i-1} + \frac{47}{60}\bar{u}_i + \frac{9}{20}\bar{u}_{i+1} - \frac{1}{20}\bar{u}_{i+2} \quad (4.38)$$

or

$$\begin{aligned} \hat{u}_{i+1/2} &= -\frac{1}{12}\bar{u}_{i-1} + \frac{7}{12}\bar{u}_i + \frac{7}{12}\bar{u}_{i+1} - \frac{1}{12}\bar{u}_{i+2} \\ &\quad - \frac{1}{30}(-\bar{u}_{i-2} + 4\bar{u}_{i-1} - 6\bar{u}_i + 4\bar{u}_{i+1} - \bar{u}_{i+2}). \end{aligned} \quad (4.39)$$

The last form of Eq. (4.39) shows that the WENO approximation of the numerical flux $\hat{u}_{i+1/2}$ is a sum of a centered flux

$$\hat{u}_{i+1/2}^c = \frac{1}{12}(-\bar{u}_{i-1} + 7\bar{u}_i + 7\bar{u}_{i+1} - \bar{u}_{i+2})$$

plus a dissipative portion of the WENO scheme.

Replacing ω_1 by $\omega_1 = 1 - \omega_0 - \omega_2$ and using Eqs. (4.36) in Eq. (4.37) obtain

$$\begin{aligned} \hat{u}_{i+1/2} &= \frac{1}{12}(-\bar{u}_{i-1} + 7\bar{u}_i + 7\bar{u}_{i+1} - \bar{u}_{i+2}) \\ &\quad + \frac{1}{3}(\bar{u}_{i-2} - 3\bar{u}_{i-1} + 3\bar{u}_i - \bar{u}_{i+1})\omega_0 \\ &\quad + \frac{1}{6}(\bar{u}_{i-1} - 3\bar{u}_i + 3\bar{u}_{i+1} - \bar{u}_{i+2})(\omega_2 - \frac{1}{2}) \\ &= \frac{1}{12}(-\bar{u}_{i-1} + 7\bar{u}_i + 7\bar{u}_{i+1} - \bar{u}_{i+2}) \\ &\quad - \phi_w(\Delta\bar{u}_{i-3/2}, \Delta\bar{u}_{i-1/2}, \Delta\bar{u}_{i+1/2}, \Delta\bar{u}_{i+3/2}) \\ &= \frac{1}{12}(-\bar{u}_{i-1} + 7\bar{u}_i + 7\bar{u}_{i+1} - \bar{u}_{i+2}) \\ &\quad - \frac{1}{3}\omega_0(D_0 - 2D_1 + D_2) \\ &\quad + \frac{1}{6}(\omega_2 - \frac{1}{2})(D_1 - 2D_2 + D_3), \end{aligned} \quad (4.40)$$

where $\Delta\bar{u}_{i-3/2} = D_0 = \bar{u}_{i-2} - \bar{u}_{i-1}$, $D_1 = \bar{u}_{i-1} - \bar{u}_i$, $D_2 = \bar{u}_i - \bar{u}_{i+1}$, $D_3 = \bar{u}_{i+1} - \bar{u}_{i+2}$.

The weights are defined as

$$\omega_0 = \frac{\alpha_0}{\alpha_0 + \alpha_1 + \alpha_2}, \quad \omega_2 = \frac{\alpha_2}{\alpha_0 + \alpha_1 + \alpha_2} \quad (4.41)$$

$$\alpha_r = d_r/(SI_r^k + \varepsilon), \quad r = 0, 1, 2.$$

Summarizing:

For $k = 3$ the centered stencil of the $(2k - 1)$, fifth-order scheme is

$$\hat{u}_{i+1/2}^c = \frac{1}{12}(-\bar{u}_{i-1} + 7\bar{u}_i + 7\bar{u}_{i+1} - \bar{u}_{i+2}) + \mathcal{O}(\Delta x^4) \quad (4.42)$$

the optimal weights are $d_0 = \frac{1}{10}$, $d_1 = \frac{6}{10}$, $d_2 = \frac{3}{10}$.

For the smooth regions the numerical flux is evaluated using optimal weights by

$$\begin{aligned} \hat{u}_{i+1/2} = & \frac{1}{30}\bar{u}_{i-2} - \frac{13}{60}\bar{u}_{i-1} + \frac{47}{60}\bar{u}_i \\ & + \frac{9}{20}\bar{u}_{i+1} - \frac{1}{20}\bar{u}_{i+2} + \mathcal{O}(\Delta x^5). \end{aligned} \quad (4.43)$$

The dissipative WENO part is

$$\begin{aligned} \phi_\omega^3 = & \frac{1}{3}\omega_0(D_0 - 2D_1 + D_2) \\ & + \frac{1}{6}(\omega_2 - \frac{1}{2})(D_1 - 2D_2 + D_3). \end{aligned} \quad (4.44)$$

The smoothness indicators $\beta_r^3 = SI_r^3$, $r = 0, 1, 2$ are given by

$$\begin{aligned} SI_0^3 &= D_0(4D_0 - 11D_1) + 10D_1^2, \\ SI_1^3 &= D_1(4D_1 - 5D_2) + 4D_2^2, \\ SI_2^3 &= D_2(10D_2 - 11D_3) + 4D_3^2. \end{aligned} \quad (4.45)$$

Using this notation the high-order WENO reconstructions $\hat{u}_{i+1/2} = \sum_{r=i-k+2}^{i+k-1} c_r^k \bar{u}_r$ of Balsara and Shu [34] for $k = 4$ and 5, which yield the seventh- and ninth-order accurate WENO schemes can be obtained.

The component-wise application of the finite-volume ENO and WENO schemes is straightforward. Furthermore, the characteristic variables $\bar{w}_i = R^{-1}\bar{u}_i$ for the divided differences (or undivided differences for equal grid spacing) for all cell averages can be used for ENO and WENO approximation. The local characteristic field is then used to perform scalar ENO or WENO reconstruction for each component of the characteristic variables w to obtain the reconstruction $w_{i+1/2}^\pm$. Transforming back into physical space $u_{i+1/2}^\pm = R w_{i+1/2}^\pm$ apply on exact or approximate Riemann solver to compute the flux $f_{i+1/2}$. The finite-difference ENO or WENO for uniform meshes follows the same steps considering the point values u_i as cell averages. Using then u_i compute the undivided differences for the fluxes $f(u_i)$.

4.8. Multidimensional ENO and WENO reconstruction

The multidimensional ENO and WENO schemes are based on the preliminaries of the previous sections. For fully unstructured meshes, however, the identification of suitable stencils is not straightforward. Presentation of multidimensional algorithms starts from the ENO in Cartesian meshes.

4.8.1. Finite-volume reconstruction for Cartesian mesh

Multidimensional reconstruction and approximation without loss of generality is considered in two dimensions. The ideas described carry over to three dimension as well. The two-dimensional ENO reconstruction problem is as follows. Given the cell I_{ij} and the order of accuracy k , choose a stencil $S(i,j)$ based on $k(k + 1)/2$ neighboring cells, and find a polynomial $p(x,y)$ of degree $k - 1$ at most whose cell average in each of the cells in the stencil $S(i,j)$ agrees with $u(x,y)$

$$\bar{u}_{ij} = \frac{1}{\Delta x_i \Delta y_j} \int_{y_{j-1/2}}^{y_{j+1/2}} \int_{x_{i-1/2}}^{x_{i+1/2}} p(\xi, \eta) d\xi d\eta, \quad I_{ij} \in S(i,j). \quad (4.46)$$

The multidimensional ENO reconstruction is more complex than the one-dimensional case because there are many more candidate stencils $S(i,j)$ and has the following difficulties: Some candidate stencils cannot be used to obtain the polynomial $p(x,y)$ that satisfies Eq. (4.46). Some of the polynomials do not satisfy the accuracy condition $p_{ij}(x,y) = u(x,y) + \mathcal{O}(\Delta^k)(x,y) \in I_{ij}$, $i = 1, \dots, N_x$, $j = 1, \dots, N_y$.

These difficulties are more profound for unstructured meshes [164]. For rectangular meshes [165] the tensor products of one-dimensional polynomials are used and $p(x,y)$ is written as

$$p(x,y) = \sum_{m=0}^{k-1} \sum_{n=0}^{k-1} a_{mn} x^m y^n. \quad (4.47)$$

Furthermore, by restricting the search in the following tensor product stencils (see Fig. 47)

$$S_{rs}(i,j) = \{I_{mn} : i - r \leq m \leq i + k - 1 - r, \\ j - s \leq n \leq j + k - 1 - s\}$$

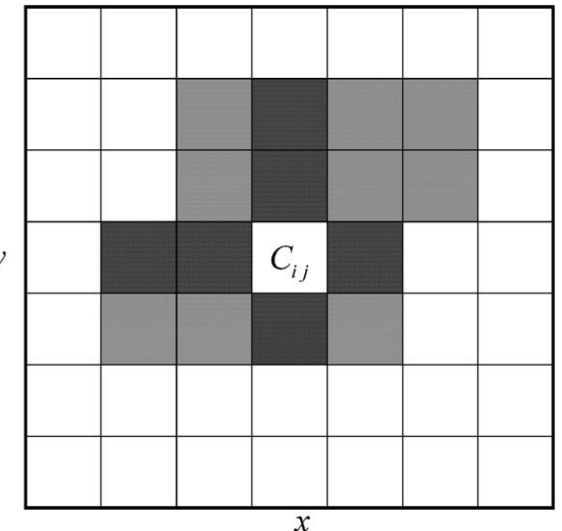


Fig. 47. Possible reconstruction stencils in a Cartesian mesh.

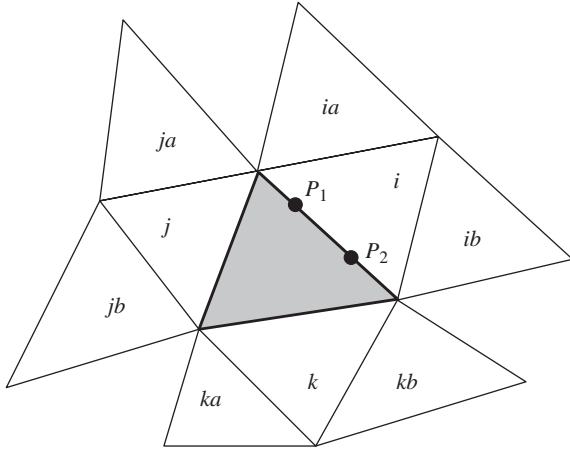


Fig. 48. Stencil definition for reconstruction in a triangular mesh.

the reconstruction proceeds as in one dimension. The computing cost for two-dimensional reconstruction is high because for each point the reconstruction cost is double. Casper and Atkins [165] give details about possible reconstruction stencils (see Fig. 47).

4.8.2. Two-dimensional reconstruction for triangles

The reconstruction problem for triangular meshes is:

Given the cell averages \bar{u}_i of $u(x, y)$ on a triangulation T_i

$$\bar{u}_i = \frac{1}{|T_i|} \int_{T_i} u(\xi, \eta) d\xi d\eta, \quad (4.48)$$

where $|T_i|$ is the area of the triangle T_i find a polynomial $p_i(x, y)$ of degree $k - 1$ at most for each triangle T_i such that the k th order accurate approximation of $u(x, y)$ inside the triangles T_i is

$$p_i(x, y) = u(x, y) + \mathcal{O}(\Delta^k), \quad (x, y) \in T_i \quad i = 1, \dots, N, \quad (4.49)$$

where Δ denotes a typical length of the triangle for example the longest edge. For finite-volume schemes, the approximation of $u(x, y)$ at the triangle boundaries (see points P_1, P_2 in Fig. 48) is needed to apply quadratures as in Eq. (4.49) yields the approximation of $u(x, y)$ at these points.

Similar to the finite volume for Cartesian mesh, given the triangle T_i and the order of accuracy k , again choose a stencil based on $m = k(k + 1)/2$ neighboring triangles, which form the stencil $S(i)$. For $S(i)$, find a polynomial $p(x, y)$ of degree $k - 1$ the most whose cell average in each of the triangles in the stencil $S(i)$ agrees with the average of $u(x, y)$ given by Eq. (4.48). This condition yields on $m \times m$ linear system, and if this system has a unique solution then the stencil $S(i)$ is admissible. For

second-order linear reconstruction, $k = 1$ the stencil formed by T_i plus two immediate neighbors is admissible for most triangulations. For third-order reconstruction $k = 3$, (quadratic polynomial $k - 1 = 2$ is needed), $m = 6$, some of the stencils consisting of T_i and five of its neighbors may not be admissible. For fourth-order reconstruction $k = 4$, (cubic polynomial), $m = 10$, the stencil consists of T_i plus nine of the immediate neighbors shown in Fig. 48. The most robust way for third- and fourth-order reconstruction is the least-squares reconstruction procedure suggested by Barth and Frederickson [131] where the polynomial p is determined by requiring that p has the same cell average as u on T_0 and also has the same cell average as u on the collection of the neighboring triangles but only in a least-squares sense. The reconstruction problem becomes extremely time consuming for high-order reconstructions in three dimensions.

For completeness, the k -exact reconstruction of Barth and Frederickson [131] that is used in ENO and WENO finite-volume sachems is briefly summarized. The basic idea for arbitrary order (k -exact) reconstruction in two dimensions is to determine the following reconstruction polynomials for each subdomain Ω_i :

$$u^k(x, y)_i = \sum_{m+n \leqslant k} \alpha_{(m,n)} P_{(m,n)}(x - x_c, y - y_c), \quad (4.50)$$

where $P_{(m,n)}(x - x_c, y - y_c) = (x - x_c)^m (y - y_c)^n$ and (x_c, y_c) is the centroid of the volume. The k -exact reconstruction strategy optimizes efficiency by precomputing the weights W_i in each cell Ω_i using a neighbor set N_i as follows

$$\alpha_{(m,n)} = \sum_{i \in N_i} W_{(m,n)} \bar{u}_i, \quad (4.51)$$

where $\alpha_{(m,n)}$ are the polynomial coefficients in Eq. (4.50). For k -exact reconstruction in two dimensions, the set N_i of the control volume neighbors must contain at least $(k + 1)(k + 2)/2$ members. The reconstruction is complemented by a monotonicity enforcing procedure as described in [130].

Friedrich [166] proposed to use a weighted sum of all reconstruction polynomials p_1, \dots, p_m as follows:

$$p = \sum_{i=1}^m \omega_i p_i, \quad (4.52)$$

where the weights of p_i are chosen such that ω_i is low if the oscillation of p_i is high. As computational cells in Friedrich formulation [166] were considered the dual cells resulting from the lines joining the barycenters with the midpoints of the edges. The cell averages are defined as

$$\bar{u}_k = \frac{1}{|\Omega_k|} \int_{\Omega_k} u(\mathbf{x}) d\mathbf{x}, \quad (4.53)$$

where Ω_k are polygonally bounded by a finite number of line segments. Further details on the full reconstruction algorithm the selection of admissible stencils and the choice of smoothness indicators and the WENO reconstruction weights ω_i in Eq. (4.49) can be found in [166].

4.8.3. Multidimensional finite-difference ENO

For finite-difference methods for hyperbolic conservation laws, the problem is to obtain high order, conservative approximation of the derivative from point values [32,167]. Similar to the one-dimensional case, in multidimensions the uniform mesh assumption is essential. For finite-difference methods in two dimensions the statement of the problem is:

Given the point u_{ij} values of $u(x, y)$ on a uniform mesh

$$u_{ij} \equiv u(x_i, y_j) \quad \begin{matrix} i = 1, 2, \dots, N_x, \\ j = 1, 2, \dots, N_y, \end{matrix} \quad (4.54)$$

find the numerical flux functions

$$\begin{aligned} \hat{u}_{i+1/2,j} &= \hat{u}(u_{i-r,j}, \dots, u_{i+k-1-r,j}) \quad i = 0, 1, \dots, N_x, \\ u_{i,j+1/2} &= \hat{u}(u_{i,j-s}, \dots, u_{i,j+k-1-s}) \quad j = 0, 1, \dots, N_y \end{aligned} \quad (4.55)$$

that obtain a k th order conservative approximation of the derivative by Eq. (4.14). Therefore, the conservative approximation of the derivative from point values is accomplished in multidimensions as in the one-dimensional case, e.g. considering $w(x) = u(x, y_j)$ obtain $u_x(x_i, y_j) = w'(x_i)$ and $v(y) = u(x_i, y)$ obtain $v_y(x_i, y_j) = v'(y_j)$.

An example of multidimensional ENO or WENO scheme is the characteristic-wise ENO or WENO implementation for the Euler equations in the finite-difference context on uniform meshes. The Lax–Friedrich’s or Roe’s approximate Riemann solver can be used to split the fluxes. For example, using the Lax–Friedrich’s flux as building block obtain

$$\begin{aligned} f_{\text{LF}}(x, y) &= \frac{1}{2}[f(x) + f(y) - \lambda(y - x)], \\ \lambda &= \max |f'(u)|. \end{aligned}$$

Perform the following steps in each of the (i, j, k) or (x, y, z) directions

- (1) Project the positive and negative part of the flux in the i direction, to the characteristic field in the i direction by multiplying with the left eigenvectors l_i^m ($m = 1 - 4$ for 2D or $m = 1 - 5$ for 3D) to obtain f_{LF}^W as follows:

$$(f_{\text{LF}}^W)_{i+1/2}^m = \sum_{n=1}^m (f_{\text{LF}})_{i+1/2}^n l_i^n.$$

- (2) Perform k th order ENO or WENO reconstruction to obtain the numerical fluxes \hat{f}_{LF}^W in the characteristic field.

- (3) Project the numerical (\hat{f}_{LF}^W) fluxes to the physical space by multiplying with the right eigenvectors r_i^m to obtain the numerical fluxes \hat{f} in the conservative variable space

$$\hat{f}_{i+1/2}^m = \sum_{n=1}^m r_i^n (\hat{f}_{\text{LF}}^W)_{i+1/2}^n.$$

- (4) Compute the k th order accurate conservative approximation of the derivative f_x as

$$f_x = \frac{\hat{f}_{i+1/2} - \hat{f}_{i-1/2}}{\Delta x} + \mathcal{O}(\Delta x^k).$$

Repeat steps 1–4 for the other directions to obtain the flux derivatives g_y and h_z .

4.9. Optimization of WENO schemes

WENO schemes have been successfully applied to problems with shocks and complex smooth flow features [168]. Direct application of WENO schemes to wave propagation problems, such as computational aeroacoustics (CAA) and computational electromagnetics (CEM), where resolution of short waves is important is not optimal because WENO schemes are designed for high resolution of discontinuities and to achieve the formal order of accuracy of the reconstruction. Efficient and accurate resolution of short waves is achieved in CAA with the optimized schemes where the coefficients of the scheme are altered to minimize a particular type of error instead of the truncation error. These optimized schemes [100,111,112,132,169,170] have been used very successfully for better resolution of short waves in broadband acoustic wave propagation.

Recently, Wang and Chen [171] using ideas of CAA-optimized schemes proposed modification of the WENO smoothness measures and developed an optimized WENO (OWENO) scheme. Following the practice of the dispersion relation Preserving (DRP) scheme [86] presented in Section 3.4.2, Wang and Chen [171] achieved high resolution for short waves with OWENO. The OWENO schemes of Wang and Chen [171] optimizes all candidate stencils and finds the best weights to combine them. The approach of Wang and Chen [171] was a significant improvement over previous attempts to optimize WENO schemes [172], where only the weights of the WENO schemes were optimized.

The development of the OWENO scheme is based on the DRP idea [86]. The OWENO scheme instead of achieving the maximum order of accuracy k , compromises the accuracy requirement by setting $p_1 < k$ in the conservative approximation of the derivative

$$\frac{\partial u_i}{\partial x} = \frac{(\hat{u}_{i+1/2} - \hat{u}_{i-1/2})}{\Delta x} + \mathcal{O}(\Delta x^{p_1}), \quad r + s + 1 = k \quad (4.56)$$

and minimizes the difference between the numerical wavenumber and the actual wave number. The numerical wavenumber for the scalar wave equation $u + \alpha u_x = 0$ where the spatial derivative is evaluated as in Eq. (4.56) becomes

$$\bar{a}^r = \frac{-i}{\Delta x} \sum_{m=-r}^s c_{r,j+r} \exp(im\alpha\Delta x)[1 - \exp(-i\alpha\Delta x)] \\ = \alpha + \mathcal{O}(\alpha\Delta x)^{p_1}. \quad (4.57)$$

Optimized coefficient c_{rj} in the approximation of the numerical flux $\hat{u}_{i+1/2} = \sum_{j=0}^{k-1} c_{rj} u_{i-r+j}$ are obtained by minimizing the L_2 norm of the difference between the numerical wavenumber of Eq. (4.57) and the actual wavenumber for a particular range $[-\alpha\Delta x, \alpha\Delta x]$. These coefficients c_{rj} are obtained by minimizing the integral

$$E_r = \int_{-\alpha_0\Delta x}^{\alpha_0\Delta x} \lambda [R_e(\bar{a}^r \Delta x) - \alpha \Delta x]^2 \\ + (1 - \lambda) [\ln(\bar{a}^r \Delta x)]^2 d(\alpha \Delta x). \quad (4.58)$$

The OWENO scheme is then obtained in two steps:

- (1) For p_1 th order of accuracy with Eq. (4.56) the following p_1 linear equations must be satisfied

$$\sum_{j=0}^{k-1} b_{mj} c_{rj} = z_m, \quad m = 1, \dots, p_1, \quad (4.59)$$

where b_{mj} and z_m are constants the rest $k - p_1$ are obtained from the minimization of E_r in Eq. (4.58)

$$\frac{\partial E_r}{\partial c_{rj}} = 0, \quad j = p_1, \dots, k - 1. \quad (4.60)$$

- (2) Perform a convex combination of the k candidate p_1 th order accurate stencils to obtain OWENO as

$$\hat{u}_{i+1/2}^{\text{OWENO}} = \sum_{r=0}^{k-1} h_r \hat{u}_{i+1/2}^r \\ \text{so that } \sum_{r=0}^{k-1} h_r = 1, h_r \geq 0, p_2 \leq k + 1 \\ \frac{1}{\Delta x} (\hat{u}_{i+1/2}^{\text{OWENO}} - \hat{u}_{i+1/2}^{\text{OWENO}}) = \left(\frac{\partial u}{\partial x} \right)_i + \mathcal{O}(\Delta x^{p_1+p_2}). \quad (4.61)$$

The $k - 1 - p_2$ free weight parameters of Eq. (4.61) are $p_2 \leq k - 1$ then determined by minimizing again the integral of Eq. (4.58) but with \bar{a}^r replaced by $\bar{a} = \sum_{r=0}^{k-1} h_r \bar{a}^r$.

The coefficients of several high-order accurate OWENO schemes can be found in [171].

The new smoothness indicators of the $k = 4$, OWENO scheme that satisfy

$$\beta_r = \sum_{m=2}^{k-1} \sum_{k>2} \left[\int_{x_{i-1/2}}^{x_{i+1/2}} \Delta x^{m-1} \frac{\partial^m p_r(x)}{\partial x^m} dx \right]^2, \\ r = 0, \dots, k - 1 \quad (4.62)$$

instead of Eq. (4.33) are given by

$$\beta_0 = (2u_i + 5u_{i+1} + 4u_{i+2} - u_{i+3})^2 \\ - (u_i + 3u_{i+1} - 3u_{i+2} + u_{i+3})^2,$$

$$\beta_1 = (u_{i-1} - 2u_i + u_{i+1})^2 \\ + (-u_{i-1} + 3u_i - 3u_{i+1} + u_{i+2})^2,$$

$$\beta_2 = (u_{i-1} - 2u_i + u_{i+1})^2 \\ + (-u_{i-2} + 3u_{i-1} - 3u_i + u_{i+1})^2,$$

$$\beta_3 = (-u_{i-3} + 4u_{i-2} - 5u_{i-1} + 2u_i)^2 \\ + (-u_{i-3} + 3u_{i-2} - 3u_{i-1} + u_i)^2. \quad (4.63)$$

Taylor expansion of $\beta_0, \beta_1, \beta_2, \beta_3$ yields

$$\beta_r = (u_i'' \Delta x^2) + (u_i''' \Delta x^3)^2 + \mathcal{O}(\Delta x^6), \\ r = 0, \dots, 3 \quad (4.64)$$

therefore in the case $u_i'' = u_i''' = 0$ the OWENO scheme for $k = 4$ does not have the formal accuracy of standard WENO scheme $(2k - 1) = 7$ but achieves better resolution of high wavenumbers.

4.10. Compact WENO approximation

It was pointed out in Section 3 that two advantages of compact schemes compared to non-compact (explicit) counterparts are: (i) they yield better accuracy and wave-space resolution for the same number of points in the stencil, and (ii) they offer an advantage in the implementation of boundary conditions because fewer boundary points must be handled. These advantages are achieved at a moderate increase in computing cost resulting from the matrix inversion. Recently, Pirozzoli [173], exploiting the advantages of compact schemes and developed a narrow-stencil, fifth-order accurate WENO compact scheme referred to from now on as CWENO5 scheme.

Starting with the same formulation as in Section 4.3 (see Eq. (4.9)–(4.14)) considered the following compact representation for the reconstruction of the numerical flux $\hat{u}_{i+1/2}$

$$\sum_{l=-L_1}^{L_2} A_l \hat{u}_{i+1/2+l} = \sum_{m=M_1}^{M_2} a_m \bar{u}_{i+m}. \quad (4.65)$$

The Taylor series expansion of u up to order K around $x_{i+1/2}$ is

$$u(x) = \sum_{n=0}^{K-1} \frac{\partial^n u}{\partial x^n} \Big|_{i+1/2} \frac{(x - x_{i+1/2})^n}{n!} + \mathcal{O}(h^K) \quad (4.66)$$

and recalling that the points values at the nodes, u_i , which are considered as cell averages for the finite-difference ENO reconstruction, e.g. $u_i \equiv \bar{u}_i$, satisfy

$$\bar{u}_{i+m} = \frac{U_{i+m+1/2} - U_{i+m-1/2}}{\Delta x}, \quad (4.67)$$

where $U(x)$ is the primitive function of $u(x)$ satisfying

$$U(x) = \sum_{n=0}^{K-1} \frac{\partial^n u}{\partial x^n} \Big|_{i+1/2} \frac{(x - x_{i+1/2})^{n+1}}{(n+1)!} + \mathcal{O}(\Delta x^{K+1}) \quad (4.68)$$

therefore

$$\begin{aligned} \bar{u}_{i+m} &= \sum_{n=0}^{K-1} \frac{\partial^n u}{\partial x^n} \Big|_{i+1/2} \frac{1}{(n+1)!} [m^{n+1} - (m-1)^{n+1}] \Delta x^n \\ &\quad + \mathcal{O}(\Delta x^{K+1}). \end{aligned} \quad (4.69)$$

Inserting the Taylor series expansions for $\hat{u}_{i+1/2}$ and \bar{u}_{i+m} from Eqs. (4.66) and (4.69), respectively, in Eq. (4.65) and matching the coefficients of like powers of h requiring k th order accurate approximation (with $k \leq K$) obtain

$$\begin{aligned} (n+1) \sum_{l=-L_1}^{L_2} A_l l^n - \sum_{m=-M_1}^{M_2} a_m [m^{n+1} - (m-1)^{n+1}] &= 0 \\ n = 0, \dots, k-1. \end{aligned} \quad (4.70)$$

Solving the system of Eq. (4.70) for $L_1 + L_2 + 1$, A_l unknowns and $M_1 + M_2 + 1$, a_m unknowns obtain the coefficients of the compact upwind scheme. The only fifth-order accurate compact scheme ($k = 5$) for $L_1 = L_2 = M_1 = M_2 = 1$, which involves tridiagonal matrix inversion is

$$3\hat{u}_{i-1/2} + 6\hat{u}_{i+1/2} + \hat{u}_{i+3/2} = \frac{1}{3}u_{i-1} + \frac{19}{3}u_i + \frac{10}{3}u_{i+1}. \quad (4.71)$$

The numerical fluxes $u_{i+1/2}$ obtained from the point values $u_i \equiv \bar{u}_i$ through the solution of the system of Eq. (4.71) yield a fifth-order accurate, conservative evaluation of the derivative as

$$\frac{1}{\Delta x} (\hat{u}_{i+1/2} - \hat{u}_{i-1/2}) = u'(x_i) + \mathcal{O}(\Delta x^k). \quad (4.72)$$

Furthermore, the following explicit WENO approximations were obtained fifth-order upwind-biased approximation:

$$\hat{u}_{i+1/2} = \frac{1}{60} (2u_{i-2} - 13u_{i-1} + 47u_i + 27u_{i+1} - 3u_{i-2}). \quad (4.73)$$

Seventh-order upwind-biased approximation:

$$\begin{aligned} \hat{u}_{i+1/2} &= \frac{1}{420} (-3u_{i-3} + 25u_{i-2} - 101u_{i-1} \\ &\quad + 319u_i + 214u_{i+1} - 38u_{i+2} + 4u_{i+3}). \end{aligned} \quad (4.74)$$

The approximations of Eqs. (4.73) and (4.74) can be used as fifth- or seventh-order WENO schemes in smooth flow regions.

The resolution properties of the WENO approximations of Eqs. (4.71), (4.73), and (4.74) were demonstrated in [173]. The linear advection equation $u_x + au_x = 0$,

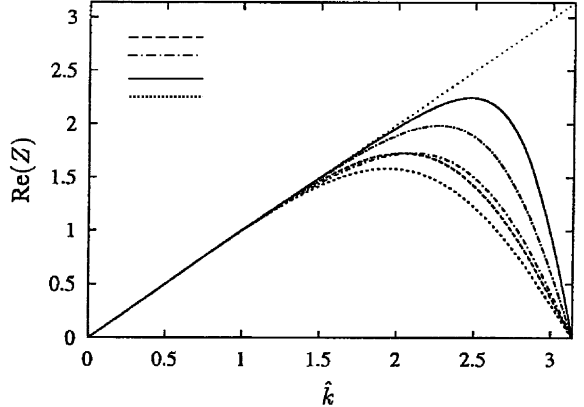


Fig. 49. Dispersion of compact WENO schemes; seventh-order WENO —, fifth-order compact WENO ——, fifth-order WENO - - -, sixth-order centered ——·—, fourth-order centered ---, exact ······.

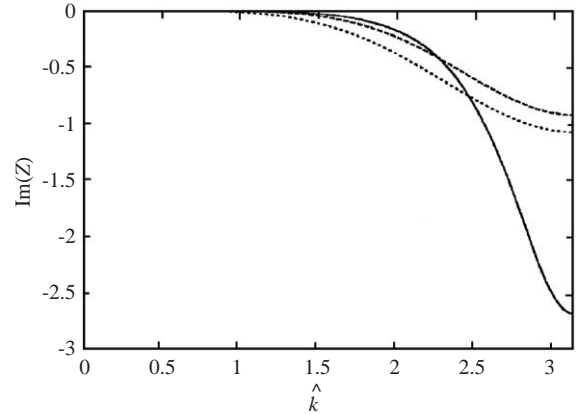


Fig. 50. Dissipation of compact WENO schemes: fifth-order compact WENO —, sixth-order centered - - -, fourth-order centered ······.

$a > 0$ was considered for the evaluation of the resolving ability. The dispersion properties of the new schemes are compared with the classical, symmetric compact schemes in Fig. 49. The upwind-biased approximations of Eqs. (4.68), (4.73), and (4.74) introduce in addition dissipation errors. The dissipation error is shown in Fig. 50. It can be seen that the compact WENO scheme of Eq. (4.71) has very small dissipation error, smaller than the fifth- and seventh-order explicit schemes of Eqs. (4.73) and (4.74), for the range $0 < \hat{k} < \pi/2$.

For non-periodic domains, the following fourth-order accurate boundary closures were proposed for the implementation of Eq. (4.71).

$$\hat{u}_{1/2} = \frac{1}{12} (3u_0 + 13u_1 - 5u_2 + u_3),$$

$$\hat{u}_{N+1/2} = \frac{1}{12} (25u_N - 23u_{N-1} + 13u_{N-2} - 3u_{N-3}). \quad (4.75)$$

A Roe-type, characteristic-wise, finite-difference, implementation of the compact CWENO5 scheme developed by Pirozzoli [173] was recently presented by Ren et al. [174]. The formulation of Ren et al. [174] closely follow the hybrid compact-ENO ideas introduced by Adams and Shariff [175]. The implementation proposed in [174] for the scalar hyperbolic conservation law $u_t + f_x(u) = 0$ is as follows.

The numerical flux function $\hat{f}_{i+1/2}$ for the evaluation of the conservative approximation of the derivative f_x is obtained by

$$\begin{aligned} & 3\hat{f}_{i-1/2} + 6\hat{f}_{i+1/2} + \hat{f}_{i+3/2} \\ &= \frac{1}{3}(f_{i-1} + 19f_i + 10f_{i+1}) \quad \text{if } \tilde{a}_{i+1/2} \geq 0, \end{aligned} \quad (4.76)$$

$$\begin{aligned} & \hat{f}_{i-1/2} + 6\hat{f}_{i+1/2} + 3\hat{f}_{i+3/2} \\ &= \frac{1}{3}(10f_i + 19f_{i+1} + f_{i+2}) \quad \text{if } \tilde{a}_{i+1/2} < 0, \end{aligned} \quad (4.77)$$

where $\tilde{a}_{i+1/2}$ is the numerical wave speed defined by

$$\tilde{a}_{i+1/2} = \begin{cases} \frac{\hat{f}_{i+1} - \hat{f}_i}{u_{i+1} - u_i} & \text{if } u_{i+1} - u_i \neq 0, \\ \left(\frac{\partial f}{\partial u}\right)_i & \text{otherwise.} \end{cases} \quad (4.78)$$

Denoting $S_{i+1/2} = \text{sign}(\tilde{a}_{i+1/2})$ Eqs. (4.76) and (92) can be combined to

$$A_{i+1/2}\hat{f}_{i-1/2} + \hat{f}_{i+1/2} + B_{i+1/2}\hat{f}_{i+3/2} = b_{i+1/2}, \quad (4.79)$$

where

$$\begin{aligned} A_{i+1/2} &= \frac{1}{3} + \frac{S_{i+1/2}}{6}, \quad B_{i+1/2} = \frac{1}{3} + \frac{S_{i+1/2}}{6}, \\ b_{i+1/2} &= \frac{1 + S_{i+1/2}}{2} \left(\frac{1}{18}f_{i-1} + \frac{19}{18}f_i + \frac{5}{9}f_{i+1} \right) \\ &\quad + \frac{1 - S_{i+1/2}}{2} \left(\frac{5}{9}f_i + \frac{19}{18}f_{i+1} + \frac{1}{18}f_{i+2} \right). \end{aligned}$$

The compact WENO scheme of Eq. (4.79) gives very satisfactory results for smooth flow regions. However, at the discontinuities of the solution the Gibbs phenomenon will occur that contaminates the solution and eventually leads to nonlinear instability.

For these regions, a hybrid method is proposed in [174] where the compact scheme of Eq. (4.79) is coupled with the WENO procedure. The hybrid scheme is the weighted average of the compact scheme in Eq. (4.79) and WENO of Section 4.7.

This hybrid scheme [174] has the following form:

$$\begin{aligned} & \sigma_{i+1/2}A_{i+1/2}\hat{f}_{i-1/2} + \hat{f}_{i+1/2} \\ &+ \sigma_{i-1/2}B_{i+1/2}\hat{f}_{i+3/2} = \hat{c}_{i+1/2}, \end{aligned} \quad (4.80)$$

where σ is the weight and

$$c_{i+1/2} = \sigma_{i+1/2}b_{i+1/2} + (1 - \sigma_{i+1/2})f_{i+1/2}^{\text{WENO}}.$$

For $\sigma_{i+1/2} = 1$, Eq. (4.80) reduces to the compact scheme of Eq. (4.79) and for $\sigma_{i+1/2} = 0$ becomes a WENO scheme. It is necessary, therefore, that the weight be directly related to the smoothness of the numerical solution. This is achieved through the definition of a smoothness indicator $r_{i+1/2}$ defined by Ren et al. [174] by

$$\begin{aligned} r_{i+1/2} &= \min(r_j, r_{j+1}), \\ r_j &= \frac{2|\Delta f_{i+1/2}\Delta f_{i-1/2}| + \varepsilon}{(\Delta f_{i+1/2})^2 + (\Delta f_{i-1/2})^2 + \varepsilon}, \\ \Delta f_{i+1/2} &= f_{i+1} - f_i, \\ \varepsilon &= \frac{0.9r_c}{1 - 0.9r_c} \xi^2, \quad \xi > 0, \quad r_c \simeq 1. \end{aligned} \quad (4.81)$$

Note that Pirozzoli simply defined the smoothness indicator as $r_{i+1/2} = |f_{j+1} - f_j|$ and determined $\sigma_{i+1/2}$ by

$$\sigma_{j+1/2} = \begin{cases} 1 & \text{if } r_{j-1/2} \leq \tilde{r}_c \text{ and } r_{j+1/2} \leq \tilde{r}_c \\ & \text{and } r_{j+3/2} \leq \tilde{r}_c, \\ 0 & \text{otherwise,} \end{cases} \quad (4.82)$$

where r_c is a problem-dependent threshold. Using the definition of Ren et al. [174] for $r_{i+1/2}$ the weight $\sigma_{i+1/2}$ is computed by

$$\sigma_{i+1/2} = \min\left(1, \frac{r_{i+1/2}}{r_c}\right). \quad (4.83)$$

4.11. Hybrid compact-WENO scheme for the Euler equations

A characteristic-wise approach is used in [174] with the hybrid, compact WENO scheme for the numerical solution of the Euler equations. The numerical flux evaluation is performed in the following steps:

- (1) Compute an average state $U_{i+1/2}$ by the simple mean $U_{i+1/2} = (U_i + U_{i+1})/2$ or the Roe average.
- (2) Compute the eigenvalues $\lambda_{i+1/2} i + 1/2 = 1, 2, 3, 4$ and the left eigenvectors $\mathbf{l}_{i+1/2}^{(m)}$ at the average state.
- (3) Perform local characteristic decomposition

$$\mathbf{w}_n^{(m)} = \mathbf{l}_{i+1/2} F_n \quad m = 1, 2, 3, 4, \quad n = i-1, \dots, i+2.$$

- (4) Define

$$\begin{aligned} s_{i+1/2}^{(m)} &= \text{sign}(\lambda_{i+1/2}^{(m)}), \\ r_{i+1/2}^{(m)} &= \min(r_j^{(i)}, r_{i+1}^{(i)}), \\ r_i^{(m)} &= \frac{|2\Delta w_{i+1/2}^{(m)}\Delta w_{i-1/2}^{(m)}| + \varepsilon}{(\Delta w_{i+1/2}^{(m)})^2 + (\Delta w_{i-1/2}^{(m)})^2 + \varepsilon}, \\ \sigma_{i+1/2}^{(m)} &= \min\left(1, \frac{r_{i+1/2}^{(m)}}{r_c}\right). \end{aligned}$$

- (5) Apply the hybrid, compact-WENO scheme for the local characteristic variables as

$$\begin{aligned} & \sigma_{i+1/2}^{(m)} A_{i+1/2}^{(m)} w_{i-1/2}^{(m)} + w_{i+1/2}^{(m)} \\ & + \sigma_{i+1/2}^{(m)} B_{i+1/2}^{(m)} w_{i+3/2}^{(m)} = c_{i+1/2}^{(m)}, \\ & A_{i+1/2}^{(m)} = \frac{2 + s_{i+1/2}^{(m)}}{6}, \quad B_{i+1/2}^{(m)} = \frac{2 - s_{i+1/2}^{(m)}}{6}, \\ & c_{i+1/2}^{(m)} = \sigma_{i+1/2}^{(m)} b_{i+1/2} + (1 - \sigma_{i+1/2}^{(m)}) w_{i+1/2}^{(m)\text{WENO}}, \\ & b_{i+1/2}^{(m)} = \frac{1}{18} \left(\frac{1 + s_{i+1/2}^{(m)}}{2} \right) (w_{i-1}^{(m)} + 19w_i^{(m)} + 10w_{i+1}^{(m)}) \\ & = + \frac{1}{18} \left(\frac{1 - s_{i+1/2}^{(m)}}{2} \right) \\ & \times (10w_i^{(m)} + 19w_{i+1}^{(m)} + w_{i+2}^{(m)}), \end{aligned} \quad (4.84)$$

where $w^{(m)\text{WENO}}$ is computed with the WENO scheme of Section 4.5.

- (6) Project Eq. (4.84) back to conservative variables and solve the following block-tridiagonal system of equations too obtain the numerical flux in the conservative variable space

$$\begin{aligned} & [A]_{i+1/2} \mathbf{F}_{i-1/2} + L_{i+1/2} \mathbf{F}_{i+1/2} \\ & + [B]_{i+1/2} \mathbf{F}_{i+3/2} = \mathbf{c}_{i+1/2}, \\ & [\mathbf{A}]_{i+1/2} = \begin{bmatrix} \sigma_{i+1/2}^{(1)} A_{i+1/2}^{(1)} \mathbf{l}_{i+1/2}^{(1)} \\ \sigma_{i+1/2}^{(4)} A_{i+1/2}^{(4)} \mathbf{l}_{i+1/2}^{(4)} \end{bmatrix}, \\ & [\mathbf{B}]_{i+1/2} = \begin{bmatrix} \sigma_{i+1/2}^{(1)} B_{i+1/2}^{(1)} \bar{\mathbf{l}}_{i+1/2}^{(1)} \\ \sigma_{i+1/2}^{(4)} B_{i+1/2}^{(4)} \bar{\mathbf{l}}_{i+1/2}^{(4)} \end{bmatrix}, \\ & L_{i+1/2} = \begin{bmatrix} \mathbf{l}_{i+1/2}^{(1)} \\ \mathbf{l}_{i+1/2}^{(2)} \\ \mathbf{l}_{i+1/2}^{(3)} \\ \mathbf{l}_{i+1/2}^{(4)} \end{bmatrix}, \quad \mathbf{c}_{i+1/2} = \begin{bmatrix} c_{i+1/2}^{(1)} \\ c_{i+1/2}^{(2)} \\ c_{i+1/2}^{(3)} \\ c_{i+1/2}^{(4)} \end{bmatrix}. \end{aligned} \quad (4.85)$$

4.12. Applications of ENO and WENO

It is well known in CFD that the solution error for a given problem strongly depends on the smoothness of the computational grid. Uniform or smoothly varying grids always yield smaller solution errors than non-uniform or non-smooth grids. For example, many second-order structured or unstructured grid CFD

algorithms often degrade into first order for non-smooth grids. Analogous behavior should be expected for higher-order methods. The dependence on grid smoothness of the numerical solutions obtained with ENO was investigated by Casper and Atkins [176].

The two basic formulations, finite volume (FV) and finite difference (FD), of ENO were considered by Casper and Atkins [176]. The FD and FV fourth-order accurate algorithms were compared for accuracy, sensitivity to grid irregularities, wave resolution, and computational efficiency. It was found [176] (see Fig. 51) that for fourth-order design accuracy the two-dimensional FD ENO numerical solution is approximately two times more efficient than the FV ENO numerical solution. The CPU time for three-dimensional implementation (see Fig. 52) shows more dramatic increase for the FV formulation. For example, the CPU time required for FV ENO with fourth-order formal accuracy is approximately three times higher than the FD ENO with equivalent formal accuracy. It was shown,

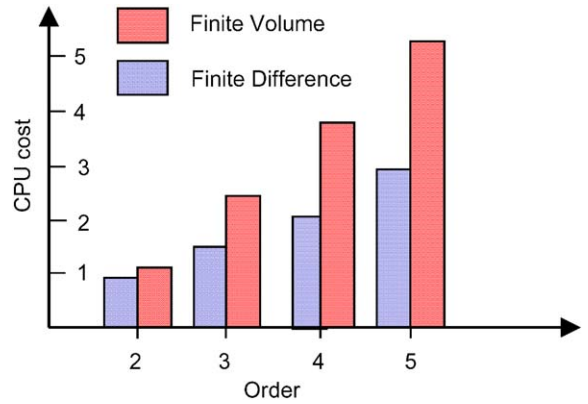


Fig. 51. Comparison of the required CPU time for FV and FD ENO in two dimensions.

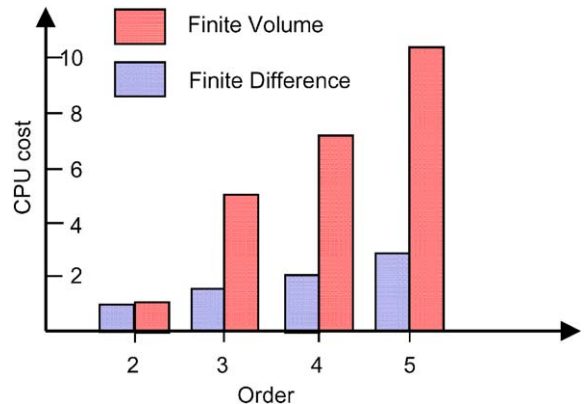


Fig. 52. Comparison of the required CPU time for FV and FD ENO in three dimensions.

however, in [176] that the formal accuracy of the FD ENO can only be achieved with smooth grids. The finite-volume implementation was found [176] less sensitive to derivative discontinuities, whether in the computational mesh or the solution. Therefore, for applications where the computational domain is known to be sufficiently smooth and can be suitably structured the FD ENO algorithm must be the method of choice. Taking, however, into account that the formal accuracy of the FD ENO can significantly degrade for non-smooth meshes [176] (see Fig. 53), for problems with complex geometries it may pay to use the more expensive FV algorithm.

The resolving ability and the performance for long-time integration of the WENO and other numerical schemes presented in the previous sections was evaluated

for simple linear problems by Ekaterinaris [177]. The performance of centered and WENO schemes for aeroacoustics using the full Euler equations was also considered. In addition, centered schemes with characteristic based filters were compared with WENO schemes for problems with strong shocks in curvilinear coordinates. The computed solutions were compared with available exact solutions.

Long-time integration is important in many practical applications, such as aeroacoustics, LES and helicopter rotor calculations where the tip vortex and the rotor wake need to propagate for long distances. Therefore the ability of symmetric, centered compact and non-compact schemes as well as several WENO high-order accurate stencils was also evaluated in [177], for wave convection. Sufficiently accurate convection of simple

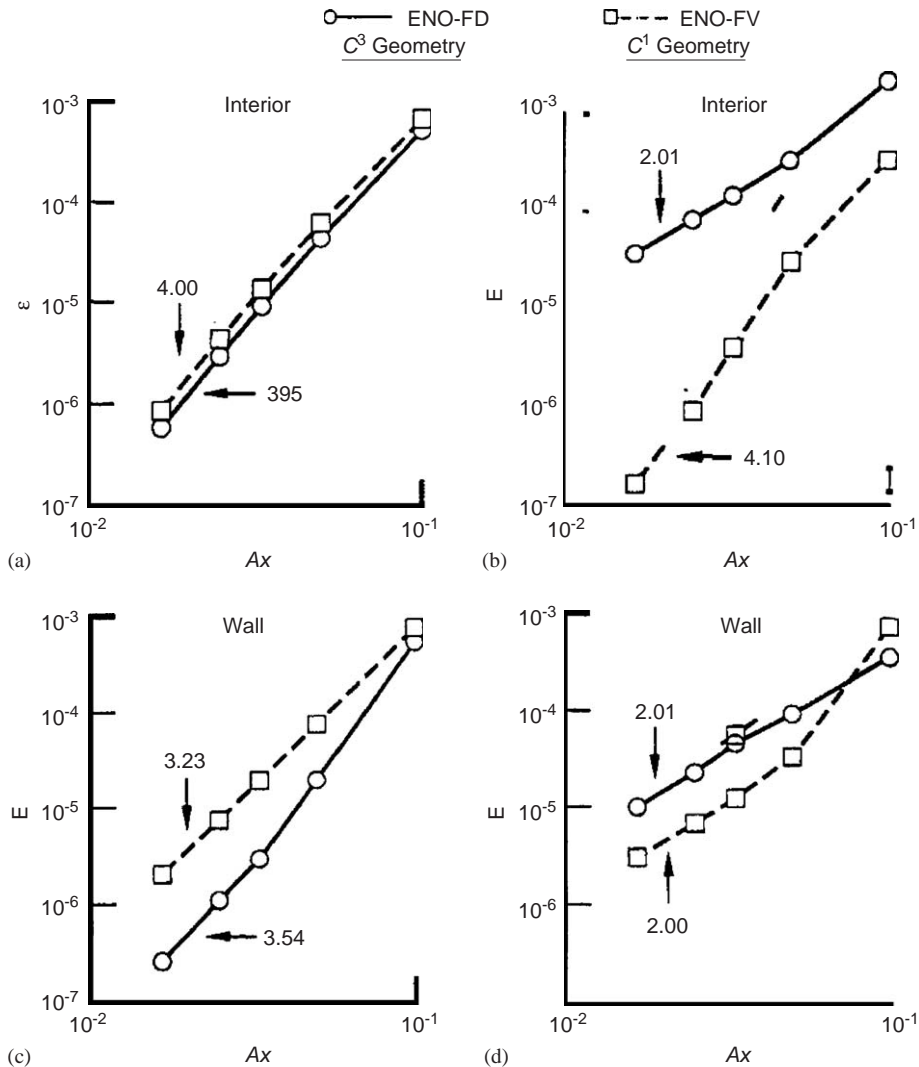


Fig. 53. L1 entropy errors, steady two-dimensional channel flow.

Table 3

 L_2 error at $T = 200$ for the convection of $\sin(\pi x/6)$ with explicit schemes

Explicit schemes	Fourth-order centered	Sixth-order centered	Fifth-order WENO	Seventh-order WENO
L_2 error	0.2E00	0.11E – 2	0.12E – 1	0.14E – 3

Gaussian pulses, $u(x, t = 0) = e^{-ax^2}$, with 12 points per waveform (not shown here) was achieved even with explicit fourth-order accurate in space methods.

Further accuracy test were shown for linear wave convection by the one-dimensional wave equation $u_t + cu_x = 0$. Numerical solutions with unit wavespeed, $c = 1$, were obtained for long propagation times. Time marching was performed with the third-order accurate Runge–Kutta method. A time step of $\Delta t = 0.1$, which is below the stability limit of the method, was used for all tests in order to keep time integration errors at low level.

The first test was propagation of a high-frequency sinusoidal wave $u_0(x) = \sin(\pi x/6)$. Convection of the sinusoidal wave was obtained with $\Delta x = 0.1$ (12 points per wavelength) and periodic boundary conditions. The mean square error obtained from explicit space discretizations with the symmetric fourth-, and sixth-order accurate schemes and with WENO schemes of fifth- and seventh-order accuracy, Eqs. (4.43), is shown in Table 3. It appears that only the schemes with formal accuracy more than five were capable to obtain sufficiently accurate solution for long-time integration.

Further evaluation of high-order accurate symmetric explicit and compact schemes and WENO stencils to perform linear wave convection was carried out using the following modulated wave $u_0(x) = \cos(a|x|)e^{-b|x|}$ with $a = \frac{3}{4}$ and $b = \frac{1}{10}$ as initial condition. For explicit schemes, time integration was performed until $T = 200$. For compact schemes, which have increased resolving ability, time integration was performed until the final time $T = 500$. A comparison of the solutions computed using explicit high-order symmetric schemes and WENO stencils with the exact result is shown in Fig. 54. It can be seen that at least sixth order of accuracy is needed for long-time propagation. The mean square error of the solutions computed with different schemes is shown in Tables 4 and 5. It appears that the ninth-order accurate WENO stencil provides uniformly high order of accuracy for smooth initial data.

The mean square error for long-time integration, $T = 500$, of high-order compact schemes (see Table 5) also remains at low levels. It can be seen that compact schemes with formal order of accuracy more than four perform adequately. The high-order accurate compact schemes appear to be particularly suitable for linear aeroacoustic problems. The computing time of the explicit schemes was proportional to the width of the

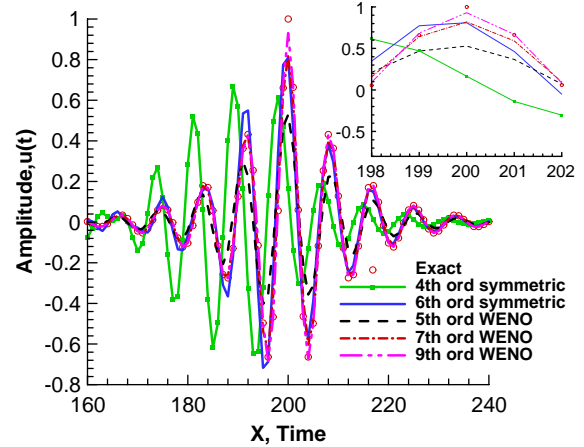


Fig. 54. Comparison of the exact solution $u_0(x) = \cos(a|x|)e^{-b|x|}$ at $T = 200$ with results computed with explicit schemes.

stencil. The computing cost of the eighth- and tenth-order compact schemes that require pentadiagonal matrix inversion was the highest and almost double compared to the time required by the explicit schemes. However, use of very high-order centered methods may be required for wave convection over long-time periods.

Symmetric schemes with spectral-type filtering and characteristic-based filters of Section 3, as well as WENO schemes off different order of accuracy were used to compute spread and reflection of a pressure disturbance. The full nonlinear Euler equations were used for this test. At the far-field boundaries of the domain a radiation boundary condition was used. On the solid surface the normal to the wall velocity component was set to zero while the density and pressure were extrapolated from the interior assuming that $\partial\rho/\partial n = \partial p/\partial n = 0$ or $\partial\rho/\partial y = \partial p/\partial y = 0$. It was found that it was required to use high-order accurate approximations of the derivatives at the wall in order to retain the accuracy of the numerical solution. For example, the pressure was extrapolated using the following one-seeded, fourth-order accurate approximation of the first derivative $(dp/dy)_1 = (-25p_1 + 48p_2 - 36p_3 + 16p_4 - 3p_5)/12$. The computed results were compared with the exact solution which gives the time variation of an initial pressure disturbance

Table 4

 L_2 error at $T = 200$ for the convection of $\cos(a|x|)e^{-b|x|}$ with explicit schemes

Scheme	Sixth-order centered	Fifth-order WENO	Seventh-order WENO	Ninth-order WENO
L_2 error	0.4E – 3	0.1E – 2	0.7E – 4	0.7E – 5

Table 5

 L_2 error at $T = 500$ for the convection of $\cos(a|x|)e^{-b|x|}$ with compact schemes

Compact schemes	Fifth-order WENO	Sixth-order centered	Eighth-order centered	Tenth-order centered
L_2 error	0.19E – 3	0.57E – 4	0.92E – 5	0.53E – 5

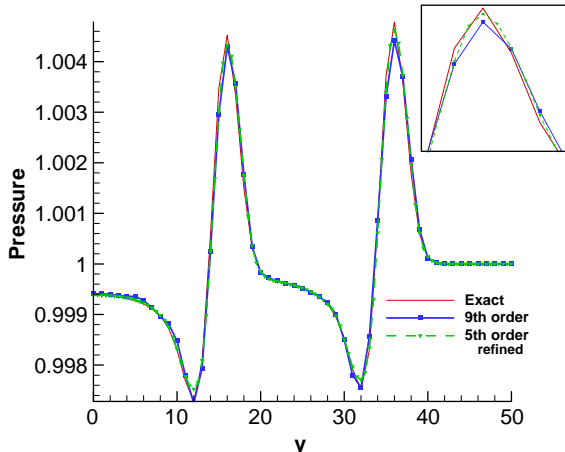


Fig. 55. Comparison of WENO scheme computations with the exact solution.

$p(x, y) = \exp\{-\ln 2[x^2 - (y - y_0)^2]\}$. The initial disturbance is located at $y = y_0$, and as it spreads, reflects from a solid wall at $y = 0$.

A comparison of the solutions computed on an artificially distorted mesh with fifth and ninth WENO schemes ($r = 3$, and 5, respectively) is shown in Fig. 55. It can be seen that the solution computed with the ($r = 5$) ninth-order accurate WENO scheme on a the baseline, 100×50 point grid, which provides 12 points per wave, is almost indistinguishable from the solution computed with the ($r = 3$) fifth-order accurate WENO scheme on a 200×100 point grid, refined in both directions. It is important to note that the full WENO scheme with the appropriate smoothness measures must be used for the propagation of the pressure disturbance with the nonlinear Euler equations. Numerical solutions of the linearized Euler equations that describe the propagation of the acoustic-type pressure disturbance may be possible only with the optimal WENO stencils of high-order WENO schemes.

A grid-independent solution was obtained for the solution computed with the ninth-order accurate ($r = 5$) WENO scheme since the error does not change for computations performed with the baseline 100×50 point grid and refined 200×100 and 400×200 point grids. Therefore, the errors of the baseline grid are mainly due to the temporal integration scheme. The error of the solutions obtained with different methods, along the normal to the wall symmetry line, is shown in Figs. 56 and 57. Similarly to the WENO scheme that required use of smoothness, characteristic-based filters were used for the computation of aeroacoustic pulse propagation with the full nonlinear Euler equations. For the comparisons of Fig. 56, the same value of the ACM filter parameter ($\kappa = 0.1$) was used. It can be seen that the WENO schemes provide a comparable level of accuracy with the centered schemes.

The effect of the order of the ACM filter parameter on the accuracy of the computed solution is shown in Fig. 57. It can be seen that increase of κ deteriorates the accuracy of the solution. The comparisons of Fig. 57 demonstrate that reduction of the ACM filter parameter below a certain level does not improve the solution. The solution obtained with the spectral-type filter has the smallest error. Among the results compared in Fig. 57, the solution computed with the spectral-type filter was the most efficient. The results computed with the ACM filter required approximately 20% more time compared to the solution obtained with the spectral filter. The solution obtained with the WENO scheme required approximately 30% more time compared to the solution obtained with the spectral filter. Despite the longer computing time, both WENO schemes and the ACM filter provide shock capturing capability which is of interest in aeronautical applications.

It can be concluded that both centered and WENO schemes of seventh order or higher are appropriate for aeroacoustic computations of subsonic flows. For flows with shocks, however, WENO schemes appear to be

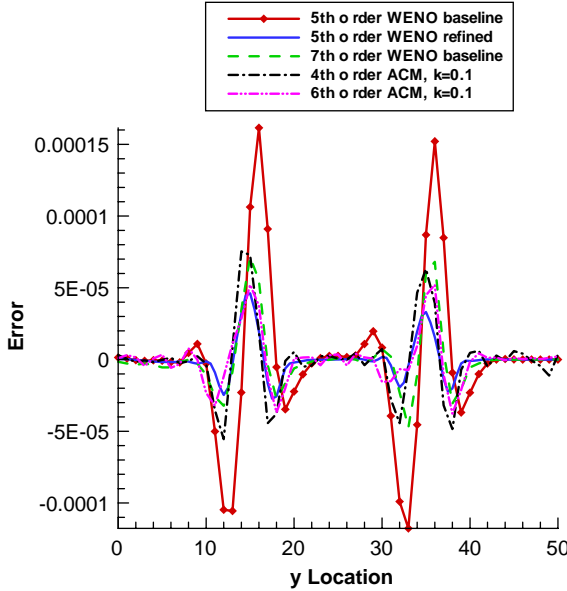


Fig. 56. Comparison of the error obtained with WENO schemes and centered schemes with characteristic-based filters $\kappa = 0.1$.

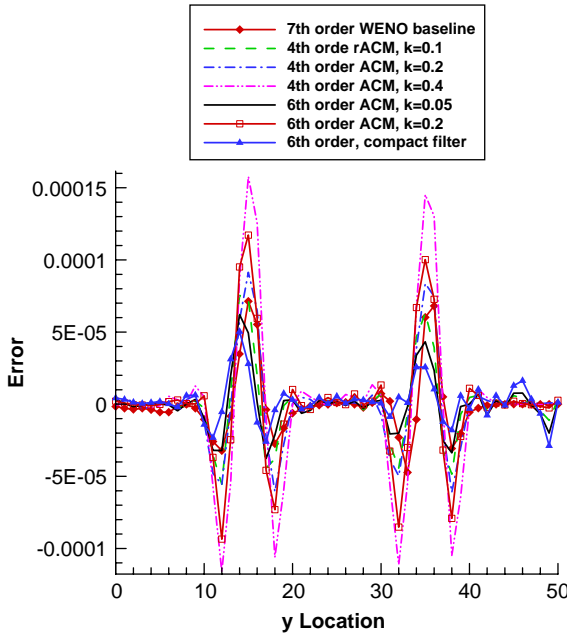


Fig. 57. Effect of the ACM filter parameter on the accuracy of the computed solution.

more appropriate for aeroacoustics, because computation of these flows require high values of the ACM filter parameter ($\kappa > 0.5$) in order to prevent numerical oscillations. Numerical solutions obtained for the same problem on artificially distorted meshes have demon-

strated that the accuracy of the solution does not deteriorate when the definition of the metrics is consistent and the metrics were computed with a high-order method.

In previous comparisons, the third-order accurate Runge-Kutta of Ref. [81] was used, even though higher-order or optimized Runge-Kutta methods can further reduce temporal errors. Furthermore, it was found that sufficiently accurate computations of aeroacoustic phenomena can be obtained when implicit time marching is performed with the BW implicit algorithm with $p = 2 - 3$ subiterations within each physical time step. The error of the solutions computed with the explicit RK-3 method and the modified implicit Beam-Warming algorithm with $n = 2$ is almost the same. The error of these computations is shown in Fig. 58.

The performance of WENO and centered schemes with characteristic-based filters is evaluated for flows with shocks. The oblique shock reflection problem at $M_\infty = 2.9$ is chosen as test case. The pressure at $y = 0.5$ computed with WENO schemes of fifth, seventh, and ninth-order accuracy is compared with the exact solution in Fig. 59. The computations were performed on a uniformly spaced 200×50 point grid in a domain $-2.0 \leq x \leq 2.0, 0 \leq y \leq 1.0$. At the left inflow boundary, free stream was specified. At the right outflow boundary, all quantities were extrapolated. On the solid wall at $y = 0$, slip boundary condition was specified, and at the top the flow quantities were specified as: $\rho = 1.69997, u = 2.61934, v = -0.506, p = 1.528$. Sufficient number of ghost points, depending on the order of the scheme, were used at the edges of the domain in order to retain the formal order of the scheme. For example, computations with the seven-point wide WENO5 scheme required three ghost points while

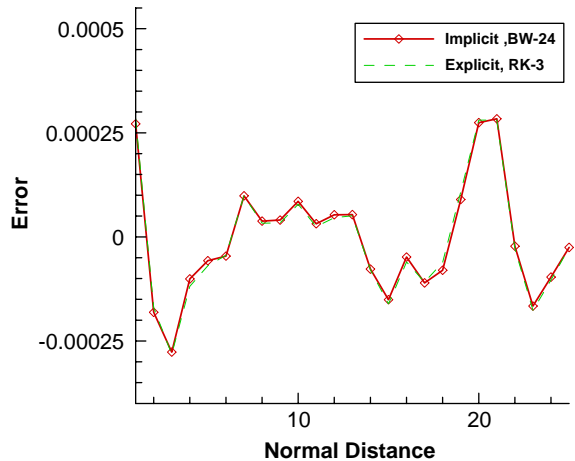


Fig. 58. Error of the solutions computed with implicit and explicit time integration.

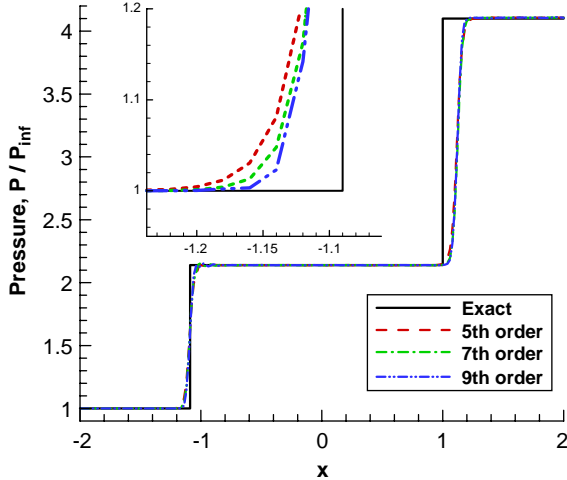


Fig. 59. Comparison of the computed pressure at $y = 0.5$ with the exact solution.

solutions with the sixth-order accurate ACM method require two ghost points.

At steady state, an oblique incident shock and a reflected shock were generated. The comparison of the computed pressure with the exact solution of Fig. 59 shows that as the order of the WENO scheme increases the computed solution approaches the exact solution. For all computations, the shocks were captured within two cells. The pressure field obtained from the numerical solutions with the fourth-order accurate compact centered scheme with $\kappa = 0.7$ and the fifth-order accurate WENO scheme on an artificially distorted mesh is shown in Fig. 60. Both solutions were computed with the explicit time marching scheme. It can be seen that both methods can capture the oblique strong shock without oscillations. Furthermore, the artificially distorted mesh does not cause oscillations.

The numerical solution for the same problem was also computed with the implicit BW time marching scheme. The convergence rates of the numerical solutions obtained for different number of subiterations is shown in Fig. 61. For reference, the convergence rate of the solution obtained with the explicit third order Runge–Kutta method of Ref. [81] is shown in the same figure. At convergence all solutions were the same and computed pressure and density obtained from implicit or explicit time marching were almost identical. A comparison of the computed pressure at $y = 0.5$ from the solution obtained with the fifth-order accurate WENO scheme and the solutions obtained with different values of the ACM parameter is shown in Fig. 62. It appears that the computed solution is sensitive to the selection of the ACM parameter. Furthermore, the choice of the upwind TVD limiter affects the solution.

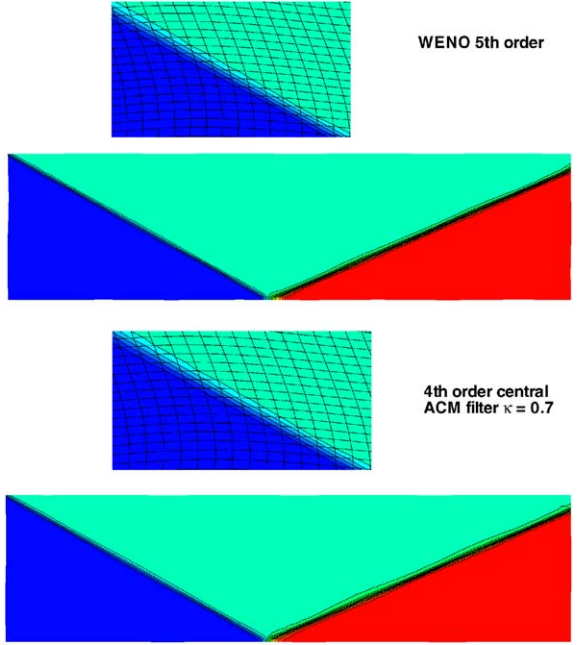


Fig. 60. Pressure field computed with WENO fifth-order and with the fourth-order centered scheme with characteristic-based filter (ACM parameter $\kappa = 0.7$) on an artificially distorted mesh.

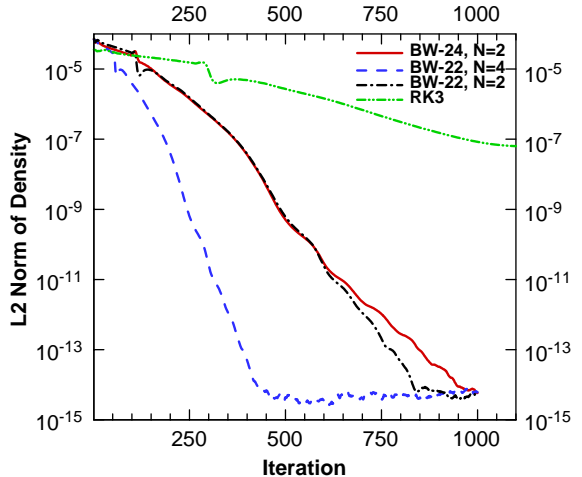


Fig. 61. Convergence rate of solutions computed with implicit time marching.

Computations of supersonic flows over a cylinder at various Mach numbers for Ref. [177] are shown next. These solutions were obtained using WENO schemes. An algebraically generated 181×51 point grid was used for this computation of supersonic flows over the cylinder. Similarly to the shock reflection case sufficient number of ghost points depending on the order of the

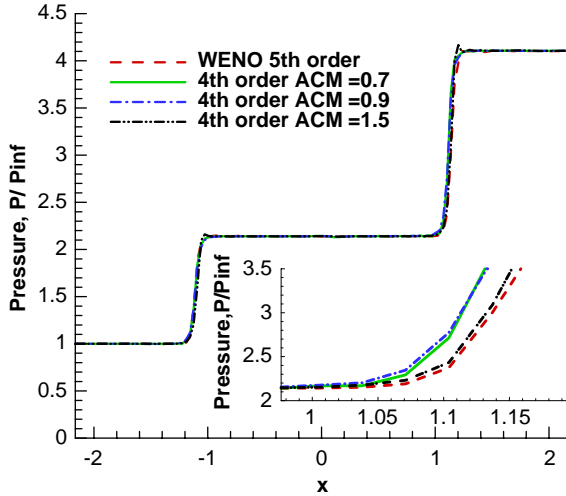


Fig. 62. Effect of ACM parameter on the computed pressure at $y = 0.5$.

scheme was used at the edges of the domain. At the inflow free stream supersonic flow was specified. At the outflow all quantities were extrapolated from the interior. On the cylinder solid surface the normal to the surface velocity component was set to zero and all the other quantities were extrapolated from the interior using high-order extrapolation and assuming that the normal derivative is zero.

The computed pressure and entropy fields at $M_\infty = 5.0$ are shown in Fig. 63. The resolution of the strong shock generated by the high-speed flow is captured without oscillations. Similar to the oblique shock computations of the previous section the shock for the supersonic cylinder flow (see Fig. 63) is captured within two cells. The convergence rate obtained at different Mach numbers, order of accuracy, and for baseline (91×51) and refined (181×101) grids is shown in Fig. 64. All computations were obtained at the same time step and the third-order TVD Runge–Kutta method of Ref. [81]. For all cases, the convergence was satisfactory and the solution practically remained unchanged when the residuals drop four orders of magnitude. A comparison of the computed pressure distributions for the grid line on the symmetry axis that passes through the stagnation point is shown in Fig. 65. It can be seen that the shock is captured within two computational cells and the solution is free from oscillations.

Inviscid flows solutions over a NACA-0015 airfoil were computed using the fifth-order accurate WENO scheme. The computed pressure fields at transonic and supersonic speed are shown in Figs. 66 and 67. The solutions were computed with the explicit time marching scheme on a 261×51 point, C-type grid. The airfoil grid

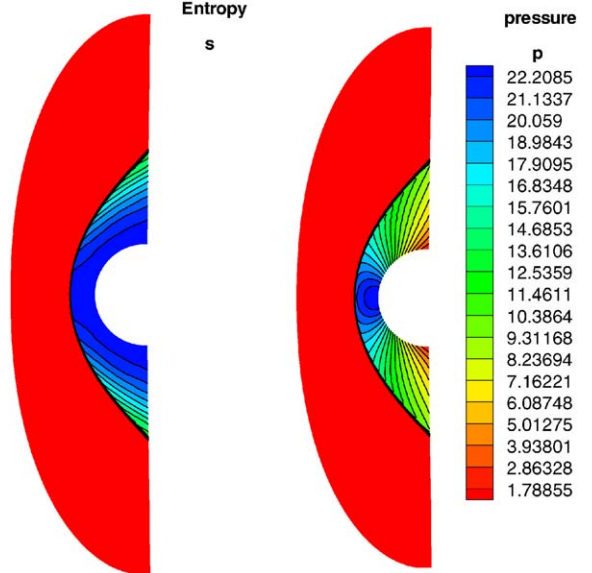


Fig. 63. Computed entropy and pressure fields with the ninth-order accurate WENO scheme at $M_\infty = 5.0$.

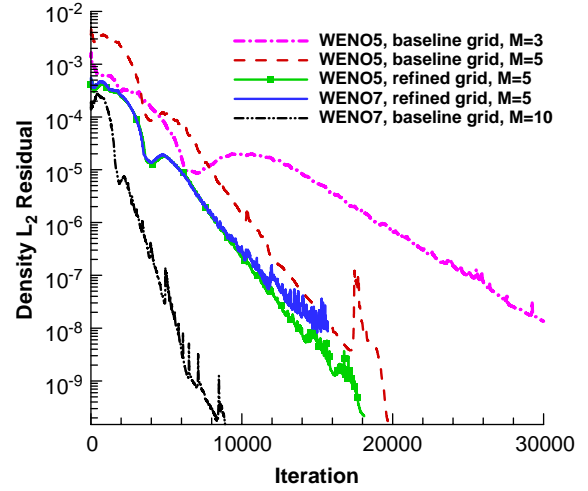


Fig. 64. Convergence history at $M_\infty = 3.0$, $M_\infty = 5.0$, and $M_\infty = 10.0$ with the baseline and refined grids.

included three ghost points at the edges of the domain in order to use the WENO5 scheme for the entire domain without dropping the stencil accuracy at the airfoil surface and the wake. The supersonic and transonic flow computations were obtained on the same grid. For both flow speeds, a smooth solution is obtained on the highly stretched, high aspect ratio C-type grid.

The computed pressure field at $M_\infty = 2.0$ is shown in Fig. 66. The computed pressure field shows adequate resolution of the leading edge bow shock and the two

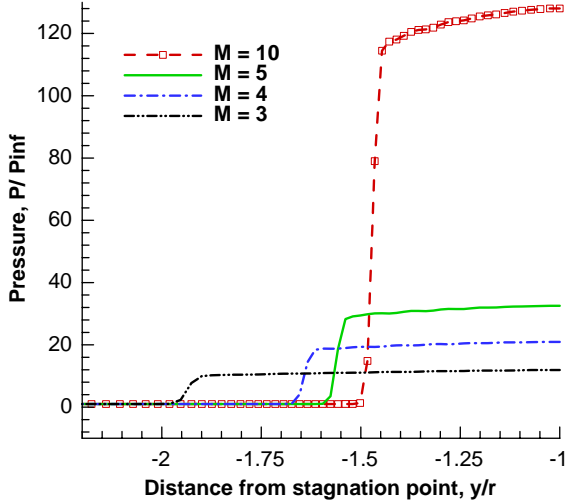


Fig. 65. Pressure at the symmetry line for $M = 3, 4, 5$, and $M = 10$.

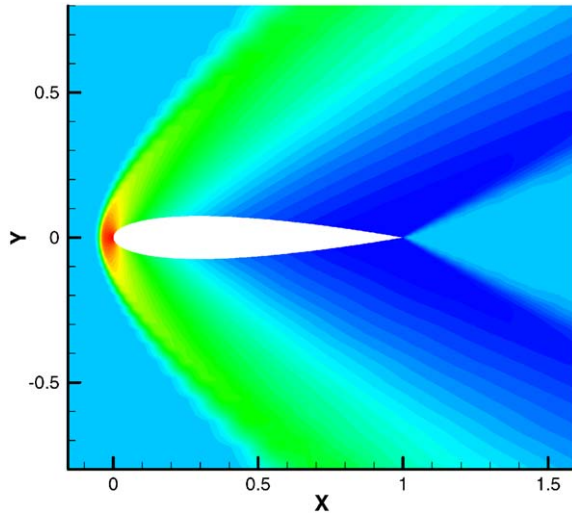


Fig. 66. Computed pressure field over a NACA-0015 airfoil at $M = 2.0$, $\alpha = 0.0^\circ$.

shocks at the trailing edge despite of the coarseness of the grid. The same type of inflow/outflow and solid wall boundary conditions as the supersonic cylinder flow was used. At the wake of the C-type grid averaging was used. For the transonic flow computation at $M_\infty = 0.8$, the shocks of the upper and lower surface shown by the pressure contours of Fig. 67 are well resolved. For this computation the inflow and outflow boundary conditions were specified using one-dimensional Riemann invariants. A comparison of the computed surface pressure coefficient for transonic flow over the NACA-0012 airfoil with the experimental data is shown in Fig. 68. The overall agreement of the computed inviscid

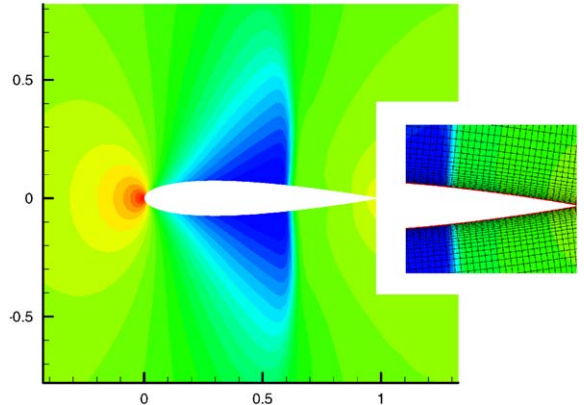


Fig. 67. Computed pressure field over a NACA-0015 airfoil at $M = 0.8$, $\alpha = 0.1^\circ$.

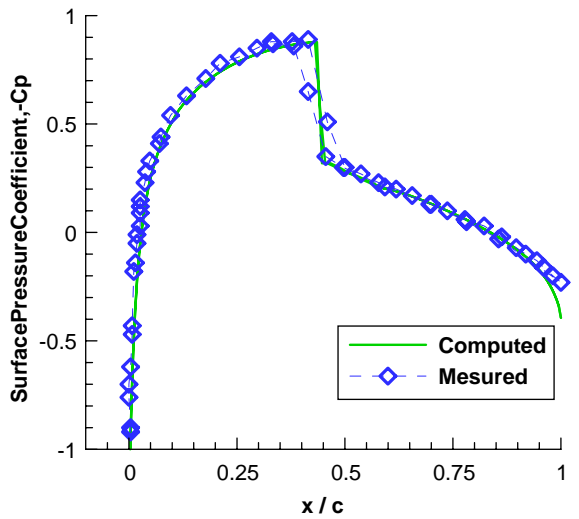


Fig. 68. Comparison of the computed pressure surface pressure coefficient for NACA-0012 airfoil at $M = 0.8$, $\alpha = 0.1^\circ$ with the experiment.

solution with the experiment is satisfactory and the shock is resolved within two cells.

Numerical solutions of two-dimensional viscous transonic flow over airfoils were obtained using a second-order accurate FV ENO or WENO scheme by Yang et al. [178]. The LU-SGS scheme of Section 4.3 was used for time integration to avoid stability limitations from the highly clustered viscous meshes. The computations of Yang et al. [178] showed sharp capturing of discontinuities (see Fig. 69) without oscillations. It was found (see Fig. 70) that after the residuals of the ENO2 scheme have decayed for three orders of magnitude the convergence leveled off. In contrast, as expected (see remarks in Section 4.4) a monotone convergence was achieved with the WENO2

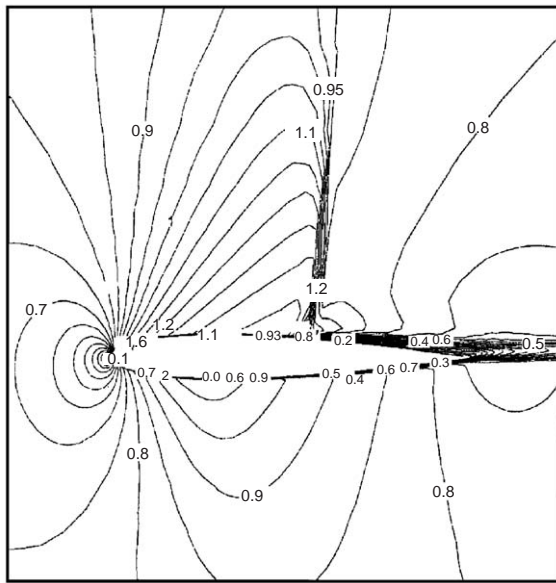


Fig. 69. Mach number contours for NACA 0012 airfoil at $M_{\infty} = 0.799$, $\alpha = 2.26^\circ$ and $R_{e_c} = 9 \times 10^6$; WENO2-Roe scheme.

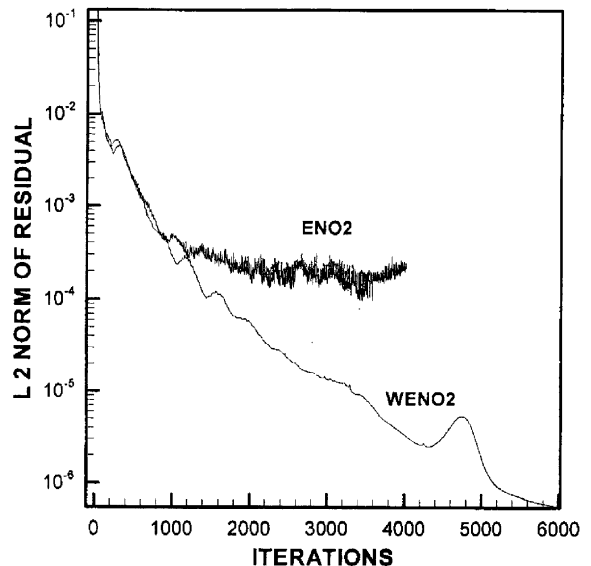


Fig. 70. Convergence history for NACA 0012 airfoil at $M_{\infty} = 0.799$, $\alpha = 2.26^\circ$ and $R_{e_c} = 6.5 \times 10^6$.

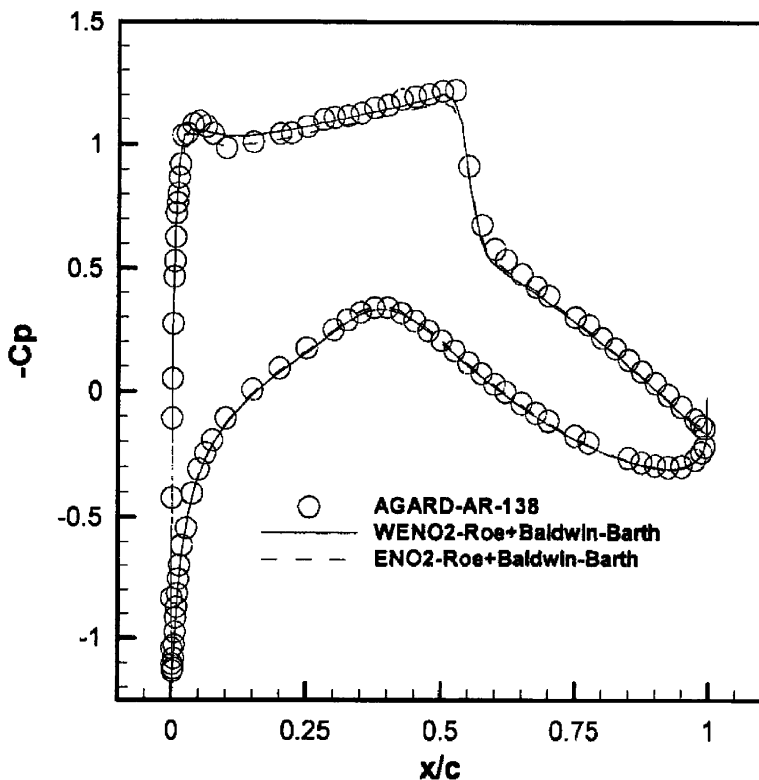


Fig. 71. RAE 2822 airfoil surface pressure distribution at $M_{\infty} = 0.731$, $\alpha = 2.51^\circ$ and $R_{e_c} = 6.5 \times 10^6$; comparison of WENO2 and ENO2 schemes.

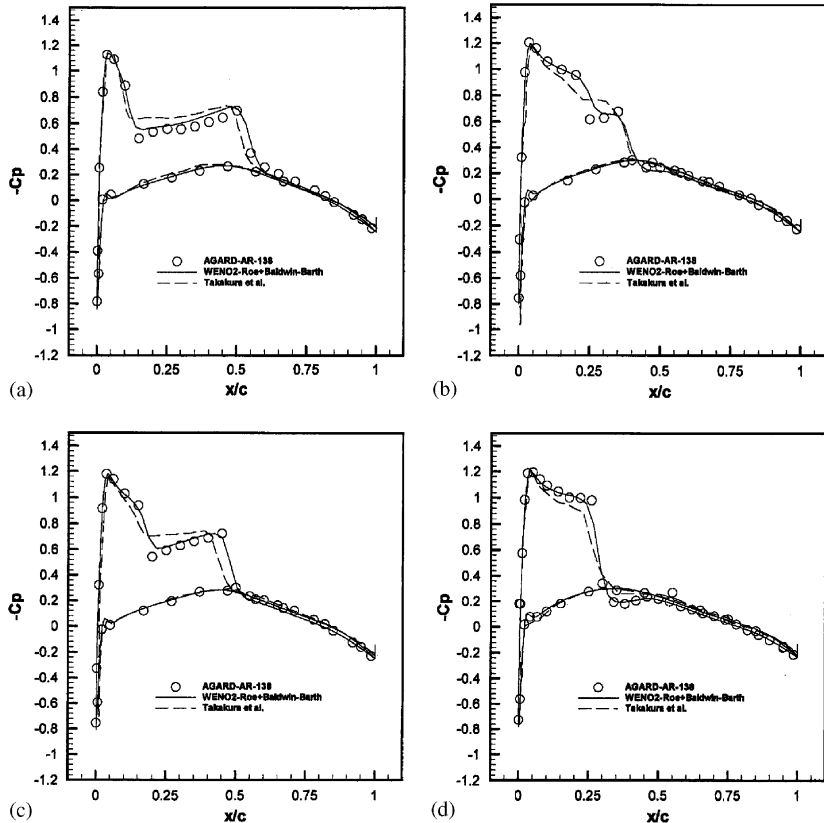


Fig. 72. Steady pressure distributions for ONERA M6 wing at $M_\infty = 0.8395$, $\alpha = 3.06^\circ$ and $R_{e_c} = 2.6 \times 10^6$.

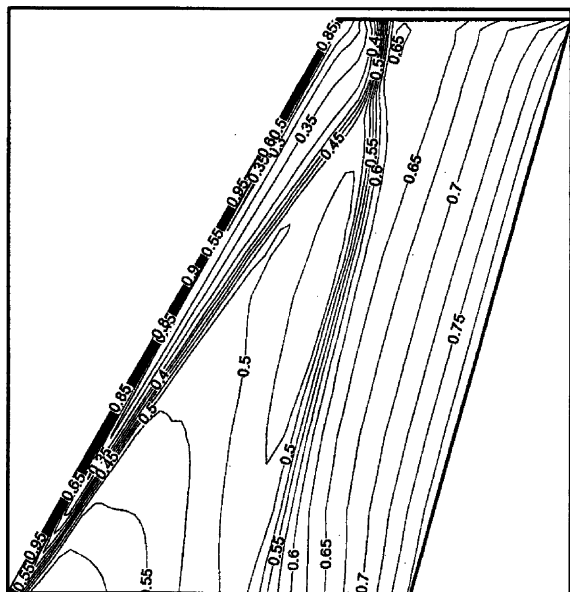


Fig. 73. Upper surface contours for ONERA M6 wing at $M_\infty = 0.8395$, $\alpha = 3.06^\circ$ and $R_{e_c} = 2.6 \times 10^6$.

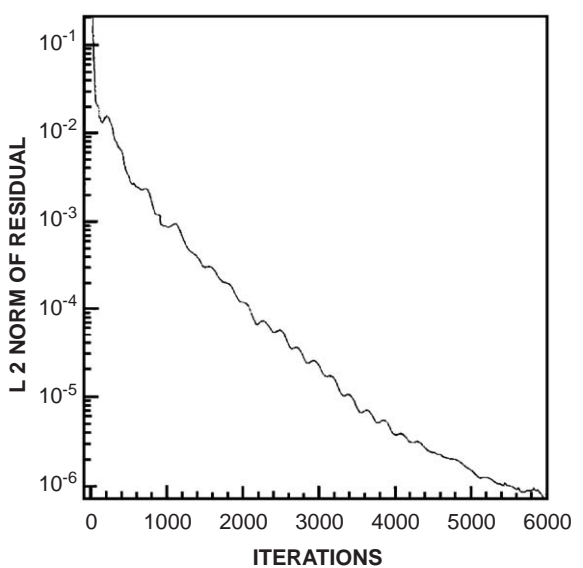


Fig. 74. Convergence history for ONERA M6 wing at $M_\infty = 0.8395$, $\alpha = 3.06^\circ$ and $R_{e_c} = 2.6 \times 10^6$.

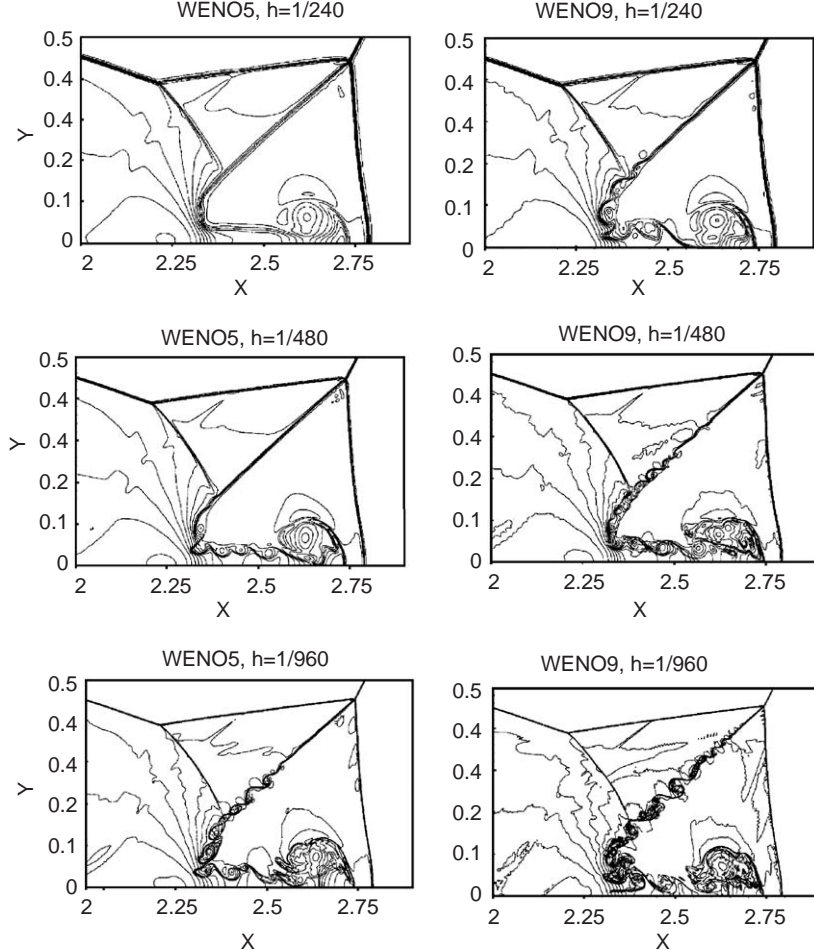


Fig. 75. Double Mach reflection problem. Blown-up region around the double Mach stems. Density ρ ; 30 equally spaced contour lines from $\rho = 1.5$ to $\rho = 22.9705$. Left from top to bottom: fifth-order WENO results with $h = \frac{1}{240}, \frac{1}{480}, \frac{1}{960}$; right from top to bottom: ninth-order WENO results with $h = \frac{1}{240}, \frac{1}{480}, \frac{1}{960}$.

scheme. The computed surface pressure distributions from the ENO and WENO algorithms (see Fig. 71) were almost indistinguishable. Very good agreement with the measured pressure coefficient distribution was found in [178] for three-dimensional flow over the ONERA M6 computed with the WENO2 scheme. Comparisons of the surface pressure distribution are shown in Fig. 72. The computed surface pressure distribution and the convergence rate are shown in Figs. 73 and 74, respectively.

The resolution and efficiency of high-order accurate WENO schemes for computing flows containing both discontinuities and complex flow features was recently demonstrated by Shi et al. [168]. The first representative numerical example was the double Mach reflection, a problem that includes strong shock waves and very complex flow features. This problem was initially proposed by Woodward and Colella [179] and

has been used extensively in the literature as a test for high-resolution schemes. A Mach 10, right moving shock at an angle of 60° is reflected from a wall (for more details see [179]). The flow is computed as inviscid and the results are displayed in Fig. 75 at $t = 0.2$ in the domain $[0, 3] \times [0, 1]$. Three different uniform meshes $h = \frac{1}{240}$, $h = \frac{1}{480}$, and $h = \frac{1}{960}$ were used in [168]. The computed solutions are compared in Fig. 75. It is clear that WENO9 with $h = \frac{1}{240}$ produces qualitatively the same resolution as WENO5 with $h = \frac{1}{480}$. The same is true for WENO5 with $h = \frac{1}{960}$ and WENO9 with $h = \frac{1}{480}$. It is evident that the resolution increases consistently with the order of accuracy and mesh refinement. Furthermore, the ability to obtain the same resolution with half the mesh by increasing the order of the method (compare WENO5 with $h = \frac{1}{960}$ and WENO9 with $h = \frac{1}{480}$) is clearly demonstrated.

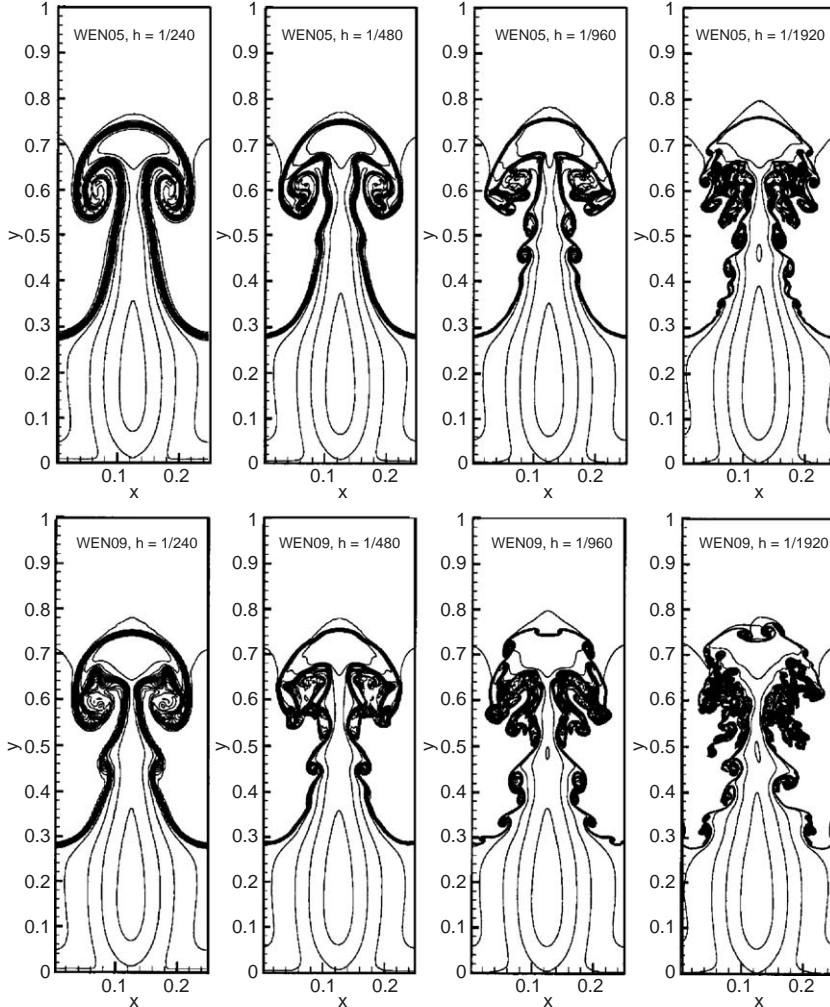


Fig. 76. Rayleigh–Taylor instability. Density ρ ; 15 equally spaced contour lines from $\rho = 0.952269$ to $\rho = 2.14589$. Top from left to right: fifth-order WENO results with $h = \frac{1}{240}, \frac{1}{480}, \frac{1}{960}, \frac{1}{1920}$; bottom left to right: ninth order WENO results with $h = \frac{1}{240}, \frac{1}{480}, \frac{1}{960}, \frac{1}{1920}$.

The second problem considered in [168] is the Rayleigh–Taylor (RT) instability. This instability happens on an interface between fluids with different densities due to the motion of the heavy fluid. The numerical solution of the RT problem demonstrates the ability of WENO schemes to consistently capture smooth, complex flow features with increased resolution either by grid refinement or the increase of the order of the method. Inviscid flow in a computational domain $[0, \frac{1}{4}] \times [0, 1]$ was computed in [168] with the heavy fluid with density $\rho = 2$ below, the interface at $y = \frac{1}{2}$, and the light fluid with $\rho = 1$ above the interface. The solutions of Fig. 76 were computed on uniform meshes with $h = \frac{1}{240}, \frac{1}{480}, \frac{1}{960}$, and $\frac{1}{1920}$. Again the WENO9 scheme yields the same resolution with the WENO5 scheme at double grid resolution. In both cases of Figs. 75 and 76,

the comparable resolution obtained with the WENO9 scheme using half the number of grid points in each direction than WENO5 implies significant saving in computing time since the WENO9 scheme needs only approximately 30% more CPU time than the WENO5 scheme.

The dynamics of shock–vortex interactions and the coupling of counter-rotating compressible vortices interacting with a planar shock wave were investigated by Grasso and Pirozzoli in [180–182]. The numerical solutions of the inviscid, compressible flow equations was obtained using a finite volume WENO scheme for Cartesian-type meshes. The simulations for the single vortex–shock wave interaction [180] initiated with a homoentropic Taylor vortex. Results from the simulations of [180] are shown in Figs. 77 and 78. Fig. 77 shows

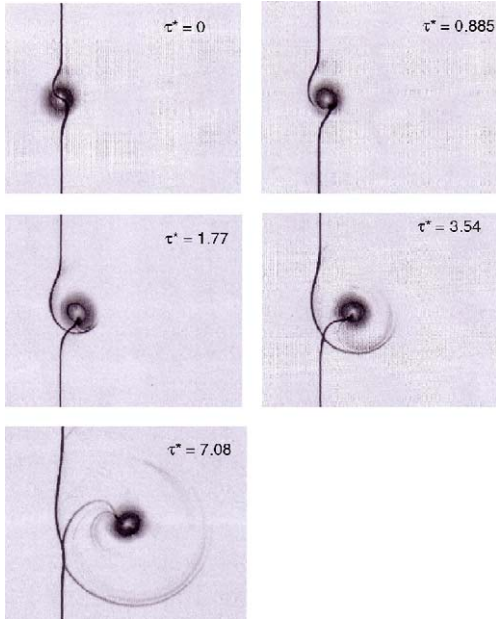


Fig. 77. Computed Schlieren for shock–vortex interaction.

the evolution of shock–vortex interaction with the computed Schlieren plot for a shock at $M_s = 1.2$ and vortex Mach number $M_v = 0.8$. Fig. 78 shows the computed pressure contour plots at the same times with Fig. 77.

The dynamics of the interaction of shock wave at $M_s = 5.0$ colliding with a counter-rotating vortex pair at $M_v = 0.26$ from [181] are shown in Fig. 79. The numerical Schlieren for shock wave–colliding vortex pair interaction at $M_v = 0.9$, $M_s = 1.2$ [182] is shown in Fig. 80. The acoustic pressure field computed in [182] at $M_v = 0.1$, $M_s = 1.2$ is shown in Fig. 81. It can be seen that in all cases the dynamics of the interaction and the flowfield structure is very complex. The computed solutions in [180,181] were found in very good agreement with measurement and analytic solutions from acoustic analogies. These results show that high-order WENO schemes are appropriate for the computation of noise. Further investigation of three-dimensional shock ring–vortex interaction was carried out by Pirozzoli [183] using the compact WENO scheme he developed in [173]. The computed complex interaction of the impact

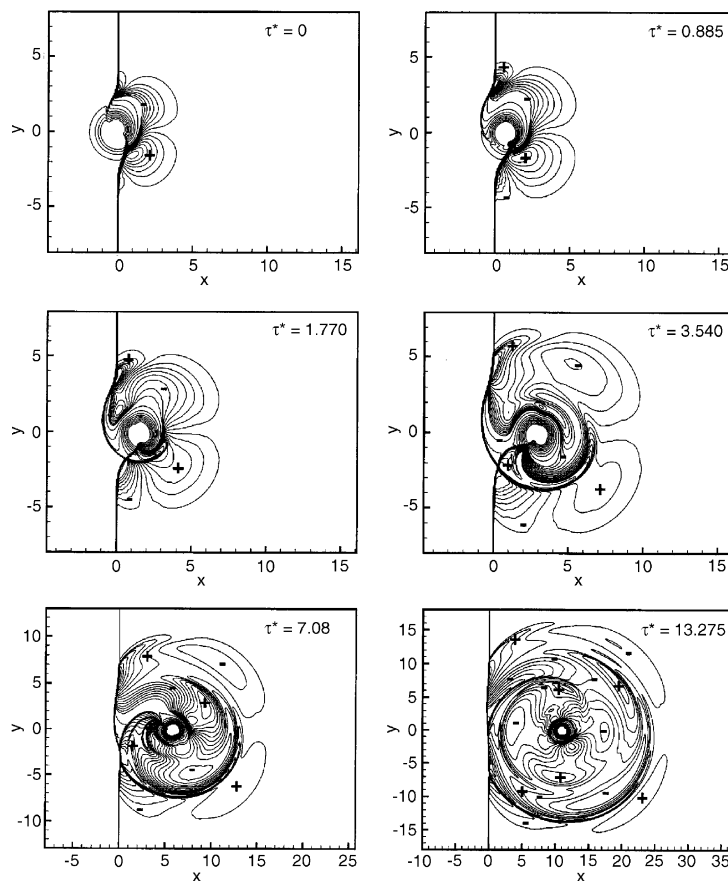


Fig. 78. Computed pressure field for shock–vortex interaction.

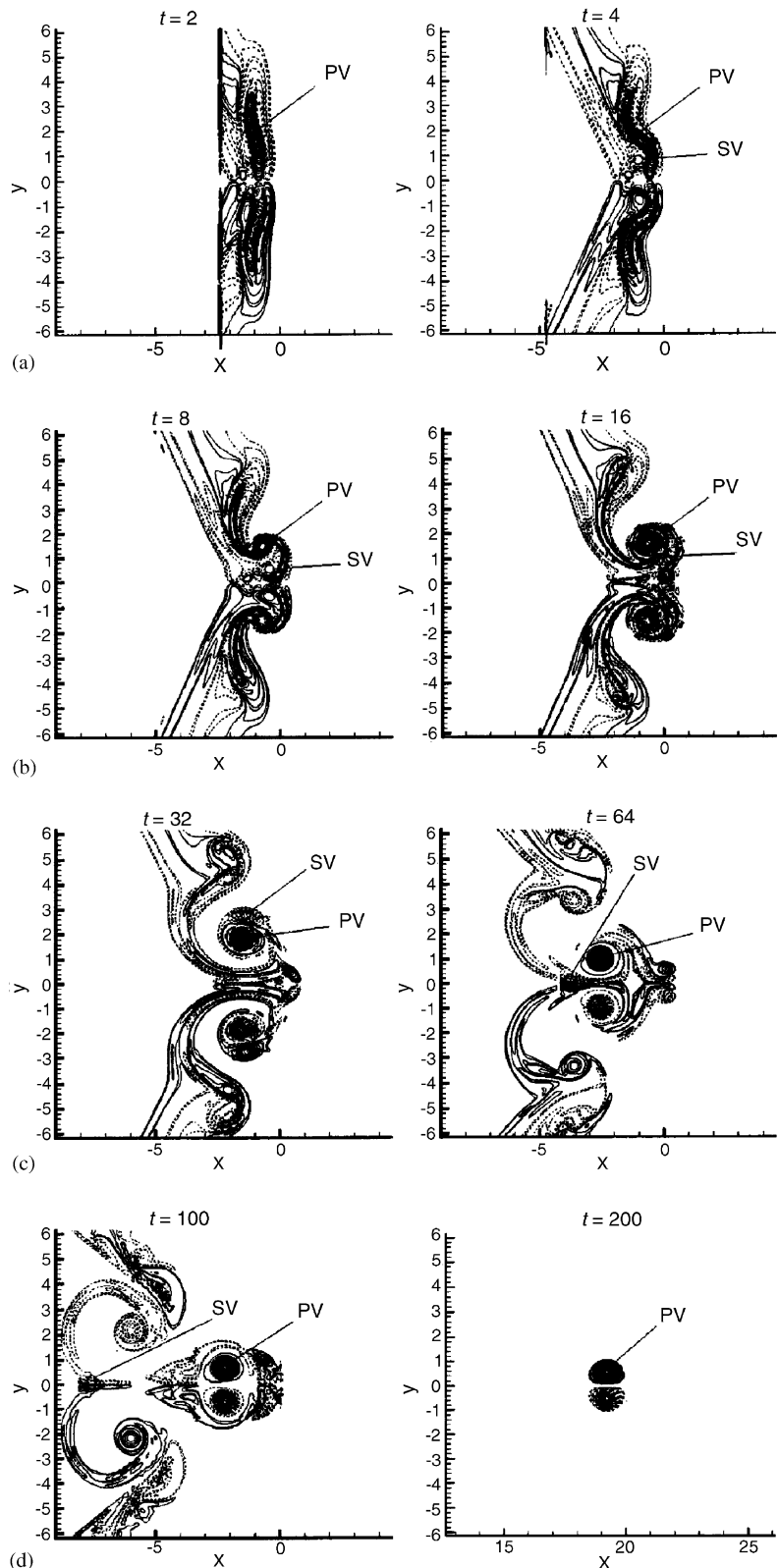


Fig. 79. Computed pressure field for shock counter-rotating vortex pair interaction.

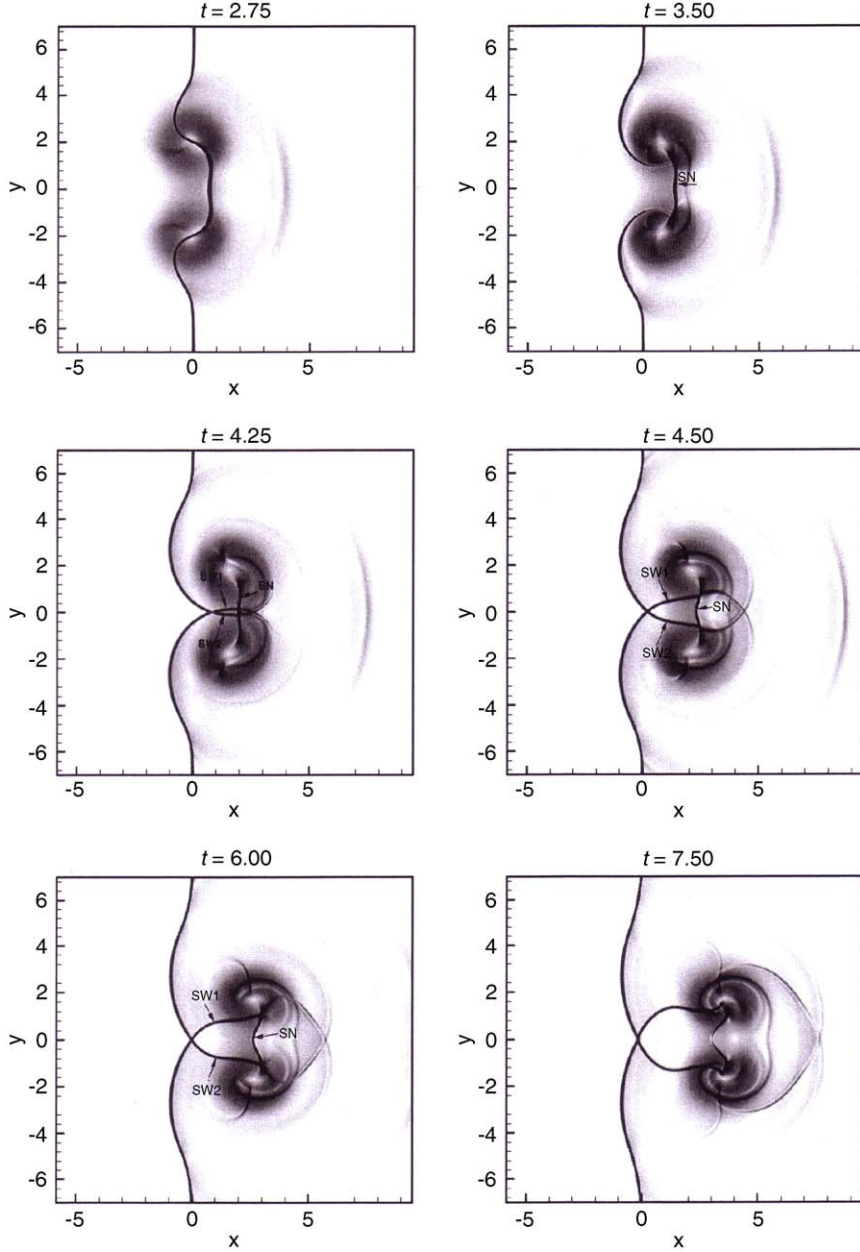


Fig. 80. Shock wave–colliding vortex pair interaction: numerical Schlieren at $M_v = 0.9$, $M_s^- = 1.2$, $d = 4r_v$ -Type-V interaction. SW, shock wave; SN, diffracted shock.

of a vortex ring $M_v = 0.25$ on a planar shock $M_s = 1.5$ is shown in Fig. 82.

Adams [184] used the hybrid compact-ENO finite-difference scheme of [175] to perform direct simulation of the flow over a compression ramp. The scheme used for this DNS is fifth-order accurate in smooth flow regions and around the discontinuities becomes the

fourth-order ENO scheme. The viscous terms in [175] are discretized with the sixth-order accurate compact finite-difference scheme of Lele [100]. Time marching of the DNS in [184] is performed with a RK3 method. Computed Schlieren from the DNS in Fig. 83 are in good agreement with similar measurement shown for comparison in Fig. 84. The computed density field is

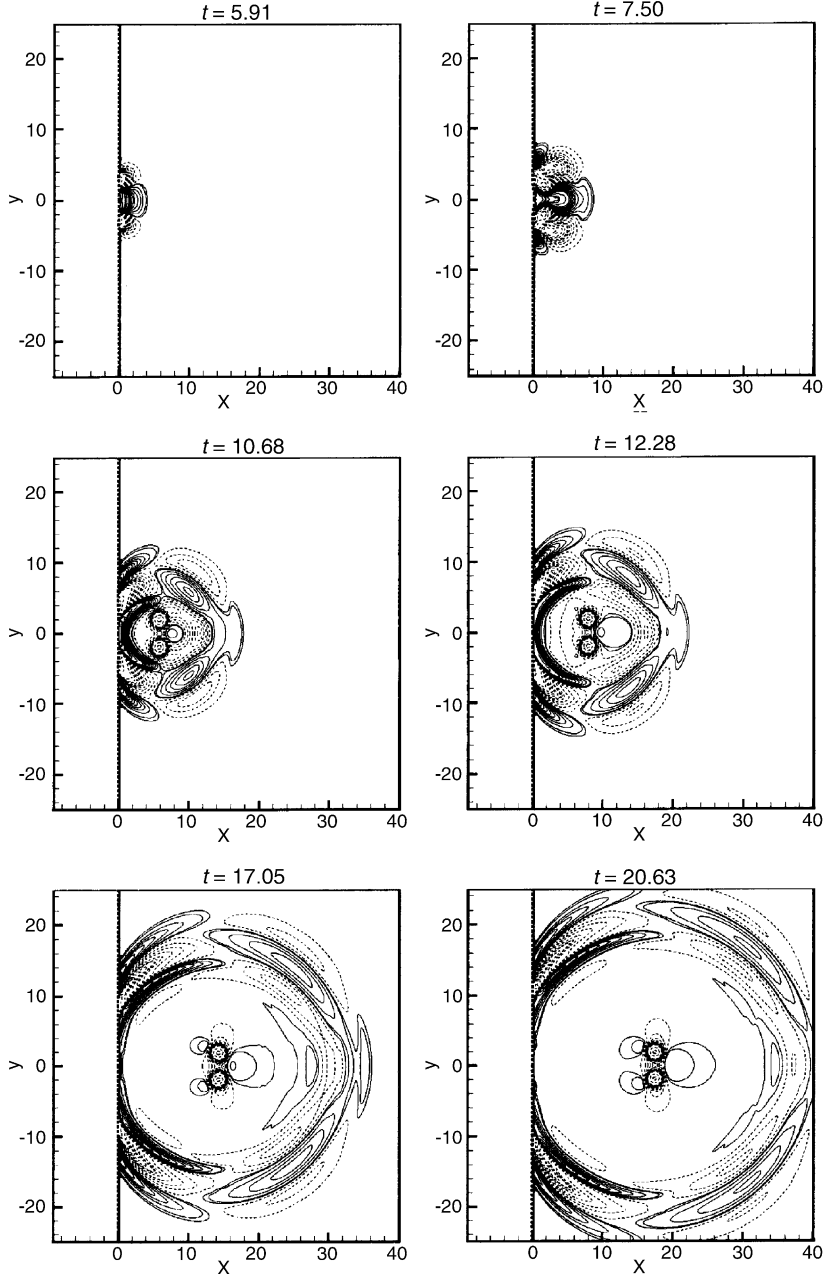


Fig. 81. Shock wave–colliding vortex pair interaction: acoustic pressure field at $M_v = 0.1$, $M_s^- = 1.2$, $d = 4r_v$ -Type-I interaction. $-0.1 \leq p' \leq 0.5$, 72 contour levels. Dashed lines stand for $p' \leq 0$, while solid lines stand for $p' \geq 0$.

shown in Fig. 85. The sequence of shock evolution obtained from the DNS of [175] is shown in Fig. 86. The good agreement of the DNS of [184] with the experiments demonstrates that high-order accurate ENO discretization yields the necessary resolution and keeps

the numerical diffusion at a low level. These are key ingredients required for accurate capturing of turbulent fluctuations in compressible turbulence DNS and LES. Additional computations with ENO and WENO schemes can be found in [185–190].

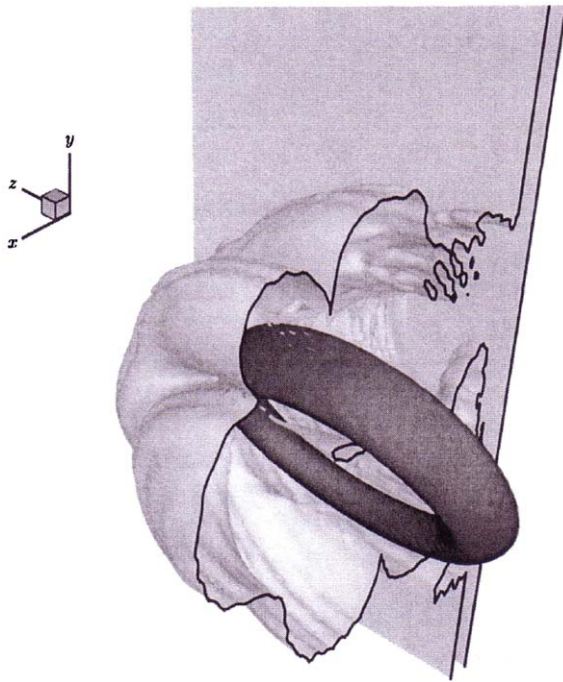


Fig. 82. Impact of a vortex on a planar shock wave for $M_s = 1.5$, $M_v = 0.25$, $\phi_0 = 3\pi/4$ at $t = 8$. The gray shading represents the 0.01 isosurface of λ_2 ; the lighter shading represents the -0.1 isosurface of $\nabla \cdot \mathbf{u}$, which has been cut at the intersection with the symmetry plane.

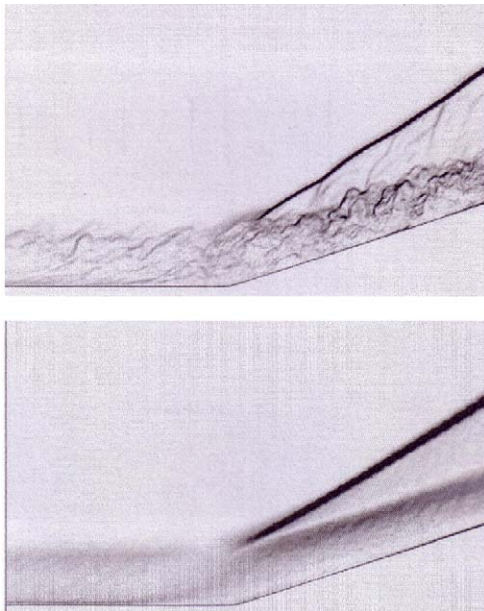


Fig. 83. Flow-field Schlieren imitation, $\|\nabla \rho\|$ contours, (a) instantaneous x_2 -average, (b) x_2 -average and time average using 100 samples.

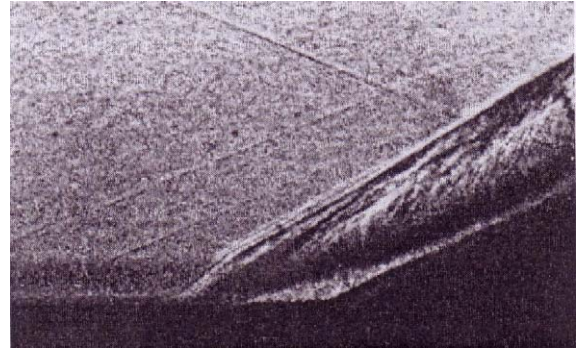


Fig. 84. Flow-field experimental Schlieren visualization of a 25° compression ramp at $M_\infty = 2.9$, $Re_\theta = 9600$, provided by A. Zheltovodov, ITAM, Novosibirsk.

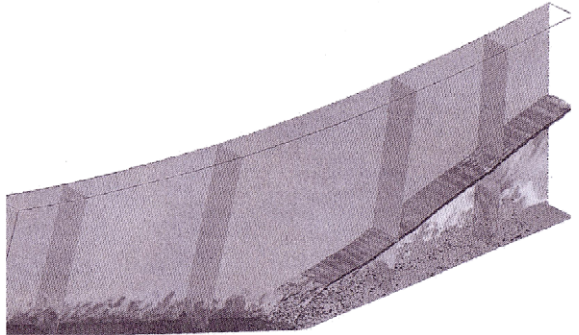


Fig. 85. Density at the wall, in the plane $x_2 = 2.9$ and 4 cross-flow planes; shock-surface with $\partial_{x_i} u_i = -0.4$.

5. The discontinuous Galerkin (DG) method

Generation of three-dimensional meshes even in domains with moderate complexity, such as a wing body junction for example, is not trivial. On the other hand, the performance of most high-resolution accurate methods depends on the smoothness of the grid. The difficulty in generating smooth-structured grids for complex geometries has promoted the development of finite-volume algorithms for unstructured grids [191–195]. However, most of these unstructured grid methods are second-order accurate. High-order finite-volume schemes were pioneered by Barth and Frederickson [131] with the k -exact finite-volume scheme that can be used for arbitrary high-order reconstruction in triangular or tetrahedral meshes. The implementation of ENO for unstructured grids was developed by Abgrall [164], while WENO schemes for triangular meshes were developed by Friedrich [166] and Hu and Shu [196]. Theoretically, the k -exact approach [131,196], or other approaches [164] can be used to obtain arbitrarily high-order accurate finite-volume schemes with high-order polynomial data reconstructions. However, in practice

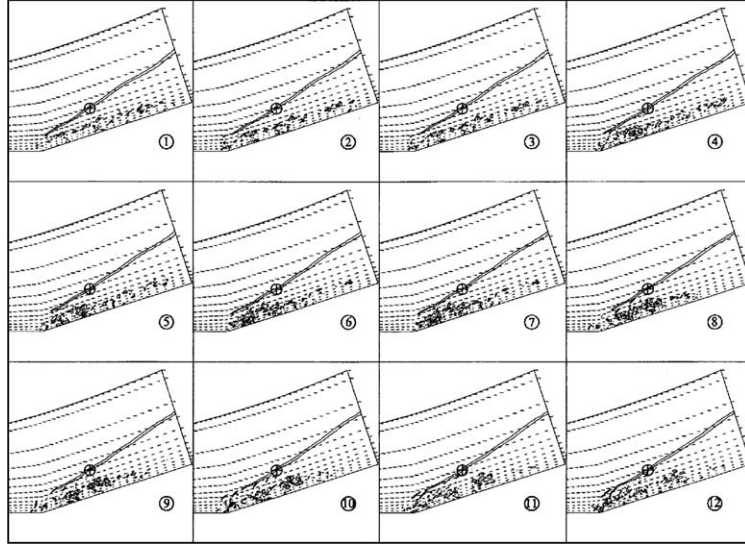


Fig. 86. Sequence of shock evolution (iso-contours) of $\|\nabla\rho\|$ and velocity vectors at $x_2 = 0.72$ for a sequence of equal time steps between $t_l = 309.00$ and $t_r = 325.34$; sequence from bottom to top and left to right (numbers 1–12); the marker indicates the sensor position for Fig. 14; flow direction is from bottom up.

higher than linear reconstructions are not used in three dimensions because of the difficulty to construct non-singular stencils and the large memory required to store the reconstruction coefficients. It was shown by Delanaye and Liu [197] that for the third-order (quadratic reconstruction) FV scheme in three dimensions, the average size of the reconstruction stencils is about 50–70. The size of reconstruction stencils increases nonlinearly with the order of accuracy and it was estimated that for the fourth-order FV scheme the stencil size would be approximately 120.

The high-order accurate conservative scheme called the discontinuous Galerkin (DG) method developed by Cockburn et al. in a series of papers [198–201] shows promise for high-resolution simulations in fully unstructured meshes. The DG method assumes a high-order expansion for the distribution of the state variables for each element and solves for the coefficients of the expansion polynomials. The resulting state variables are usually not continuous across the element boundaries. Therefore, the fluxes through the element boundaries are computed using an approximate Riemann solver and the residual is minimized with a Galerkin approach. It is the use of Riemann fluxes across element boundaries that makes the DG method fully conservative.

5.1. DG space discretization

The DG method is briefly described in this section. Further information and more details can be found in the original references [200,205,206] and the reviews of

[45,201]. For each time $t \in [0, T]$ the approximate solution, u_h , of hyperbolic equations in conservation law form, $\partial_t \mathbf{u} + \operatorname{div} \mathbf{F}(\mathbf{u}) = 0$, is sought in the following finite-element space of discontinuous functions V_h

$$V_h = \{\phi_h \in \mathbf{L}^\infty(\Omega) : \phi_h|_{\mathbf{K}} \in \mathbf{V}(\mathbf{K}) \ \forall \mathbf{K} \in T_h\}, \quad (5.1)$$

where T_h is a discretization of the domain Ω using triangular or quadrilateral elements and $\mathbf{V}(K)$ is the local space that contains the collection of polynomials up to degree k .

The development of the DG method starts from weak formulation of hyperbolic-type governing equations

$$\begin{aligned} & \frac{d}{dt} \int_K u(x, t) \phi(x) dx \\ &= \int_K \mathbf{F}(u(x, t)) \cdot \nabla(\phi(x)) dx \\ & - \sum_{e \in \partial K} \oint_e \mathbf{F}(u(x, t)) \cdot \mathbf{n}_{e,K} \phi(x) d\Gamma, \end{aligned} \quad (5.2)$$

where $\phi(x)$ is any sufficiently smooth function and $\mathbf{n}_{e,K}$ denotes the outward, unit normal to the face or edge e .

The stiffness matrix integral at the left-hand side of Eq. (5.2) is evaluated numerically using Gauss–Radau integration rules. The integrals on the right-hand side of Eq. (5.2) are evaluated using quadrature rules as follows:

$$\begin{aligned} & \int_e \mathbf{F}(u(x, t)) \cdot \mathbf{n}_{e,K} \phi(x) d\Gamma \\ & \approx \sum_{l=1}^L \psi_l \mathbf{F}(u(x_{el}, t)) \cdot \mathbf{n}_{e,K} \phi(x_{el}) |e|, \end{aligned} \quad (5.3)$$

$$\begin{aligned} & \int_K F(u(x, t)) \cdot \nabla(\phi(x)) dx \\ & \approx \sum_{j=1}^J \omega_j F(u(x_{Kj}, t)) \cdot \nabla(\phi(x_{Kj})) |K|. \end{aligned} \quad (5.4)$$

The line integrals of Eq. (5.3) are computed using appropriate high-order Gaussian quadrature. For example, for a third-order polynomial basis a quadrature rule that integrates exactly at least sixth-order polynomial is used. In general, a k th order DG method ($k - 1$ order polynomial reconstruction) requires a $2k$ th order quadrature formula for the surface (line) integrals of Eq. (5.3), and a $(2k - 1)$ th order quadrature formula for the volume integrals of Eq. (5.4).

The data are assumed discontinuous across the interfaces of the continuous domain and at each interface two values are available. Therefore, the flux $F(u(x, t))$ is replaced by a suitable numerical flux $\tilde{F}_{e,K}(x, t)$ for the approximate solution u_h and the test function $\phi_h \in V(K)$. Using $\tilde{F}_{e,K}(x, t)$ in Eqs. (5.3) and (5.4) the approximate solution u_h is given by

$$\begin{aligned} & \frac{d}{dt} \int_K u_h(x, t) \phi_h(x) dx \\ & = \sum_{j=1}^J \omega_j F(u_h(x_{Kj}, t)) \cdot \nabla(\phi_h(x_{Kj})) |K| \\ & \quad - \sum_{e \in \partial K} \sum_{l=1}^L \psi_l \tilde{F}_{e,K}(u(x_{el}, t)) \cdot \mathbf{n}_{e,K} \phi(x_{el}) |e|, \\ & \forall \phi_h \in V(K) \quad \forall K \in T_h, \end{aligned} \quad (5.5)$$

where time advancement of Eq. (5.5) is performed with the third-order accurate TVD Runge–Kutta method of [81].

The major difference of the GD formulation with a standard modal or node-based Galerkin finite-element method is that the expansion in each element is local without any continuity across the element boundaries. The value of the numerical flux $\tilde{F}_{e,K}(x, t)$ at the edge of the boundary of the element K depends on two values of the approximate solution, one from the interior (right) of the element K , $u^R = u_h(x^{int(K)}, t)$, and the other from the exterior (left) of the element K , $u^L = u_h(x^{ext(K)}, t)$. Any consistent, conservative exact or approximate Riemann solver can be used to obtain the numerical flux $\tilde{F}_{e,K}(u(x^{int(K)}, t), u(x^{ext(K)}, t))$ or $\tilde{F}_{e,K}(u^L, u^R)$ as follows

$$\begin{aligned} \tilde{F}_{e,K}(u^L, u^R) = & \frac{1}{2}[F(u^L) \cdot \mathbf{n}_{e,K} + F(u^R) \cdot \mathbf{n}_{e,K} \\ & - F^*(u^L, u^R)], \end{aligned} \quad (5.6)$$

where $F^*(u^L, u^R)$ is the dissipative part of the numerical flux. The computationally efficient local Lax–Friedrichs flux is used in many applications. The flux F is split as $F = F^+ + F^-$ where $F^\pm = F + \alpha u$ where $\alpha = \lambda$ and λ is the maximum eigenvalue of the flux Jacobian. For the

linearized Euler equations the eigenvalues are constant and the derivatives are continuous for the nonlinear case, however, in order to obtain continuous higher derivatives $\alpha = \sqrt{\varepsilon^2 + \lambda^2}$ with $\varepsilon = 0.05$. The DG method can be applied for discretizations on all triangular, quadrilateral or mixed-type of elements. Expansion bases of different order for triangular and quadrilateral elements are shown next.

Large portion of computing resources during the implementation of the DG method is devoted for the evaluation of integrals, such as the mass and stiffness matrices using quadrature rules. For linear systems of hyperbolic equations, such as the linearized Euler equations, the computing cost of the DG method can be significantly reduced using the quadrature-free DG method. Then time integration of the semi-discrete DG formulation with RK3 or RK4 yields the quadrature-free Runge–Kutta DG approach of Atkins and Shu [208].

5.2. Element bases

For the general nonlinear case, the order of accuracy of the DG method (see Ref. [45] and references therein) is at least $k + 1/2$ if polynomials of degree at most k are used as basis functions. Furthermore, it was shown (see Ref. [45]) that for linear problems that for canonical semi-uniform triangular grids the order of accuracy is $(k + 1)$. For simplicity in the rest of this section, the method is called $(k + 1)$ th order accurate if the basis functions are polynomials of degree at most k .

The approximate solution within each element is expanded in a series of local bases functions (polynomials) as follows

$$u_h(x, y, t) = \sum_{j=1}^d c_j(t) P_j^k(x, y), \quad (5.7)$$

where $c_j(t)$, $j = 1, 2, \dots, d$ are expansion coefficients or degrees of freedom for each element, to be evolved in time, and $P_j^k(x, y)$ are polynomial bases of degree k the most. In two dimensions, the range of d , or number of polynomials in Eq. (5.7) (also the number of nodes on a triangle for nodal expansions) is related to the degree of the polynomial by $d = (k + 1)(k + 2)/2$. For example, cubic reconstruction $k = 3$ requires $d = 10$ e.g. 10 nodes (see Fig. 87).

The value of d for bases in two and three dimensions (triangles or tetrahedra) is given by

$$d = \binom{n+k}{k} = \frac{(n+k)!}{n!k!}, \quad (5.8)$$

where k is the order of the polynomial P_j^k and $j = 1, \dots, d$. It can be seen that in three dimensions the third-order basis includes 20 polynomials and the fifth-order basis 56 polynomials. It appears therefore, that for

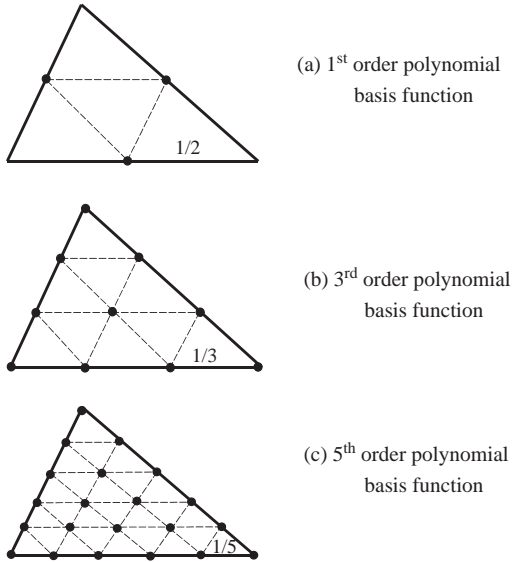


Fig. 87. Nodal points for polynomial bases P^1 , P^3 , and P^5 bases on triangular meshes.

realistic, three-dimensional problems, it could be very intensive computationally to achieve accuracy higher than fourth order.

In two dimensions, a first-order basis ($d = 3$), $P_1^1 = 1 - 2y$, $P_2^1 = 2x + 2y - 1$, $P_3^1 = 1 - 2x$, can be used to achieve second-order accuracy. Each of these polynomials (see Fig. 88) takes unit value at one node, located in the middle of an edge, and zero value at the other nodes located at the middle of the other edges. The first-order polynomials P_1^1 , P_2^1 , P_3^1 are orthogonal ($\int_{el} P_i^1 P_j^1 = 0, i \neq j$) and the mass matrix resulting from the integration at the left-hand side of Eq. (5.2) is diagonal. For the first as well as the higher-order bases all calculations of Eq. (5.5), except the numerical flux evaluation, are carried out on the reference element. The numerical flux computation along the edges of the element, which depends on the neighboring element, can be carried out at the physical space.

Third- and higher-order polynomial nodal bases in two dimensions can be systematically generated with Lagrange interpolation in triangular coordinates $x, y, t = 1 - x - y$. More details on polynomial bases can be found in [40,42,43]. The general form of Lagrange interpolation in triangular coordinates is given by

$$P_L(x, y, t) = L_i(x)L_j(y)L_k(t), \quad (5.9)$$

where $L_m(x)$ are one-dimensional $(m - 1)$ order Lagrange polynomials [43] and $L = L(i, j, k)$ (see Fig. 89) denotes the nodal index. For example, in Fig. 89 at the nodal index $L(2, 3, 3)$ the base polynomial

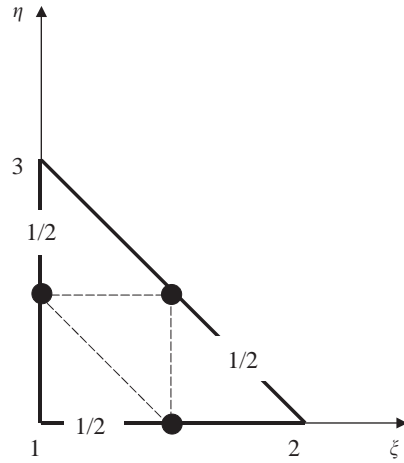


Fig. 88. Reference element for first-order polynomial basis.

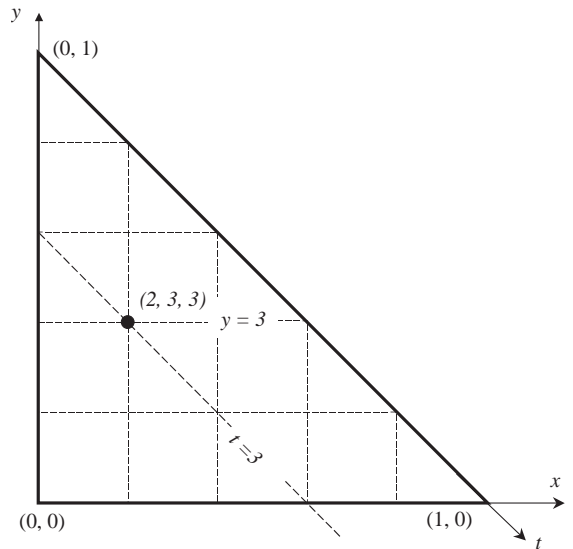


Fig. 89. Reference element and nodal points for fifth-order polynomial basis.

is defined as

$$P_{(2,3,3)}(x, y, t) = 5x \frac{y(y-1/5)}{(\frac{2}{25})} \frac{t(t-1/5)}{(\frac{2}{25})}. \quad (5.10)$$

The fifth-order polynomial basis is also non-orthogonal and the mass matrix is computed using Gauss Radau integration. Note that the P_j^1 and P_j^3 bases can be constructed using the procedure followed for the construction of the P_j^5 basis. The bases based on Lagrange interpolation for triangular elements have good condition number [43]. In addition, they offer

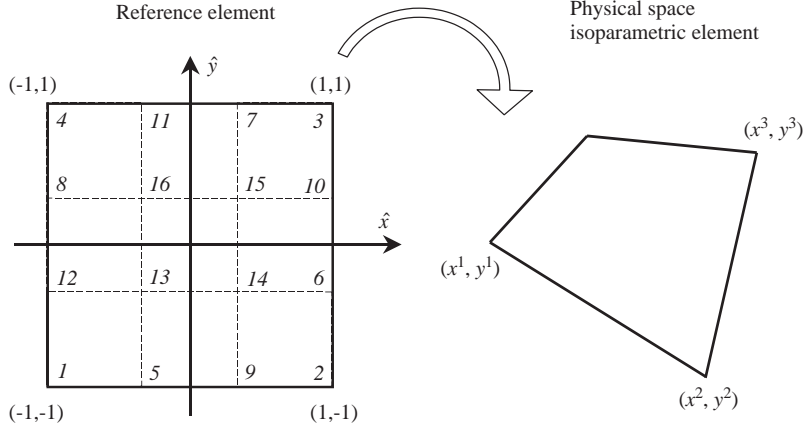


Fig. 90. Reference element with nodal points for third-order polynomial basis and isoparametric mapping for the arbitrary shape quadrilateral element in physical space.

implementation advantages compared to hierarchical bases, which are more appropriate for multigrid [207], because for these bases the nodal values are known.

Space discretization can be in addition be obtained using quadrilateral isoparametric elements of arbitrary shape (see Fig. 90). The reference element is a square (see Fig. 90) with vertices at the points $(-1, -1)$, $(1, -1)$, $(1, 1)$, $(-1, 1)$. In Fig. 90, the physical space arbitrary shape quadrilateral and the nodal points of the third-order accurate polynomial basis on the reference element are also shown. The coordinates x_j^k , $j = 1, 2, k = 1, 2, 3, 4$ ($x_1^k = x^k, x_2^k = y^k$) of the arbitrary shape quadrilateral elements in the physical space are related to the square reference element coordinates \hat{x}_j ($\hat{x}_1 = \hat{x}, \hat{x}_2 = \hat{y}$) through the map

$$x_j = \sum_{k=1}^4 \hat{f}_k(\hat{x}_1, \hat{x}_2) x_j^k, \quad (5.11)$$

where $\hat{f}_k(\hat{x}_1, \hat{x}_2)$ are first-order Lagrange polynomials $\hat{f}_k(\hat{x}_1, \hat{x}_2) = (1 + \hat{x}_1^k \hat{x}_2)(1 + \hat{x}_2^k \hat{x}_1)/4$. The basis polynomials $P_i^k(x, y) \in Q^k$ for finite-element discretization with quadrilateral elements are tensor products of appropriate order one-dimensional Lagrange polynomials. For example, the basis with third-order accurate polynomials is $P_i^3(x, y) = L_j(x)L_k(y)$, $i = 1, \dots, 16$, $j, k = 1, 2, 3, 4$.

5.3. Arbitrary high-order DG schemes

The ADER (Arbitrary high-order scheme which utilizes the hyperbolic Riemann problem for the advection, of the higher-order DERivatives) can be applied for DG numerical solutions of linear hyperbolic systems to obtain a quadrature-free, explicit single-step method of arbitrary order of accuracy in both space and time.

Note that for the nonlinear case, the ADER-DG scheme requires Gaussian quadratures of suitable order of accuracy. The ADER approach of Titarev and Toro [209] is based on the solution of the generalized Riemann problems (GRPs) at the cell boundaries and application of the Lax-Wendroff procedure for highly accurate time integration of the numerical flux.

It was shown numerically by Dumbser and Munz that the ADER-DG scheme is $3N + 3$ order accurate for N th order basis functions.

The main ingredients of the ADER-DG-Discretization are:

- Taylor expansion in time of the solution.
- Use of the Lax-Wendroff procedure to replace time derivatives by space derivatives.
- Solution of generalized Riemann problems (GRP) to approximate space derivatives.

5.4. Analysis of the DG method for wave propagation

Hu et al. [210] carried out a study of wave propagation properties of the semi-discrete DG method for conservation laws with linear flux given by $\mathbf{F}_{\text{num}}(\mathbf{u}_1, \mathbf{u}_2, \mathbf{n}) = \tilde{A}_{\text{av}}^+ \mathbf{u}_1 + \tilde{A}_{\text{av}}^- \mathbf{u}_2$, where $\tilde{A} = \sum_{k=1}^d A_k n_k$, the averages are defined as $\tilde{A}_{\text{av}}^+ = \frac{\tilde{A} + \alpha |\tilde{A}|}{2}$, $\tilde{A}_{\text{av}}^- = \frac{\tilde{A} - \alpha |\tilde{A}|}{2}$, and $\alpha = 0$ yields a centered flux while $\alpha = 1$ yields the Roe flux. Considering the approximate solution \mathbf{u}_h is written as an expansion of the local basis set $\mathbf{u}_h(\mathbf{x}, t) = \sum_{l=0}^{N-1} \mathbf{c}_l(t) v_l(\mathbf{x})$ it was shown in [210] that for the one-dimensional scalar advection equation $u_t + cu_x = 0$, with exact dispersion relation $\omega = \alpha k$, the numerical dispersion relation for an upwind numerical flux ($\alpha = 1$) with the DG discretization is determined by

$$\det(-i\Omega \mathbf{Q} + 2e^{-ik} \mathbf{N}_1 + 2\mathbf{N}_0) = 0. \quad (5.12)$$

The solution of the numerical dispersion relation yields complex values for the numerical propagation frequency, $\Omega = \Omega_r + i\Omega_i$. In the numerical propagation frequency, the imaginary part is negative and represents the numerical damping inherent in the DG discretization process.

The solution of the numerical dispersion relation, Eq. (5.12) for a third-order DG method involves three modes, one physical mode and two parasitic modes. It was found that the numerical dispersion relation deviates from the exact one beyond $K \approx N$, where N is the order of the scheme.

Important conclusions of the analysis of Hu et al. [210] are:

- Increase of the order of the scheme significantly reduces the dissipation error.
- The sixth-order scheme is optimal for scalar advection in the sense that it is the minimal order for which the dispersion and dissipation errors are less than 0.5% for wavenumber K up to approximately N .
- The dissipation error imposes a relatively more stringent condition on the accuracy of the scheme than does the dispersion error.

For two-dimensional advection (two-dimensional wave equation) $\phi_{tt} - c^2 \nabla^2 \phi = 0$ the numerical dispersion relation was found as

$$\det(-i\Omega\mathbf{Q} + 2[\mathbf{N}_0 + e^{-iK\cos\theta}\mathbf{N}_{-1} + e^{iK\cos\theta}\mathbf{N}_{+1}] + 2\gamma[\mathbf{M}_0 + e^{-iK\sin\theta}\mathbf{M}_{-1} + e^{iK\sin\theta}\mathbf{M}_{+1}]) = 0, \quad (5.13)$$

where the value of Ω is function of the wavenumber K and the angle θ . An important conclusion of this analysis is that the wave propagation is anisotropic and the dependence on wave propagation angle is stronger for the higher wavenumbers.

5.5. Dissipative and dispersive behavior of high-order DG method

In a previous section, the dissipative and dispersive properties of the DG discretizations were analyzed and demonstrated for linear aeroacoustic problems. A systematic analysis of the DG method for linear wave propagation with very short-wave lengths was recently presented by Ainsworth [211]. This analysis targeted electromagnetic wave propagation. Efficient and accurate resolution of electromagnetic waves without excessive numerical dissipation or dispersion is important in the context of other high-frequency applications such as magneto-gas dynamics (MGD). The most promising approach for wave propagation is obtained with higher-order schemes such as spectral element methods [212,213]. Higher-order standard Galerkin finite-element methods were also used in the past by Astley et al. [214],

Ihlenburg [215], Thomson and Pinsky [216]. More recently, high-order DG finite-element methods [45,217–220] were applied and analyzed for wave propagation.

It was found that for the small wavenumber limit $hk \rightarrow 0$ the DG method gives a higher order of accuracy than the standard Galerkin methods. Hu and Atkins [220], for example, concluded that the dispersion relation of the scalar advection equation for an N th order DG method is accurate to order $2N + 3$ in hk for the dispersion error and $2N + 2$ for the dissipation error. A more systematic study of the dissipative and dispersive behavior of the DG method that gives sharp error estimates was carried out by Ainsworth [211]. Ainsworth's estimates are very sharp and agree with a posteriori error estimates of Hu and Atkins [220]. The main conclusions of the analysis performed by Ainsworth [211] are

- (1) As the order N is increased, the behavior of the error passes through three different phases depending on the size N relative to hk .
- (2) Pre-asymptotic regime $2N + 1 < hk - \mathcal{O}(hk)^{1/3}$. The resolving ability of the method is inadequate and the relative error tends to oscillate without decay.
- (3) The transition zone where $hk - \mathcal{O}(hk)^{1/3} < 2N + 1 < hk + \mathcal{O}(hk)^{1/3}$. The relative error is of order unity and decreases at an algebraic rate $N^{-1/3}$.
- (4) Asymptotic regime where N is large compared to hk $2N + 1 > hk + \mathcal{O}(hk)^{1/3}$. The relative error reduces at a super-exponential rate.

An exponential convergence on the envelope $2N + 1 \approx hk$ was also found in Ref. [211]. Namely reduction of the mesh-size to the limit $hk \ll 1$ is not possible for high frequencies. It was shown, however, that increasing the order N on a fixed mesh is more effective than reducing the mesh size. Furthermore, it was concluded [211] that it is inefficient to increase the order N much beyond the threshold $2N + 1 > hk + \mathcal{O}(hk)^{1/2}$. A more practical approach to resolve problems where $hk \gg 1$ is to work on the envelope of the region where the super-exponential convergence sets in. For these cases, the order of the method must be chosen so that $2N + 1 \approx \kappa hk$ where $\kappa > 1$ is a constant. Ainsworth [211] showed that the relative error ρ_N decays at an exponential rate as $N \rightarrow \infty$.

5.6. Limiting of DG expansions

Limiting operators $\Lambda\Pi_h$ on piecewise linear DG expansions u_h are constructed in such a way that they satisfy the following properties:

- (1) Accuracy: if u_h is linear, then $\Lambda\Pi_h u_h = u_h$.

(2) *Conservation of mass*: for every element K have

$$\int_k \Lambda \Pi_k u_h \, dV = \int_k u_h \, dV. \quad (5.14)$$

(3) *Slope limiting*: The gradient of $\Lambda \Pi_h u_h$ is not bigger than that of u_h for each element K .

Theoretical analysis of the slope limiting operators can be found in Cockburn and Shu [198] and Cockburn et al. [200].

5.6.1. Rectangular elements

The P^1 expansion of the approximate solution $u_h(x, y, t)$ inside rectangular elements $[x_{i-\frac{1}{2}}, x_{i+\frac{1}{2}}] \times [y_{j-\frac{1}{2}}, y_{j+\frac{1}{2}}]$ is

$$u_h(x, y, t) = \bar{u}(t) + u_x(t)\phi_i(x) + u_y(t)\psi_j(y), \quad (5.15)$$

where

$$\phi_i(x) = \frac{x - x_i}{(\Delta x_i/2)}, \quad \psi_j(y) = \frac{y - y_j}{(\Delta y_j/2)} \quad (5.16)$$

and the degrees of freedom that are evolved in time are $\bar{u}(t), u_x(t), u_y(t)$.

For the scalar equation, limiting for these quadrilateral element expansion is performed on u_x and u_y using the difference of the means.

For example, u_x is replaced by

$$\bar{m}(u_x, \bar{u}_{i+1,j} - \bar{u}_{i,j}, \bar{u}_{i,j} - \bar{u}_{i-1,j}), \quad (5.17)$$

where \bar{m} is the TVB corrected minmod function defined as

$$\begin{aligned} \bar{m}(\alpha_1, \alpha_2, \dots, \alpha_m) \\ = \begin{cases} \alpha_1 & \text{if } |\alpha_1| \leq M(\Delta x)^2, \\ m(\alpha_1, \alpha_2, \dots, \alpha_n) & \text{otherwise} \end{cases} \end{aligned} \quad (5.18)$$

and m is the total variation diminishing (TVD) minmod function defined as

$$\begin{aligned} m(\alpha_1, \alpha_2, \dots, \alpha_n, \dots, \alpha_N) \\ = \begin{cases} s \min_{1 \leq n \leq N} |\alpha_n| & \text{if } s = \text{sign}(\alpha_1) = \dots = \text{sign}(\alpha_N), \\ 0 & \text{otherwise.} \end{cases} \end{aligned} \quad (5.19)$$

The TVB correction is introduced in order to avoid unnecessary limiting near smooth extrema where the expansion coefficients (or degrees of freedom) u_x, u_y are on the order of $\mathcal{O}(\Delta x^2), \mathcal{O}(\Delta y^2)$, respectively. The numerical results are not usually sensitive to the choice of the constant M . The suggested value for this constant [206] is $M = 50$. Similarly, u_y is replaced (limited) by $\bar{m}(u_y, \bar{u}_{i,j+1} - \bar{u}_{i,j}, \bar{u}_i, -\bar{u}_{i-1,j})$.

For systems, such as the Euler equations, limiting is performed in the local characteristic variables as follows:

- The left and right eigenvector matrices R^{-1} and R , which diagonalize the Jacobian $A = \partial f(u)/\partial u$, are evaluated at the average state $\bar{u}_{i,j}$ in the element ij in the x and y directions as $R^{-1}AR = \Lambda$ where Λ is the diagonal matrix that contains the eigenvalues of the flux Jacobian. The columns of R are the right eigenvectors of A and the rows of R^{-1} are the left eigenvectors.

- All quantities needed for limiting are transformed to the characteristic field by left multiplying by R^{-1} . For the system version of the limiter given by Eq. (5.17) for example, the vectors $u_{x_{i,j}}, (\bar{u}_{i+1,j} - \bar{u}_{i,j}), (\bar{u}_{i,j} - \bar{u}_{i-1,j})$ are transformed to the characteristic field.
- The limiter of Eq. (5.17) is applied on each component of the characteristic variables vector.
- The limited (replaced) values are transformed back to the original conservative variables by multiplying by R .

5.6.2. Triangular elements

For the P^1 case, the following expansion inside the triangle K is used for the approximate solutions $u_h(x, y, t)$

$$u_h(x, y, t) = \sum_{i=1}^3 u_i(t) \phi_i(x, y), \quad (5.20)$$

where the degrees of freedom or expansion coefficients $u_i(t)$ are the values of the numerical solution at the midpoints of the edges. The basis function is a linear function that takes unit value at the midpoints m_i of the i th edge and zero value at the midpoints of the other two edges.

The slope limiting operator for triangular elements is constructed as follows. Consider the triangle K_0 of Fig. 91 where limiting is performed and the neighboring triangles K_1, K_2 and K_3 . Suitable choices of the triads of the vectors $c_0m_1, c_0m_2, c_0m_3, c_0c_1, c_0c_2, c_0c_3$ as shown in Fig. 91 yields the following geometrical decomposition:

$$(\overrightarrow{c_0m_1}) = \alpha_1(\overrightarrow{c_0c_1}) + \alpha_2(\overrightarrow{c_0c_2}). \quad (5.21)$$

In this decomposition, the vector joining the barycenter c_0 with the middle of an edge is between the vectors joining the barycenter c_0 with the barycenters of the neighboring triangles. The parameters α_1 and α_2 are positive coefficients that depend on the geometry.

Furthermore, for any linear function have the expansion

$$\begin{aligned} u_h(m_1) - u_h(c_0) &= \alpha_1[u_h(c_1) - u_h(c_0)] \\ &\quad + \alpha_2[u_h(c_2) - u_h(c_0)] \end{aligned} \quad (5.22)$$

and the averages over the triangles are

$$\bar{u}^{K_i} = \frac{1}{|K_i|} \int_{K_i} u_h \, dV = u_h(c_i), \quad i = 0, 1, 2, 3. \quad (5.23)$$

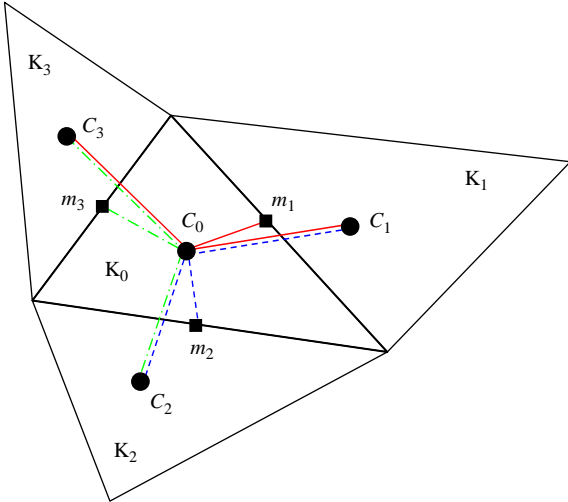


Fig. 91. Geometric definitions for arbitrary triangular mesh.

Therefore

$$\begin{aligned}\bar{u}_h^{K_0}(m_1) &\equiv u_h(m_1) - \bar{u}^{K_0} \\ &\equiv \alpha_1(\bar{u}^{K_1} - \bar{u}^{K_0}) + \alpha_2(\bar{u}^{K_2} - \bar{u}^{K_0}) \\ &\equiv \Delta\bar{u}^{K_0}(m_1).\end{aligned}\quad (5.24)$$

For a piecewise linear function u_h in K_0 and the three midpoints m_1, m_2, m_3 obtain

$$\begin{aligned}u_h^{K_0}(x, y) &= \sum_{i=1}^3 u_h(m_i)\phi_i(x, y) \\ &= \bar{u}^{K_0} + \sum_{i=1}^3 \bar{u}_h^{K_0}(m_i)\phi_i(x, y).\end{aligned}\quad (5.25)$$

The limited value $\Lambda\Pi_h u_h^{K_0}(x, y)$ is obtained by first computing the quantities

$$\Delta_i = \bar{m}(\bar{u}_h^{K_0}(m_i), \omega\Delta\bar{u}^{K_0}(m_i)), \quad (5.26)$$

where \bar{m} is the total variation bounded (TVB) modified minmod function of Eq. (5.18) and $\omega > 1$ is a weight taken $\omega = 1.5$.

Then

$$\text{if } \sum_{i=1}^3 \Delta_i = 0, \quad \Lambda\Pi_h u_h^{K_0} = \bar{u}^{K_0} + \sum_{i=1}^3 \Delta_i \phi_i(x, y),$$

if $\sum_{i=1}^3 \Delta_i \neq 0$ compute,

$$\text{pos} = \sum_{i=1}^3 \max(0, \Delta_i), \quad \text{neg} = \sum_{i=1}^3 \max(0, -\Delta_i),$$

$$\theta^+ = \min\left(1 - \frac{\text{neg}}{\text{pos}}\right), \quad \theta^- = \min\left(1, \frac{\text{pos}}{\text{neg}}\right)$$

and obtain the limited value by

$$\Lambda\Pi_h u_h(x, y) = \bar{u}^{K_0} + \sum_{i=1}^3 \widehat{\Delta}_i \phi_i(x, y), \quad (5.27)$$

where

$$\widehat{\Delta}_i = \theta^+ \max(0, \Delta_i) - \theta^- \max(0, -\Delta_i). \quad (5.28)$$

For systems of equations on triangular meshes, limiting is performed on the local characteristic variables. For triangular meshes however the following flux Jacobian

$$\frac{\partial}{\partial u} f(\bar{u}^{K_0}) \frac{\vec{m}_i \vec{c}_0}{|\vec{m}_i \vec{c}_0|} \quad (5.29)$$

e.g. the flux Jacobian $\mathbf{A} \cdot \vec{k}$ along the direction of the unit vector, $\mathbf{k} = \frac{\vec{m}_i \vec{c}_0}{|\vec{m}_i \vec{c}_0|}$, must be diagonalized to evaluate the left and right eigenvector matrices R^{-1} and R .

5.6.3. Component-wise limiters

The first way to apply a limiter to each characteristic variable was presented in the previous sections for both quadrilateral and triangular elements. The other way is to apply a limiter to each of the conservative variables. The characteristic-wise application of limiter for one-dimensional linear hyperbolic systems has the nice property of naturally degenerating to the scalar case. In multiple dimensions, the characteristic variables must be defined in a particular direction. For unstructured meshes, there is no coordinate direction to define a characteristic variable and these variables are defined in the face normal direction. The design of characteristic-based limiters in multiple directions is difficult and time consuming.

In this section, the component-wise approach for the limiter of the DG method is shown. This approach is expected to be more efficient than the characteristic approach of the previous sections. The component-wise approach is based on the following numerical monotonicity criterion for each element:

$$\bar{u}_i^{\min} < u_i(\mathbf{r}_r) < \bar{u}_i^{\max}, \quad (5.30)$$

where \bar{u}_i^{\min} and \bar{u}_i^{\max} are the minimum and maximum cell-averaged solutions among all its neighboring elements sharing a face with the triangle T_i and $u_i(\mathbf{r}_s)$ is the solution at any of the quadrature points. Violation of Eq. (5.30) for any quadrature point indicates that the element is close to a discontinuity and the solution in the element is forced locally linear, i.e.

$$u_i(\mathbf{r}) = \bar{u}_i + \nabla u_i(\mathbf{r} - \mathbf{r}_i) \quad \forall \mathbf{r} \in T_i, \quad (5.31)$$

where \mathbf{r}_i is the position vector of the centroid of T_i . The magnitude of the solution gradient is maximized subject to the monotonicity condition given in Eq. (5.30). The original DG polynomial basis is used to compute an

initial guess for the gradient as

$$\nabla u_i = \left(\frac{\partial u_i}{\partial x}, \frac{\partial u_i}{\partial y} \right) \Big|_{r_2}. \quad (5.32)$$

Using Eq. (5.31) and the gradient computed by Eqs. (5.32), (5.30) may not still be satisfied. Therefore, $u_i(\mathbf{r})$ is limited by multiplying by a scalar limiter $\phi \in [0, 1]$ so that the solution vector obtained from

$$u_i(\mathbf{r}) = \bar{u}_i + \phi \nabla u_i(\mathbf{r} - \mathbf{r}_i) \quad (5.33)$$

satisfies Eq. (5.30). The scalar limiter ϕ in Eq. (5.33) is obtained by examining the numerical solutions at all quadrature points as follows:

Denoting by

$$\Delta u_r = p_i(\mathbf{r}) - \bar{u}_i \quad (5.34)$$

$$\phi = \begin{cases} \min\left(1, \frac{\Delta u_r}{\bar{u}_i^{\max} - \bar{u}_i}\right) & \text{if } \Delta u_r > 0, \\ 1 & \text{if } \Delta u_r < 0, \\ \min\left(1, \frac{\Delta u_r}{\bar{u}_i^{\min} - \bar{u}_i}\right) & \text{otherwise.} \end{cases}$$

5.7. DG stabilization operator

High-order accurate DG finite-element solutions (with polynomial bases of degree one or higher) do not guarantee monotonicity around discontinuities and sharp gradients. The slope limiter of Cockburn et al. [200] of the previous section guarantees monotone solutions for multidimensional scalar conservation laws and its extension to the Euler equations. This slope limiter results in a robust numerical discretization and has become quite popular. However, despite its robustness the slope limiter of Cockburn et al. [200] has the following serious disadvantages. It may result in an unnecessary reduction in accuracy in smooth parts of the flow field and slows down or prevents convergence to steady state. Furthermore, its implementation for multidimensional cases and high-order discretizations is very intensive computationally.

Recently, van der Vegt and van der Ven [222] suggested that a better alternative for stabilization of the DG method is addition of artificial dissipation. This approach was also followed in the past by Cockburn and Grenaud [223] and Jaffre et al. [224]. The stabilization operators make optimal use of the information contained in a DG discretization and preserve the compactness of the DG method because they use the jump in the polynomial representation only at the element faces.

The stabilization operator $\mathcal{D} \in \mathbf{R}^{4 \times 4}$ of van der Vegt and van der Ven [222] is for quadrilateral elements and is

defined as

$$\begin{aligned} \mathcal{D}_{lm}(u_h^{K_j^n}, u_h^{*K_j^n}) &= \int_{K_j^n} \frac{\partial \psi_l}{\partial x_k} \mathbf{D}_{kp}(u_h^{K_j^n}, u_h^{*K_j^n}) \\ &\times \frac{\partial \psi_m}{\partial x_p} dK, \end{aligned} \quad (5.35)$$

where $u_h^{K_j^n}$ is the expansion in the element K_j^n , $u_h(x, t) = \sum_{k=1}^K \hat{u}_k(K_j^n) \psi_k(x)$ and $u_h^{*K_j^n}$ is the solution in the element which connect to the element K_j^n .

The stabilization operator must be applied in areas of discontinuities and regions where the residual is large due to insufficient grid resolution. This information is, however, available in the DG discretizations, and are coupled to the jump in the solution across element faces and the element residual. In the regions of smooth solution both the jumps and the residual are on the order of the truncation error. Therefore, two artificial viscosity approaches were presented by van der Vegt and van der Ven [222], a subsonic and transonic flow model, and a supersonic flow model. Full details of these models are given in [222].

5.8. DG space discretization of the NS equations

The compressible Navier–Stokes (NS) equations can be written in compact vector form as follows

$$\frac{\partial \mathbf{u}}{\partial t} + \nabla \cdot \mathbf{f}_i(\mathbf{u}) + \nabla \mathbf{f}_v(\mathbf{u}, \nabla \mathbf{u}) = 0, \quad (5.36)$$

where \mathbf{u} is the vector of the conservative variables and \mathbf{f}_i , \mathbf{f}_v denote the inviscid and viscous flux functions. The viscous flux \mathbf{f}_v is a linear function of the gradient $\nabla \mathbf{u}$ and Eq. (5.36) can be also written as

$$\frac{\partial \mathbf{u}}{\partial t} + \nabla \cdot \mathbf{f}_i(\mathbf{u}) + \nabla \cdot [\mathcal{A}(\mathbf{u}) \nabla \mathbf{u}] = 0. \quad (5.37)$$

The discretization of the viscous, diffusive part of the NS equations with the DG method is less well known and different than the method described previously for the convective, inviscid part.

A simple way to extend the scheme of Eq. (5.5), which was developed for convective problems of the form $u_t + u_x = 0$, for the diffusion equation $u_t + u_{xx} = 0$ is to simply replace u by u_x and find $u \in V_h$ such that

$$\begin{aligned} \frac{d}{dt} \int_K u(x, t) \phi(x) dx &= \int_K u_x \phi_x dx - (\hat{u}_x)_{j+1/2} \phi_{j+1/2}^- \\ &\quad + (\hat{u}_x)_{j-1/2} \phi_{j-1/2}^+, \end{aligned} \quad (5.38)$$

where for the lack of an upwind mechanism for the diffusive term the numerical flux is the centered flux $(\hat{u}_x)_{j+1/2} = \frac{1}{2}[(u_x)_{j+1/2}^L + (u_x)_{j+1/2}^R]$.

Unfortunately, this simple but naive formulation leads to numerically stable but inconsistent solutions [201,202]. The numerical solutions seem to converge with mesh refinement but have $\mathcal{O}(1)$ errors compared to

exact solutions of the heat equation [202]. This is a pitfall of the DG method when it is applied directly to diffusion-type equations. The scheme of Eq. (5.38) is therefore inconsistent because it produces stable but completely incorrect solutions.

A formulation of the DG method that is convergent and consistent was used by Bassi and Rebay [203] for the compressible Navier–Stokes equations. A second successful method that avoids the inconsistencies of the simple formulation of Eq. (5.38) was presented by Baumann and Oden [204] who added extra penalty terms to the inner boundaries.

The consistent formulation of Bassi and Rebay [203] for the spatial discretization of the viscous term in the NS equations was constructed by resorting to a mixed finite-element formulation. The second-order derivatives of the conservative variables required for the viscous terms were obtained by using the gradient of the conservative variables, $\nabla \mathbf{u} = \mathbf{S}(u)$, as auxiliary unknowns of the NS equations. The NS equations were therefore reformulated as the following coupled system to the unknowns \mathbf{S} and \mathbf{u} .

$$\begin{aligned} \mathbf{S} - \nabla \mathbf{u} &= 0, \\ \partial_t \mathbf{u} + \nabla \cdot \mathbf{f}_i(\mathbf{u}) + \nabla \cdot \mathbf{f}_v(\mathbf{u}, \mathbf{S}) &= 0. \end{aligned} \quad (5.39)$$

The weak formulation of the first equation of the system of Eq. (5.39) is

$$\int_K S_h \phi \, dx - \oint_e \mathbf{u}_h \cdot \mathbf{n} \phi \, d\Gamma + \int_K u_h \nabla \phi \, dx = 0, \quad (5.40)$$

where the term $\mathbf{u}_h \cdot \mathbf{n}$ in the second (contour) integral of Eq. (5.40) is replaced by a numerical flux $H_s(\mathbf{u}^-, \mathbf{u}^+, \mathbf{n})$. This numerical flux is a centered flux given as the average between the two interface states

$$H_s(\mathbf{u}^-, \mathbf{u}^+, \mathbf{n}) = \frac{1}{2}(\mathbf{u}^- + \mathbf{u}^+) \cdot \mathbf{n}. \quad (5.41)$$

The computed auxiliary variables S_h are used to form the second equation of the system in Eq. (5.39) as follows

$$\begin{aligned} \frac{d}{dt} \int_K \mathbf{u}_h \phi \, dx + \oint_e \mathbf{f}_i(\mathbf{u}_h) \cdot \mathbf{n} \phi \, d\Gamma \\ - \int_K \mathbf{f}_i(\mathbf{u}_h) \nabla \phi \, dx + \oint_e \mathbf{f}_v(\mathbf{u}_h, S_h) \cdot \mathbf{n} \, d\Gamma \\ - \int_K \mathbf{f}_v(\mathbf{u}_h, S_h) \nabla \phi \, dx. \end{aligned} \quad (5.42)$$

In Eq. (5.42), the term $\mathbf{f}_v(\mathbf{u}_h, S_h) \cdot \mathbf{n}$ is replaced with the following centered numerical flux

$$\begin{aligned} h_v(\mathbf{u}^-, S^-, \mathbf{u}^+, S^+, \mathbf{n}) \\ = \frac{1}{2}[\mathbf{f}_v(\mathbf{u}^-, S^-) + \mathbf{f}_v(\mathbf{u}^+, S^+)] \cdot \mathbf{n}. \end{aligned}$$

A more detailed presentation and analysis of the DG discretization of the viscous part was recently presented by Bassi et al. [221]. In Ref. [221], the main points of the DG discretizations of second-order derivatives were

described using a simple purely elliptic problem the Helmholtz equation with Dirichlet and Neumann boundary conditions. The extension to the full NS equations was carried out first. Next, an alternative scheme for “compact” DG approximation of elliptic problems was proposed [221]. This alternative scheme overcomes limitations of the method associated with not optimal accuracy for approximations with odd order polynomials and the additional computing cost occurring from the introduction of the auxiliary variable S . The auxiliary variable S is obtained in terms of u_h at the cost of a block diagonal mass matrix inversion from the first equation. However, the formulation of the second equation, which is obtained in this manner, and contains the primal variable alone involves an “enlarged stencil”. This enlarged stencil occurs because the primal unknown u_h for any internal element e is coupled not only with unknowns of the neighboring elements but also with unknowns associated to the neighbors of the neighbors (because the second derivative is evaluated as the first derivative of a first derivative). The enlarged stencil implies additional computing cost. Bassi et al. [221] showed that only the jump contribution to the auxiliary variable S is responsible for the non-compact support of the scheme described and they propose modifications that one can use to arrive at a scheme with compact support for elliptic problems and for DG discretizations of the viscous terms in the NS equations.

The modification of the new scheme for the discretization of the elliptic operators follows more closely the numerical flux function ideas usually employed in finite-volume (FV) schemes. A typical treatment of an elliptic operator in FV schemes is often based on the definition of auxiliary staggered control volumes enclosing the boundaries of the primal control volumes that are used to construct the diffusive terms, which are the analogue to the vector flux S used in the DG formulation.

5.9. The DG variational multiscale (VMS) method

The VMS method is a new approach for LES proposed by Hughes et al. in a series of papers [225–227]. The VMS method was subsequently further clarified by Collis [228] and applied with the DG method [229,230] for LES of compressible turbulence. More recently the VMS method was further developed [231] for mixed-type, Fourier-spectral/finite-volume formulation. The ideas behind the VMS method and its implementation with the DG space discretization method are briefly described.

The dynamics of turbulent shear flows are dominated by the motions of a small number of relatively large-scale structures. The separation between the large, energy containing scales and the smallest turbulent

scales increases as the Reynolds number increases. The increase in range of scales prevents DNS from being a viable tool beyond very simple, low Reynolds number flows. In contrast, LES attempts to exploit the scale separation in turbulent shear flows by representing the largest scales as accurately as possible on the computational mesh and using a model to account for the influence of the unresolved smaller scales. Important progress in turbulent flow simulations with LES was made, primarily with the application of the so-called dynamic model (see [4–6,233]). It was, however, soon recognized that the Reynolds numbers for which LES can be applied using this approach are still far too low. As a result, LES is not still an economically feasible alternative for the simulation of the vast majority of engineering flows. The deficiencies of RANS or even DES to accurately predict complex separated flows and the high computing cost of LES for flows of practical interest lead to the quest of new approaches [225,232]. These approaches overcome the weaknesses of LES and RANS while providing consistency with DNS. The Discontinuous Galerkin/Variational Multi-Scale (DG/VMS) method [229] which merges VMS turbulence modeling [225] with the high-order accurate DG discretization is a particular synergistic combination that offers a number of advantages over traditional methods.

The advantages of the VMS/DG approach for LES are:

- (1) Variational projection with a priori scale separation [225] avoids problems associated with spatial filters.
- (2) The method converges to the exact DNS.
- (3) The method is high-order with the potential for exponential (spectral) convergence.
- (4) VMS/DG is insensitive to grid quality and suitable for complex domains.
- (5) The method allows for different models to be used in different regions of the flow while still retains formal convergence to the exact solution.
- (6) The VMS/DG approach for turbulence simulations unifies traditional DNS, LES and RANS approaches in a single computational tool.

The VMS/DG method is briefly described next.

Consider the compressible Navier–Stokes equations in strong conservation law form

$$\begin{aligned} \mathcal{N}(U) &= U_t + F_{j,j}^i - F_{j,j}^v = 0, \\ U(\mathbf{x}, 0) &= U_0(\mathbf{x}), \end{aligned} \quad (5.43)$$

where $U = [\rho, \rho\mathbf{u}, \rho E]^T$ is the conservative variable vector, $F_j^i(U)$ is the inviscid flux vector in the j coordinate direction, and $F_j^v(U)$ is viscous flux vector in the j coordinate direction.

The weak form of Eq. (5.43) is

$$\begin{aligned} \int_{\Omega_e} \mathbf{W}^T U_t dx + \int_{\Omega_e} \mathbf{W}_j^T (\mathbf{F}_j^u - \mathbf{F}_j^i) dx \\ + \oint_{\partial\Omega_e} W^T (\mathbf{F}_{ne}^i - \mathbf{F}_{ne}^v) dS = 0, \end{aligned} \quad (5.44)$$

where $F_n = F_j n_j$, n_e is the outward unit normal vector on $\partial\Omega_e$, and \mathbf{W} is a continuous weighting function in the element Ω_e .

Following the VMS approach of [228] the following three-level multiscale framework is used to allow direct monitoring of unresolved scales.

$$\mathbf{U} = \overline{\mathbf{U}} + \tilde{\mathbf{U}} + \hat{\mathbf{U}}. \quad (5.45)$$

In the partition of Eq. (5.45), of the exact solution \mathbf{U} , $\overline{\mathbf{U}}$ represent the large scales, $\tilde{\mathbf{U}}$ are the small scales, and $\hat{\mathbf{U}}$ are the unresolved scales. This partition into scales is depicted in Fig. 92 as a range of Fourier modes in wavespace. The large scale equations have no modeling terms while the small scale equations have modeling terms that can range from Smagorinsky closure to a full Reynolds stress model. The large and small scales are referred to as resolved scales.

Assuming that the basis is orthogonal and substituting the partition of Eq. (5.45) in the weak form of Eq. (5.44), which in condensed form is $B(\mathbf{W}, \mathbf{U}) = 0$, obtain for the large-scale equations

$$\begin{aligned} B(\overline{\mathbf{W}}, \overline{\mathbf{U}}) - C(\overline{\mathbf{W}}, \overline{\mathbf{U}}, \tilde{\mathbf{U}}) - R(\overline{\mathbf{W}}, \tilde{\mathbf{U}}) \\ = C(\overline{\mathbf{W}}, \overline{\mathbf{U}}, \hat{\mathbf{U}}) + R(\overline{\mathbf{W}}, \hat{\mathbf{U}}) + C(\overline{\mathbf{W}}, \tilde{\mathbf{U}}, \hat{\mathbf{U}}) \end{aligned} \quad (5.46)$$

and for the small-scale equations obtain

$$\begin{aligned} B'(\tilde{\mathbf{W}}, \overline{\mathbf{U}}, \tilde{\mathbf{U}}) - R(\tilde{\mathbf{W}}, \tilde{\mathbf{U}}) \\ = R(\tilde{\mathbf{W}}, \overline{\mathbf{U}}) + C(\tilde{\mathbf{W}}, \overline{\mathbf{U}}, \hat{\mathbf{U}}) + R(\tilde{\mathbf{W}}, \hat{\mathbf{U}}) + C(\tilde{\mathbf{W}}, \tilde{\mathbf{U}}, \hat{\mathbf{U}}). \end{aligned} \quad (5.47)$$

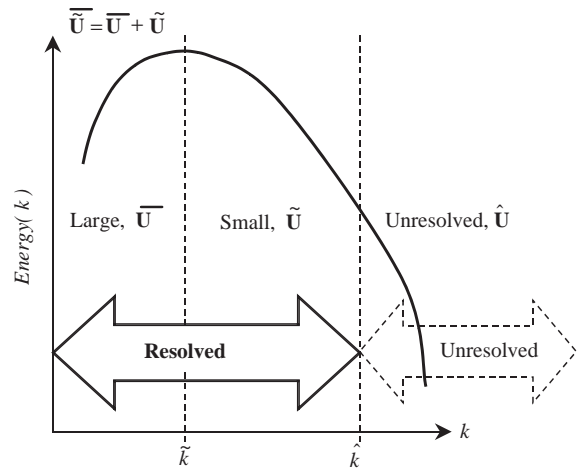


Fig. 92. Wave space decomposition for the VMS method.

The analysis for the general nonorthogonal basis can be found in [228].

In Eqs. (5.46) and (5.47) $R(\bar{W}, \tilde{U})$ is the generalized Reynolds stress, $C(\bar{W}, \tilde{U}, \hat{U})$ is the generalized cross-stress, $B'(\bar{W}, \bar{U}, \tilde{U})$ is the operator $B(\bar{W}, U)$ linearized about \bar{U} for the linear perturbation \tilde{U} .

The effect of the unresolved scales on the large scales is seen in Eq. (5.46) which contains the unresolved Reynolds stress projection onto the large scales simultaneously with the large- and small-unresolved generalized cross-stresses projections onto the large scales. The small-scale equation also contains the unresolved Reynolds stresses and cross-stresses. For truncated or discrete approximations, the combined small and large scales are identified as the resolved scales (see Fig. 92) and denoted as $\tilde{U} = \bar{U} + \tilde{U}$. Therefore, the resolved scale equation (Eq. (5.46)) is written more compactly as

$$B(\tilde{W}, \tilde{U}) = R(\bar{W}, \hat{U}) + C(\bar{W}, \bar{U}, \hat{U}). \quad (5.48)$$

The equations for small- (Eq. (5.47)) and large-scales (Eq. (5.46) or (5.48)) indicate the need to model unresolved Reynolds and cross-terms appearing on the right-hand side. The modeling assumptions introduced are:

- (1) The unresolved scales \hat{U} have negligible direct influence on the dynamic evolution of the large scales \bar{U} . Therefore, for sufficient a priori scale separation, the right-hand side of Eq. (5.46) is small, e.g. $C(\bar{W}, \bar{U}, \hat{U}) + R(\bar{W}, \hat{U}) + C(\bar{W}, \bar{U}, \hat{U}) \approx 0$.
- (2) The unresolved scales \hat{U} , however, are expected to significantly influence the small scales \tilde{U} . As a result, an appropriate model is needed for the right-hand side terms of Eq. (5.47). Therefore we set $C(\tilde{W}, \bar{U}, \hat{U}) + R(\tilde{W}, \hat{U}) + C(\tilde{W}, \bar{U}, \hat{U}) = M(\tilde{W}, \bar{U}_h, \hat{U}_h)$.

The VMS formulation can support a wide range of models. In addition, a key feature of the VMS method is that different models can be used in different spatial locations. As a result, the model used depends on the particular flow characteristics, the desired fidelity, and the location of the particular subdomain under consideration.

Using modeling assumptions (1) and (2) the equations for the large and small scales become:

$$\begin{aligned} B(\bar{W}, \bar{U}_h) - C(\bar{W}, \bar{U}, \tilde{U}) - R(\bar{W}, \tilde{U}) \\ = R(\bar{W}, \hat{U}_h), \end{aligned} \quad (5.49)$$

$$\begin{aligned} B'(\tilde{W}, \bar{U}_h, \hat{U}_h) - R(\tilde{W}, \hat{U}_h) \\ = R(\tilde{W}, \bar{U}) + M(\tilde{W}, \bar{U}_h, \hat{U}_h), \end{aligned} \quad (5.50)$$

where the subscript h in Eqs. (5.49) and (5.50) is introduced to denote that these equations contain modeling errors and that the approximate numerical solution introduces discretization errors.

The large-scale equation is an approximation because the effect of the unresolved scales has been ignored. The modeled large-scale equation takes the form of the exact equation only when all scales of motion are contained within the resolved scales. In this case, the VMS method is a DNS. However, by neglecting the influence of the unresolved scales on the large scales, the modeled large-scale equation has no direct modeling terms. The model in the small scales indirectly influences the large scales. This is achieved through the small-scale Reynolds and cross-stresses. Thus, if the exact solution is fully represented by the large scales, then the solution to the modeled equations (5.49) is exact. This consistency is an important advantage over classical methods [225]. The model applied to the large-scale equation is nothing more than the standard approach used in a Galerkin method where the projection of the residual of the unresolved scales onto the large scales is zero. Considering the simplified case where the bases are orthogonal, this amounts to weak enforcement of zero unresolved Reynolds/cross-stresses on the large scales. This indicates the particular discretizations play a role in altering the model and therefore the results.

In the small-scale equation, it is the projection of the unresolved Reynolds and cross-stresses onto the small scales that is modeled using a weak implementation of a subgrid-scale model. Again, use of different methods for the small-scale discretizations is expected to alter the model. This is an advantage of the VMS framework. Although the model is specified without regard to the specific discretization, the influence of discretization is obvious in the modeled equations. This fact has not been completely appreciated in the traditional turbulence modeling community until recently when it was realized that differences between the discretization with the “same model” might be as large or larger than differences in “models” using the same discretization. In the VMS framework, the influence of different discretizations is evident and the choice of discretization clearly plays an important role in the success of particular models. Therefore an important area for future research is to explore different bases for use in defining large and small scales. The modeled large and small scales in Eqs. (5.49) and (5.50) are combined as follows:

$$B(\tilde{W}, \bar{U}_h) = M(\tilde{W}, \bar{U}_h, \hat{U}_h) + (\tilde{W}, S) \quad \text{on } \Omega_e. \quad (5.51)$$

The model of Eq. (5.51) can be implemented with VMS by incorporating the additional model term into the small-scale equations. This model term can depend on both the large and small scales. Therefore it can take forms ranging from classical Smagorinsky model to models used in DES.

In the proceeding paragraphs, the variational multi-scale method was presented for a typical subdomain Ω_e .

Summing Eq. (5.51) over all the subdomains in the partition P_h of Ω and introducing typical continuous smooth finite-dimensional spaces for U_h and the test function \mathbf{W}_h then, subject to appropriate boundary conditions and the particular choice of model, obtain the standard variational multiscale method for classical finite elements, spectral elements, or global spectral methods (see e.g., Refs. [225,227–234]). Results from these methods are quite new, they have shown tremendous potential including the ability to accurately simulate wall-bounded and non-equilibrium turbulence using a very simple constant coefficient Smagorinsky model on the small scales [227]. However, most of the results presented to date use global spectral methods, which have a rich function space but are only feasible for very simple geometries [226,227]. The preliminary work of Jansen [234] and co-workers offsets this by using a low-order (cubic and lower) hierarchical basis within a C° finite-element method. While this method can be applied to complex geometries, the relatively low-order function spaces may not have a sufficient scale separation for effective turbulence simulation. Perhaps of even greater importance however, is that the reliance of prior approaches on C° or smoother function spaces limits ones ability to alter the large/small partition or change the form of the model as a function of space. For example, in laminar regions of a flow no model should be used, while in boundary layers a RANS type model may be appropriate (if you only are concerned with the mean flow) while in a wake region an LES type model may be used to capture the large-scale unsteadiness.

To address these limitations, the DG/VMS method introduced in [229] combines VMS turbulence modeling with a DG method in space. The combination of these two methods is particularly synergistic and the combined DG/VMS method possesses the following characteristics:

- high-order (even exponential) convergence on highly irregular unstructured meshes;
- discretization, large/small partitioning, and model equations can be changed on each subdomain, Ω_e ;
- all boundary conditions are set weakly through boundary fluxes including fluxes of turbulence stress. This enables one to directly enforce zero turbulent stress at solid walls—a feature not present in prior approaches;
- the method is highly localized leading to a great degree of parallelism which is required for the large-scale turbulence simulations we are targeting.

The additional complication with the VMS/DG method is that the typical approach for diffusive problems has been to introduce auxiliary variables for the viscous fluxes and re-write the equations of motion

as an extended first-order system of equations [206]. This mixed approach has been demonstrated by Lomtev et al. [235] for two- and three-dimensional unsteady flows. Unfortunately, the mixed approach in three-dimensions requires 6 additional unknowns and equations for three-dimensional Navier–Stokes flows. Furthermore, in applications, the model terms, $M(\tilde{\mathbf{W}}, \bar{\mathbf{U}}, \tilde{\mathbf{U}})$, often take the form of diffusive terms (eddy diffusivity models) that may require the addition of even more unknowns. Over the past few years, there has been extensive research on the use of DG methods for elliptic and mixed hyperbolic/elliptic problems (see e.g. [203,204,206,236]). Furthermore, Arnold et al. [237] showed that the flux formulation, commonly used in DG methods, can be readily converted to the primal formulation.

With this background, the variational multiscale method described above can be merged with a DG method. Denoting the boundary of the domain Ω as $\partial\Omega = \Gamma_D \cup \Gamma_N$ where Γ_D is the portion of the boundary where Dirichlet conditions are specified and Γ_N is the portion of the boundary where Neumann conditions are set. The element boundary is denoted as $\Gamma = \{\Gamma_D, \Gamma_N, \Gamma_0\}$ where Γ_0 are the inter-element boundaries. Let Ω_1 and Ω_2 be two adjacent elements. Furthermore, let $\Gamma_{12} = \partial\Omega_1 \cap \partial\Omega_2$; and $\mathbf{n}^{(1)}$ and $\mathbf{n}^{(2)}$ be the corresponding outward unit normal vectors at that point. Denoting $\mathbf{U}^{(e)}$ and $\mathbf{F}_i^{(e)}$ be the state vector \mathbf{U} and flux vectors \mathbf{F}_i , respectively, on Γ_{12} . Then, define the average $\langle \cdot \rangle$ and jump $[\cdot]$ operators on Γ_{12} as

$$\begin{aligned} (a) [\mathbf{U}n_i] &= \mathbf{U}^{(1)}n_i^{(1)} + \mathbf{U}^{(2)}n_i^{(2)}, \\ (b) [\mathbf{F}_n] &= \mathbf{F}_i^{(1)}n_i^{(1)} + \mathbf{F}_i^{(2)}n_i^{(2)}, \\ (c) \langle \mathbf{U} \rangle &= \frac{1}{2}(\mathbf{U}^{(1)} + \mathbf{U}^{(2)}), \\ (d) \langle \mathbf{F}_i \rangle &= \frac{1}{2}(\mathbf{F}_i^{(1)} + \mathbf{F}_i^{(2)}), \end{aligned} \quad (5.52)$$

where $\mathbf{F}_n = \mathbf{F}_i n_i$.

With this notation and Eq. (5.51) the discontinuous Galerkin formulation of the $B(\mathbf{W}, \mathbf{U})$ term, defined in Eq. (5.46), is applied to obtain the DG formulation for the Navier–Stokes equations as

$$\begin{aligned} B_{DG}(\mathbf{W}, \mathbf{U}) &= \sum_{\Omega_e} \int_{\Omega_e} (\mathbf{W}^T \mathbf{U}_{,t} + \mathbf{W}_{,t}^T (\mathbf{F}_i^v - \mathbf{F}_i)) dx \\ &\quad - \int_{\Gamma} ([\mathbf{W}^T n_i] (\hat{\mathbf{F}}_i^v - \hat{\mathbf{F}}_i) \\ &\quad - \langle (\mathbf{D}_i \mathbf{W})^T \rangle [\hat{\mathbf{U}} - \hat{\mathbf{U}}] n_i) ds \\ &\quad - \int_{\Gamma_0} ((\mathbf{W}^T) [\hat{\mathbf{F}}_n^v - \hat{\mathbf{F}}_n] \\ &\quad - [(\mathbf{D}_n \mathbf{W})^T] (\hat{\mathbf{U}} - \mathbf{U}) n_i) ds, \end{aligned} \quad (5.53)$$

where $\mathbf{F}_n(\mathbf{U}) = \mathbf{F}_i(\mathbf{U}) \mathbf{n}_i$, and $\mathbf{F}_n^v(\mathbf{U}) = \mathbf{F}_i^v(\mathbf{U}) \mathbf{n}_i = \mathbf{D}_n \mathbf{U}$.

Quantities with a hat in Eq. (5.53) are numerical fluxes that must be appropriately defined. For example, the term $\mathbf{F}_i(\mathbf{U}^-, \mathbf{U}^+)$ is an appropriate approximate

Riemann flux (see previous sections for various options). The particular choice of Riemann flux plays an important role in determining the dispersion/dissipation characteristics of the method [210]. For example, using the Steger–Warming flux-vector splitting where $\mathbf{F}_n(\mathbf{U})$ is split into inflow and outflow components \mathbf{F}_n^- and \mathbf{F}_n^+ as follows:

$$\mathbf{F}_n^\pm(\mathbf{U}) = \mathbf{R}\lambda^\pm \mathbf{L}\mathbf{U}, \quad \Lambda^\pm = \frac{1}{2}(\Lambda \pm |\Lambda|) \quad (5.54)$$

and the approximate Riemann flux in this case is simply $\tilde{\mathbf{F}}_n(\mathbf{U}^-, \mathbf{U}^+) = \mathbf{F}_n^+(\mathbf{U}^-) + \mathbf{F}_n^-(\mathbf{U}^+)$ where $\mathbf{U}^\pm = \lim_{\epsilon \rightarrow 0} +\mathbf{U}(\mathbf{x} \pm \epsilon \mathbf{n})$. Similarly, various options are available for the numerical viscous fluxes [237] and a particularly simple approach is the interior penalty method $\hat{\mathbf{U}} = \langle \mathbf{U} \rangle, \hat{\mathbf{F}}^v = \langle \mathbf{F}_i^v \rangle - \mu [\mathbf{U}]_{n_i}$ where $\mu > 0$ is a stabilization parameter [238,239]. Thus, the DG method is:

Given $\mathbf{U}_0 = \mathbf{U}_0(\mathbf{x})$, for $t \in (0, T)$, find $\mathbf{U}(\mathbf{x}, t) \in \mathbf{V}(P_h) \times H^1(0, T)$ such that $\mathbf{U}(\mathbf{x}, 0) = \mathbf{U}_0(\mathbf{x})$ and

$$B_{DG}(\mathbf{W}, \mathbf{U}) = M_{DG}(\tilde{\mathbf{W}}, \bar{\mathbf{U}}, \tilde{\mathbf{U}}) + (\mathbf{W}, \mathbf{S}), \quad (5.55)$$

$\forall \mathbf{W} \in \mathbf{V}(P_h)$ where $\mathbf{V}(P_h)$ is the broken space defined in [204]. If $\mathbf{V}(P_h)$ is restricted to a space of continuous functions, then one recovers the classical Galerkin approximation. Further details about turbulence modeling with the VMS approach and additional implementation issues can be found in the original references [225–229].

5.10. Implicit time marching of DG discretizations

An implicit time marching algorithm based on the backward Euler integration scheme was presented in [240] for DG discretizations. This algorithm is unconditionally stable in two dimensions and provides time accuracy only when its time step resolves the temporal scales of the problem. The advantage of the unconditional stability is lost in the case of DNS of transitional and turbulent flows where the time scales that need to be resolved are often comparable to the time step imposed by explicit schemes. Unconditional stability is exploited to obtain steady-state solutions with the DG discretization.

Application of backward Euler time integration to the weak form of the Euler or Navier–Stokes equations with the DG discretizations yields

$$\begin{aligned} & \int_{\Omega_i} \frac{\partial \mathbf{U}_i^n}{\partial t} \mathbf{v}_l^i d\Omega - \int_{\Omega_i} \mathbf{F}(\mathbf{U}_i^n + \Delta \mathbf{U}_i^n) \cdot \nabla \mathbf{v}_l^i d\Omega \\ & + \sum_j \oint_{\partial \Omega_{ij}} \mathbf{F}_{\text{num}}(\mathbf{U}_i^n + \Delta \mathbf{U}_i^n, \mathbf{U}_j^n + \Delta \mathbf{U}_j^n, \mathbf{n}) \mathbf{V}_l^i dS = 0, \\ & l = 1, \dots, N, \end{aligned} \quad (5.56)$$

where the superscript for the state variable indicates the time level and

$$\Delta \mathbf{U}_i^n = \mathbf{U}_i^{n+1} - \mathbf{U}_i^n. \quad (5.57)$$

Performing linearization of the fluxes \mathbf{F} and \mathbf{F}_{num} obtain

$$\begin{aligned} \mathbf{F}(\mathbf{U}_i + \Delta \mathbf{U}_i) &= \mathbf{F}(\mathbf{U}_i) + A(\mathbf{U}_i)\Delta \mathbf{U}_i + \partial(\Delta t^2) \\ \mathbf{F}_{\text{num}}(\mathbf{U}_i + \Delta \mathbf{U}_i, \mathbf{U}_j + \Delta \mathbf{U}_j, \mathbf{n}) \\ &= \mathbf{F}_{\text{num}}(\mathbf{U}_i, \mathbf{U}_j, \mathbf{n}) + A_{ij}^1 \Delta \mathbf{U}_i + A_{ij}^2 \Delta \mathbf{U}_j + \partial(\Delta t^2), \end{aligned} \quad (5.58)$$

where

$$A(\bar{\mathbf{U}}) = \frac{\partial \bar{\mathbf{F}}(\bar{\mathbf{U}})}{\partial \bar{\mathbf{U}}}, \quad A^1 = \frac{\partial \bar{\mathbf{F}}_{\text{num}}(\bar{u}, \bar{v}, \bar{n})}{\partial \bar{u}}, \quad A^2 = \frac{\partial \bar{\mathbf{F}}_{\text{num}}(\bar{u}, \bar{v}, \bar{n})}{\partial \bar{v}}, \\ A_{ij}^1 = A^1(\bar{u}_i, \bar{v}_j, \bar{n}), \quad A_{ij}^2 = A^2(\bar{u}_i, \bar{u}_j, \bar{n})$$

with these definitions dropping terms of higher than second order in Eq. (5.56) obtain

$$\begin{aligned} & \int_{\Omega_i} \frac{\partial \bar{\mathbf{U}}_i^n}{\partial t} V_l^i d\Omega - \int_{\Omega_i} A(\bar{\mathbf{U}}_i^n) \Delta \bar{\mathbf{U}}_i^n \cdot \nabla \bar{V}_l^i d\Omega \\ & + \sum_j \int_{\partial \Omega_i} (A_{ij}^1 \Delta \bar{\mathbf{U}}_i^n + A_{ij}^2 \Delta \bar{\mathbf{U}}_j^n) \bar{V}_l^i dS \\ & = R_{i,l}(\bar{\mathbf{U}}^n), \end{aligned} \quad (5.59)$$

$$\begin{aligned} R_{i,l}(\mathbf{U}^n) &= \int_{\Omega_i} \bar{\mathbf{F}}(\bar{u}_i^n) \cdot \nabla \bar{V}_l^i d\Omega \\ & - \sum_j \oint_{\partial \Omega_{ij}} \mathbf{F}_{\text{num}}(\bar{u}_i^n, \bar{u}_j^n, \bar{n}) \bar{V}_l^i dS. \end{aligned} \quad (5.60)$$

Let $\hat{\mathbf{U}} = (\hat{\bar{\mathbf{U}}}_1, \dots, \hat{\bar{\mathbf{U}}}_{N_e})$ be the expansion coefficient of the approximate solution where $\hat{\bar{\mathbf{U}}}_i = (\hat{\bar{\mathbf{U}}}_{i,1}, \dots, \hat{\bar{\mathbf{U}}}_{i,N_e})$.

$$\bar{\mathbf{U}}_i(\mathbf{x}) = \sum_{l=0}^N \hat{\bar{\mathbf{U}}}_{i,l} \bar{V}_l^i(\mathbf{x}), \quad i = 1, \dots, N_e. \quad (5.61)$$

The implicit scheme of Eq. (5.59) is written in matrix form as

$$\begin{aligned} M(\mathbf{U}^n) \Delta \hat{\mathbf{U}}^n &= R(\mathbf{U}^n), \\ M(\bar{\mathbf{U}}^n) &= \frac{D}{\Delta t} - \frac{\partial R(\bar{\mathbf{U}}^n)}{\partial \hat{\mathbf{U}}} \end{aligned} \quad (5.62)$$

where D denotes the block diagonal mass matrix $D = \text{diag}(d_1, \dots, d_{N_e})$.

$$[d_i]_{kl} = \int \mathbf{V}_k^i \mathbf{V}_l^i d\Omega. \quad (5.63)$$

The spatial accuracy of the solution depends on the discretization of the residual as for the implicit schemes presented in Section 2 in the finite difference context. Quadratic convergence and large-time steps are possible only when the spatial discretization of the left-hand side of Eq. (5.62) is consistent with the discretization of the right-hand side. The linear system of Eq. (5.62) can be solved with the generalized minimum residual (GMRES) Krylov method [241] with single- or two-level preconditioning.

A second-order accurate in time implicit Runge–Kutta method can also be used for time integration of DG discretizations [221] as follows:

Considering the system of the DG discretization

$$D \frac{d\mathbf{u}}{dt} - R(\mathbf{u}) = 0, \quad (5.64)$$

where D is the mass matrix the second order implicit Runge–Kutta method involves two backward Euler steps and can be written as

$$\mathbf{u}_j^{n+1} = \mathbf{u}_i^n + \gamma_1 \mathbf{K}_1 + \gamma_2 \mathbf{K}_2, \quad (5.65)$$

$$\left[\frac{D}{\Delta t} + \alpha \frac{\partial R(\mathbf{u}^n)}{\partial \mathbf{u}} \right], \quad \mathbf{K}_1 + R(\mathbf{u}^n) = 0, \quad (5.66)$$

$$\left[\frac{D}{\Delta t} + \alpha \frac{\partial R(\mathbf{u}^n)}{\partial \mathbf{u}} \right], \quad \mathbf{K}_2 + R(\mathbf{u}^n + \beta \mathbf{K}_1) = 0 \quad (5.67)$$

the constants α, β, γ_1 and γ_2 corresponding to an optimal second-order accurate scheme [242] are $\alpha = (2 - \sqrt{2})/2$, $\beta = 8\alpha(0.5 - \alpha)$, $\gamma_1 = 1 - 1/8\alpha$, $\gamma_2 = 1 - \gamma_1$.

The backward Euler scheme of Eq. (5.61) is recovered by $\gamma_1 = 1$, $\gamma_2 = 0$ and $\alpha_1 = 1$. The Crank–Nicolson algorithm is obtained for $\gamma_1 = 1$, $\gamma_2 = 0$, $\alpha = \frac{1}{2}$.

5.11. p-type multigrid for DG

A p-type multigrid acceleration method was developed [207] for convergence acceleration with the G method. A simple backward Euler discretization in time was used [207] so that the discrete equation for time advancement is

$$\mathcal{M} \frac{1}{\Delta t} (\bar{\mathbf{u}}^{n+1} - \bar{\mathbf{u}}^n) + \mathbf{R}(\bar{\mathbf{u}}^{n+1}) = 0, \quad (5.68)$$

where \mathcal{M} is the mass matrix, \mathbf{R} is the residual vector, and $\bar{\mathbf{u}}$ are the degrees of freedom to be evolved in time from time level n to $n + 1$.

For steady-state solutions the nonlinear system $\mathbf{R}(\mathbf{U}) = 0$ is solved using a p-multigrid scheme with a linear Jacobi smoother. A generic iterative scheme for Eq. (5.68) can be written as

$$\bar{\mathbf{u}}^{n+1} = \bar{\mathbf{u}}^n - \mathbf{P}^{-1} \mathbf{R}(\bar{\mathbf{u}}^n), \quad (5.69)$$

where the preconditioner, \mathbf{P} , is an approximation to $\partial R / \partial U$. In p-multigrid the low-frequency error modes can be effectively corrected by smoothing with lower order expansion of the approximate solution that serve as the worse grids [243]. p-multigrid fits naturally with the frame work of high-order DG discretizations. There is no need to store additional grid information since the same spatial grid is used by all levels. The transfer operators between the different p expansions, prolongation and restriction, are local and are stored for the reference element.

5.12. Results with the DG method

Second- fourth- and sixth-order accurate numerical solutions for wave propagation on triangular meshes were computed in [244] using polynomial base functions P^1 , P^3 , and P^5 , respectively. The accuracy of the numerical solutions was evaluated by comparing the computed results with exact solutions. The first test problem with an exact solution [245] was propagation and reflection from a solid wall of a Gaussian pressure pulse given by $p(x, y) = \exp\{-\ln 2[x^2 - (y - y_0)^2]/W\}$, where W is the width of the pulse and y_0 is the distance from the wall. The second problem with an exact solution is scattering of a similar Gaussian pressure pulse from the surface of a cylinder [246].

The solutions of the linearized Euler equations [244] were computed with third-order polynomial basis on a relatively coarse, fully unstructured mesh. The computational mesh is shown in Fig. 93. At the far-field boundaries, the radiation boundary condition [86] was used. It can be seen that the pressure waves exit the computational domain undistorted and there are no reflections in the interior from the computational boundaries. Acoustic disturbance propagation is isotropic and does not require use of meshes with pattern [210]. It appears that the unstructured mesh of Fig. 93 is more appropriate for acoustic wave propagation. For convenience, evaluation of the numerical method is performed with solutions computed on meshes obtained from triangulation of structured Cartesian-type grids. The elements of the mesh for the solution of Fig. 94 follow a uniform triangular-mesh generating pattern. It was shown in [210] that the accuracy of the computed solution depends on the triangular-mesh generating pattern. Comparing the computed solutions of Figs. 93 and 94 it appears that the coarse, canonical grid solution ($\Delta x = 2$) obtained with the third order P^3 polynomial basis shows more distortion than the fully unstructured

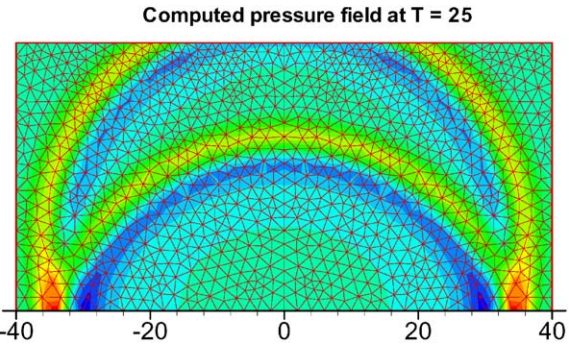


Fig. 93. Solution computed with an unstructured, triangular mesh and third-order polynomial basis.

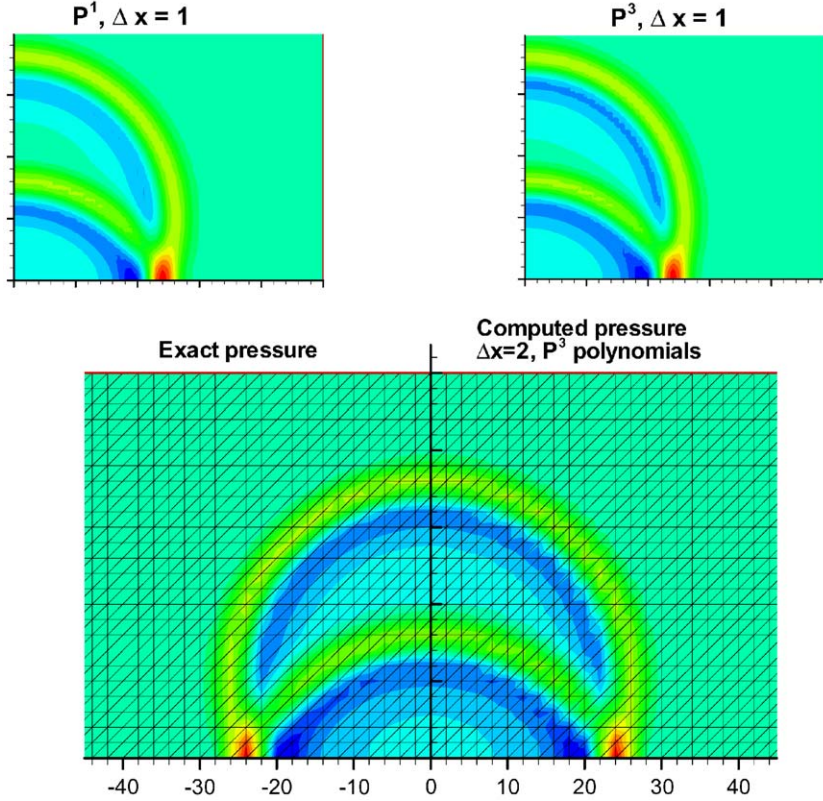


Fig. 94. Comparison of the pressure field computed with $\Delta x = 2$ triangular elements and third-order polynomial basis (right) with the exact solution (left).

mesh of Fig. 93 that has comparable resolution. The upper part of Fig. 94 shows, however, that for fine grids and high-order accuracy the bias introduced by the triangular-mesh generating pattern is very small. This is again consistent with the theoretical analysis of [210].

Solutions shown in the following paragraphs were computed [244] until final time $T = 25$ on triangular canonical meshes with mesh generating pattern (see Fig. 95). Comparisons are carried out with the exact solution given in [245]. A comparison of the solutions computed with grid spacing $\Delta x = 2.0$ is only shown in Fig. 95 because within plotting accuracy for $\Delta x = 1.0$ the differences between the fourth- and sixth order-accurate solutions are not visible. The same time step $\Delta t = 0.01$, which is below the stability limit of the Runge–Kutta method was used for all solutions. The comparison with the exact result of Ref. [245] is shown along the symmetry line, which is normal to the wall at $x = 0$. For the same location, the error $\epsilon_r = (p_{\text{com}} - p_{\text{ex}})$ of the computed solutions is shown in Fig. 96. Clearly, only for $\Delta x < 1.0$ the results computed with the first-order polynomial basis (second-order accurate solution) provide the accuracy level needed in aero-acoustic computations.

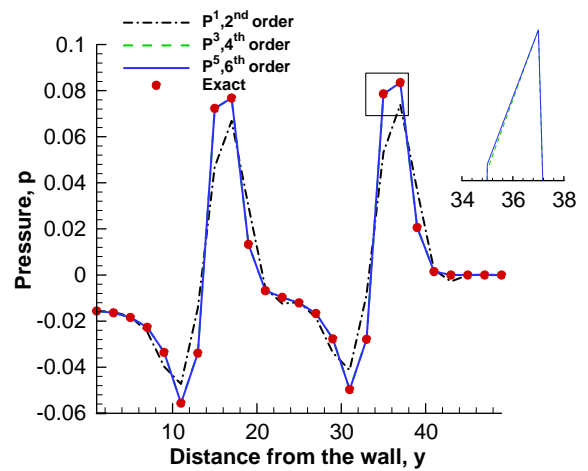


Fig. 95. Comparison of the pressure computed with P^1 , P^3 , and P^5 polynomial bases with the exact solution; in all cases the same canonical triangular mesh with $\Delta x = 2.0$ is used.

In Fig. 97, the grid convergence of the second-, fourth-, and sixth-order accurate solutions is shown. The error norm in Fig. 97 was computed on the symmetry line, where the error norm is expected to be

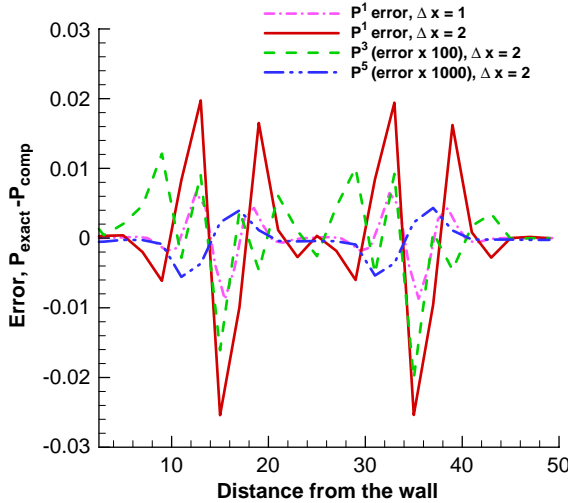


Fig. 96. Error of the solutions computed with P^1 , P^3 , and P^5 polynomial bases and canonical triangular meshes with $\Delta x = 2$.

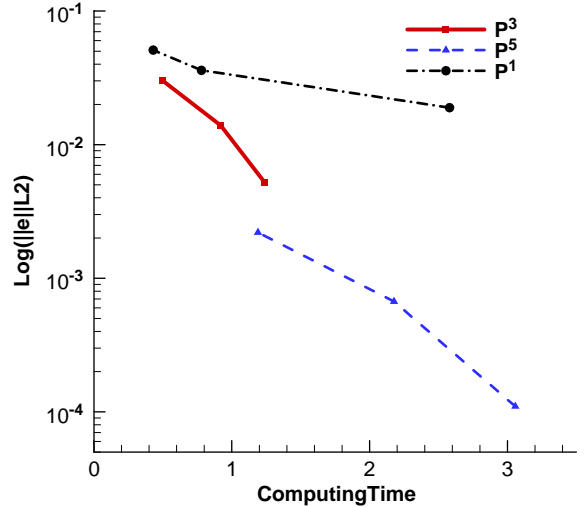


Fig. 98. Computing time required in order to achieve certain error level (L_2 error norm of the computed pressure) with second- (P^1), fourth- (P^3), and sixth-order (P^5) accurate solutions.

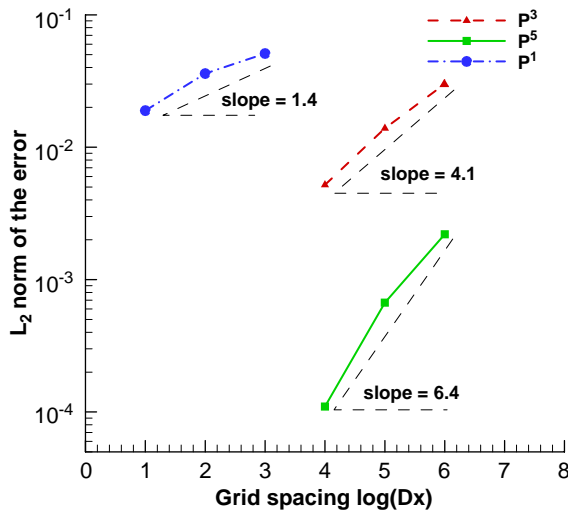


Fig. 97. Grid convergence (in the L_2 norm of the computed pressure) of the second- (P^1), the fourth- (P^3), and sixth-order (P^5) accurate solutions computed with triangular elements.

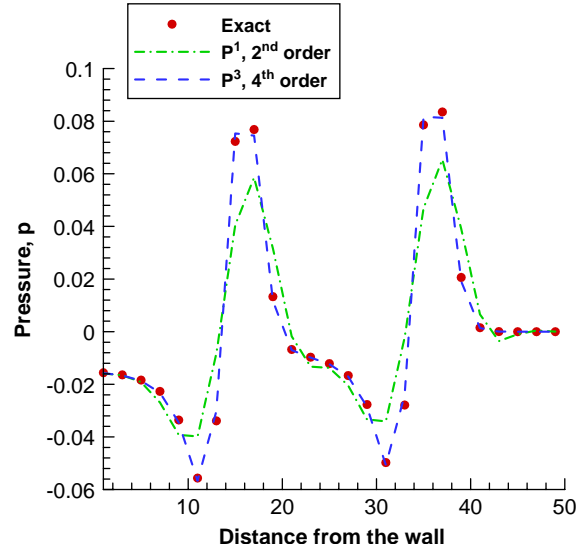


Fig. 99. Comparison of pressure field computed with quadrilateral canonical meshes and P^1 , P^3 polynomial bases with the exact solution.

the largest, and not for the entire domain. Norms of the error computed in the full domain do not differ much from the error norm obtained from the deviation of the computed solution from the exact result only on the symmetry line. The grid convergence plot of Fig. 97 shows that all solutions achieve the expected order of accuracy. Once again it is evident that the desired order of accuracy for CAA can only be achieved with higher-

order methods. Furthermore, it was found that for this simple problem the solution computed with fourth- or sixth-order accuracy and single precision practically converges when $\Delta x \approx 1.0$ and the remaining errors are mainly due to time integration. In Fig. 98, the reduction of the average error is plotted versus the required computing time for the solution. It can be seen that use of higher-order accuracy yields savings in

computing time when the solution must reach certain error level.

Solutions computed with quadrilateral meshes are presented next. A comparison of the pressure field computed with third-order polynomial basis with the exact result is shown in Fig. 99. It was found [244] that the solutions computed with quadrilateral elements do not achieve the $(k+1)$ th order of accuracy. This is expected because in a computation with third-order

basis, for example, the unit area (for $\Delta x = \delta y = 1$) is spanned by 16 polynomials in quadrilateral elements while for triangular element discretization the same area is covered by two elements and spanned by twenty ($2 \times P_{j=1,\dots,10}^3 = 20$) polynomials. In terms of computing efficiency, the solution obtained with quadrilateral elements requires slightly less computing time.

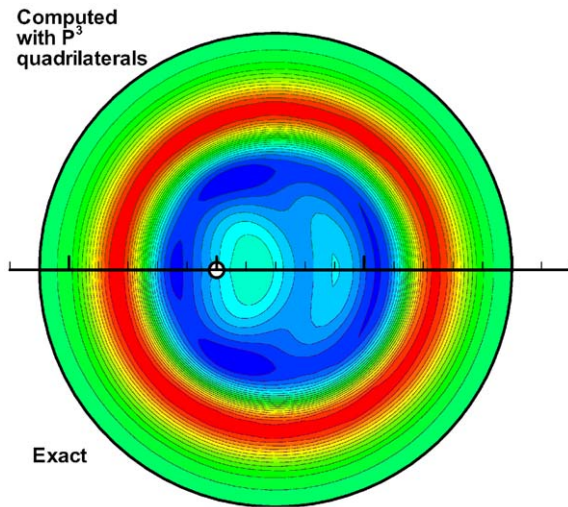


Fig. 100. Comparison of the computed pressure field obtained with P^3 quadrilateral elements with the exact solution for scattering from a cylinder surface.

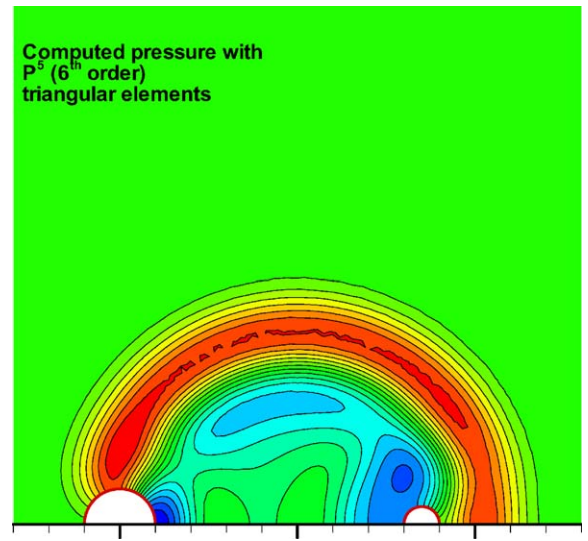


Fig. 102. Computed pressure field with triangular mesh and P^5 polynomial basis for scattering of a pressure pulse from the surfaces of two cylinders.

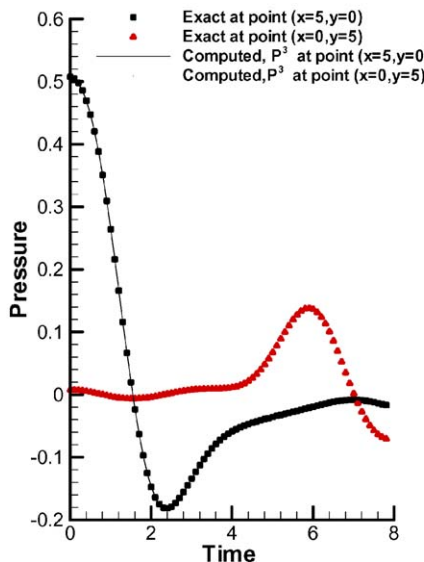
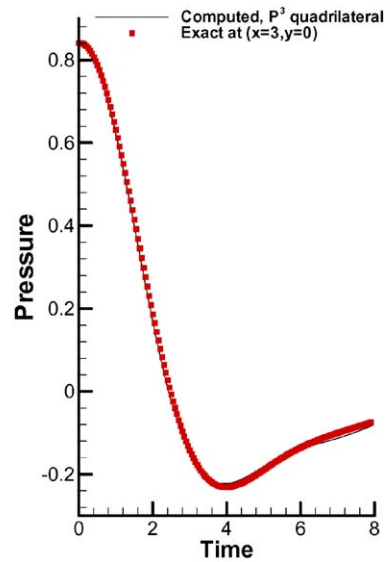


Fig. 101. Comparison of the computed pressure at $r = 5.0$ and $0 \leq T \leq 8$ for $\phi = 0^\circ$, and $\phi = 90^\circ$ with the exact solution of Ref. [33] for pulse scattering.



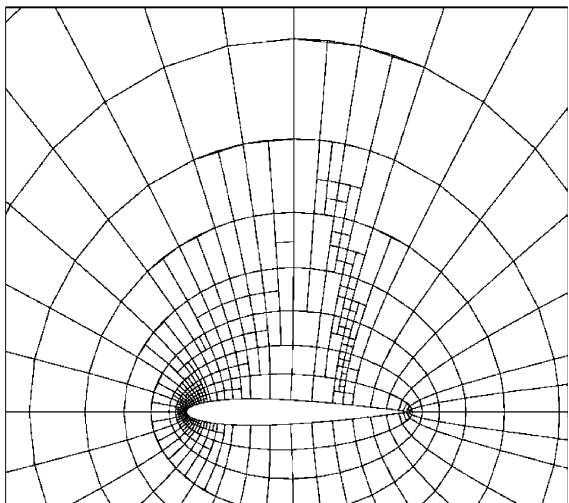
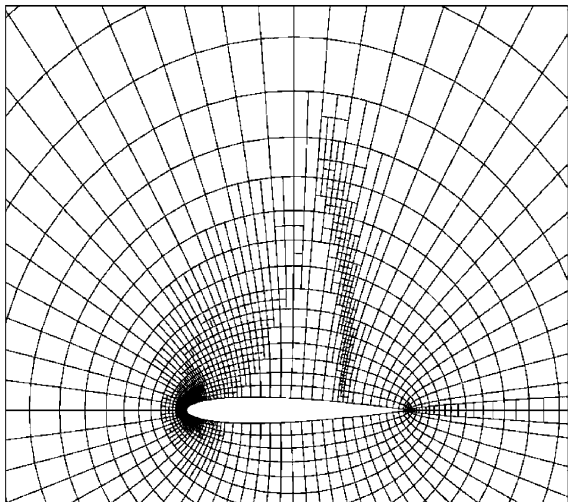
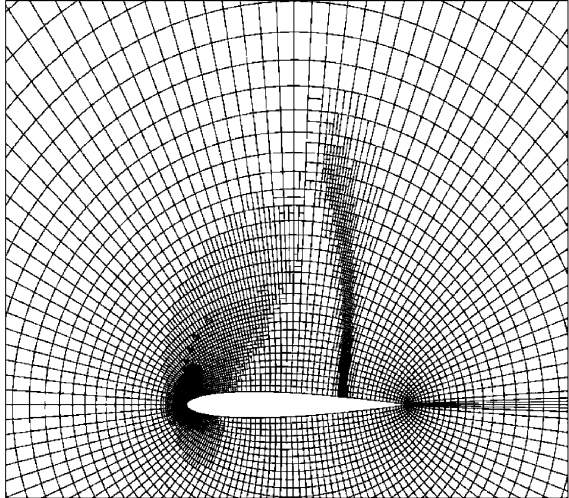


Fig. 103. Multigrid levels in an adapted mesh about the NACA 0012 airfoil.

Solutions for more complex domains were also computed. First, scattering of sound waves from the surface of a cylinder, which is one of the benchmark problems of [246], is considered. The computed solution with third-order polynomial basis and quadrilateral elements at $T = 8$ is compared qualitatively with the exact result in Fig. 100. Very good agreement with exact result is achieved for the solutions computed with both triangular and quadrilateral elements. The computational domain for the solution obtained with triangular elements contains 5437 elements or 2810 vertices. Discretization of the same domain with isoparametric quadrilaterals includes 2000 elements or 2091 vertices. In both cases the cylinder was represented by 40 elements. The time variation of the computed solution for $0 \leq T \leq 8$ is shown in Fig. 101. Again good agreement with the exact result [246] is achieved.

Next, scattering of a Gaussian pulse from the surfaces of two cylinders with different diameters is considered. The large cylinder has diameter $D_1 = 2$ and the small cylinder has diameter $D_2 = 1$. The distance between the centers is $8.5D_2$, the large cylinder center is at $(-5, 0)$, the small cylinder center is at $(3.5, 0)$ and the source is located at $(0, 0)$. The solution is computed using triangular elements because the meshing of the domain with triangular elements is easier and the resulting mesh is more isotropic. The surface of the large cylinder is represented by 40 elements and the surface of the small cylinder is represented by 20 elements. The entire domain contains 7671 elements or 3929 vertices and the solution is obtained with the p^5 polynomial basis. The computed pressure field at time $T = 10$ is shown in Fig. 102.

Numerical solutions obtained with the DG finite-element method for benchmark aeroacoustic problems demonstrated that only p^3 (fourth-order) or higher-order accurate discretizations provide the required resolution for CAA. In terms of computing time, solutions with equivalent order of accuracy obtained on triangular meshes require about 10% more resources than the solutions obtained with quadrilateral meshes. In both cases, the CFL stability limitations become more stringent, cf. [208] with the increase of the order of spatial accuracy. For isotropic meshes, the resolving ability of both triangular and quadrilateral space discretizations is approximately equivalent. For two-dimensional problems, it is feasible to achieve spatial accuracy up to sixth order. Sixth- or higher-order of accuracy is possibly advantageous for long time propagation of complex waveforms. Numerical tests for pure convection ($u_t + u_x = 0$) of complex one-dimensional waves of the form $u(x, t) = 0 = [2 + \cos(\alpha x)] \exp[-\ln 2(x/10)^2]$, $\alpha = 1.7$, using up to 10th-order accurate DG discretizations showed that for long time integration ($T > 400$) at least sixth-order accuracy is needed. Application of the DG finite-element

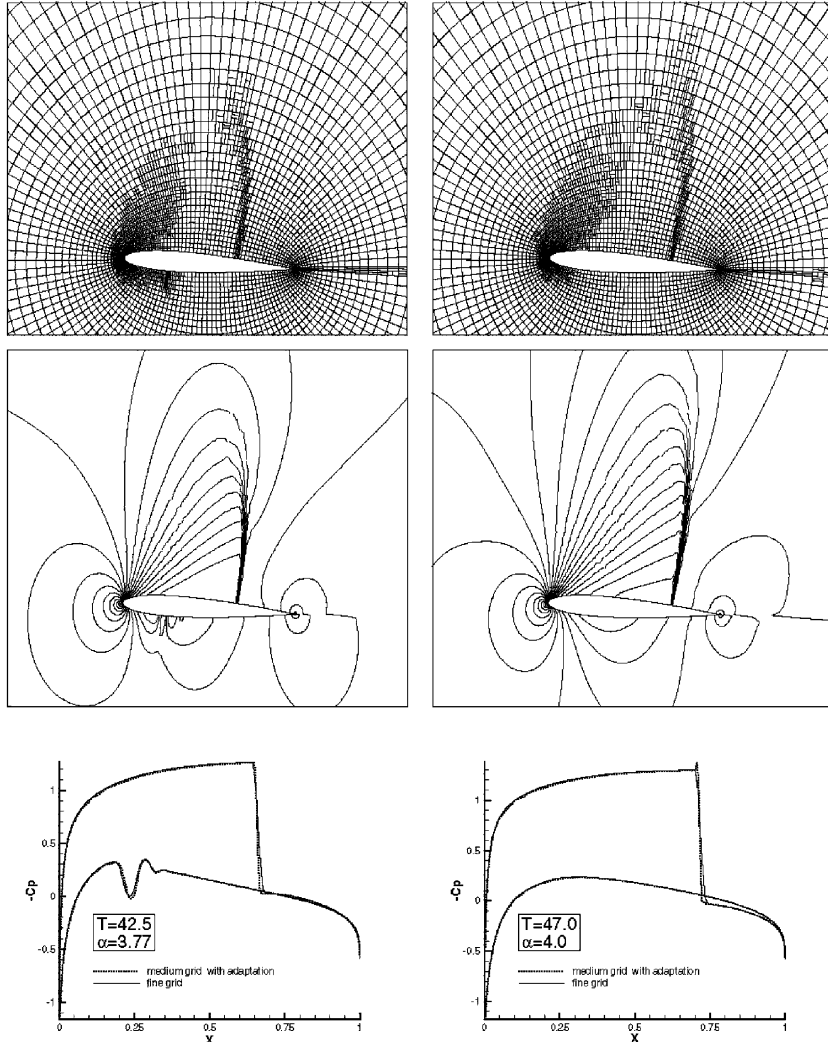


Fig. 104. Adapted mesh around an oscillating NACA0012 airfoil, contours of density and surface pressure coefficient C_p for $\alpha = 3.77^\circ$ (pitching upward) and $\alpha = 4.0^\circ$ (pitching downward); $M = 0.8$, $\omega = \pi/10$.

method for three-dimensional CAA applications is straightforward using the available finite-element framework [42] but beyond the scope of the present paper. It appears, however, that three-dimensional CAA applications with the DG method are feasible in terms of the required computing resources but discretizations with polynomial bases of order higher than three are possibly too intensive computationally.

Computations of compressible flows over realistic aerodynamic configurations with the DG method were carried out by Van der Vegt and Van der Ven [247] and more recently in [222]. Examples of the recent computations of transonic steady and unsteady airfoil flows of [222] using the space-time DG method and stabilization operators of Section 5.10 instead of slope limiters are

shown in Figs. 103 and 104. Very good resolution of transonic shocks was obtained with the stabilization operators. Adaptive grid refinement with “hanging nodes” that is possible for DG method yielded very good resolution of the shocks.

Computations of viscous turbulent flows with the DG method were recently presented by Bassi et al. [221]. Examples from these computations are shown in Figs. 105–107. Fig. 105 shows the computational mesh over turbomachinery blades. An implicit Runge–Kutta method was used for time marching in order to avoid the stringent stability limitations imposed by the small grid spacing required for the resolution of the near wall viscous phenomena. The unsteady flow field is shown with snapshots in Figs. 106 and 107. Additional results

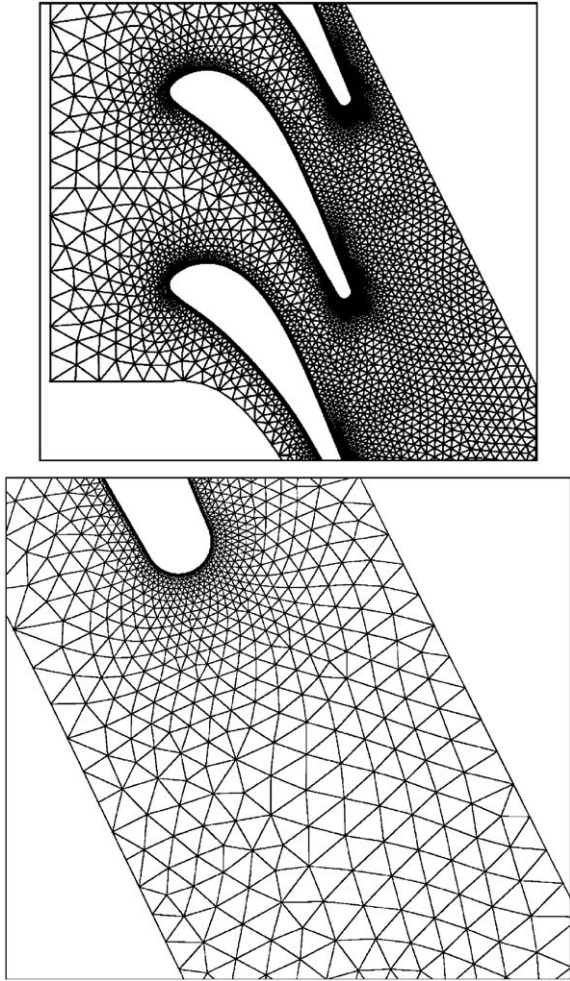


Fig. 105. Global view and detail of the grid around the blade.

with the DG method can be found in other recent publications [248–256].

6. The spectral volume (SV) method

The discontinuous Galerkin method of Section 5 is based on the finite-element framework and assumes a high-order data distribution for each element. As a result, the computed state variables are not continuous across the element boundaries and a Riemann solver is required to compute the fluxes through the element boundaries. The DG method is fully conservative and does not depend on grid smoothness. It was mentioned, however, in Section 5 that the main disadvantages of the DG method are the high computing cost and the deterioration of the CFL stability with the increase of the order of approximation. The high computing cost

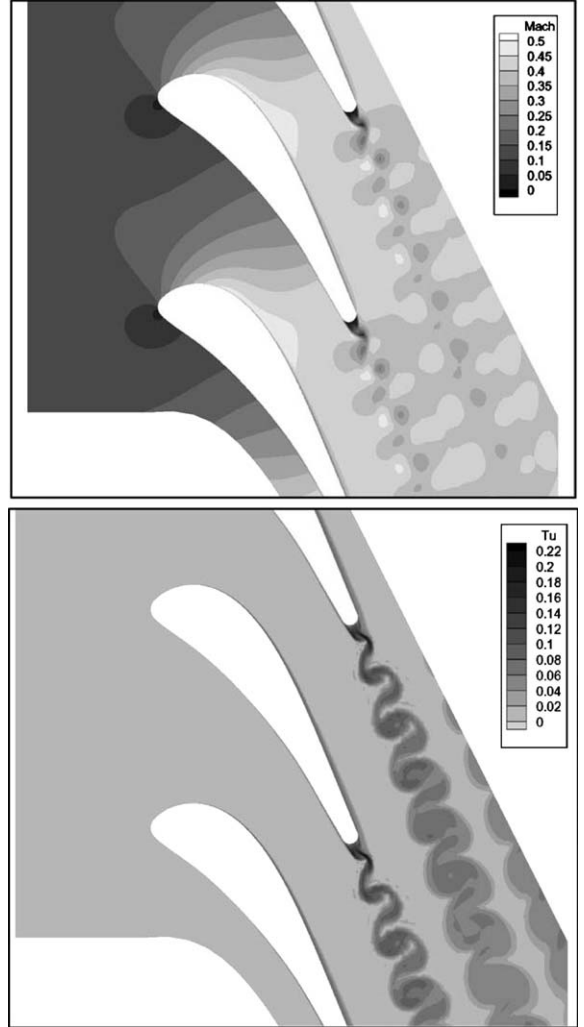


Fig. 106. Snapshot of Mach number and turbulence intensity computed with P2 elements.

for high-order solutions occurs because of the large number of the polynomial coefficients that need to be determined and the evaluation of high-order surface and volume integrals that are expensive to compute. A k th order DG method ($k - 1$ polynomial basis) requires $2k$ th accurate quadratures for the line or surface integrals and $(2k - 1)$ th order accurate quadrature formula for the volume integrals.

The spectral volume (SV) method is a new conservative high-order accurate numerical method developed by Wang in a series of papers [46,257,258]. The SV method is a finite-volume method for unstructured grids that unlike other FV methods does not require information from neighboring cells to perform reconstruction. The SV method like other FV methods and the DG method

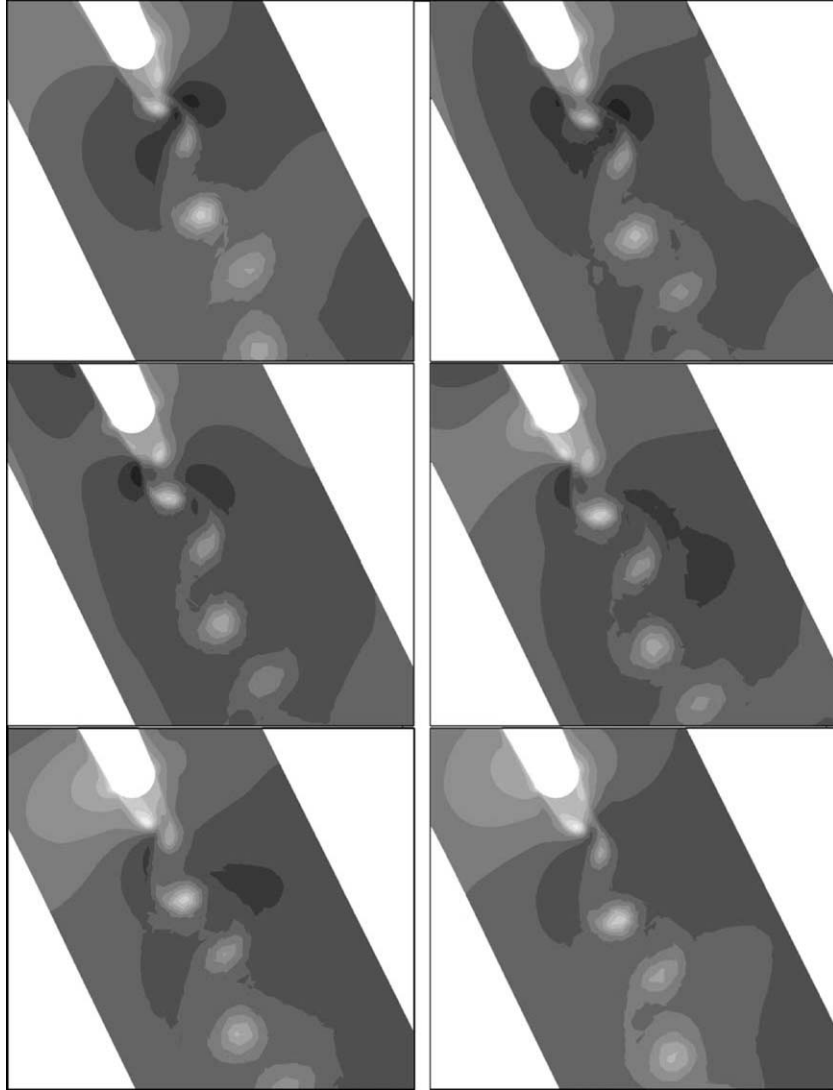


Fig. 107. Shedding from the blade trailing edge shown with density contours.

is suitable for discontinuity capturing with the application of TVD or TVB limiters.

6.1. Fundamentals of the SV method

The basic idea of the spectral volume method [46] is presented for the following multidimensional conservation law for the scalar $u(x, y, t)$

$$\frac{\partial u}{\partial t} + \frac{\partial f(u)}{\partial x} + \frac{\partial g(u)}{\partial y} = 0 \quad (6.1)$$

in the domain Ω with flux $\mathbf{F} = (f, g)$, initial condition $u(x, y, 0) = u_0(x, y)$, and appropriate boundary conditions.

The domain Ω is discretized into N nonoverlapping cells S_i called spectral volumes, which are the same as the usual finite volumes. The integral form of the scalar conservation law is

$$\int_{S_i} \frac{\partial u}{\partial t} dV + \oint_{\partial S_i} (\mathbf{F} \cdot \mathbf{n}) dA = 0, \quad (6.2)$$

where \mathbf{n} is the outward unit normal on ∂S_i . The cell-averaged state variable for the spectral volume S_i is defined in the usual way as

$$\bar{u}_i = \frac{1}{V_i} \int_{S_i} u dV, \quad (6.3)$$

where V_i is the area or volume of the spectral volume S_i .

The discrete formula of the integral conservation law, Eq. (6.2), for a spectral volume with M faces is expressed as

$$\frac{d\bar{u}_i}{dt} + \frac{1}{V_i} \sum_{m=1}^M \int_{A_m} (\mathbf{F} \cdot \mathbf{n}) dA. \quad (6.4)$$

The surface or line integral on each face or edge, respectively can be performed with a k th order accurate Gauss quadrature as follows

$$\begin{aligned} \int_{A_m} (\mathbf{F} \cdot \mathbf{n}) dA &= \sum_{j=1}^J \omega_{mj} F(u(x_{mj}, y_{mj})) \cdot \mathbf{n}_m A_m \\ &+ \mathcal{O}(h^k), \end{aligned} \quad (6.5)$$

where ω_{mj} are the Gauss quadrature weights and x_{mj}, y_{mj} are the Gauss quadrature points.

A k th order accurate approximation of the state variable in the spectral volume (SV) S_i can be obtained with a $(k-1)$ th order polynomial in x and y as

$$p_i(x, y) = u(x, y) + \mathcal{O}(h^k), \quad (x, y) \in S_i. \quad (6.6)$$

This approximation of the state variable is in general discontinuous across the SV boundaries unless the state variable is a $(k-1)$ th order polynomial or less. Similar to the FV or DG methods, the flux integration on the two sides of the SV faces involves two discontinuous state variables. Therefore, this flux integration is carried out using an exact or an approximate Riemann solver

$$\begin{aligned} F(u(x_{mj}, y_{mj})) \cdot \mathbf{n}_m \\ \cong F_{\text{Riemann}}(p_i(x_{mj}, y_{mj}), p_{i,m}(x_{mj}, y_{mj}), \mathbf{n}_m) + \mathcal{O}(h^k), \end{aligned} \quad (6.7)$$

where $p_{i,m}$ is the k th order approximation of the exact state variable in the neighboring cell.

The k th order accurate scheme of the SV, S_i is

$$\frac{d\bar{u}_i}{dt} + \frac{1}{V_i} \sum_{m=1}^M \sum_{j=1}^J \omega_{mj} F_R(p_i, p_{i,m}, \mathbf{n}_m) A_m = \mathcal{O}(h^k). \quad (6.8)$$

For a high-order FV method, including FV ENO and WENO schemes, the high-order polynomial approximation of the state variable on the cell under consideration (see Fig. 108a) is obtained using a stencil that contains the cell and sufficient number of neighboring cells. For a DG method, on the other hand, the polynomial form is assumed and the expansion coefficients are the variables. In the SV method, instead of using a large number of neighboring cells, the reconstruction is performed by partitioning the SV into subcells called control volumes (see Fig. 108b). The order of accuracy of the SV method is determined by the number of CVs in which each SV is subdivided. The weak analogy between the DG method and the SV method is that for the DG method the order of accuracy is related to the number of nodes on the

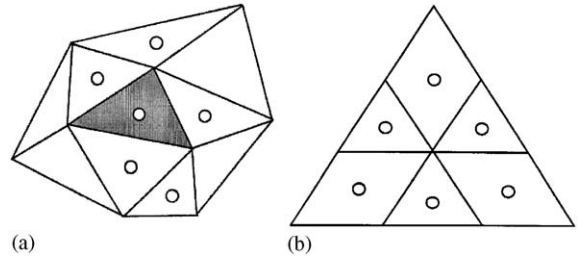


Fig. 108. (a) A possible reconstruction stencil for a quadratic reconstruction in high-order k -exact finite-volume scheme. (b) The partition of a spectral volume into six control volumes supporting a quadratic reconstruction.

element while in the SV method is determined by the number of subdivisions in control volumes. Possible minimum CVs subdivisions of a SV for linear, quadratic, and cubic data reconstructions are shown in Figs. 109–111, respectively.

The cell-averaged state variables \bar{u}_i for the spectral volumes S_i are updated from the time level n to the time level $n+1$ with Eq. (6.8). The crucial step in the SV method is that the update $\Delta\bar{u}_i = \bar{u}_i^{n+1} - \bar{u}_i^n$ must be scattered back to the cell-averaged variables in the control volumes $c_{i,j}$ in S_i . Then the same high-order reconstruction can be used again at the time level $n+1$ to the time level $n+2$, etc. The relationship between the cell-averaged variables for S_i and the cell-averaged variables for the CV in S_i is

$$\bar{u}_i = \frac{\sum_{j=1}^K \bar{u}_{i,j} V_{i,j}}{V_i}, \quad (6.9)$$

where $\bar{u}_{i,j}$ denotes the cell-averaged state variable of the j th control volume $c_{i,j}$ of S_i and $V_{i,j}$ is its volume. The total number of CV in S_i is K and $V_i = \sum_{j=1}^K V_{i,j}$. Furthermore, in order to ensure conservation the CVs updates must satisfy

$$\Delta\bar{u}_i = \frac{\sum_{j=1}^K \Delta\bar{u}_{i,j} V_{i,j}}{V_i}. \quad (6.10)$$

A scattering scheme for high-order ($k > 2$) reconstruction is obtained as follows. Each CV inside a SV is treated separately to update the cell-averaged state variable for the CV. Inside a particular SV, however, the state variables are continuous across the interior boundaries of the CV. Therefore, it is not necessary to use a Riemann flux or flux splitting for the boundaries of the CVs. At the CVs boundaries analytic fluxes are used and Riemann fluxes are only necessary at the SV boundaries. High-order accuracy is preserved by using high-order quadratures not only for the Riemann fluxes at the SV boundaries, but also for the analytical fluxes through the interior CV boundaries within the SV.

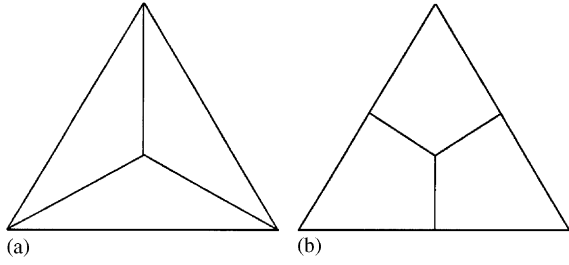


Fig. 109. Control volumes in a triangular *linear* spectral volume. (a) Type 1, $n_1 = 0, n_3 = 1, n_6 = 0$. (b) Type 2, $n_1 = 0, n_3 = 1, n_6 = 0$.

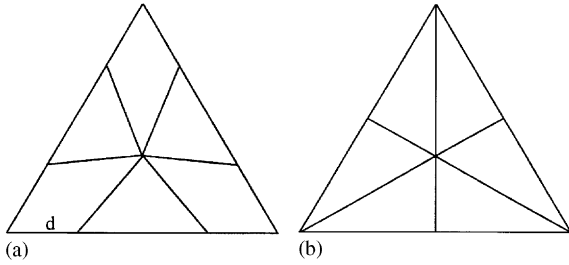


Fig. 110. Possible triangular *quadratic* spectral volume partitions. (a) Type 1 with $d = \frac{1}{3}$ and Type 2 with $d = \frac{1}{4}$; $n_1 = 0, n_3 = 2, n_6 = 0$. (b) A singular partition; $n_1 = 0, n_3 = 0, n_6 = 1$.

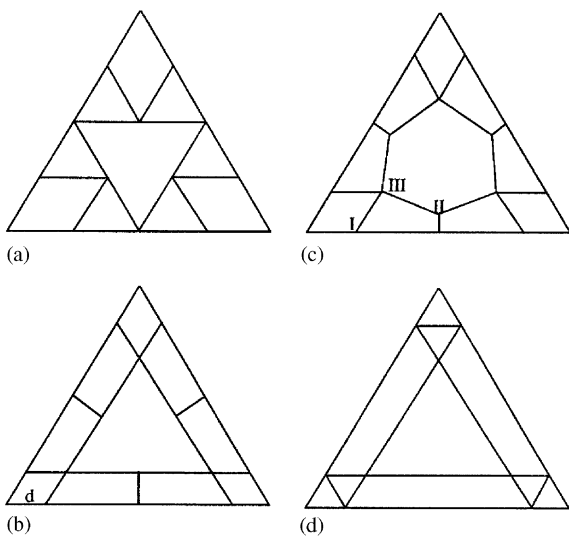


Fig. 111. Possible *cubic* triangular spectral volumes. (a) Type 1, $n_1 = 1, n_3 = 1, n_6 = 1$. (b) Type 2 with $d = \frac{1}{6}$ and Type 3 with $d = \frac{1}{15}$; $n_1 = 1, n_3 = 1, n_6 = 1$. (c) $n_1 = 1, n_3 = 1, n_6 = 1$. (d) $n_1 = 1, n_3 = 3, n_6 = 0$.

In summary, the main steps for a k th order ($k - 1$ polynomial reconstruction) SV method include:

- (1) Computation of the state variables at the quadrature points.

- (2) Use of a k th order quadrature (exact for $k - 1$ polynomial) and a Riemann solver to compute the surface fluxes at the SV boundaries.
- (3) Use of a k th order quadrature and analytic fluxes to compute the surface fluxes at the CV boundaries.
- (4) Use of a suitable time marching scheme.

It appears that the SV method shares many of the DG method desirable features, e.g. it is compact, therefore suitable for parallel implementation, high-order accurate, conservative and capable of handling complex geometries. In fact, Zhang and Shu [259] performed an analysis of the SV method considering the SV method as a Petrov–Galerkin finite-element method where the solution space and the test function space are different. The SV method requires larger number of flux computations at the CV boundaries, while the DG method requires evaluation of volume integrals. The implementation of the SV method is presented in detail starting from the one-dimensional scalar conservation law.

6.2. SV method in one dimension

Consider the one-dimensional conservation law in $[a, b]$

$$\frac{\partial u(x, t)}{\partial t} + \frac{\partial f(u(x, t))}{\partial x} = 0.$$

$$u(x, 0) = u_0(x). \quad (6.11)$$

The domain $[a, b]$ is divided into N nonoverlapping SVs

$$[a, b] = \bigcup_{n=1}^N S_i, \quad S_i = [x_{i-1/2}, x_{i+1/2}], \quad (6.12)$$

where $x_{i+1/2} - x_{i-1/2} = h_i$.

Given the desired order of accuracy k , for the numerical solution of Eq. (6.11), each spectral volume S_i is subdivided into k control volumes $\{x_{i,j+1/2}\}_{j=0}^k$ denoted $c_{i,j}$ with $x_{i,j+1/2} = x_{i-1/2}$ and $x_{i,k+1/2} = x_{i+1/2}$ (see Fig. 112).

The cell-averaged state variables for $c_{i,j}$ are

$$\bar{u}_{i,j} = \frac{\int_{x_{i,j-1/2}}^{x_{i,j+1/2}} u(x, t) dx}{h_{i,j}}, \quad i = 1, \dots, N, \quad j = 1, \dots, k, \quad (6.13)$$

where $h_{i,j} = x_{i,j+1/2} - x_{i,j-1/2}$.

6.2.1. Reconstruction for SV in one dimension

The reconstruction problem is: Given the cell-averaged values $\bar{u}_{i,j}$ for all CVs in S_i construct a polynomial $p_i(x)$ for S_i of degree $k - 1$ the most such that $p_i(x)$ is a k th order accurate approximation of $u(x)$ inside S_i , e.g.

$$p_i(x) = u(x) + \mathcal{O}(h^k), \quad x \in S_i, \quad i = 1, \dots, N. \quad (6.14)$$

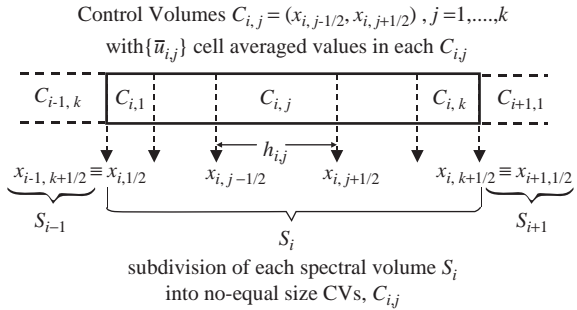


Fig. 112. Subdivision of the spectral volume S_i into control volumes for the one-dimensional problem.

In particular, $p_i(x)$ gives the following approximation of $u(x)$ on the CV boundaries

$$\begin{aligned} u_{i,j+1/2} &\equiv p_i(x_{i,j+1/2}) \\ &= u(x_{i,j+1/2}) + \mathcal{O}(h^k), \quad i = 1, \dots, N, \\ &\quad j = 0, \dots, k. \end{aligned} \quad (6.15)$$

This reconstruction problem is solved with the same method presented in Section 4 for the ENO reconstruction. For completeness, the procedure of Section 4 is repeated here in SV context.

There is a unique polynomial of degree $k - 1$ at most whose cell average in each of the CVs in S_i (see Fig. 112) satisfies

$$\frac{\int_{x_{i,j-1/2}}^{x_{i,j+1/2}} p_i(x) dx}{h_{i,j}} = \bar{u}_{i,j}, \quad j = 1, \dots, k. \quad (6.16)$$

This is the polynomial we are looking for in Eqs. (6.14) and (6.15). The mappings from given cell averages $\bar{u}_{i,j}$ to the CV boundary values of the state variables are linear. Therefore, coefficients c_{rj} can be found, which depend on the order of accuracy k and the CV size $h_{i,j}$ in S_i but not on u itself, such that

$$u_{i,j+1/2} = \sum_{r=1}^k c_{rj} \bar{u}_{i,r}, \quad j = 0, \dots, k. \quad (6.17)$$

As a result, given the k cell averages $\bar{u}_{i,1}, \dots, \bar{u}_{i,k}$ for the CVs in S_i the reconstructed point values at the CV boundaries $x_{i,j+1/2}$, computed from Eq. (6.17), are k th order accurate

$$u_{i,j+1/2} = u(x_{i,j+1/2}) + \mathcal{O}(h^k), \quad j = 0, \dots, k. \quad (6.18)$$

The primitive function $U(x)$ of $u(x)$ is used to obtain the constants c_{rj} in Eq. (6.17). The primitive function of $u(x)$ is

$$U(x) = \int_{x_{i,1/2}}^x u(\xi) d\xi, \quad x \in S_i. \quad (6.19)$$

At the control volume boundaries, $U(x_{i,j+1/2})$ is exactly known from the cell averages $\bar{u}_{i,j}$.

$$\begin{aligned} U(x_{i,j+1/2}) &= \sum_{r=1}^j \int_{x_{i,r-1/2}}^{x_{i,r+1/2}} u(\xi) d\xi \\ &= \sum_{r=1}^j \bar{u}_{i,r} h_{i,r}, \quad j = 1, \dots, k \end{aligned}$$

$$U(x_{i,1/2}) = 0 \quad \text{for } j = 0. \quad (6.20)$$

The unique polynomial that interpolates $U(x_{i,j+1/2})$, $j = 0, \dots, k$ is $P_i(x)$. Then for $p_i(x) = P'_i(x)$ have

$$\begin{aligned} \frac{1}{h_{i,j}} \int_{x_{i,j-1/2}}^{x_{i,j+1/2}} p_i(x) dx &= \frac{1}{h_{i,j}} \int_{x_{i,j-1/2}}^{x_{i,j+1/2}} u(x) dx \\ &= \bar{u}_{i,j}, \quad j = 1, \dots, k. \end{aligned} \quad (6.21)$$

Therefore, $p_i(x) \equiv P'_i(x)$ is the polynomial of Eq. (6.14) that satisfies the accuracy requirement of Eq. (6.15).

The constants c_{rj} are obtained considering the Lagrange interpolation polynomial $P_i(x)$

$$P_i(x) = \sum_{r=0}^k U_{i,r+1/2} \prod_{\substack{m=0 \\ m \neq r}}^k \frac{x - x_{i,m+1/2}}{x_{i,r+1/2} - x_{i,m+1/2}}, \quad x \in S_i, \quad (6.22)$$

$$\begin{aligned} p_i(x) &= \sum_{r=1}^k \left\{ h_{i,r} \sum_{q=r}^k \frac{1}{[(x_i - x_{i,1/2}) \dots (x - x_{i,q+1/2})']} \right. \\ &\quad \times \sum_{\substack{m=0 \\ m \neq q}}^k \prod_{\substack{p=0 \\ p \neq q, m}}^k (x - x_{i,p+1/2}) \left. \right\} \bar{u}_{i,r} \sum_{r=1}^k \phi_r(x) \bar{u}_{i,r}. \end{aligned} \quad (6.23)$$

Considering that $p_i(x) = P'_i(x)$ and substituting Eq. (6.17) in the expression for $p_i(x)$ obtain

$$\begin{aligned} c_{rj} &= h_{i,r} \sum_{q=r}^k \frac{1}{(x - x_{i,1/2})(x - x_{i,3/2}) \dots (x - x_{i,q+1/2})} \\ &\quad \times \sum_{\substack{m=0 \\ m \neq q}}^k \prod_{\substack{p=0 \\ p \neq q, m}}^k (x_{i,j+1/2} - x_{i,p+1/2}). \end{aligned} \quad (6.24)$$

For CV of equal size Eq. (6.24) simplifies to

$$c_{rj} = \sum_{q=r}^k \frac{1}{\prod_{p=0}^k (r-p)} \sum_{\substack{m=0 \\ m \neq q}}^k \prod_{\substack{p=0 \\ p \neq q, m}}^k (j-q). \quad (6.25)$$

At the interior CV boundaries in S_i the state variables are continuous and it is not necessary to use a numerical flux to update the reconstructed variables at the CV boundaries. In other words, for the update at the

interior

$$\frac{d\bar{u}_{i,j}}{dt} = -\frac{1}{h_{i,j}}(\hat{f}_{i,j+1/2} - \hat{f}_{i,j-1/2}) \quad (6.26)$$

the numerical flux is the analytical flux function

$$\hat{f}_{i,j+1/2} = f(u_{i,j+1/2}), \quad j = 1, \dots, k-1.$$

At the SV boundaries $x_{i-1/2}$ and $x_{i+1/2}$ or $x_{i,1/2}$ and $x_{i,k+1/2}$ (see Fig. 112) the state variables are discontinuous because at $x_{i-1/2}$ for example there is one value due to the reconstruction in S_i and another due to the reconstruction in S_{i-1} . Therefore, a numerical flux is computed at $x_{i-1/2}$ with a Riemann solver

$$\hat{f}_{i,1/2} = \hat{f}_{\text{Riemann}}(u_{i-1,k+1/2}, u_{i,1/2}) = \hat{f}_{i-1,k+1/2}. \quad (6.27)$$

The numerical flux must satisfy the following condition to ensure monotonicity of the first-order scheme

- (1) Locally Lipschitz and consistent $\hat{f}(u, u) = f(u)$,
- (2) \hat{f} is a nondecreasing function of its first argument,
- (3) \hat{f} is a non-increasing function of the second argument.

The Lax–Friedrich’s or the Roe flux can be used as numerical fluxes. Time marching of the semidiscrete form

$$\frac{d\bar{u}}{dt} = L(\bar{u}), \quad (6.28)$$

$$\bar{u} = \begin{bmatrix} \bar{u}_{1,1} \\ \vdots \\ \bar{u}_{i,j} \\ \vdots \\ \bar{u}_{N,k} \end{bmatrix}, \quad L(\bar{u}) = \begin{bmatrix} L_{1,1}(\bar{u}) \\ \vdots \\ L_{i,j}(\bar{u}) \\ \vdots \\ L_{N,k}(\bar{u}) \end{bmatrix},$$

$$L_{i,j} = -\frac{1}{h_{i,j}}[f_{i,j+1/2}(\bar{u}) - f_{i,j-1/2}(\bar{u})]$$

can be obtained with TVD RK schemes of Section 2.

The reconstruction quality strongly depends on the choice for CV subdivision. The obvious choice of equal size CVs subdivision of a spectral volume is not optimal for high-order ($k > 3$) reconstruction. It was found in [46] that high-order reconstructions on uniform CV subdivisions are highly oscillatory near the two SV boundary grid points $x_{i,1/2}$ and $x_{i,k+1/2}$. The source of this oscillatory behavior for high-order reconstructions was identified to be the oscillatory behavior of Lagrange polynomials that interpolate non-polynomial functions on equidistant points. Taking into account that Lagrange polynomials are used for the interpolations of Eqs. (6.22) and (6.23) it is expected that the subdivision of a SV into equal size CVs is not optimal. It was found

in [46] that it is necessary to cluster “grid points” near the boundaries of the SV interval to make the reconstruction less oscillatory.

One way to perform CV subdivision is to use the Gauss-Lobatto points for CV subdivision. For the standard interval $[-1, 1]$ the Gauss-Lobatto points are defined by

$$x_{i,j+1/2} = -\cos\left(\frac{j\pi}{k}\right), \quad j = 0, \dots, k. \quad (6.29)$$

Another clustering function is the hyperbolic tangent function defined by

$$x_{i,j+1/2} = \frac{\tanh\left(\frac{2\beta j}{k} - \mu\right)}{\tanh(\beta)}, \quad j = 0, \dots, k, \quad (6.30)$$

where β is a constant controlling the degree of clustering near the endpoints. Large values of β result in stronger grid clustering. The value $\beta = 0.6$ in Eq. (6.30) yields quite even distribution and the polynomials are highly oscillatory at the end points. For $\beta = 1.6$ a grid similar to the Gauss-Lobatto grid is obtained and the oscillations of the polynomials diminishes significantly.

It is well known that the Gibbs phenomenon associates with high-order schemes in the presence of discontinuities causes loss of monotonicity in the solution of hyperbolic conservation laws. The SV method is not excluded for Gibbs phenomenon. In particular, since the lowest order reconstruction for the SV method is linear (second-order accurate scheme), and there are no linear second- or higher-order schemes which guarantee monotonicity, some limiting approach must be applied to the SV method to achieve monotonicity. In Ref. [46] the limiting approach originally developed by van Leer [127,128], is applied. The van Leer’s approach limits the reconstruction so that the reconstructed solution is monotonic. Details about limiting for the SV method in one dimension can be found in [46].

6.3. Polynomial reconstruction in triangular SVs

Further development of the SV method for two-dimensional scalar equations was presented by Wang and Liu in [257]. The two-dimensional formulation of the SV method is becomes

$$\frac{d\bar{u}_{i,j}}{dt} + \frac{1}{V_{i,j}} \sum_{r=1}^K \int_{S_r} (\mathbf{F} \cdot \mathbf{n}) dS = 0, \quad (6.31)$$

where $\bar{u}_{i,j} = 1/V_{i,j} \int_{c_{i,j}} u dV$ are the cell-averaged variables for $c_{i,j}$, K is the total number of faces (or edges in 2D) in $c_{i,j}$ and S_r denotes the r th face of $c_{i,j}$. Using a k th order accurate Gauss quadrature ($k = m + 1$) for the evaluation of the surface integral

in Eq. (6.31)

$$\int_{S_r} (\mathbf{F} \cdot \mathbf{n}) dS = \sum_{q=1}^J \omega_{rq} \mathbf{F}(u(x_{rq}, y_{rq})) \cdot \mathbf{n}_r S_r + \mathcal{O}(A_r h^k), \quad (6.32)$$

where $J = (k+1)/2$ is the total number of quadrature points, ω_{rq} are the Gaussian quadrature weights, and h is the maximum length of all CVs obtain

$$\frac{d\bar{u}_{i,j}}{dt} + \frac{1}{V_{i,j}} \sum_{r=1}^K \sum_{q=1}^J \omega_{rq} \mathbf{F}(u(x_{rq}, y_{rq})) \cdot \mathbf{n}_r S_r + \mathcal{O}(h^k). \quad (6.33)$$

Assuming that a multidimensional polynomial in x and y of degree $k-1$ the most exists on S_i which is the k th order approximation of the state variable in S_i

$$p_i(x, y) = u(x, y) + \mathcal{O}(h^k) \quad (x, y) \in S_i. \quad (6.34)$$

This polynomial approximation yields discontinuous state variables across the SV boundaries (unless the variables are polynomials of $k-1$ degree or less) and a flux integration with an exact or approximate Riemann solver is needed, i.e.

$$F(u(x_{rq}, y_{rq})) \cdot \mathbf{n}_r = F_{\text{Riemann}}(p_i(x_{rq}, y_{rq}), p_{i,r}(x_{rq}, y_{rq}), \mathbf{n}_r) + \mathcal{O}(p_i - p_{i,r}), \quad (6.35)$$

where $p_{i,r}$ denotes the reconstruction polynomial of a neighboring CV $c_{i,j}^r$ which shares the face A_r with the $c_{i,j}$ and since both p_i and $p_{i,r}$ are k th order accurate approximations of the exact state variables the semi-discrete k th order accurate scheme for $c_{i,j}$ is

$$\begin{aligned} \frac{d\bar{u}_{i,j}}{dt} + \frac{1}{V_{i,j}} \sum_{r=1}^K \sum_{q=1}^J \omega_{rq} \\ \times F_{\text{Riemann}}(p_i(x_{rq}, y_{rq}), p_{i,r}(x_{rq}, y_{rq}), \mathbf{n}_r) S_r + \mathcal{O}(h^k) \end{aligned} \quad (6.36)$$

or in vector form

$$\frac{d\bar{u}}{dt} = \mathbf{R}_h(\bar{u}), \quad (6.37)$$

$$\bar{u} = \begin{bmatrix} \bar{u}_{1,1} \\ \bar{u}_{i,j} \\ \bar{u}_{I,N} \end{bmatrix}, \quad \mathbf{R}_h(\bar{u}) = \begin{bmatrix} R_{1,1}(\bar{u}) \\ R_{i,j}(\bar{u}) \\ R_{I,N}(\bar{u}) \end{bmatrix},$$

$$R_{i,j} = -\frac{1}{V_{i,j}} \sum_{r=1}^K \sum_{q=1}^J \omega_{rq} F_{\text{Riemann}}(p_i(x_{rq}, y_{rq}), p_{i,r}(x_{rq}, y_{rq}), \mathbf{n}_r) S_r.$$

Approximation of the solution can be obtained with any linearly independent functions. Reconstruction in [257] is obtained with polynomial basis functions as in Eq. (6.34). The dimension of the polynomial approx-

imation space P_m of degree m polynomials in two dimensions is

$$N_m = \binom{m+2}{2} = \frac{(m+1)(m+2)}{2}. \quad (6.38)$$

The reconstruction of u in P_m is achieved by partitioning S_i into a N_m nonoverlapping CVs, $c_{i,j}$, $j = 1, \dots, N_m$. The reconstruction problem is to find a polynomial $p_m \in P_m$ such that

$$\int_{c_{i,j}} p_m(x, y) dV = \int_{c_{i,j}} u(x, y) dV, \quad j = 1, \dots, N_m. \quad (6.39)$$

Introducing the complete polynomial basis $e_l(x, y) \in P_m$, the polynomial p_m can be expressed as

$$p_m = \sum_{l=1}^{N_m} c_l e_l(x, y), \quad (6.40)$$

where $e = [e_1, \dots, e_N]^T$ is the basis function vector and c_l , $l = 1, \dots, N$ are the reconstruction coefficients, and substituting Eq. (6.40) in Eq. (6.39) obtain

$$\frac{1}{V_{i,j}} \sum_{l=1}^{N_m} c_l \int_{c_{i,j}} e_l(x, y) dV = \bar{u}_{i,j}, \quad j = 1, \dots, N_m. \quad (6.41)$$

This equation is written in matrix form as

$$[R]\mathbf{c} = \bar{u}, \quad (6.42)$$

where $\bar{u} = [\bar{u}_{1,1} \dots \bar{u}_{i,N}]^T$ and $[R]$ is the reconstruction matrix given by

$$[R] = \begin{bmatrix} \frac{1}{V_1} \int_{c_{1,1}} e_1(x, y) dV & \frac{1}{V_1} \int_{c_{1,1}} e_N(x, y) dV \\ \frac{1}{V_N} \int_{c_{i,N}} e_1(x, y) dV & \frac{1}{V_N} \int_{c_{i,N}} e_N(x, y) dV \end{bmatrix} \quad (6.43)$$

and the reconstruction coefficients in Eq. (6.40) are obtained by

$$\mathbf{c} = [R]^{-1} \bar{u}. \quad (6.44)$$

Substituting of Eq. (6.44) in Eq. (6.39) yield an expression of p_m in terms of the basis functions as

$$p_m = \sum_{j=1}^{N_m} L_j(x, y) \bar{u}_{i,j} = [L]\bar{u}, \quad (6.45)$$

$$[L] = \mathbf{e}[R]^{-1}. \quad (6.46)$$

The values of u at the quadrature points x_{rq}, y_{rq} within the SV are given according to Eq. (6.45) by

$$p_m(x_{rq}, y_{rq}) = \sum_{j=1}^{N_m} L_j(x_{rq}, y_{rq}) \bar{u}_{i,j}. \quad (6.47)$$

This equation expresses an interpolation of a functional value at a point using the cell-averaged values with

weights equal to the basis functional value evaluated at the corresponding point.

Spectral volumes of various types, e.g. triangular, quadrilateral, or polygons of other types are possible choices. The special case where all SVs are triangular and all CVs are polygons with straight edges is considered. For this case, SVs with different shapes, which are partitioned in CVs of similar geometrical shape, have the same reconstruction, e.g. the functional values of the bases at corresponding mesh points are the same.

For triangular shape SVs, consider the map $\psi : s \rightarrow D$, of Fig. 113a. This “map” transforms an arbitrary triangle s to a right triangle D . Another map (see Fig. 113b) often used transforms s to an equilateral triangle E . Assume that one node of s is at the origin $\mathbf{r}_0 = (0, 0)$ and the other two at $\mathbf{r}_1 = (x_1, y_1)$ and $\mathbf{r}_2 = (x_2, y_2)$. The nodes corresponding to \mathbf{r}_0 , \mathbf{r}_1 and \mathbf{r}_2 in D are $(0, 0)$, $(1, 0)$ and $(0, 1)$, respectively. The map ψ can be written as

$$\psi : \mathbf{r} = \mathbf{r}_1\xi + \mathbf{r}_2\eta, \quad \xi \geq 0, \eta \geq 0, \xi + \eta \leq 1. \quad (6.48)$$

The map of Eq. (6.48) is linear therefore for a complete set of basis functions $e(x, y) \in P_m$ have

$$dV = dx dy = 2V d\xi d\eta, \quad V = \frac{1}{2}|\mathbf{r}_1 \times \mathbf{r}_2|, \quad (6.49)$$

$$e(x, y) = e(\xi, \eta)T, \quad (6.50)$$

where T is the transformation matrix containing only the geometry information. For example, if $e(x, y) = [1, x, y, x^2, xy, y^2]$ is the hierarchical basis then T becomes

$$T = \begin{bmatrix} 1 & 0 & 0 & 0 & 0 & 0 \\ 0 & x_1 & y_1 & 0 & 0 & 0 \\ 0 & x_2 & y_2 & 0 & 0 & 0 \\ 0 & 0 & 0 & x_1^2 & x_1y_1 & y_1^2 \\ 0 & 0 & 0 & 2x_1x_2 & x_1y_2 + x_2y_1 & 2y_1y_2 \\ 0 & 0 & 0 & x_2^2 & x_2y_2 & y_2^2 \end{bmatrix}. \quad (6.51)$$

the Eq. (6.46) becomes

$$\begin{aligned} L &= [e_1(\xi, \eta), \dots, e_N(\xi, \eta)] \\ &= \begin{bmatrix} \int_{c_{i,1}} e_1(\xi, \eta) d\xi d\eta & \dots & \int_{c_{i,1}} e_N(\xi, \eta) d\xi d\eta \\ \vdots & & \vdots \\ \int_{c_{i,N}} e_1(\xi, \eta) d\xi d\eta & \dots & \int_{c_{i,N}} e_N(\xi, \eta) d\xi d\eta \end{bmatrix}^{-1} \\ &\times \begin{bmatrix} \frac{V_1}{2V} \\ \ddots \\ \frac{V_N}{2V} \end{bmatrix}. \end{aligned} \quad (6.52)$$

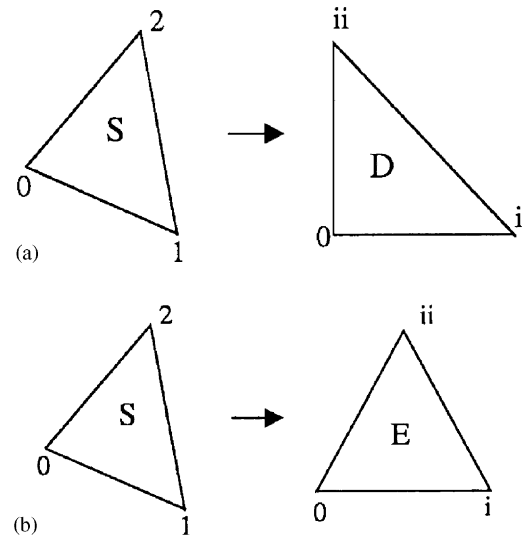


Fig. 113. The schematic of the mapping from the physical triangle to the standard triangle.

The reconstruction formula of Eq. (6.47) with Eq. (6.52) are used to evaluate the state variables at the quadrature points. Triangles of different shape have identical bases $L_j(\xi, \eta)$ in the transformed space D if their partition into polygonal CVs are similar. The reconstruction is carried out only once for an arbitrary shape triangle. The matrix R in Eq. (6.43) is inverted analytically with *Mathematica* using exact arithmetic to derive the reconstruction coefficients, which are identical for all triangles. Exact integration formulas of polynomials over polygons with arbitrary shape can be found in [261].

All the CVs in a SV use the same data reconstruction therefore, it is not necessary to use a Riemann solver for the interior boundaries between the CVs of a particular SV. For the interior CV boundaries, exact fluxes are used. Use of Riemann fluxes is only necessary at the spectral volume boundaries.

6.4. Linear, quadratic, and cubic SV reconstructions

In the previous section, it was shown that the reconstruction problem is equivalent for all triangles. Different order reconstructions are carried out for the transformed space using the equilateral triangle E of Fig. 113b. The triangle E is partitioned into N nonoverlapping CVs that satisfy the conditions:

- The CVs are symmetric with respect to all symmetries of the triangle.
- The CVs are convex.
- The CVs are polygons with straight lines.

The last condition is not absolutely required but simplifies the formulation. In general, however, isoparametric SV can be used to handle curved boundaries. Possible partitions of the standard equilateral triangle for cubic reconstruction were shown in Fig. 111.

Given a partition a necessary condition for valid reconstruction is that the matrix R of Eq. (6.43) is nonsingular. Furthermore, in the one-dimensional SV it was mentioned that not all nonsingular reconstructions are convergent. High-order polynomial reconstruction based on equidistant CVs, for example, are not convergent in one dimension although the reconstructions are nonsingular.

A criterion for valid, convergent partitions [257] is based on the value of

$$\|\Gamma_{II}\| = \max_{\xi \in E} \sum_{j=1}^N |L_j(\xi, \eta)|, \quad (6.53)$$

where

$$\lambda(\xi, \eta) = \sum_{j=1}^N |L_j(\xi, \eta)| \quad (6.54)$$

is referred to as Lebesgue function of the interpolation and $\|\Gamma_{II}\|$ is the Lebesgue constant. The smaller the Lebesgue constant the better the interpolation polynomial. Therefore the criterion for the best partition is to obtain small $\|\Gamma_{II}\|$. Partitions of the standard equilateral triangle E which support linear, quadratic, and cubic reconstructions with small Lebesgue constants were given in [257].

6.5. Spectral volume partitions

Consider the standard equilateral triangle E and partitions of E in convex, symmetric CVs with straight edges. Partitions in CVs that contain the centroid of E must be symmetric with respect to the three edges and vertices. Simple inspection shows that at most one type of CV can exist, and this CV is said to possess degree 1 symmetry. Similarly, a CV is said to possess degree 3 symmetry when two other symmetric CVs exist in the same partition, and 6 symmetry when five other symmetric CVs exist in the same partition. The degrees of 1, 3, and 6 symmetry groups in a partition are denoted as n_1 , n_3 , and n_6 . Partitions with different degrees of symmetry are shown in Fig. 111 for cubic spectral volumes. Different partitions for linear and quadratic spectral volumes are shown in Figs. 109 and 108, respectively.

The total number of CVs in the partition $n_1 + 3n_3 + 6n_6$ is equal to the dimension of the approximation space that supports the unique reconstruction polynomial of

degree m , i.e.

$$n_1 + 3n_3 + 6n_6 = \frac{(m+1)(m+2)}{2}. \quad (6.55)$$

Linear SV ($m = 1$): The solution of Eq. (6.55) for $m = 1$ yields two partitions. These partitions, Type 1 and Type 2 are shown in Fig. 109a and b, respectively. The Lebesgue constant for Type 1 is $\frac{13}{3} = 4.3333$ and for Type 2 $\frac{43}{15} = 2.8667$, therefore, the \mathcal{L}_∞ error with Type 2 should be smaller than the error with Type 1 SV located at the middle of the edge.

Linear reconstruction requires 1G quadrature point, for the evaluation of the line integral. Due to symmetry, functional values of the cardinal bases are required at two quadrature points, i.e. total of six coefficients which are the same for all triangles with similar partitions.

Quadratic SV ($m = 2$): The solution of Eq. (6.55) for $m = 2$ yields two partitions. These partitions are shown in Figs. 110a and b, respectively. The partition of Fig. 110b is singular. For the partition of Fig. 110a all partitions with $0 < d < 0.5$ are admissible. The partitions $d = \frac{1}{3}$ and $d = \frac{1}{4}$ (corresponding to the Gauss-Lobatto points of the edge) were considered in [257]. The partition with $d = \frac{1}{3}$ is called Type 1 and the partition with $d = \frac{1}{4}$ is called Type 2. The Type 1 partition has Lebesgue constant 9.3333 and for the Type 2 partition the Lebesgue constant is 8, and this partition is expected to yield more accurate results. Quadratic reconstruction requires 2G quadrature points for the evaluation of the line integral. Due to symmetry, 30 coefficients corresponding to functional values of the bases at five quadrature points must be computed and stored.

Cubic SV ($m = 3$): The solution of Eq. (6.55) for $m = 3$ yields two different types of partitions. Among possible partitions shown in Fig. 111, only the partitions of Fig. 111a and c are admissible while the partition of Fig. 111d is singular. Variation of the partition distance d in Fig. 111b affects the value of Lebesgue constant. The smallest value of the Lebesgue constant 3.44485 is obtained for $d = \frac{1}{15}$. Cubic reconstruction requires two Gauss quadrature points for the evaluation of the line integral. Due to symmetry, 100 coefficients corresponding to functional values of the bases at 10 quadrature points must be computed and stored.

6.6. Multidimensional limiters

The TVB idea [262] is used in [257] for the construction of limiters in order to obtain uniform accuracy away from discontinuities. Consider a SV with a partition into N control volumes. Given the cell-averaged values $\bar{u}_{i,j}$ of the variables for all CVs and the $k - 1$ reconstruction polynomial

$\int_{c_{i,j}} p_i(x, y) dV = V_{i,j} \bar{u}_{i,j}$ $j = 1, \dots, N$ and denoting

$$\Delta u_{rq} = p_i(x_{rq}, y_{rq}) - \bar{u}_{i,j}, \quad r = 1, \dots, K, \quad q = 1, \dots, J \quad (6.56)$$

it is not necessary to limit the data if

$$|\Delta u_{rq}| \leq 4Mh_{rq}^2, \quad r = 1, \dots, K, \quad q = 1, \dots, J. \quad (6.57)$$

Similar to the one-dimensional case in Eq. (6.57) M represents some measure of the second derivative of the solution and h_{rq} is the distance from (x_{rq}, y_{rq}) to the centroid of $c_{i,j}$. In Ref. [257], M was selected close to the maximum absolute value of the second derivative over the domain.

If Eq. (6.57) is violated for any r and q , then it is assumed that $\bar{u}_{i,j}$ is near a steep gradient and limiting is applied. Therefore, instead of the polynomial $p_i(x, y)$ in $c_{i,j}$ where Eq. (6.57) is violated it is assumed that the data is linear, i.e.

$$u_{i,j}(x, y) - \bar{u}_{i,j} + \nabla u_{i,j} \cdot (\mathbf{r} - \mathbf{r}_{i,j}) \quad \forall \mathbf{r} \in c_{i,j}, \quad (6.58)$$

where $\mathbf{r}_{i,j}$ is the position vector of the centroid of $c_{i,j}$. At the same time, it is required that the reconstructed solutions at the quadrature points of $c_{i,j}$ satisfy the monotonicity constraint.

$$\bar{u}_{i,j}^{\min} \leq u_{i,j}(x_{rq}, y_{rq}) \leq \bar{u}_{i,j}^{\max}, \quad r = 1, \dots, K, \quad q = 1, \dots, J, \quad (6.59)$$

where $\bar{u}_{i,j}^{\min}$ and $\bar{u}_{i,j}^{\max}$ are

$$\bar{u}_{i,j}^{\max} = \max \left(\bar{u}_{i,j} \max_{1 \leq r \leq K} \bar{u}_{i,j,r} \right),$$

$$\bar{u}_{i,j}^{\min} = \min \left(\bar{u}_{i,j} \min_{1 \leq r \leq K} \bar{u}_{i,j,r} \right), \quad (6.60)$$

where $\bar{u}_{i,j,r}$ denotes cell averages at neighboring CV of $c_{i,j}$ sharing the face r . For highest resolution, the magnitude of the solution gradient $\nabla u_{i,j}$ in Eq. (6.58) must be maximized. Several different approaches were suggested in [257] for the estimation of $\nabla u_{i,j}$.

In the first approach, all gradients are reconstructed using cell-averaged data at $c_{i,j}$ and its neighbors. If any of the reconstructed variable at the quadrature points is out of the range $[\bar{u}_{i,j}^{\min}, \bar{u}_{i,j}^{\max}]$ then the gradient is limited. In the second approach, only one gradient is computed and limited using so that the reconstructed solution at all quadrature points satisfy the monotonicity constraint. This limiter is called “minmod” limiter in [257]. In addition to these approaches where the gradients of the solution are reconstructed using data from neighboring CVs, a third approach was suggested in Ref. [257] that uses the polynomials, which are available in the SV for the reconstruction. The limiter of this approach, which is named “CV” limiter in Ref. [257], is more efficient than the limiters in the other two approaches.

6.7. The SV method for two-dimensional systems

Following the basic formulation for the development of the SV method of [257,258], which was presented in the previous section, Wang et al. [260] continued the development of the SV method for hyperbolic conservation laws. The two-dimensional Euler equations in conservative form $U = [\rho, \rho u, \rho v, \rho E]$ were considered [260]. The cell-averaged conservative variable u of any conservative variable in U is

$$\bar{u}_{i,j}(t) = \frac{\int_{c_{i,j}} u(x, y, t) dx dy}{V_{i,j}}, \quad j = 1, \dots, m, \quad i = 1, \dots, N, \quad (6.61)$$

where $V_{i,j}$ is the volume of $c_{i,j}$. Given the cell averages from Eq. (6.61) a polynomial $p_i(x, y)$ of degree $k-1$ at most ($p_i(x, y) \in P^{k-1}$) can be obtained such that $p_i(x, y)$ is a k th order accurate approximation of $u(x, y)$ inside S_i , i.e.

$$p_i(x, y) = u(x, y) + \mathcal{O}(h^k), \quad (x, y) \in S_i, \quad i = 1, \dots, N. \quad (6.62)$$

The reconstruction polynomial

$$\frac{\int_{c_{i,j}} p_i(x, y) dx dy}{V_{i,j}} = \bar{u}_{i,j}, \quad j = 1, \dots, m \quad (6.63)$$

can be found analytically as for the scalar equation case and is expressed as

$$p_i(x, y) = \sum_{j=1}^m L_j(x, y) \bar{u}_{i,j}, \quad (6.64)$$

where $L_j(x, y) \in P^{k-1}$ are the shape functions satisfying

$$\frac{\int_{c_{i,j}} L_m(x, y) dx dy}{V_{i,j}} = \delta_{jm}. \quad (6.65)$$

The shape functions can be obtained analytically. The values of the shape functions at the Gauss quadrature points are given by Wang et al. [260].

The integral form of the Euler equations for CV mean values is

$$\frac{d\bar{U}_{i,j}}{dt} + \frac{1}{V_{i,j}} \sum_{r=1}^K \oint_{S_r} (\mathbf{f} \cdot \mathbf{n}) dS = 0, \quad (6.66)$$

where $\bar{U}_{i,j}$ is the CV-averaged vector of the conservative variables in $c_{i,j}$, $\mathbf{f} = (E, F)$, is the flux vector K is the number of faces of the control volume $c_{i,j}$, and S_r denotes the r th face (edge) of $c_{i,j}$. The surface (line) integrals are evaluated numerically using a k th order accurate Gauss quadrature formula as follows

$$\oint_{S_r} (\mathbf{f} \cdot \mathbf{n}) dS = \sum_{q=1}^J \omega_{rq} \mathbf{f}(U(x_{rq}, y_{rq})) \cdot \mathbf{n}_r S_r + \mathcal{O}(A_r h)^k, \quad (6.67)$$

where $J = \text{integer}[(k+1)/2]$ is the number of quadrature points on the r th edge, and ω_{rq} are the Gauss quadrature weights. The resulting conservative variables obtained with the polynomial distribution of Eq. (6.64) on each SV are discontinuous across the SV boundaries and flux integration is carried out using approximate Riemann solvers as

$$\mathbf{f}(U(x_{rq}, y_{rq})) \cdot \mathbf{n}_r \\ \approx f_{\text{Riemann}}(U_L(x_{rq}, y_{rq}), U_R(x_{rq}, y_{rq}), \mathbf{n}_r). \quad (6.68)$$

Using Eqs. (6.65)–(6.67) obtain the following semi-discrete scheme for the CV $c_{i,j}$

$$\frac{d\bar{U}_{i,j}}{dt} + \frac{1}{V_{i,j}} \sum_{r=1}^K \sum_{q=1}^J \omega_{rq} \\ \times f_{\text{Riemann}}(U_L(x_{rq}, y_{rq}), U_R(x_{rq}, y_{rq}), \mathbf{n}_r) S_r = 0. \quad (6.69)$$

The Roe's and Rusanov approximate Riemann solvers were used in [260]. The flux evaluation with these Riemann solvers is obtained as

Roe's flux:

$$f_{\text{Roe}}(U_L, U_R, \mathbf{n}) \\ = \frac{1}{2}[f(U_L) + f(U_R) - |\bar{A}|(U_R - U_L)], \quad (6.70)$$

where $A = \frac{\partial E}{\partial U} n_x + \frac{\partial F}{\partial U} n_y$ and

$$|\bar{A}| = R|\bar{A}|R^{-1} \quad (6.71)$$

with R and R^{-1} the right and left eigenvector matrices, and Λ the diagonal eigenvalue matrix all evaluated at the Roe-averages.

Rusanov flux:

$$f_{\text{Rusanov}}(U_L, U_R, \mathbf{n}) \\ = \frac{1}{2}[f(U_L) + f(U_R) - \alpha(U_R - U_L)], \quad (6.72)$$

where α is the maximum absolute eigenvalue

$$\alpha = |\bar{v}_n| + \bar{c}, \quad (6.73)$$

where \bar{v}_n and \bar{c} are the average normal velocity and sound speed computed from U_L and U_R .

6.8. Multidimensional TVD and TVB limiters

Stability is maintained for the nonlinear Euler equations by performing data limiting with TVD or TVB limiters. TVD limiters enforce strict monotonicity by degrading solution accuracy at local extrema. TVB limiters relax monotonicity requirements in order to achieve uniform accuracy away from discontinuities.

The limiters in [260] the component-wise limiting approach was chosen because of its efficiency compared with the characteristic-wise approach of limiting. The following numerical monotonicity criterion was established in [260] for each CV.

$$\bar{u}_{i,j}^{\min} \leq u_{i,j}(x_{rq}, y_{rq}) \leq \bar{u}_{i,j}^{\max}, \quad (6.74)$$

where $\bar{u}_{i,j}^{\min}$ and $\bar{u}_{i,j}^{\max}$ are the minimum and the maximum cell-averaged solutions among all neighboring CVs. The neighboring CVs either share a face (face neighbors) or a node (node neighbors) with $c_{i,j}$, which is the control volume under consideration. For the second-order scheme, the face neighbors (see Fig. 109a) were used to define $\bar{u}_{i,j}^{\min}$ and $\bar{u}_{i,j}^{\max}$ for the limiter. This choice was made in order to reduce the number of cells that are limited in the higher-order schemes. The TVB idea is employed for limiting in [260] and small oscillations are allowed in the solution. Expressing the reconstruction for the quadrature points as

$$\Delta u_{rq} = p_i(x_{rq}, y_{rq}) - \bar{u}_{i,j} \quad (6.75)$$

no limiting is required if

$$|\Delta u_{rq}| \leq 4M_q h_{rq}^2, \quad (6.76)$$

where $h_{rq} = |r_{i,j} - r_{rq}|$ is the distance of the CV centroid to the quadrature point. Similar to the scalar case, M_q can be chosen to be the maximum second derivative of the solution. In [260], M_q was scaled as

$$M_q = M(\bar{u}^{\max} - \bar{u}^{\min}), \quad (6.77)$$

where \bar{u}^{\min} and \bar{u}^{\max} are computed over the entire computational domain. No data limiting is applied when Eq. (6.76) is satisfied, even if the condition of Eq. (6.75) is not fulfilled. A CV is assumed to be close to a discontinuity of Eq. (6.76) and (6.75) are violated. For limiting, the solution in the CV is assumed locally linear, i.e.

$$u_{i,j}(x, y) = \bar{u}_{i,j} + \nabla u_{i,j} \cdot (\mathbf{r} - \mathbf{r}_{i,j}) \quad \forall \mathbf{r} \in c_{i,j}. \quad (6.78)$$

Furthermore, the solution is assumed linear for all other CVs inside an SV if any of the CVs in the SV is limited. The gradient computed with cell-averaged solution that satisfies Eq. (6.76) is limited (replaced) by multiplying with a scalar $\phi \in [0, 1]$ so that Eq. (6.78) becomes

$$u_{i,j}(x, y) = \bar{u}_{i,j} + \phi \nabla u_{i,j} \cdot (\mathbf{r} - \mathbf{r}_{i,j}), \quad (6.79)$$

where the scalar ϕ is computed as

$$\phi = \begin{cases} \min\left(1, \frac{\Delta u_{rq}}{\bar{u}_{i,j}^{\max} - \bar{u}_{i,j}}\right) & \text{if } \Delta u_{rq} > 0, \\ \min\left(1, \frac{\Delta u_{rq}}{\bar{u}_{i,j}^{\min} - \bar{u}_{i,j}}\right) & \text{if } \Delta u_{rq} < 0, \\ 1 & \text{otherwise.} \end{cases} \quad (6.80)$$

For $M = 0$, this limiter becomes TVD.

At the interior CV boundaries inside a SV the reconstructed conservative variables are continuous, since the analytical flux is used if no limiters are imposed. The monotonicity condition of Eq. (6.75) does not guarantee positive pressure for problems with strong discontinuities because it strictly enforces monotonicity

only for the conserved variables. To ensure positive pressure near strong discontinuities it is suggested in [260] to limit pressure instead of total energy. The total energy is computed at the quadrature points using the limited reconstructed density, momentum and pressure. This limiting that guarantees positivity in both density and pressure was found very robust [260].

6.9. The SV method for the Navier–Stokes equations

The SV method was recently extended to solve the Navier–Stokes equations [263]. The viscous terms were treated with a mixed formulation named in [263] local discontinuous Galerkin approach. It was shown [263] that the desired order of accuracy is achieved with this formulation for the scalar advection diffusion equation and for the Navier–Stokes with reconstruction polynomials of all orders. The extension of the SV method to the Navier–Stokes equations is based on developments for the SV method based on the one-dimensional pure diffusion equation [264]. The local SV (LSV) and the penalty SV (PSV) approaches were found consistent, stable and convergent. Furthermore, it was shown [264] that the LSV approach achieved the optimal order of accuracy, i.e. $(k+1)$ th order for degree k polynomial reconstruction, while the PSV approach achieved only k th order accuracy for even k . As a result, the LSV approach was selected in [263] for the extension to the Navier–Stokes equations. The LSV formulation is briefly presented for one-dimensional linear and nonlinear and two-dimensional convection–diffusion equations.

6.9.1. SV formulation for 2D convection–diffusion equation

The convection–diffusion equation in the domain Ω is

$$\frac{\partial u}{\partial t} + \nabla \cdot (\beta u) - \nabla \cdot (\mu \nabla u) = 0, \quad (6.81)$$

where β is the convective speed and μ is the diffusion coefficient. The domain Ω is discretized with the spectral volume method. Following the local DG (LDG) approach an auxiliary variable $q = \nabla u$ was defined in [263] to obtain the following system:

$$q = \nabla u,$$

$$\frac{\partial u}{\partial t} + \nabla \cdot (\beta u) - \nabla \cdot (\mu q) = 0. \quad (6.82)$$

Integrating Eq. (6.82) by parts in $c_{i,j}$ obtain

$$\bar{q}_{i,j} = \frac{1}{V_{i,j}} \sum_{r=1}^K \oint_{S_r} \hat{u} \mathbf{n} dS,$$

$$\frac{d\bar{u}_{i,j}}{dt} + \frac{1}{V_{i,j}} \times \left(\sum_{r=1}^K \oint_{S_r} \beta \hat{u} \cdot \mathbf{n} dS - \sum_{r=1}^K \oint_{S_r} \mu \hat{q} \cdot \mathbf{n} dS \right) = 0. \quad (6.83)$$

Using the Roe approximate Riemann solver, which degenerates in the scalar case to an upwind flux, obtain for the inviscid flux

$$\tilde{u} = \begin{cases} u_L & \beta \cdot \mathbf{n} > 0, \\ u_R & \beta \cdot \mathbf{n} < 0. \end{cases} \quad (6.84)$$

The other two numerical fluxes are defined as

$$\hat{u} = u_L, \quad \tilde{u} = u_R$$

or

$$\hat{q} = q_R, \quad \tilde{q} = q_L. \quad (6.85)$$

The numerical solution of Eqs. (6.83) follows the SV method described in the previous sections.

6.9.2. Extension of the SV method to the NS equations

Consider the two-dimensional Navier–Stokes equations written in conservation form

$$\frac{\partial U}{\partial t} + \nabla \cdot \mathbf{F}_i(U) - \nabla \cdot \mathbf{F}_v(U, \nabla u) = 0, \quad (6.86)$$

where U is the conservative variables vector and \mathbf{F}_i , \mathbf{F}_v are the inviscid and viscous flux vectors, respectively.

Following the LDG approach for the convection–diffusion equation define the following auxiliary variable:

$$G = \nabla U. \quad (6.87)$$

Then Eq. (6.86) becomes

$$\frac{\partial U}{\partial t} + \nabla \cdot \mathbf{F}_i(U) - \nabla \cdot \mathbf{F}_v(U, G) = 0. \quad (6.88)$$

Considering the integral form of Eq. (6.88) for the CV $c_{i,j}$ and integrating by parts obtain

$$\begin{aligned} \bar{G}_{i,j} &= \frac{1}{V_{i,j}} \sum_{r=1}^K \oint_{S_r} U \mathbf{n} dS, \\ \frac{d\bar{U}_{i,j}}{dt} + \frac{1}{V_{i,j}} &\left[\sum_{r=1}^K \oint_{S_r} F_i(U) \cdot \mathbf{n} dS \right. \\ &\left. - \sum_{r=1}^K \oint_{S_r} F_v(U, G) \cdot \mathbf{n} dA \right] = 0. \end{aligned} \quad (6.89)$$

Both U and G are discontinuous at SV boundaries. Therefore, the auxiliary flux, the inviscid fluxes and the viscous fluxes are replaced by numerical fluxes \tilde{U} , \tilde{F}_i , and \tilde{F}_v . The auxiliary and viscous fluxes are defined [263] as

$$\hat{U} \approx U_L,$$

$$\tilde{F}_v \approx \mathbf{F}_v(U_L, G^R). \quad (6.90)$$

For the inviscid fluxes Roe or any other consistent flux splitting can be used.

Numerical tests were carried out in [263] for the linear convection-diffusion equation and for the viscous Burger's equation. It was found that for the linear one-dimensional convection-diffusion equation $u_x + u_x + u_{xx}$ the LSV approach achieved the optimum order of accuracy. For the one-dimensional viscous Burger's equation $u_t + uu_x - \mu u_{xx} = 0$, $\mu = 0.1$, $x \in (0, 1)$ with initial condition $u(x, 0) = -\tanh(x/2\mu)$, boundary condition $u(0, t) = 0$, $u(1, t) = -\tanh(1/2\mu)$, and exact solution $u(x, t) = -\tanh(x/2\mu)$ it was found again that the LSV approach achieved the optimum orders of accuracy in all cases, e.g. second-, third- and fourth-order of accuracy. The LSV approach achieved also optimum orders of accuracy for the two-dimensional convection-diffusion equation $u_t + c(u_x + u_y) - \mu(u_{xx} + u_{yy}) = 0$. Furthermore, the LSV method was tested for laminar flow over a flat plate at $R_e = 500$ and $M = 0.3$. The computed results were in good agreement with the Blasius solution.

6.10. The SV method in three dimensions

The high-order SV method was extended to three dimensions in Ref. [265]. Similar to the two-dimensional case presented in the previous section it was shown [265] that if all grid cell are partitioned into structured subcells, the discretizations become universal and are reduced to the same weighted sum of unknowns involving just a few simple adds and multiplies.

The development of the SV method in three dimensions starts with the integral form for a control volume. Similar to the two-dimensional case the partitions of each SV into CVs depends on the choice of the basis functions for the reconstruction. For a complete polynomial basis, the reconstruction of degree of accuracy k requires a partition into at least N CVs where

$$N = \begin{cases} k+1 & \text{1D}, \\ \frac{(k+1)(k+2)}{2} & \text{2D}, \\ \frac{(k+1)(k+2)(k+3)}{6} & \text{3D}. \end{cases} \quad (6.91)$$

The order of accuracy of the SV method is one order higher than the reconstruction polynomial degree. The optimum choice of parameters for the partitions of the SV in CVs required for certain degree of accuracy is determined by minimizing the Lebesgue constant of the reconstruction matrix (see [265] for details). The partitioning of tetrahedra makes use of the partitioning of the triangular faces. Comments on the partition of triangular faces can be found in previous section. Further information on triangle partitions is given in [265]. Tetrahedra SV partitions, which yield degree of accuracy up to three, all CVs have at least one face of the SV boundary and there are no CVs in the interior of the SV. All the CVs consist of vertices of the 2D CVs for each face of the SV connected to the SV centroid with straight edges. Fig. 114a shows the partition of a SV face into CVs. For linear partition the four CVs are hexahedra with all faces being planar quadrilaterals. There are 12 CV faces on the boundary of the SV and 6 interior CV faces. The CVs for quadratic partitioning (see Fig. 114b) are members of two symmetry groups. For the one-parameter partition, one consists of the four hexahedra at the corners of the SV and includes three interior no planar faces. The other group consists of the six mid-edge polyhedra. Each polyhedron consists of two exterior triangular faces and the two quadrilateral interior faces it shares with the corner CVs. As in the two-dimensional case, an analytic minimum value of the Lebesgue constant does not exist this constant. However, the Lebesgue constant asymptotes to a value of approximately 11. A quadratic partition is shown in Fig. 114b. The six mid-edge CVs are now octahedra with two pentagonal faces on the SV boundary and six interior planar quadrilateral faces.

6.11. Results with the SV method

Application of the spectral volume method showed very good performance for test problems used to demonstrate the accuracy of other high-order accurate methods presented in the previous sections.

The first problem considered in [260] is the isentropic vortex convection (see Section 3 for details on problem definition). Numerical simulations were carried out until

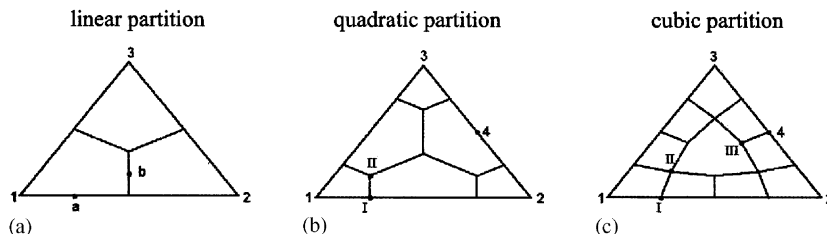


Fig. 114. Two-dimensional faces for three-dimensional SV partitions.

$t = 2$ on both regular and irregular meshes. The Rusanov flux was used and no limiting was necessary for this problem that has smooth solution at all times. It was found that the second-order SV is less accurate than the FV method with the same number of degrees of freedom. However, the third-order SV method was found 3.81 times more accurate than the second-order FV scheme and the fourth-order SV method 435 times more accurate than the second-order FV scheme with the same degrees of freedom. The high-order SV schemes were shown to be [260] more efficient than the second-order FV scheme in achieving the same solution quality. For example, the third-order SV scheme had a relative cost 0.44, and the fourth-order SV scheme had a 0.023 relative cost compared to the FV scheme for the same solution accuracy.

The performance of the spectral volume method was tested extensively in [258] for two problems, suggested by Woodward and Colella [179]. Both problems were used widely to assess the performance of shock-capturing methods. The first problem is the Mach 3 wind tunnel with a step and the second problem is the double Mach reflection. Results for these problems from Ref. [261] that demonstrate the effectiveness and resolution characteristics of the SV method variants, including numerical flux evaluation and effect of limiters, are shown next.

For the Mach 3 wind tunnel problem it is well known that the corner of the step is a singularity that often

leads to a spurious Mach stem at the downstream bottom wall. In the numerical test of [260] no special treatment was used for the singularity. The effect of the

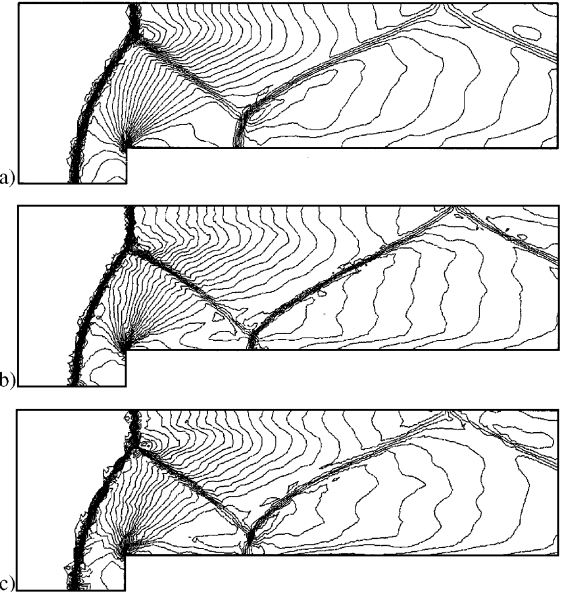


Fig. 116. Density contours computed on the coarse mesh using the Rusanov flux and TVD limiter. Thirty even contour lines between 0.09 and 4.53; (a) second-order SV scheme; (b) third-order SV scheme; (c) fourth-order SV scheme.

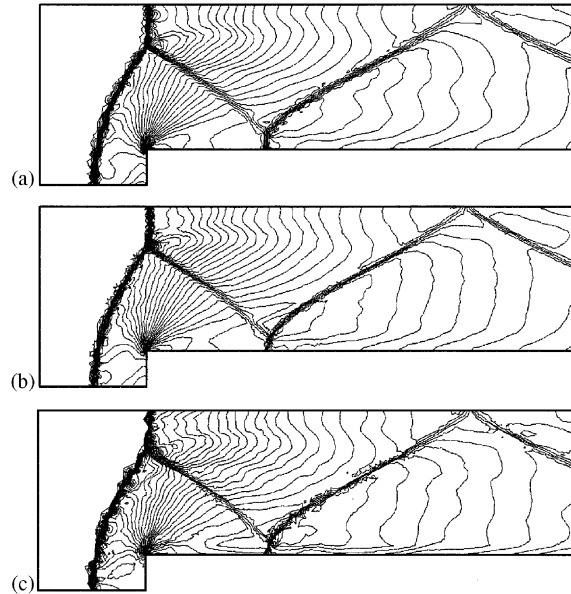


Fig. 115. Density contours computed on the coarse mesh using the Roe flux and TVD limiter. Thirty even contour lines between 0.09 and 4.53; (a) second-order SV scheme; (b) third-order SV scheme; (c) fourth-order SV scheme.

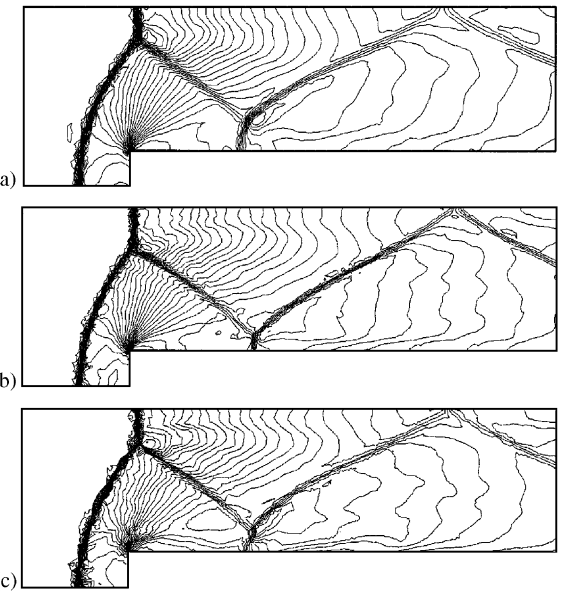


Fig. 117. Density contours computed on the coarse mesh using the Rusanov flux and TVB limiter with $M = 10$. Thirty even contour lines between 0.09 and 4.53; (a) second-order SV scheme; (b) third-order SV scheme; (c) fourth-order SV scheme.

Riemann solver and order of accuracy was tested using a coarse mesh with 1763 triangular elements and $h = \frac{1}{20}$. All simulations for the wind tunnel were carried out until $t = 4$. The computed density contours obtained from numerical solutions with the second-, third-, and fourth-order accurate SV methods, using the Roe flux and the TVD limiter are shown in Fig. 115. The same computations with the Rusanov flux are shown in Fig. 116. In Fig. 117 the effect of the limiter (TVD versus TVB) is demonstrated using again the Rusanov flux. It can be seen that the fourth-order SV performed worse than the second- and third-order SV scheme because many reconstructions were linear due to data

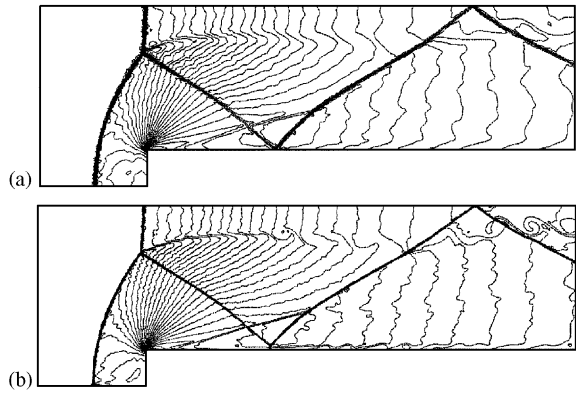


Fig. 118. Density contours computed using a third-order SV scheme with the Rusanov flux and TVD limiter. Thirty even contour lines between 0.09 and 4.53; (a) $h = \frac{1}{40}$ (52,476 DOFs); (b) $h = \frac{1}{80}$ (222,876 DOFs).

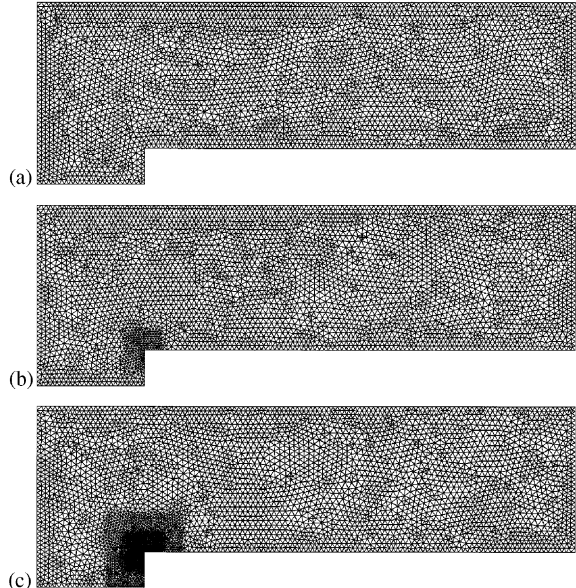


Fig. 119. Three computational grids with different degrees of refinement near the singular corner point.

limiting and the non-uniform subcell mesh produced large errors. The Roe's flux was found less dissipative and produced weaker Mach stems than the Rusanov flux. For the TVB limiter test of Fig. 117 the Mach number was increased to $M = 10$. The performance of the TVB limiter was still very similar with that of the TVD limiter except that the TVB limiter produced more oscillations.

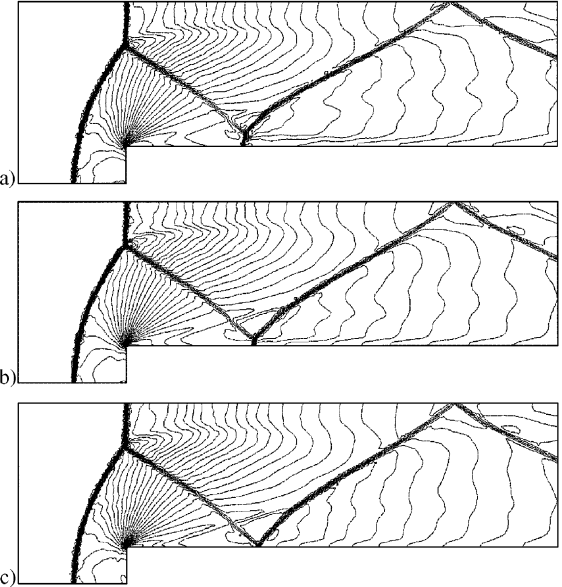


Fig. 120. Computed density contours with the second-order SV scheme using the Rusanov flux and TVD limiter.

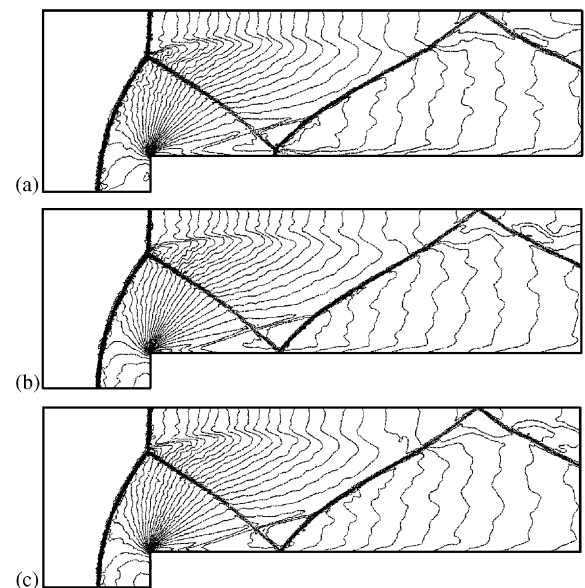


Fig. 121. Computed density contours with the third-order SV scheme using the Rusanov flux and TVD limiter.

Grid refinement studies performed in [260] demonstrated (see Fig. 118) that resolution of the third-order scheme for the medium $h = \frac{1}{40}$ and fine $h = \frac{1}{80}$ grids

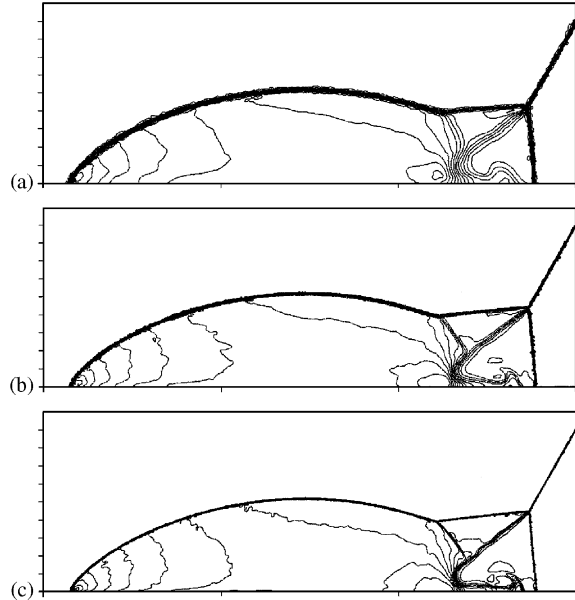


Fig. 122. Density contours computed using a second-order SV scheme with the Rusanov flux and TVD limiter. Thirty even contours between 1.25 and 21.5. (a) $h = \frac{1}{30}$ (24,600 DOFs), (b) $h = \frac{1}{60}$ (98,808 DOFs), (c) $h = \frac{1}{120}$ (392,484 DOFs).

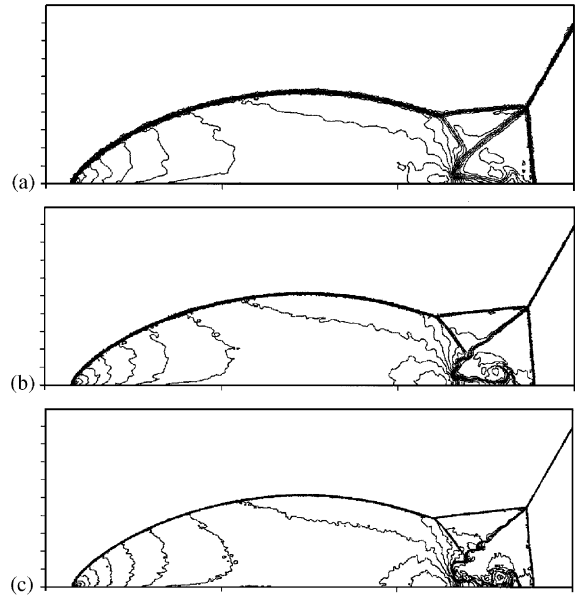


Fig. 123. Density contours computed using a third-order SV scheme with the Rusanov flux and TVD limiter. Thirty even contours between 1.25 and 21.5. (a) $h = \frac{1}{30}$ (49,200 DOFs), (b) $h = \frac{1}{60}$ (197,616 DOFs), (c) $h = \frac{1}{120}$ (784,968 DOFs).

increases significantly. Even though the third-order results were more oscillatory than the second-order results the spurious Mach stems were weaker.

Successive grid refinement, with the meshes shown in Fig. 119, was used to demonstrate that the singular corner is the cause of the spurious Mach stem. Computed density contours from the second- and third-order accurate schemes with the Rusanov flux and the TVD limiter are shown in Figs. 120 and 121, respectively. It can be seen that increased grid density weakened the spurious Mach stem and the entropy layer

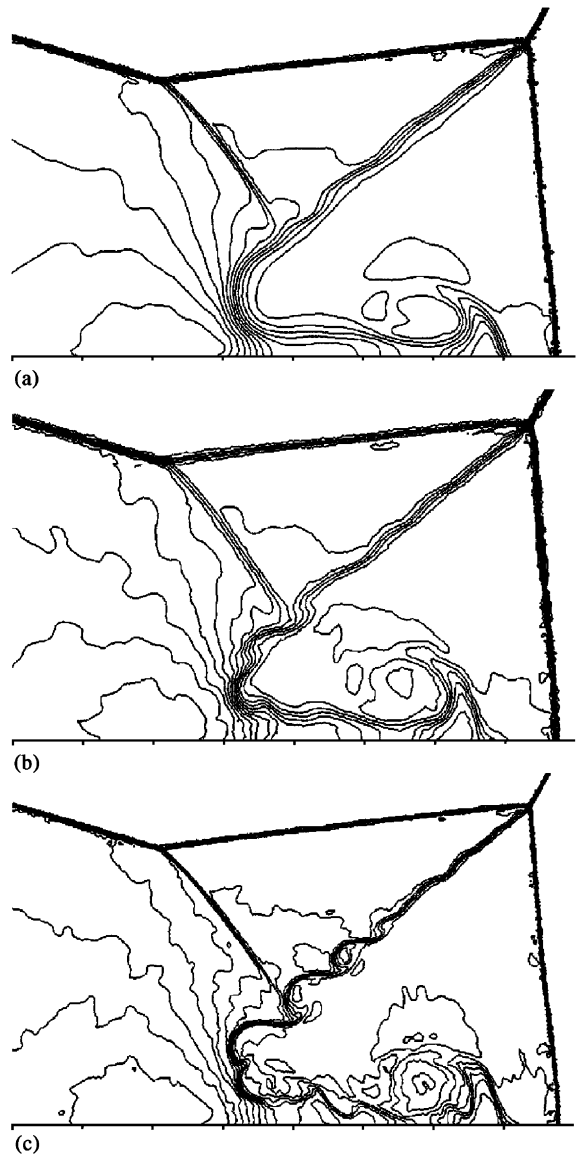


Fig. 124. Close-up view of the density contours near the double Mach stem: (a) second-order SV scheme, $h = \frac{1}{120}$ (392,384 DOFs); (b) third-order SV scheme, $h = \frac{1}{60}$ (197,616 DOFs); (c) third-order SV scheme, $h = \frac{1}{120}$ (784,968 DOFs).

downstream the shock reflection. Higher resolution of shock waves and contact was obtained with the third-order accurate scheme.

The double Mach reflection problem (see Section 4 for the description of the problem) tests were carried out for the Rusanov flux, the TVD limiter, and approximate mesh sizes $\frac{1}{30}$, $\frac{1}{60}$ and $\frac{1}{120}$. The density contours at $t = 0.2$ for the second- and third-order SV schemes are shown in Figs. 122 and 123, respectively. The third-order SV scheme has much higher resolution than the second-order scheme for complex flow structures near the double Mach stem. Fig. 124 shows that the density contours computed with the third-order scheme and half the mesh size ($h = \frac{1}{60}$) display finer structures than the computation performed with the second-order scheme on a fine mesh with mesh size $h = \frac{1}{120}$. The third-order accurate computations of [260] were found to have better resolution than the DG scheme on the same mesh even for computations obtained with DG methods of the same order on finer meshes.

7. Conclusions

For vortical flows without discontinuities, many different numerical schemes can achieve high accuracy. Centered schemes with spectral-type filters work well for these problems. So do all other shock-capturing methods such as schemes with explicit, characteristic-type filters [28,36], essentially non-oscillatory (ENO) schemes [32], weighted WENO schemes [33,34], and the discontinuous Galerkin method. However, only the high-order accurate shock-capturing methods, such as WENO schemes, the DG method, and centered schemes with characteristic-type filters, are suitable for computations of high-speed flows with shocks. Finite-difference centered compact differentiation formulas and WENO schemes are quite efficient computationally. In addition, when combined with implicit time integration methods [149,29] are suitable for the numerical solution of time-dependent high Reynolds number viscous flows. Numerous applications of Sections 3 and 4 demonstrate the potential of these methods.

In Ref. [266], additional important observations were made regarding the efficiency with high-order accurate schemes by examining the local errors achieved when employing polynomial base functions or high-order accurate stencils. These observations stem from the study of a steady advection problem with source in one direction. If the exact solution has a discontinuity in the m th derivative ($m = 0$ denoting discontinuity in the solution), the local error in L_∞ norm is no better than $\mathcal{O}(h^m)$, where h is the mesh size, regardless of the polynomial basis or the stencil order being used. The $\mathcal{O}(h^m)$ accuracy in L_∞ norm is achieved by using k th degree polynomial basis functions with $k \geq m$. In this

case, $\mathcal{O}(h^{m+1/2})$ accuracy is obtained L_2 norm and $\mathcal{O}(h^{m+1})$ accuracy is L_1 norm. For $k > m$, or for regions away from the discontinuities when $k \geq m$, $\mathcal{O}(h^{k+1})$ accuracy is obtained in L_1 , L_2 , and L_∞ norms. Therefore, there is no advantage when a polynomial of degree $k > m$ is used in the vicinity of the discontinuity and for maximal efficiency a polynomial of degree $k = m$ should be used near the discontinuity. For a better capturing of the discontinuity itself, locally h -refinement must be employed. For smooth analytic solutions ($m \rightarrow \infty$), on the other hand, high degree numerical approximations should be used with no or little reliance on local h -refinement similar to spectral methods.

Another aspect of high-order accurate methods is robustness. When the solution has a discontinuity in the m th derivative, then oscillations in the vicinity of the discontinuity appear because of the Gibbs' phenomenon. Oscillations could lead to unphysical states, such as regions with negative pressure or density, during the course of the solution process unless care is taken with slope limiters [38] or shock switches [60,63]. The oscillations, which could appear in the commutated solution for degree of accuracy $k < m$ on coarse or purely resolved meshes, would disappear with grid refinement. In CFD (also in many CAA) applications the governing equations and in many cases the numerical scheme as well is nonlinear. In these cases, inadequate resolution of features could present serious problems, primarily having to do with the solvability of the nonlinear system and secondary, possibly with the unphysical nature of the convergent solution.

The sensitivity to grid quality is another major problem that is common even for second-order accurate methods. Grids are generated based on a priori knowledge of the solution. For example, the number of points and stretching ratio required to resolve boundary layers, vortical structures, and detached layers is usually predetermined. The real power of unstructured grid methods is their ability to adapt to complex flow features without being constrained by considerations such as grid structure and topology. As a result, once a valid solution is obtained on any initial grid, it is at least conceptually possible to adapt the grid, either through grid refinement/coarsening and/or by moving grid points. To date there have been a few notable efforts [267] for relatively simple CFD problems. The real challenge is application of anisotropic grid adaptation for high Reynolds number complex flows. For example, in rotorcraft and high lift applications the flow features of interest are attached and separated boundary layers, wake roll-ups and tip vortices, possible shocks on slats or blade tips and interactions among all these features. It is very likely that the grids produced by adaptation would be highly stretched, deformed, and anisotropic. It is a challenge for current flow solvers to achieve solution reliability and accuracy on anisotropic adapted grids.

The ability to retain high-order accuracy on any grid is even more difficult, but nevertheless remains a key requirement. Several of the recently proposed high-order methods, such as the discontinuous Galerkin finite-element method and the spectral volume methods have the potential to overcome problems associated with anisotropic meshes. However, demonstration was shown only for simple cases.

The discontinuous Galerkin (DG) and the spectral volume (SV), which can be interpreted as a Petrov–Galerkin method where the test and basis functions are different, methods have the potential for grid adaptation. In addition the discontinuous Galerkin method is well suited for *hp*-type refinement and anisotropic adaptation with hanging nodes [222,247]. Second-order accurate discretization with the DG and SV methods are comparable in computing cost to the finite-volume methods. Application of TVB limiters with high-order accurate DG discretizations is computationally intensive. Recently, progress was achieved for efficient high-order computation of flows with discontinuities with the introduction of stabilization operators [222]. A major obstacle for the application of the DG and SV methods in large scale, high-Reynolds number aerodynamic simulations is time step limitation that deteriorates with the increase of the order of the method. Recent progress in implicit time marching algorithms [210,221], space/time DG discretizations [222], and p-type multigrid [207] is expected to make possible high-order accurate computations of practical aerodynamic flows. These developments combined with the DG/VMS method, which combines VMS modeling with the ability of the DG method to obtain high accuracy in complex domains, offer tremendous potential for the accurate simulation of wall-bounded and non-equilibrium turbulence.

Appendix

The Lagrange interpolation polynomials are given by

$$P(x) = \sum_{m=0}^k U(x_{i-r+m-1/2}) \prod_{\substack{l=0 \\ l \neq m}}^k \frac{x - x_{i+r+l-1/2}}{x_{i-r+m-1/2} - x_{i-r+l-1/2}}. \quad (\text{A.1})$$

Subtracting $U(x_{i-r-1/2})$ from both sides of Eq. (A.1) and after some algebra (see article by Shu in [158, pp. 439–582]) obtain the values

$$c_{rj} = \Delta x_{i-r+j} \sum_{m=j+1}^k \frac{\sum_{l=0}^k \prod_{\substack{q=0 \\ q \neq m, l}}^k (x_{i+1/2} - x_{i-r+q-1/2})}{\prod_{\substack{l=0 \\ l \neq m}}^k (x_{i-r+m-1/2} - x_{i-r+l-1/2})} \quad (\text{A.2})$$

Table A.1

k	r	$j = 0$	$j = 1$	$j = 2$	$j = 3$
1	-1	1			
	0	1			
2	-1	$\frac{3}{2}$	$-\frac{1}{2}$		
	0	$\frac{1}{2}$	$\frac{1}{2}$		
	1	$-\frac{1}{2}$	$\frac{3}{2}$		
3	-1	$\frac{11}{6}$	$-\frac{7}{6}$	$\frac{1}{3}$	
	0	$\frac{1}{3}$	$\frac{5}{6}$	$-\frac{1}{6}$	
	1	$-\frac{1}{6}$	$\frac{5}{6}$	$\frac{1}{3}$	
	2	$\frac{1}{3}$	$-\frac{7}{6}$	$\frac{11}{6}$	
4	-1	$\frac{25}{12}$	$-\frac{23}{12}$	$\frac{13}{12}$	$-\frac{1}{4}$
	0	$\frac{1}{4}$	$\frac{13}{12}$	$-\frac{5}{12}$	$\frac{1}{12}$
	1	$-\frac{1}{12}$	$\frac{7}{12}$	$\frac{7}{12}$	$-\frac{1}{12}$
	2	$\frac{1}{12}$	$-\frac{5}{12}$	$\frac{13}{12}$	$\frac{1}{4}$
	3	$-\frac{1}{4}$	$\frac{13}{12}$	$-\frac{23}{12}$	$\frac{25}{1}$

that simplifies for uniform grid to

$$c_{rj} = \sum_{m=j+1}^k \frac{\sum_{l=0}^k \prod_{\substack{q=0 \\ q \neq m, l}}^k (r - q + 1)}{\prod_{\substack{l=0 \\ l \neq m}}^k (l - m)}. \quad (\text{A.3})$$

The values of the constants c_{rj} for uniform grid and order of accuracy between $k = 1$ and $k = 6$ are given in Table A.1.

From Table A.1 and Eq. (4.5) obtain for example

$$\begin{aligned} u_{i+1/2} &= -\frac{1}{12}\bar{u}_{i-1} + \frac{7}{12}\bar{u}_i + \frac{7}{12}\bar{u}_{i+1} - \frac{1}{12}\bar{u}_{i+2} + \mathcal{O}(\Delta x^4), \\ u_{i+1/2} &= \frac{49}{20}\bar{u}_{i-1} - \frac{71}{20}\bar{u}_{i+2} + \frac{79}{20}\bar{u}_{i+3} \\ &\quad - \frac{163}{60}\bar{u}_{i+4} + \frac{31}{30}\bar{u}_{i+5} - \frac{1}{6}\bar{u}_{i+6} + \mathcal{O}(\Delta x^6). \end{aligned}$$

References

- [1] Yee HC, Sandham ND, Djomehri MJ. Low-dissipative high-order shock capturing methods using characteristic-based filters. J Comp Phys 1999;150(1):199–238.
- [2] Sagaut P, Germano M. Large eddy simulation for incompressible flow flows. Berlin: Springer; 2001.
- [3] Germano M, Piomelli U, Moin P, Gobato WH. A dynamic subgrid-scale eddy viscosity model. Phys Fluids A 1991; 3(7):1760–5.
- [4] Lilly DK. A proposed modification of the Germano subgrid-scale closure method. Phys Fluids A 1992;4(3): 633–5.
- [5] Balaras E, Benocci C, Piomelli U. Finite-difference computations of high-Reynolds number flows using

- dynamic subgrid-scale model. *Theoret Comput Fluid Dyn* 1995;7:207–16.
- [6] Ghosal S, Lund TS, Moin P, Akselvoll K. A dynamic localization model for large-eddy simulation of turbulent flows. *J Fluid Mech* 1995;286:229–55.
- [7] Ghosal S, Moin P. The basic equations for large-eddy simulation of turbulent flows in complex geometry. *J Comp Phys* 1995;118(1):24–37.
- [8] Spalart PR. Strategies for turbulence modeling and simulations. *Inter J Heat Fluid Flow* 2000;21(3):252–63.
- [9] Nikitin NV, Nicoud F, Wasistho B, Squires KD, Spalart PR. Approach to wall modeling in large-eddy simulation. *Phys Fluids* 2000;12(7):1629–32.
- [10] Stelzer M. Detached eddy simulation of massively separated flows. *AIAA Paper* 2001-0897, AIAA 2001.
- [11] Canuto C, Hussaini MY, Quarteroni A, Zang TA. Spectral methods in fluid dynamics. New York: Springer; 1987.
- [12] Kopriva DA. A conservative staggered-grid Chebyshev multidomain method for compressible flows, II. A semi-structured method. *J Comp Phys* 1996;128(2):475–88.
- [13] Menter FR, Kuntz M, Benter R. A Scale-adaptive simulation model for turbulent flow predictions. *AIAA Paper* 2003-0767, AIAA 2003.
- [14] Ekaterinaris JA. Effects of spatial order of accuracy on the computation of vortical flowfields. *AIAA J* 1994; 32(12):2471–4.
- [15] Dacles-Mariani J, Zilliac GG, Chow JS, Bradshaw P. Numerical experimental wingtip vortex in the near field. *AIAA J* 1995;33(9):1561–8.
- [16] Strawn R, Ahmad J. Computational modeling of hovering rotors and wakes. *AIAA Paper* 2000-0110, AIAA 2000.
- [17] Strawn RC, Barth TJ. A finite-volume Euler solver for computing rotary-wing aerodynamics of unstructured meshes. Proceeding of 48th annual helicopter society forum, vol. 1. Washington, DC: American Helicopter Society, 1992. p. 419.
- [18] Ahmad JU, Strawn RC. Hovering rotor and wake calculations with an overset-grid Navier–Stokes solver. 55th annual forum of the American helicopter society, Montreal, Canada, 1999. p. 25–7.
- [19] Rai MM. Navier–Stokes simulations of blade–vortex interaction using high-order accurate upwind schemes. *AIAA Paper* 1987-0543, AIAA 1987.
- [20] Wake BE, Choi D. Investigation of high-order upwinded differencing for vortex convection. *AIAA J* 1996; 34(2):332–7.
- [21] Hariharan N, Sankar LN. High-order numerical simulations of rotor flow field. Proceeding of 50th annual helicopter society forum, vol. 2. Washington, DC: American Helicopter Society; 1992. p. 1275.
- [22] Usta E. Application of a symmetric TVD scheme to aerodynamics of rotors. PhD thesis, GA Institute of Technology, Atlanta, GA, 2002.
- [23] von Neumann J, Richtmyer RD. A method for the numerical calculation of hydrodynamic shocks. *J Appl Phys* 1950;21:232–7.
- [24] Drikakis D. Advances in turbulent flow computations using high resolution methods. *Prog Aerospace Sci* 2003;39(6–7):405–24.
- [25] Fureby C, Grinstein FF. Monotonically integrated large eddy simulation of free shear flows. *AIAA J* 1999; 37(5):554–6.
- [26] Lee S, Lele SK, Moin P. Interaction of isotropic turbulence with shock waves: effect of shock strength. *J Fluid Mech* 1997;340:225–47.
- [27] Garnier E, Mossi M, Sagaut P, Comte P, Deville M. On the use of shock-capturing schemes for large-eddy simulations. *J Comp Phys* 1999;153(2):273–311.
- [28] Gaitonde DV, Visbal MR. Pade-type high-order boundary filters for the Navier–Stokes equations. *AIAA J* 2000;38(11):2103–12.
- [29] Rizzetta DP, Visbal MR, Gaitonde DP. Large-eddy simulation of supersonic compression ramp flow by high-order method. *AIAA J* 2001;39(12):2283–92.
- [30] Engquist B, Loetstedt P, Sjögreen B. Nonlinear filters for efficient shock computation. *Math Comp* 1989;52: 232–48.
- [31] Yee HC. Explicit and implicit multidimensional compact high-resolution shock-capturing methods: formulation. *J Comp Phys* 1997;131(2):216–32.
- [32] Shu CW, Osher S. Efficient implementation of essentially non-oscillatory shock-capturing schemes. *J Comp Phys* 1988;77(2):439–71.
- [33] Jiang GS, Shu CW. Efficient implementation of weighted ENO schemes. *J Comp Phys* 1996;126(1):202–28.
- [34] Balsara DS, Shu CW. Monotonicity preserving weighted essentially non-oscillatory schemes with increasingly high order of accuracy. *J Comp Phys* 2000;160(2):405–52.
- [35] Harten A. The artificial compression method for computation of shocks and contact discontinuities, III self-adjusting hybrid schemes. *Math Comp* 1978;32:363–89.
- [36] Garnier E, Sagaut P, Deville M. A class of explicit ENO filters with application to unsteady flows. *J Comp Phys* 2001;170(1):184–204.
- [37] Anderson DA, Tannehill JC, Pletcher RH. Computational fluid mechanics and heat transfer. New York: McGraw-Hill; 1984.
- [38] LeVeque RJ. Finite volume methods for hyperbolic problems. Cambridge Text in Applied Mathematics. Cambridge: Cambridge University Press; 2002.
- [39] Drikakis D, Rider W. High resolution methods for incompressible and low speed flows. Berlin: Springer; 2004.
- [40] Ciarlet PG. The finite element method for elliptic problems. Amsterdam: North-Holland; 1980.
- [41] Baker AJ. Finite element computational fluid mechanics. New York: Hemisphere Publication Corporation; 1983.
- [42] Hughes TJR. The finite element method. Englewood Cliffs, NJ: Prentice-Hall; 1987.
- [43] Karniadakis GE, Sherwin SJ. Spectral-hp element methods. Oxford: Oxford University Press; 1999.
- [44] Solin P, Segeth K, Dolezel I. Higher-order finite element methods. London/Boca Raton: Chapman & Hall/CRC; 2004.
- [45] Cockburn B, Karniadakis GE, Shu CW. Discontinuous Galerkin methods. Berlin: Springer; 1999.
- [46] Wang ZJ. Spectral (Finite) volume method for conservation laws on unstructured grids. *J Comp Phys* 2002; 178(1):210–51.

- [47] Kopriva DA. Multidomain spectral solution of the Euler gas-dynamics equations. *J Comp Phys* 1991;96(2):428–50.
- [48] Kopriva DA. Multidomain spectral solution of compressible viscous flows. *J Comp Phys* 1994;115(1):184–99.
- [49] Kopriva DA, Kolas JH. A conservative staggered-grid Chebyshev multidomain method for compressible flows. *J Comp Phys* 1996;125(1):244–61.
- [50] Patera A. A spectral element method for fluid dynamics: laminar flow in a channel with an expansion. *J Comp Phys* 1984;54(2):468–88.
- [51] Hesthaven JS, Teng CH. Stable spectral methods on tetrahedral elements. *SIAM J Sci Comput* 2000;21:2352–80.
- [52] Abgrall R, Roe PL. High order fluctuation splitting schemes on triangular mesh. *J Sci Comput* 2003;19:3–36.
- [53] Carpenter MH, Gottlieb D. Spectral methods on arbitrary grids. *J Comp Phys* 1996;129(1):74–86.
- [54] Hauke G, Hughes TJR. A comparative study of different sets of variables for solving compressible and incompressible flows. *Comput Methods Appl Mech Eng* 1998;153:1–44.
- [55] Chakravarthy SR, Anderson DA, Salas MD. The split-coefficient matrix method for hyperbolic systems of gas dynamic equations. *AIAA Paper* 80-0268, AIAA 1980.
- [56] Rai MM, Moin P. Direct numerical simulation of transition and turbulence in a spatially evolving boundary layer. *J Comp Phys* 1993;109(2):169–92.
- [57] Hirsch C. Numerical computation of internal and external flows. New York: Wiley; 1990.
- [58] Lax P. Hyperbolic systems of conservation laws and the mathematical theory of shock waves, 2nd ed., vol. 11. SIAM Series on Applied Mathematics, Philadelphia, PA: SIAM; 1973.
- [59] Venkatakrishnan V. Perspective on unstructured grid flow solvers. *AIAA J* 1996;34(3):533–47.
- [60] Jameson A, Schmidt W, Turkel E. Numerical simulation of the Euler equations by finite volume methods using Runge–Kutta time stepping schemes. *AIAA Paper* 81-1259, AIAA 1981.
- [61] Jameson A. Solution of the Euler equations for two dimensional transonic flow by a multigrid method. *Appl Math Comput* 1983;13:327–56.
- [62] Hughes TJR, Engel G, Mazzei L, Larson MG. The continuous Galerkin method is locally conservative. *J Comp Phys* 2000;163(2):467–88.
- [63] Hughes TJR, Mallet M. A new finite element formulation for CFD: IV A discontinuity-capturing operator for multidimensional advective–diffusive systems. *Comput Methods Appl Mech Eng* 1986;58(3):329–56.
- [64] Hughes TJR, Franka LP, Hulbert GM. A new finite element formulation for computational fluid dynamics: VIII The Galerkin/least-squares method for advective–diffusive systems. *Comput Methods Appl Mech Eng* 1989;73(2):173–89.
- [65] Shakib F, Hughes TJR, Johan Z. A multi-element group preconditioned GMRES algorithm for nonsymmetric problems arising in finite element analysis. *Comput Methods Appl Mech Eng* 1989;75(1–3):415–56.
- [66] Shabot C. *p-* and *hp-* finite element methods. Theory and applications in solid and fluid mechanics. Oxford; 1998.
- [67] Benek JA, Bunning PG, Steger JL. A 3-D Chimera grid embedding technique. *AIAA Paper* 85-1523, AIAA 1985.
- [68] Steger JL. Implicit finite-difference simulations of flow about arbitrary two-dimensional geometries. *AIAA J* 1978;17(7):679–86.
- [69] Wilcox DC. Turbulence modeling for CFD. DCW Industries Inc.; 1993.
- [70] Steger JL, Warming RF. Flux vector splitting of inviscid gas dynamics equations with application to finite difference methods. *J Comp Phys* 1981;40(2):263–93.
- [71] Yee HC, Vinokur M, Djomehri MJ. Entropy splitting and numerical dissipation. *J Comp Phys* 2000;162(1):33–81.
- [72] Harten A. On the symmetric form of systems of conservation laws with entropy. *J Comp Phys* 1983;49(1):151–64.
- [73] Gerritsen M, Olsson P. Designing efficient solution strategy for fluid flows: I. A stable high-order finite difference scheme and sharp shock resolution for the Euler equations. *J Comp Phys* 1996;129(2):245–62.
- [74] Gerritsen M, Olsson P. Designing efficient solution strategy for fluid flows: II. Stable high-order finite difference schemes on composite adaptive grids with sharp shock resolution. *J Comp Phys* 1998;147(2):293–317.
- [75] Briley RW, McDonald H. An overview and generalization of implicit Navier–Stokes algorithms and approximate factorization. *Comput Fluids* 2001;30(7–8):807–28.
- [76] Brand A, Dendy JE, Ruppel H. The multigrid method for semi-implicit hydrodynamic codes. *J Comp Phys* 1980;34(2):348–70.
- [77] Briggs WL, Henson VE, McCormick SF. *A multigrid tutorial*, 2nd ed. Philadelphia, PA: SIAM; 2000.
- [78] Gear CW. Numerical initial value problems in ordinary differential equations. Englewood Cliffs, NJ: Prentice-Hall; 1971.
- [79] Lambert JD. Computational methods in ordinary differential equations. New York: Wiley; 1973.
- [80] Bucher JC. Numerical analysis of ordinary differential equations. Chichester: Wiley; 1987.
- [81] Gottlieb S, Shu CW. Total variation diminishing Runge–Kutta schemes. *Math Comput* 1998;67:73–85.
- [82] Carpenter M, Kennedy C. Fourth-order 2N-storage Runge–Kutta schemes. NASA TM 109112. NASA Langley Research Center, 1991.
- [83] Williamson JH. Low-storage Runge–Kutta schemes. *J Comp Phys* 1980;35(1):48–56.
- [84] Hu FQ, Hussaini MY, Manthey JL. Low-dissipation and low-dispersion Runge–Kutta schemes for computational acoustics. *J Comp Phys* 1996;124(1):177–91.
- [85] Haras Z, Ta’asan S. Finite difference schemes for long-time integration. *J Comp Phys* 1994;114(2):265–79.
- [86] Tam CKW, Webb JC. Dispersion-relation-preserving finite difference schemes for computational acoustics. *J Comp Phys* 1993;107(1):262–81.
- [87] Hixon R, Turkel E. Compact implicit Mac Cormack-type schemes with high accuracy. *J Comp Phys* 2000;158(1):51–70.
- [88] Beam RM, Warming RF. An implicit finite difference algorithm for hyperbolic systems in conservation-law form. *J Comp Phys* 1976;22(1):87–110.

- [89] Rai MM, Chakravarthy SR. An implicit form of the Osher upwind scheme. *AIAA J* 1986;24(5):735–43.
- [90] Ekaterinaris JA. Implicit, high-resolution, compact schemes for gas dynamics and aeroacoustics. *J Comp Phys* 1999;156(1):272–99.
- [91] Ekaterinaris JA. Implicit high-order accurate-in-space algorithms for the Navier–Stokes equations. *AIAA J* 2000;38(9):1594–602.
- [92] Yoon S, Jameson A. Lower–upper symmetric Gauss–Seidel method for the Euler and Navier–Stokes equations. *AIAA J* 1988;26(9):1025–6.
- [93] Zhang LP, Wang ZJ. A block LU-SGS implicit dual time-stepping algorithm for hybrid dynamic meshes. *Comput Fluids* 2004;33(7):891–916.
- [94] Venkatakrishnan V, Mavriplis DJ. Implicit method for the computation of unsteady flows on unstructured grids. *J Comp Phys* 1996;127(2):380–97.
- [95] Jameson A. Time-dependent calculations using multigrid with applications to unsteady flows past airfoils and wings. *AIAA Paper 91-1596*, AIAA 1991.
- [96] Rai MM, Moin P. Direct simulations of turbulent flow using finite-difference schemes. *J Comp Phys* 1991;96(1):15–53.
- [97] Rogers SE, Kwak D. An upwind difference scheme for time-accurate incompressible Navier–Stokes equations. *AIAA Paper 88-2883*, AIAA 1988.
- [98] Ekaterinaris JA. Numerical simulation of incompressible two-blade rotor flowfields. *AIAA J Propulsion Power* 1998;14(3):367–74.
- [99] Ekaterinaris JA. Upwind scheme for acoustic disturbances generated by low-speed flows. *AIAA Paper 1997;34(9):1448–55*.
- [100] Lele SK. Compact finite difference scheme with spectral-like resolution. *J Comp Phys* 1992;103(1):16–42.
- [101] Vichnevetsky R. Wave propagation analysis of different schemes for hyperbolic equations: a review. *Int J Numer Meth Fluids* 1987;7:409–52.
- [102] Vichnevetsky R, Bowles JB. Fourier analysis of numerical approximations of hyperbolic equations. *SIAM Stud Appl Math* 1995;5.
- [103] Carpenter MH, Gottlieb D, Abarbanel S. The stability of numerical boundary treatments for compact high-order finite-difference schemes. *J Comp Phys* 1993;108(2):272–95.
- [104] Kreiss HO. Stability theory for difference approximations of mixed initial boundary value problems, I. *Math Comp* 1968;22:703–14.
- [105] Gustafsson B, Kreiss HO, Sundstrom A. Stability theory of difference approximations for mixed initial boundary value problems, II. *Math Comp* 1972;26:649–86.
- [106] Adams NA. Direct numerical simulation of turbulent compression ramp flow. *Theoret Comput Fluid Dyn* 1998;12:109–29.
- [107] Chung YM, Tucker PG. Accuracy of higher-order finite-difference schemes on nonuniform grids. *AIAA J* 2003;41(8):1609–11.
- [108] Mahesh K. A family of high-order finite difference schemes with good spectral resolution. *J Comp Phys* 1998;145(1):332–58.
- [109] Zhong X. High-order finite-difference schemes for numerical simulation of hypersonic boundary-layer transition. *J Comp Phys* 1998;144(2):662–709.
- [110] Lockard DP, Brentner KS, Atkins HL. High-accuracy algorithms for computational aeroacoustics. *AIAA J* 1995;33(2):246–53.
- [111] Zhuang M, Chen RF. Optimized upwind dispersion-relation-preserving finite difference schemes for computational aeroacoustics. *AIAA J* 1998;36(12):2146–8.
- [112] Zingg DW. A review of high-order and optimized finite-difference methods for simulating linear wave phenomena. *AIAA Paper 97-2088*, AIAA 1997.
- [113] Gustafsson B, Olsson O. Fourth-order difference method for hyperbolic IBVPs. *J Comp Phys* 1995;117(2):300–13.
- [114] Harten A. On a class of high resolution total-variation-stable finite-difference schemes. *SIAM J Numer Anal* 1984;21:1.
- [115] Yee HC. On symmetric and upwind TVD schemes. *Proceedings of the sixth GAMM-conference on numerical methods in fluid mechanics*, 1985.
- [116] Yee HC, Harten A. Implicit TVD schemes for hyperbolic conservation laws in curvilinear coordinates. *AIAA J* 1987;25:266.
- [117] Sjogreen B, Yee HC. Grid convergence of high order methods for multiscale complex unsteady viscous compressible flows. *J Comp Phys* 2003;185(1):1–26.
- [118] Yee HC. Construction of explicit and implicit symmetric TVD schemes and their applications. *J Comp Phys* 1987;68(1):151–79.
- [119] Roe PL. Approximate Riemann solvers, parameter vectors, and difference schemes. *J Comp Phys* 1981;43(2):357–72.
- [120] Harten A, Hyman JM. A self-adjusting grid for the computation of weak solutions of hyperbolic conservation laws. *J Comp Phys* 1983;50(2):235–69.
- [121] Sjogreen B, Yee HC. Multiresolution wavelet based adaptive numerical dissipation control for shock-turbulence computation. RIACS Report 01.01, NASA Ames Research Center, 2000.
- [122] Roe PL. Upwind schemes using various formulations of the Euler equations. *Numer Methods Euler Equations Fluid Dyn* 1985; 14–31.
- [123] Levy D. Use of a rotated Riemann solver for two-dimensional Euler equations. PhD thesis, The University of Michigan, 1990.
- [124] Danone A, Grossman B. A rotational upwind scheme for the Euler equations. *AIAA Paper 1991*, 91-0635.
- [125] Rumsey CL, vanLeer B, Roe PL. A multidimensional flux function with applications to the Euler and Navier–Stokes equations. *J Comp Phys* 1993;105(2):306–23.
- [126] Godunov SK, Zabrodin AW, Prokopov GP. A difference scheme for two-dimensional unsteady problems of gas dynamics and computation of flow with detached shock wave. *Mater I Mat Fyz* 1961;1:1020.
- [127] Van Leer B. Towards the ultimate conservative difference scheme II. Monotonicity and conservation combined in a second-order scheme. *J Comp Phys* 1974;14(4):361–70.
- [128] Van Leer B. Towards the ultimate conservative difference scheme V. A second order sequel to Godunov's method. *J Comp Phys* 1979;32(1):101–36.

- [129] Colella P, Woodward P. The piecewise parabolic method for gas-dynamical simulations. *J Comp Phys* 1984;54(1): 174–201.
- [130] Barth TJ. Aspects of unstructured grids and finite-volume solvers for the Euler and Navier–Stokes equations. Notes for VKI Lecture Series, 1994. p. 105.
- [131] Barth T, Frederickson P. High order solution of the Euler equations on unstructured grids using quadratic reconstruction. AIAA Paper 90-0013.
- [132] Gaitonde D, Shang JS. Optimized compact-difference-based finite-volume schemes for linear wave phenomena. *J Comp Phys* 1997;138(2):617–43.
- [133] Mitchell BE, Lele SK, Moin P. Direct computation of the sound from a compressible co-rotating vortex pair. *J Fluid Mech* 1995;285:181–202.
- [134] Colonius T, Lele SK, Moin P. Boundary conditions for direct computation of aerodynamic sound generation. *AIAA J* 1993;31(11):1574–82.
- [135] Mohring W. On vortex sound at low Mach number. *J Fluid Mech* 1978;85:685–91.
- [136] Colonius T, Lele SK, Moin P. Sound generation in a mixing layer. *J Fluid Mech* 1997;333:375–409.
- [137] Freund JB. Noise sources in a low-Reynolds-number turbulent jet at Mach 0.9. *J Fluid Mech* 2001;438: 277–305.
- [138] Bodony DJ, Lele SK. Jet noise prediction of cold and hot jet using large-eddy simulation. AIAA Paper 2004-3022, AIAA 2004.
- [139] Lee IC, Kim JW, Lee DJ. An analysis of screech tone noise and its mode change of an axisymmetric supersonic jet using an optimized compact scheme. AIAA Paper 2004-2952, AIAA 2004.
- [140] Li XD, Gao JH. Numerical simulation of axisymmetric supersonic screech tones. AIAA Paper 2004-2951, AIAA 2004.
- [141] Pan FL, Uzun A, Lyrintzis AS. Refraction correlations for surface integral methods in jet aeroacoustics. AIAA Paper 2004-2873, AIAA 2004.
- [142] Tam CWK, Pastouchenka NN. Fine scale turbulence noise from dual stream jets. AIAA Paper 2004-2871, AIAA 2004.
- [143] Inoue O, Hatakeyama N. Sound generation by a two-dimensional circular cylinder in a uniform flow. *J Fluid Mech* 2002;471:285–314.
- [144] Marsden O, Bogey C, Bailly C. High-order curvilinear simulations of flows around non-Cartesian bodies. AIAA Paper 2004-2813, AIAA 2004.
- [145] Golubev VV, Mankbadi RR, Scott JR. Numerical inviscid analysis of nonlinear airfoil response to impinging high-intensity high-frequency gust. AIAA Paper 2004-3002, AIAA 2004.
- [146] Ran H, Colonius T. Numerical simulation of sound radiated from turbulent vortex ring. AIAA Paper 2004-2918.
- [147] Zingg DW, DeRango S, Nemec M, Pulliam TH. Comparison of several spatial discretizations for the Navier–Stokes equations. *J Comp Phys* 2000;160(2): 683–707.
- [148] Visbal MR, Gaitonde DV. High-order-accurate methods for complex unsteady subsonic flows. *AIAA J* 1999; 37(10):1231–9.
- [149] Visbal MR, Gaitonde DV. On the use of higher-order finite-difference schemes on curvilinear and deforming meshes. *J Comp Phys* 2002;181(1):155–85.
- [150] Gamet L, Ducros F, Nicoud F, Poinsot T. Compact finite difference schemes on non-uniform meshes. Application to direct numerical simulations of compressible flows. *Int J Num Meth Fluids* 1999;29(2):159–91.
- [151] Rizzetta DP, Visbal MR, Blaisdell GA. A time-implicit high-order compact differencing and filtering scheme for large-eddy simulation. *Int J Num Meth Fluids* 2003;42(6): 665–93.
- [152] Collis SS, Ghayour K, Heinkenschloss M, Ulbrich M, Ulbrich S. Optimal control of unsteady compressible viscous flows. *Int J Num Meth Fluids* 2002;40(1): 1401–29.
- [153] Kim JW, Morris PJ. Computation of supersonic inviscid flow past a cone using high order schemes. *AIAA 2002;40(10):1961–8.*
- [154] Garnier E, Sagaut P, Deville M. Large eddy simulation of shock/boundary-layer interaction. *AIAA J* 2002;40(10): 1933–44.
- [155] Harten A, Osher S. Uniformly high-order accurate nonoscillatory schemes. I. *SIAM J Num Anal* 1987;24(2): 279–309.
- [156] Harten A, Osher S, Engquist B, Chakravarthy S. Uniformly high order essentially non-oscillatory schemes, III. *J Comp Phys* 1987;71(2):231–303.
- [157] Osher S, Chakravarthy S. Upwind schemes and boundary conditions with applications to Euler equation in general geometries. *J Comp Phys* 1983;50(3):447–81.
- [158] Barth TJ, Deconinck H. High-order methods for computational physics. Berlin: Springer; 1999.
- [159] Rogerson A, Meiberg F. A numerical study of the convergence properties of ENO schemes. *J Sci Comput* 1990;5:151–67.
- [160] Shu CW. Numerical experiments on the accuracy of ENO and modified ENO schemes. *J Sci Comput* 1990;5:127–49.
- [161] Fatemi E, Jerome J, Osher S. Solution of the hydrodynamic device model using high order non-oscillatory shock capturing algorithms. *IEEE Trans Comput Aided Des Integrated Circuits Systems* 1991;10:232–44.
- [162] Liu XD, Osher S, Chan T. Weighted essentially non-oscillatory schemes. *J Comp Phys* 1994;115(1):200–12.
- [163] Jiang GS, Wu CC. A high-order WENO finite difference scheme for the equations of ideal magnetohydrodynamics. *J Comp Phys* 1999;150(2):561–94.
- [164] Abgrall A. On essentially non-oscillatory schemes on unstructured meshes: analysis and implementation. *J Comp Phys* 1994;114(1):45–58.
- [165] Casper J, Atkins HL. A finite volume high-order ENO scheme for two-dimensional hyperbolic system. *J Comp Phys* 1993;106(1):62–76.
- [166] Friedrich O. Weighted essentially non-oscillatory schemes for the interpolation of mean values on unstructured grids. *J Comp Phys* 1998;144(1):194–212.
- [167] Shu CW, Osher S. Efficient implementation of essentially non-oscillatory shock capturing schemes II. *J Comp Phys* 1989;83(1):32–78.
- [168] Shi J, Zhang YT, Shu CW. Resolution of high order WENO schemes for complicated flow structures. *J Comp Phys* 2003;186(2):690–6.

- [169] Liu Y. Fourier analysis of numerical algorithms for the Maxwell equations. *J Comp Phys* 1996;124(2):396–416.
- [170] Weirs VG, Candler GV. Optimization of weighted ENO schemes for DNS of compressible turbulence. AIAA Paper 97-1940, AIAA 1997.
- [171] Wang ZJ, Chen RF. Optimized weighted essentially non-oscillatory schemes for linear waves with discontinuity. *J Comp Phys* 2001;174(1):381–404.
- [172] Lin SY, Hu JJ. Parameter study of weighted essentially non-oscillatory schemes for computational aeroacoustics. *AIAA J* 2001;39(3):371–9.
- [173] Pirozzoli S. Conservative hybrid compact-WENO schemes for shock-turbulence interaction. *J Comp Phys* 2002;178(1):81–117.
- [174] Ren YX, Liu M, Zhang H. A characteristic-wise hybrid compact-WENO scheme for solving hyperbolic conservation laws. *J Comp Phys* 2003;192(2):365–86.
- [175] Adams NA, Shariff KA. A high-resolution hybrid compact-ENO scheme for shock-turbulence interaction problems. *J Comp Phys* 1996;127(1):27–51.
- [176] Casper J, Atkins H. Comparison of two formulations for high-order accurate essentially nonoscillatory schemes. *AIAA J* 1994;32(4):1970–7.
- [177] Ekaterinaris JA. Performance of high-order accurate low-diffusion numerical schemes for compressible flow. *AIAA J* 2004;42(3):493–500.
- [178] Yang JY, Perng YC, Yen RH. Implicit weighted essentially nonoscillatory schemes for the compressible Navier-Stokes equations. *AIAA J* 2001;39(11):2082–90.
- [179] Woodward P, Colella P. The numerical simulation of two-dimensional fluid flow with strong shocks. *J Comp Phys* 1984;54(1):115–73.
- [180] Grasso F, Pirozzoli S. Shock-wave vortex interactions: shock and vortex deformations, and sound production. *Theoret Comput Fluid Dyn* 2000;13(6):421–56.
- [181] Grasso F, Pirozzoli S. Simulations and analysis of the coupling process of compressible vortex pairs: free evolution and shock induced coupling. *Phys Fluids* 2001;13(5):1343–66.
- [182] Pirozzoli S, Grasso F, D'Andrea A. Interaction of a shock wave with two counter-rotating vortices: shock dynamics and sound production. *Phys Fluids* 2001;13(11):3460–81.
- [183] Pirozzoli S. Dynamics of ring vortices impinging on planar shock waves. *Phys Fluids* 2004;16(5):1171–85.
- [184] Adams NA. Direct simulation of the turbulent boundary layer along a compression ramp at $M = 3$ and $R_e = 1685$. *J Fluid Mech* 2000;420:47–83.
- [185] Ponziani D, Pirozzoli S, Grasso F. Development of optimized weighted-ENO schemes for multiscale compressible flows. *Int J Num Meth Fluids* 2003;42(9):953–77.
- [186] Dexun F, Yanwen M. Analysis of super compact finite difference method and application to simulation of vortex–shock interaction. *Int J Num Meth Fluids* 2001;36(7):773–805.
- [187] Hadjadj A, Kudryavtsev AN, Ivanov MS. Numerical investigation of shock-reflection phenomena in over-expanded supersonic jets. *AIAA J* 2004;43(3):570–7.
- [188] Liang SM, Chen CT, Chen H. Numerical study of supersonic, underwater flows past a blunt body. *AIAA J* 2001;39(6):1123–6.
- [189] Liang SM, Hsu JL, Wang JS. Numerical study of cylindrical blast-wave propagation and reflection. *AIAA J* 2001;39(6):1152–8.
- [190] Chen H, Liang SM. Planar blast/vortex interaction and sound generation. *AIAA J* 2002;40(11):2298–304.
- [191] Hassan O, Morgan K, Peraire J. An implicit finite element method for high speed flows. AIAA Paper 90-0402, AIAA 1990.
- [192] Kallinderis Y, Khawaja A, McMorris H. Hybrid prismatic/tetrahedral grid generation for complex geometries. *AIAA J* 1996;34(2):291–8.
- [193] Luo H, Sharov J, Baum D, Lohner R. On the computation of compressible turbulent flows on unstructured grids. AIAA Paper 2000-0927, AIAA 2000.
- [194] Venkatakrishnan V, Mavriplis DJ. Implicit solvers for unstructured meshes. *J Comp Phys* 1993;105(1):83–91.
- [195] Wang ZJ, Chen RF. Anisotropic Cartesian grid method for viscous turbulent flow. AIAA Paper 2000-0395, 2000.
- [196] Hu C, Shu CW. Weighted essentially non-oscillatory schemes on triangular meshes. *J Comp Phys* 1999;150(1):97–127.
- [197] Delanaye M, Liu Y. Quadratic reconstruction finite volume schemes on 3D arbitrary unstructured polyhedral grids. AIAA Paper 99-3259, 1999, AIAA 1997.
- [198] Cockburn B, Shu CW. TVB Runge–Kutta local projection discontinuous Galerkin finite element method for conservation laws II: general framework. *Math Comp* 1989;52:411–35.
- [199] Cockburn B, Lin SY, Shu CW. TVB Runge–Kutta local projection discontinuous Galerkin finite element method for conservation laws III: one-dimensional systems. *J Comp Phys* 1989;84(1):90–113.
- [200] Cockburn B, Hou S, Shu CW. TVB Runge–Kutta local projection discontinuous Galerkin finite element method for conservation laws IV: the multidimensional case. *Math Comp* 1990;54:545–81.
- [201] Cockburn B, Shu CW. Runge–Kutta discontinuous Galerkin methods for convection-dominated problems. *J Sci Comput* 2001;16(3):173–261.
- [202] Zhang M, Shu CW. An analysis of three different formulations of the discontinuous Galerkin method for diffusion equations. *Math Models Methods Appl Sci* 2003;13(3):395–413.
- [203] Bassi F, Rebay S. A high-order accurate discontinuous finite element method for the numerical solution of the compressible Navier–Stokes equations. *J Comp Phys* 1997;131(1):267–79.
- [204] Baumann CE, Oden JT. A discontinuous hp finite element method for convection–diffusion problems. *Comput Methods Appl Mech Eng* 1999;175:311–41.
- [205] Reed WH, Hill TR. Triangular mesh methods for the neutron transport equation. Technical report LA-UR-73-479, Los Alamos Scientific Laboratory, 1973.
- [206] Cockburn B, Shu CW. The Runge–Kutta discontinuous Galerkin method for conservation laws V: multidimensional systems. *J Comp Phys* 1998;141(2):199–224.

- [207] Fidkowski KJ, Darmofal DL. Development of a higher-order solver for aerodynamic applications. AIAA Paper 2004-0436, AIAA 2004.
- [208] Atkins H, Shu CW. Quadrature-free implementation of the discontinuous Galerkin method for hyperbolic equations. *AIAA J* 1998;36:775–82.
- [209] Titarev VA, Toro EF. ADER: arbitrary high order Godunov approach. *J Sci Comput* 2002;17:609–18.
- [210] Hu FQ, Hussaini MY, Rasetarinera P. An analysis of the discontinuous Galerkin method for wave propagation problems. *J Comp Phys* 1999;151(2):921–46.
- [211] Ainsworth M. Dispersive and dissipative behavior of high order discontinuous Galerkin finite element methods. *J Comp Phys* 2004;198(1):106–30.
- [212] Gottlieb D, Hesthaven J. Spectral methods for hyperbolic problems. *J Comp Appl Math* 2001;128:83–131.
- [213] Dyson R. Technique for very high order nonlinear simulation and validation. *J Comp Acoustics* 2002;10:211–29.
- [214] Astley J, Gerdes K, Givoli D, Harari I. Special issue on finite elements for wave problems-preface. *J Comp Acoustics* 2000;8:vii–ix.
- [215] Ihlenburg F. Finite element analysis of acoustic scattering. *Appl Math Sci* 1998;132.
- [216] Thompson L, Pinsky P. Complex wavenumber Fourier analysis of the p-version finite element method. *Comp Mech* 1994;13:255–75.
- [217] Bey KS, Oden JT. hp-version discontinuous Galerkin methods for hyperbolic conservation laws. *Comp Meth Appl Mech Eng* 1996;133:259–86.
- [218] Biswas R, Devine KD, Flaherty JE. Parallel, adaptive finite element methods for conservation laws. *Appl Numer Math* 1994;14:255–83.
- [219] Warburton T, Lomtev I, Du S, Sherwin S, Karniadakis G. Galerkin and discontinuous Galerkin spectral/hp methods. *Comp Meth Appl Mech Eng* 1999;175:343–59.
- [220] Hu FQ, Atkins H. Eigensolution analysis of the discontinuous Galerkin method with non-uniform grids, Part 1: one space dimension. *J Comp Phys* 2002;182(2):516–45.
- [221] Bassi F, Crivellini A, Rebay S, Savini M. Discontinuous Galerkin solutions of the Reynolds-averaged Navier–Stokes and $K-\omega$ turbulence model equations. *Comput Fluids* 2005;34(4–5):507–40.
- [222] Van der Vegt JJW, Van der Ven H. Space time discontinuous Galerkin finite element method with dynamic grid motion for inviscid compressible flows: I. General formulation. *J Comp Phys* 2002;182(2):546–85.
- [223] Cockburn B, Grenaud PA. Error estimates for finite element methods for nonlinear conservation laws. *SIAM J Numer Anal* 1996;33:522–47.
- [224] Jaffre J, Johnson C, Szepessy A. Convergence of the discontinuous Galerkin finite element method for hyperbolic conservation laws. *Math Models Meth Appl Sci* 1995;5:367–81.
- [225] Hughes TJR, Mazzei L, Jansen KE. Large eddy simulation and the variational multiscale method. *Comput Visualization Sci* 2000;3:47–59.
- [226] Hughes TJR, Mazzei L, Oberai AA, Wray AA. The multiscale formulation of large eddy simulation: decay of homogeneous isotropic turbulence. *Phys Fluids* 2001;13(2):505–12.
- [227] Hughes TJR, Oberai AA, Mazzei L. Large eddy simulation of turbulent channel flows by the variational multiscale method. *Phys Fluids* 2001;13(6):1755–4.
- [228] Collis SS. Monitoring unresolved scales in multiscale turbulence modeling. *Phys Fluids* 2001;13(6):1800–6.
- [229] Collis SS. The DG/VMS method for unified turbulence simulation. AIAA Paper 2002. p. 3124.
- [230] Munts EA, Hulshoff SJ, de Borst R. A space–time variational multiscale discretization for LES. AIAA Paper 2004-2132, AIAA 2004.
- [231] Ramakrishnan S, Collis SS. Turbulence control simulation using the variational multiscale method. *AIAA J* 2004;42(4):745–53.
- [232] Karamanos GS, Karniadakis GE. Spectral vanishing viscosity method for large-eddy simulations. *J Comp Phys* 2000;163(1):22–50.
- [233] Germano M, Piomelli U, Moin P, Cabot WH. A dynamic subgrid-scale eddy viscosity model. *Phys Fluids A* 1991;3(7):1760–5.
- [234] Jansen K. The effect of element topology on variational multiscale methods for LES. *Bull Am Phys Soc* 2000;45(9):56.
- [235] Lomtev I, Kirby RM, Karniadakis GE. A discontinuous Galerkin ALE method for compressible viscous flows in moving domains. *J Comp Phys* 1999;155(1):128–59.
- [236] Oden JT, Babuska I, Baumann CE. A discontinuous hp finite element method for diffusion problems. *J Comp Phys* 1998;146(2):491–519.
- [237] Arnold DN, Brezzi F, Cockburn B, Marin LD. Unified analysis of discontinuous Galerkin methods for elliptic problems. *SIAM J Numer Anal*, 2001.
- [238] Wheeler MF. An elliptic collocation-finite element method with interior penalties. *SIAM J Numer Anal* 1978;15:152–61.
- [239] Jr JD, Dupont BL. Interior penalty procedures for elliptic and parabolic Galerkin methods. *Lecture Notes in Physics*, vol. 58. Berlin: Springer; 1976.
- [240] Rasetarinera P, Hussaini MY. An efficient implicit discontinuous Galerkin method. *J Comp Phys* 2001;172(2):718–38.
- [241] Saad Y, Schultz MH. GMRES: a generalized minimum residual algorithm for solving nonsymmetric linear systems. *SIAM J Sci Stat Comp* 1986;7:865–73.
- [242] Iannelli GS, Baker AJ. A stiffly-stable implicit Runge–Kutta algorithm for CFD applications. AIAA Paper 88-0416, AIAA 1988.
- [243] Helenbrook B, Mavriplis D, Atkins H. Analysis of p-multigrid for continuous and discontinuous finite element discretizations. AIAA Paper 2003-3989, AIAA 2003.
- [244] Touloupoulos I, Ekaterinaris JA. High-order discontinuous-Galerkin discretizations for Computational aero-acoustics in complex domains. AIAA Paper 2004-0522, AIAA 2004.
- [245] Hardin JC, Ristorcelli JR, Tam CK. ICASE/LaRC Workshop on Benchmark Problems in Computational Aeroacoustics (CAA), NASA CP 3300, 1995.
- [246] Tam CK, Hardin JC. Second computational aeroacoustics (CAA) workshop on benchmark problems. NASA CP 3352, 1997.

- [247] Van der Vegt JJW, Van der Ven H. Discontinuous Galerkin finite element method with anisotropic local grid refinement for inviscid compressible flow. *J Comp Phys* 1998;141(1):46–77.
- [248] Lin SY, Chin YS. Discontinuous Galerkin finite element method for Euler and Navier–Stokes equations. *AIAA J* 1993;31(11):2016–26.
- [249] Rasentarinera P, Kopriva DA, Hussaini MY. Discontinuous spectral element solution of acoustic radiation from thin airfoils. *AIAA J* 2001;39(11):2070–5.
- [250] Dolejí V. On the discontinuous Galerkin method for the numerical solution of the Navier–Stokes equations. *Int J Num Meth Fluids* 2004;45(10):1083–106.
- [251] Yuzhi SY, Wang ZJ. Evaluation of discontinuous Galerkin and spectral volume methods for scalar and system conservation laws on unstructured grids. *Int J Num Meth Fluids* 2004;45(8):819–38.
- [252] Remaki M, Habashi WG. A discontinuous Galerkin method/HLLC solver for the Euler equations. *Int J Num Meth Fluids* 2003;43(12):1391–405.
- [253] Bassi F, Rebay S. Numerical evaluation of two discontinuous Galerkin methods for the compressible Navier–Stokes equations. *Int J Num Meth Fluids* 2002;40(1):197–207.
- [254] Baumann CE, Oden TJ. A discontinuous hp finite element method for the Euler and Navier–Stokes equations. *Int J Num Meth Fluids* 1999;31(1):79–95.
- [255] Lomtev I, Karniadakis GE. A discontinuous Galerkin method for the Navier–Stokes equations. *Int J Num Meth Fluids* 1999;29(5):587–603.
- [256] Rider WJ, Lowrie RB. The use of classical Lax–Friedrichs Riemann solvers with discontinuous Galerkin methods. *Int J Num Meth Fluids* 2002;40(3):479–86.
- [257] Wang ZJ, Liu Y. Spectral (finite) volume method for conservation laws on unstructured grids II: extension to two-dimensional scalar equation. *J Comp Phys* 2002;179(2):665–97.
- [258] Wang ZJ, Liu Y. Spectral (finite) volume method for conservation laws on unstructured grids III: one-dimensional systems and partition optimization. *J Sci Comp* 2004;20:137–57.
- [259] Zhang M, Shu CW. An analysis and a comparison between the discontinuous Galerkin method and the spectral finite volume methods. *Comput Fluids* 2005;34(4–5):581–92.
- [260] Wang ZJ, Zhang L, Liu Y. Spectral finite volume method for conservation laws on unstructured grids IV: extension to two-dimensional systems. *J Comp Phys* 2004;194(2):716–41.
- [261] Liu Y, Vinokur M. Exact integration of polynomials and symmetric quadrature formulas over arbitrary polygonal grids. *J Comp Phys* 1998;140(1):122–47.
- [262] Shu CW. TVB uniformly high-order schemes for conservation laws. *Math Comp* 1987;49:105–17.
- [263] Sun Y, Wang ZJ. High-order spectral volume method for the Navier–Stokes equations on unstructured grids. *AIAA Paper* 2004-2133, AIAA 2004.
- [264] Sun Y, Wang ZJ. Formulation and analysis of the spectral volume method for the diffusion equation. *Comm Numer Methods Eng*, in press.
- [265] Liu Y, Vinokur M, Wang ZJ. Three-dimensional high-order spectral finite volume method for unstructured grids. *AIAA Paper* 2003-3837, AIAA 2003.
- [266] Venkatakrishnan V, Allmaras SR, Kamenetski DS, Johnson FT. Higher order schemes for the compressible Navier–Stokes equations. *AIAA 2003-3987*, AIAA 2003.
- [267] Habashi WG, Domptierre J, Bourgalut Y, Vallet MG. Certifiable CFD through mesh optimization. *AIAA Journal* 1998;36(5):703–11.
- [268] Panchapakesan NR, Lumley JL. Turbulence measurements in axisymmetric jets of air and helium. Part 1. Air jets. *J Fluid Mech* 1993;246:197–223.
- [269] Hussein HJ, Capp SP, George WK. Velocity measurements in a high Reynolds number momentum-conserving, axisymmetric jet. *J Fluid Mech* 1994;258:31–75.
- [270] Stromberg JL, McLaughlin DK, Troutt TR. Flow field and acoustic properties of a Mach number 0.9 jet at a low Reynolds number. *J Sound Vib* 1980;72:159–76.
- [271] Mollo-Christensen E, Kolpin MA, Martucelli JR. Experiments on jet flows and jet noise far-field spectra and directivity patterns. *J Fluid Mech* 1964;18:285–301.
- [272] Lush PA. Measurements of subsonic jet noise and comparison with theory. *J Fluid Mech* 1971;46:477–500.